Phase Behavior of Binary Ionic Liquid Systems: Ionic Liquids with Ammonia, Carbon dioxide, and Dihydroxy Alcohols

By

Tugba Turnaoglu
M.S., University of Oklahoma, 2013
B.S., Ankara University, 2009

Submitted to the graduate degree program in the Department of Chemical and Petroleum Engineering and the Graduate Faculty of the University of Kansas in partial fulfillment of the requirements for the degree of Doctor of Philosophy.

_____

Chair: Dr. Mark B. Shiflett

_____

Dr. Aaron M. Scurto

_____

Dr. Laurence Weatherley

_____

Dr. Bala Subramaniam

_____

Dr. Brian B. Laird

Date Defended: 10 December 2019

The dissertation committee for Tugba Turnaoglu certifies that this is the approved version of the following dissertation:

Phase Behavior of Binary Ionic Liquid Systems: Ionic Liquids with Ammonia, Carbon dioxide, and Dihydroxy Alcohols

_____

Chair: Mark B. Shiflett

Date Approved: 10 December 2019

This thesis is dedicated to my mother, **Süreyya Turnaoğlu,**
who always lights up my life with
her unconditional love, endless support, and extraordinary wisdom.

Abstract

Solvents play a crucial role in industrial processes, which might directly or indirectly have a bearing on the environment. As engineers and scientists, our goal is to advance or develop more sustainable chemicals to overcome the environmental challenges of the 21st century. Therefore, ionic liquids (ILs) might offer a unique solution.

Ionic liquids are low melting point salts composed entirely of ions. The characteristics of ILs can be designed by varying both the cation, anion, and substituents. Therefore, ILs can be designed to be non-volatile, non-toxic, and environmentally benign. ILs are soluble with a wide range of compounds, allowing the use in various applications such as catalysis, separation, and solvents, to name a few. In order to develop these processes, fundamental phase behavior knowledge is required. The main objective of this thesis is to investigate the phase behavior of ionic liquids with gases (ammonia and carbon dioxide) and organic solvents (diols) over a wide temperature and pressure range. ILs are relatively viscous compared to traditional solvents like water; therefore, in addition to the thermodynamic measurements and modeling, the kinetics of gas dissolution in the ILs were also explored. Nuclear Magnetic Resonance (NMR) spectroscopy was utilized to further advance the understanding of the interaction in binary ionic liquid mixtures (i.e., NH_3+ILs).

In the investigation of the ionic liquid and ammonia system, vapor-liquid equilibrium (VLE) measurements for the binary systems of ammonia (NH_3) with aprotic and protic ionic liquids have been successfully measured using a new Hiden XEMIS gravimetric microbalance. This study reports the first gravimetric measurements conducted for the solubility of NH_3 in ionic liquids and provides the most accurate data to date. The NH_3 sorption measurements were conducted at temperatures of 283.15, 298.15, 323.15, and 348.15 K and at pressures up to 0.7 MPa. The VLE data were correlated using the Peng-Robinson equation of state, the Non-Random Two Liquid

(NRTL), and the Flory-Huggins model. All models are in excellent agreement with the experimental data. The Flory-Huggins model demonstrated that the non-idealities in NH_3 solubility in the imidazolium-based ILs are due to both entropic and enthalpic impacts. The Fickian diffusivities of NH_3 in imidazolium-based ILs were obtained by fitting experimental concentration to the one-dimensional (1D) mass diffusion equation and found to be about 3 to 5 times slower than the diffusion of NH_3 in water. The semi-theoretical Stokes-Einstein equation was used to model diffusivities and to obtain the diffusing radius of NH_3 in imidazolium-based ILs. NMR spectroscopy is utilized to investigate the interaction between NH_3 and imidazolium-based ILs. NMR spectra of the NH_3 systems revealed that the NH_3 interacts with all protons in the cation while interacting with the most acidic hydrogen more profoundly. One exception is the system of ammonia and 1-ethyl-3-methylimidazolium 1,1,2,2-tetrafluoroethanesulfonate where NH_3 interacts with all hydrogens in a similar manner.

In the investigation of IL and carbon dioxide system, the high-pressure vapor-liquid equilibrium for the binary systems of carbon dioxide and a series of 1-alkyl-1-methyl pyrrolidinium bis(trifluoromethylsulfonyl)imide ionic liquids ($[C_nC_1pyr][NTf_2]$ (n = 3,4,6)) are measured at 298.15, 318.15, and 338.15 K and at pressures up to 20 MPa. Experiments were conducted using gravimetric (IGA and XEMIS microbalances) and volumetric (high-pressure view cell) methods. In this study, the solubility of CO_2 in pyrrolidinium ionic liquids increases with increasing pressure and decreasing temperature. However, the high-pressure behavior (above 10 MPa) approaches almost a vertical slope, which indicates the CO_2 solubility only slightly increases despite large increases in pressure. The CO_2 solubility is found to be slightly dependent on the alkyl chain length on the pyrrolidinium cation, which is potentially due to the steric impacts. Molar volume and volume expansion of CO_2 + IL mixtures at high pressures were also measured

and reported. The Fickian diffusion of CO_2 in pyrrolidinium-based ionic liquids (~10^{-10} $m^2 \cdot s$) was calculated at pressures up to 2 MPa and found to be slightly lower than the diffusivity of CO_2 in an imidazolium-based ionic liquid with the [NTf_2] anion.

In the investigation of ionic liquids and dihydroxy alcohols system, liquid-liquid equilibria (LLE) for the mixtures with three imidazolium-based ionic liquids were measured. The dihydroxy alcohols were 1,3-propanediol, 1,4-butanediol, and 1,5-pentanediol and the ionic liquids were 1-ethyl-3-methylimidazolium tetrafluoroborate ([C_2C_1im][BF_4]), 1-ethyl-3-methylimidazolium bis(trifluoromethylsulfonyl)imide ([C_2C_1im][NTf_2]), and 1-ethyl-3-methylimidazolium 1,1,2,2-tetrafluoroethanesulfonate ([C_2C_1im][TFES]). The experimental LLE data were well correlated using the NRTL activity coefficient model, which allows quantification of the miscibility gaps. All binary diol systems with [C_2C_1im][BF_4] or [C_2C_1im][NTf_2] demonstrated an upper critical solution temperature (UCST) between 310 to 360 K. An equimolar mixture of diols and [C_2C_1im][TFES] showed complete miscibility between 293.15 to 373.15 K. An increase in alkyl chain length of the dihydroxy alcohols and/or changing the anion from [BF_4] to [NTf_2] for a given [C_2C_1im] cation results in an increase in the UCST. The excess molar volume of diols with ILs was, in most cases, larger than those of ordinary solutions.

Acknowledgments

During my six-year Ph.D. journey, I worked with many people who helped me to reach this point, and each of them deserves sincere recognition in this thesis.

First and foremost, I would like to give my deepest and sincere gratitude to my thesis advisor Dr. Mark B. Shiflett for his guidance throughout my doctoral degree. I wish there would be enough words to express my unrestrained and grateful appreciation to him for his supervision, advising, support, and guidance throughout my doctoral study. Thanks to him, I was provided numerous opportunities to grow academically over a short period of three years, and his extensive knowledge of science and chemical engineering guided me along the journey. His professionalism, kindness, exemplary leadership, and his continuous passion for research brought motivational energy to the lab every day, which I am thankful for. In our weekly safety meeting breakfasts, we not only embraced the importance of safety but also celebrated each other's success and shared the best moments as a group. It was a great opportunity to work in a highly professional and friendly lab environment, and it was an incredible honor to study under his supervision.

I would also like to extend my deepest and sincere gratitude to Dr. Aaron M. Scurto for being a supportive teaching mentor and a role model for me. I am grateful for the knowledge he instilled in me in years through many scientific discussions. I am deeply indebted to him for the significant contribution he made to my academic development. He was a true role model for me with his commendable work ethics, genuine dedication and passion for teaching, and sincere concerns for his students' success. I am genuinely inspired by his enthusiasm for research, his immense knowledge in science, chemical engineering, and thermodynamics, his contagious positivity, his genuine kindness, thoughtfulness, and generosity. It was a tremendous honor to work with him.

I would also like to express my sincere gratitude and appreciation to Dr. Laurence Weatherley for his extraordinary wisdom, great kindness, fairness, and support. I feel extremely lucky to be a graduate student at the time he has been a department head as he embraces the diversity and equity in our department, welcomes all students from different backgrounds, and sincerely supports our success. I very much enjoyed learning from his exceptional knowledge in chemical engineering and nuclear science over the past six years, and I will truly miss learning from his tremendous experience in industry and academia. I would not be here without his support.

I would also like to extend my sincere gratitude to my committee members, Dr. Bala Subramaniam and Dr. Brian Laird for their time and attention during my studies at the University of Kansas. I also extend my gratitude to Dr. Paul Willhite for his support throughout my degree.

I would like to thank my geology professors, Dr. Gwen Machperson and Dr. Gene Rankey. Dr. Macpherson's classes were two of the best classes that I took at KU. It was a rather challenging but enjoyable experience to apply fundamental physics, chemistry, thermodynamics, and kinetics knowledge to geology. I have learned in-depth water chemistry and the fundamentals of ICP-MS from her, which I very much appreciate. Dr. Rankey's class was the most interesting class I have ever taken in my entire graduate career because I literally knew nothing about Geology, and it was notoriously the most difficult class in the Geology Department. He and the entire class helped me to get through his class successfully. Surely, with their help, I became one of a kind chemical engineer who is knowledgeable about geology. But, more importantly, I made lifelong friends. Thank you all for being great professors, colleagues, friends, and teammates.

I also had the great pleasure of working with many staff in the School of Engineering. I very much appreciate Anna Paradis, Lynn Villafuerte, and Martha Kehr, who I closely teamed up with as a Graduate Engineering Ambassador. Anna, Lynn, and Martha inspire me with their

continuous positive energy. I would also like to thank Adam Lett (Senior IT staff for the School of Engineering) for his continuous, patient, and kind support during the past six years. He and his team have patiently solved many technical IT challenges I encountered. I cannot imagine I could overcome these technical challenges without their support. I also would like to thank Heather Abernathy for her kind and prompt assistance on financial matters. I also would like to thank our building manager Nathan Fortner, who always promptly addresses our issues with kindness and a positive smile.

I also would like to thank the technicians Zach Kessler, Jeff Worth, Scott Ramskill, and Ed Atchison for their assistance with various instrument issues. I would like to also thank Virgil Debique, Katherine McKie, Matt Gee, and Mathew Powner at Hiden Isochema for their technical support last over the past three years with the XEMIS gravimetric microbalance.

I would also like to thank all of the Shiflett research group members, specifically Dr. David Minnick, Dr. William Gilbert, and Alejandra Rocha for their support when I joined the group three years ago.

I also would like to extend my gratitude to my fellow graduate students and dear friends, Dhruv Konwar, John (Changhong) Liu, Aishik Chakraborty, Katie Kuklewicz, Tom Neal, Alejandra Rocha, Simon Morales, Kyle Stephens, Gamze Kati for the best and the most fun memories I had at KU.

Special thanks to Dr. Sarah Neuenswander and Dr. Justin T. Douglas for running NMR samples at the KU NMR Core Lab; Dr. Rajkumar Kore for his help on NMR results; Dr. David Minnick for measuring the solubility and diffusivity of CO_2 in pyrrolidinium ILs using the IGA instrument; Dr. Elim Myers and Dr. David Griffin for their assistance with the MATLAB programming; and undergraduate research assistant Sally Ritchie for working with me on the

liquid-liquid equilibria study. I also would like to acknowledge the financial support of the Idaho National Laboratory on the carbon dioxide study in this dissertation.

I would like to give my special thanks to my dear close friends Burcu Bolukbasi Arikan and Mazhar Arikan, Yanger Tapp, Sevgi Mise, Mesude Ozturk for supporting me for many years with their generous and loving friendships.

I want to express my deepest and special gratitude to my family members. I must thank my parents Sureyya and Metin Turnaoglu, who I constantly feel their support and love. They always emphasized the priority of education, the importance of being independent as a woman, the vitality of integrity and honesty. I am very lucky to have them as my parents. I must thank my siblings and my best friends Jale Turnaoglu, Hale Turnaoglu, and Suleyman Turnaoglu, for their love, understanding, and endless support during the long years of my educational journey. Their continuous attention made my days more cheerful. I also must thank my lovely niece Defne Duru Altunoglu for bringing joy and happiness with her laughter and sweet spirit to me.

Finally, I would like to emphasize my deepest gratitude, sincere appreciation to my mother, Sureyya Turnaoglu for her unconditional support, love, and prayers every day. She patiently and genuinely listened to me, filled me in with her extraordinary wisdom, and supported me despite being thousands of miles away and having an eight-hour difference. It was impossible to complete this degree without her continuous support and love. I am truly thankful to her.

The last but not the least, I am thankful to God. I have seen no person, no injustice, and no disappointment can stop his great plans for me. I am truly blessed.

Additional Acknowledgments

Portions of this thesis have been previously published as articles in journals by the American Chemical Society (ACS) and the American Institute of Physics (AIP) Publishing. The publishers allow the author to reuse published works in the author's thesis, which the author writes and is required to submit to satisfy the criteria of degree-granting institutions. Portions reused from references 1–4.

(1) Turnaoglu, T.; Shiflett, M. B. 110th Anniversary: The First Thermodynamic and Kinetic Analysis of Ammonia in Imidazolium Based Ionic Liquids Using a Gravimetric Microbalance. Ind. Eng. Chem. Res. 2019, 58 (11), 4644–4655.

(2) Turnaoglu, T.; Minnick, D. L.; Morais, A. R. C.; Baek, D. L.; Fox, R. V.; Scurto, A. M.; Shiflett, M. B. High-Pressure Vapor−Liquid Equilibria of 1-Alkyl-1-Methylpyrrolidinium Bis(trifluoromethylsulfonyl)imide Ionic Liquids and CO_2. J. Chem. Eng. Data 2019. https://doi.org/10.1021/acs.jced.8b01236.

(3) Turnaoglu, T.; Ritchie, S. G.; Shiflett, M. B. Liquid-Liquid Equilibria in Binary Mixtures of Dihydroxy Alcohols and Imidazolium-Based Ionic Liquids. J. Chem. Eng. Data 2019, 64 (7), 3179–3186.

(4) Minnick, D. L.; Turnaoglu, T.; Rocha, M. A.; Shiflett, M. B. Review Article: Gas and Vapor Sorption Measurements Using Electronic Beam Balances. J. Vac. Sci. Technol. A 2018, 36 (5), 050801.

Table of Contents

List of Tables

List of Figures

Abbreviations

CO_2	Carbon dioxide
NH_3	Ammonia
H_2O	Water
$[C_2C_1im][BF_4]$	1-ethyl-3-methylimidazolium tetrafluoroborate
$[C_2C_1im][PF_6]$	1-ethyl-3-methylimidazolium hexafluorophosphate
$[C_2C_1im][NTf_2]$	1-ethyl-3-methylimidazolium bis(trifluoromethylsulfonyl)imide
$[C_2C_1im][NO_3]$	1-ethyl-3-methylimidazolium nitrate
$[C_4C_1im][PF_6]$	1-butyl-3-methylimidazolium hexafluorophosphate
$[C_4C_1im][BF_4]$	1-butyl-3-methylimidazolium tetrafluoroborate
$[C_4C_1im][NTf_2]$	1-butyl-3-methylimidazolium bis(trifluoromethylsulfonyl)imide
$[C_6C_1im][BF_4]$	1-hexyl-3-methylimidazolium tetrafluoroborate
$[C_6C_1im][NTf_2]$	1-hexyl-3-methylimidazolium bis(trifluoromethylsulfonyl)imide
$[C_8C_1im][BF_4]$	1-octyl-3-methylimidazolium tetrafluoroborate
$[N_{111}C_2OH][NTf_2]$	choline bis(trifluoromethylsulfonyl)imide
$[(HOC_2)C_1im][BF_4]$	1-(2-hydroxyethyl)-3-methylimidazolium tetrafluoroborate
$[(HOC_2)C_1im][DCA]$	1-(2-hydroxyethyl)-3-methylimidazolium dicyanamide
$[(HOC_2)C_1im][NTf_2]$	1-(2-hydroxyethyl)-3-methylimidazolium bis(trifluoromethylsulfonyl)imide
$[(HOC_2)C_1im][NO_3]$	1-(2-hydroxyethyl)-3-methylimidazolium nitrate
$[(HOC_2)C_1im][PF_6]$	1-(2-hydroxyethyl)-3-methylimidazolium hexafluorophosphate
$[(HOC_2)C_1im][SCN]$	1-(2-hydroxyethyl)-3-methylimidazolium thiocynate
$[N_1(C_2OH)_3][C_1OSO_3]$	tris(2-hydroxyethyl)methyl-ammonium methylsulfate
$[C_4C_1im]Zn_2Cl_5$	1-butyl-3-methylimidazolium chloride-zinc chloride
$[C_2C_1im]Cu_2Cl_5$	1-ethyl-3-methylimidazolium chloride-copper chloride

$[C_4im][NTf_2]$	1-butyl imidazolium bis(trifluoromethylsulfonyl)imide
$[(HOOCC_3)C_1im][NTf_2]$	1-n-butyrate-3-methylimidazoliumbis(trifluoromethylsulfonyl)imide
$[C_3C_1pyr][NTf_2]$	1-propyl-1-methylpyrrolidnium bis(trifluoromethylsulfonyl)imide
$[C_3C_1pyr][DCA]$	1-propyl-1-methylpyrrolidinium dicyanamide
$[C_4C_1pyr][OAc]$	1-butyl-1-methylpyrrolidinium acetate
$[C_4C_1pyr][NTf_2]$	1-butyl-1-methylpyrrolidnium bis(trifluoromethylsulfonyl)imide
$[C_4C_1pyr][DCA]$	1-butyl-1-methylpyrrolidinium dicyanamide
$[C_4C_1pyr][C_1SO_4]$	1-butyl-1-methylpyrrolidinium methylsulfate
$[C_4C_1pyr][FEP]$	1-butyl-1-methylpyrrolidinium tris(pentafluoroethyl)trifluorophosphate
$[C_4C_1pyr][OTf]$	1-butyl-1-methylpyrrolidinium trifluoromethanesulfonate
$[C_5C_1pyr][NTf_2]$	1-pentyl-1-methylpyrrolidinium bis(trifluoromethylsulfonyl)imide;
$[C_6C_1pyr][NTf_2]$	1-hexyl-1-methylpyrrolidnium bis(trifluoromethylsulfonyl)imide;
$[C_7C_1pyr][NTf_2]$	N-heptyl-N-methylpyrrolidinium bis(trifluoromethylsulfonyl)imide
$[C_8C_1pyr][NTf_2]$	1-octyl-methylpyrrolidinium bis(trifluoromethylsulfonyl)imide
$[C_9C_1pyr][NTf_2]$	N-nonyl-N-methylpyrrolidinium bis(trifluoromethylsulfonyl)imide
	$[(C_1OC_1)C_1pyr][NTf_2]$, N-methoxymethyl-N-methylpyrrolidinium bis(trifluoromethanesulfonyl)imide
$[(C_1OC_1)C_1pyr][FSA]$	N-methoxymethyl-N-methylpyrrolidinium bis(fluorosulfonyl)imide
AARD	Average Absolute Relative Deviation
EoS	Equation of State
GM	Gravimetric Microbalance
IGA	Intelligent Gravimetric Analyzer
IL	Ionic Liquid
IUPAC	an International Union of Pure and Applied Chemistry

NIST REFPROP	National Institute of Standard and Technology Reference Fluid Thermodynamic and Transport Properties Database
NMR	Nuclear Magnetic Resonance
NRTL	Non-Random Two Liquid
PR EoS	Peng-Robinson Equation of State
UCST	Upper Critical Solution Temperature
VLE	Vapor-Liquid Equilibria
LLE	Liquid-Liquid Equilibria

Chapter 1. Introduction

"Don't let anyone rob you of your imagination, your creativity, or your curiosity. It's your place in the world; it's your life. Go on and do all you can with it, and make it the life you want to live."

Mae Jemison, first African American woman astronaut in space

One of the major challenges of the 21st century is environmental issues as a result of global warming, high carbon energy, deforestation, air pollution, and many more. Our role as scientists and engineers is to develop sustainable, environmentally benign, and green energy and processes to "meet the needs of the present without compromising the ability of future generations to meet their own needs." To that end, solvents play an incredibly important role as they are involved in numerous industrial applications, from reaction engineering to separation. Surely, one of the ways to address our world's issues is to optimize the current technologies, which can be accomplished by searching for innovative and sustainable working fluids for industries. Therefrom, ionic liquids might offer a unique solution.

1.1. Ionic Liquids

Ionic liquids (ILs) are low melting point salts composed entirely of ions.[5] ILs differ from traditional salts because the charge delocalization, the size of the ion, and the ion asymmetry prevent the formation of stable crystals.[5] Ionic liquids have been emphasized with unique physical and chemical properties that can be finely tuned by varying both the cation, anion, and substituents. It has been predicted 10^{18} ionic liquids can be prepared by changing anion, cation, and substituents.[6] The unique structure of ILs, along with the possibility of countless numbers of cation

and anion combinations, offers unique properties such as low vapor pressure, good electrochemical and thermal stability, and high solvation capability, to name a few.

Novel characteristics of ILs have led to extensive research over the past decade to explore the feasibility of ILs in various applications such as separation, electrochemical and battery applications, catalysis, and many more.[6] ILs have received increasing attention because they are considered to be "green solvents" due to their negligibly small vapor pressure. However, ILs as a class of solvent cannot be distinguished based on only this property for two reasons. First, some ionic liquids possess a measurable vapor pressure, although most ILs indeed have a negligible vapor pressure. For example, the imidazolium- and pyrrolidinium- based ionic liquids discussed in this dissertation maintained their total weight even under vacuum for one day at a temperature of 348.15 K. On the other hand, some ionic liquids have detectable vapor pressure at high temperatures.[7] Second, ILs have been considered as "green solvents" due to their non-volatility, which prevents the loss of the solvent.[6] However, this perspective as a "green solvent" has been significantly challenged in the literature due to the toxicity and environmental persistence of some common ILs. ILs are not intrinsically green; in fact, many ILs are highly toxic. Nevertheless, the merit of ILs is not necessarily their negligible vapor pressure or their inherent environmental friendliness, rather it is their tunable characteristic depending on the desired properties such as physical parameters (viscosity, melting point), thermal stability, chemical properties (inert, catalytically active, shifting equilibria), price/performance ratio ("simple" ionic liquid or highly functionalized), toxicology (non-toxic, biodegradable) and many others.[6,8]

Regardless of the debate, two main factors still define ionic liquids as *greener* solvents. First, as discussed above, ILs are designable solvents. Therefore, ILs can be designed to be non-volatile,

non-toxic, and environmentally benign. Second and more importantly, the solvents are more acceptably judged based on the total environmental impact of the overall process.[9] Therefore, intrinsically hazardous solvents might be the greener solvent in the processes if the total environmental impact of the overall process is improved with using a hazardous substance.[9] Tom Welton's perspective about ionic liquids in 2011 is a quite appropriate stating that the most important thing for green chemistry is to create more sustainable chemicals and processes; ILs have already achieved significant successes to that end, and more will follow.[9]

1.2. Gases

1.2.1. Ammonia

Ammonia (NH_3) is one of the most important and largest volumes of industrial chemicals produced today. Ammonia is used in fertilizers, in water purification, in the manufacture of plastics, explosives, textiles, pesticides, dyes, and other chemicals.[10] The majority of ammonia produced today (80%) is used as fertilizer in the agriculture industry.

Ammonia is also used as a refrigerant due to its excellent thermodynamic and transport properties. It is also known as R-717 in the refrigeration industry. Due to its zero global warming potential and zero ozone layer depletion, it is one of the most widely used environmentally benign refrigerants.[11] Ammonia as a refrigerant provides certain benefits compared to some other refrigerants such as R-22 (chlorodifluoromethane) as follows: lower cost, better cycle efficiency, high critical temperature, lower pumping cost, more tolerance to water contamination, and relatively high insolubility in lubricating oils.[11] The two concerns about ammonia as a refrigerant are its toxicity and flammability. Even though ammonia is flammable, it is not highly flammable, and is classified as combustible and is hard to ignite.[11] Ammonia is, however, toxic, and proper

safety precautions are required. In the event of a leak, ammonia is less dense than air and moves upward which can help reduce risk.[11]

1.2.2. Carbon dioxide

Carbon dioxide (CO_2) is a colorless, non-flammable, non-toxic, and relatively inexpensive gas. The major applications of carbon dioxide are in fire extinguishers, oil industry (e.g., enhanced oil recovery), food industry, agricultural, and medical applications. CO_2 is also used as a refrigerant due to its zero-ozone depletion potential, thermal stability, availability, and low cost.[11] The global warming potential of CO_2 is 1, and it is the largest volume greenhouse gas being emitted to the atmosphere posing a threat to the climate-energy balance of the Earth. However, there is an increasing interest in utilizing CO_2 for a variety of applications, including producing new materials and as a refrigerant.[11]

1.3. Organic Solvents

1.3.1. Dihydroxy alcohols

Dihydroxy alcohols (diols) such as 1,3-propanediol and 1,4-butanediol are important industrial intermediates (i.e., monomers) in the polymer industry and are primarily produced from petroleum feedstocks. The production of diols from biomass has continued to gain interest as it is a sustainable alternative to petroleum-based processes.[12–14] Bioprocesses also provide an opportunity to produce certain diols such as 1,5-pentanediol that are not economically feasible to produce from petroleum feedstocks.[13]

1.4. Ionic Liquid Binary Mixtures

1.4.1. Ionic Liquids and Ammonia

Most of the research involving NH_3 and ILs has been directed at reducing NH_3 emissions or to improve the NH_3-H_2O absorption-refrigeration cycle. In 2007, Yokozeki and Shiflett pioneered the investigation of NH_3 and IL mixtures by measuring the NH_3 solubility in eight imidazolium-based ILs, suggesting that NH_3+IL might be an alternative refrigerant-absorbent pair for the NH_3-H_2O absorption refrigeration cycle.[15,16] Huang et al. showed the solubility of NH_3 in guanidinium based ILs was comparable with imidazolium-based ILs and suggested the cation dominated the interactions between NH_3 and the IL.[17] Shi and Maginn using Monte Carlo simulations showed that the basic nitrogen of NH_3 associates with the acidic hydrogen that is attached to the C(2) carbon of the imidazolium ring and the anion has little effect on the solubility of NH_3 for $[C_2C_1im][NTf_2]$.[18] Li et al. also found the length of the alkyl chain has an impact on NH_3 sorption in imidazolium-based ILs. For example, the NH_3 solubility in imidazolium ILs increased with longer alkyl chains on the cation ($[C_nC_1im][BF_4]$, n=2,4,6,8).[19] Tomida et al. recently measured the solubility of NH_3 in $[C_4C_1im][PF_6]$ over a wide temperature range (283.15 to 363.15 K) and at pressures up to 3 MPa.[20]

The NH_3 absorption capacity was also measured in various hydroxyl functionalized ILs: $[N_{111}C_2OH][NTf_2]$[21–23], $[(HOC_2)C_1im][BF_4]$[21–24], $[(HOC_2)C_1im][DCA]$[22], $[N_1(C_2OH)_3][C_1OSO_3]$[22] and $[(HOC_2)C_1im][NTf_2]$[23]. Palomar et al. showed the hydroxyl functionalized cations ($[(HOC_2)C_1im]$ or $[N_{111}C_2OH]$) with fluorinated anions enhance the solubility compared to non-functionalized analogs.[21] Li et al. also reported that the NH_3 absorption capacity for hydroxyl functionalized ILs (($[(HOC_2)C_1im][X]$ (X= PF_6, BF_4, DCA, SCN, NO_3) with

any given anion was larger compared to the traditional imidazolium-based counterparts ([C_2C_1im][X](X = NTf_2, BF_4, NO_3)).[24] Also, they found that ILs with fluorine-containing anions have a higher NH_3 solubility compared with non-fluorinated anions with hydroxyl-containing cations.[24] However, the hydroxyl group on the imidazolium cation led to an increase in viscosity and, consequently, a longer time to reach equilibrium.[24]

Metal ion-containing ILs ([C_4C_1im]Zn_2Cl_5[25] and [C_2C_1im]Cu_2Cl_5[26]) were also investigated to improve NH_3 absorption and to overcome issues with using the metal chloride/NH_3 adsorption system. The metal ion containing ILs have shown the highest amount of NH_3 absorption to date.

In addition to aprotic ILs, protic ILs have also been studied.[27,28] Shang et al. showed the protic IL [C_4im][NTf_2] had higher NH_3 solubility compared to traditional imidazolium-based ILs such as [C_4C_1im][NTf_2] or functionalized ILs such as [($HOOCC_3$)C_1im][NTf_2].[27] Also, contrary to aprotic ILs, the cation chain length for protic ILs was found to have little effect on the NH_3 solubility; however, fluorinated anions such as [NTf_2] had higher NH_3 absorption compared to non-fluorinated anions [SCN] and [NO_3].[28]

Thermodynamic models such as the Redlich-Kwong cubic equation of state (EoS)[15,16], Flory-Huggins model[29], van der Waals EoS[30], Peng Robinson EoS with Kwak and Mansoori mixing rule (PR/KM)[31], Artificial Neural Networks method (AAN) [32], modified UNIFAC model[25,26], UNIFAC model[33], COSMO-based process simulation with Aspen Plus/Aspen HYSY[34], Non-Random Two Liquids (NRTL) model[23] and Antoine equation[20] have been used to correlate experimental VLE data for NH_3 + IL mixtures.

Traditional aprotic ILs (i.e., imidazolium-based ILs) have shown a relatively low affinity for NH_3 compared to functionalized ILs, metal-containing ILs, and protic ILs. However, the latter

suffers from a few major drawbacks. For example, hydroxyl functionalized ILs have higher viscosities, metal-containing ILs chemically interact/react with NH_3, and protic ILs are not stable even at room temperature. Therefore, traditional aprotic ILs are still preferable based on reversible NH_3 sorption, lower viscosity, good thermal stability, and lower cost.

1.4.2. Ionic Liquids and Carbon dioxide

Carbon dioxide is the most studied gas in ionic liquids, and a large amount of data have been published for the solubility of CO_2 in various imidazolium, pyridinium, phosphonium, and ammonium-based ionic liquids.[35] Although the most commonly used cations are those of the imidazolium family, pyrrolidinium-based ionic liquids have gained importance in recent years due to their high thermal stability and lower toxicity compared to pyridinium, phosphonium, imidazolium, and ammonium ILs even though the viscosities are slightly higher than imidazolium ILs.[36] Pyrrolidinium-based ionic liquids have been considered for applications such as heat transfer fluids[37], energy storage devices[38], solar cells[39], and lubricants[40]. Several research groups have measured the solubility of CO_2 in various pyrrolidinium-based ionic liquids, which are summarized in Table 1.1.

The CO_2 solubility in pyrrolidinium ILs is primarily a function of the anion. Several groups have studied pyrrolidinium-based ionic liquids with the bis(trifluoromethylsulfonyl)imide anion $[NTf_2]^-$ which is one of the most thermally stable anions.[36] Anthony et al. found slightly higher CO_2 solubility in pyrrolidinium-based ILs compared to ammonium and some imidazolium-based ILs, all with the $[NTf_2]$ anion.[41] Similar findings were reported by Hong et al. who found that changing the cation from an imidazolium to pyrrolidinium cation with the $[NTf_2]$ anion slightly increased the solubility of CO_2.[42] Furthermore, both Yim et al. and Kim et al. reported that the

solubility of CO_2 increases with an increase in the alkyl chain length on the pyrrolidinium cation.[43–45]

In addition to experimental studies, Lourenco et al. performed molecular simulations to understand the local environment of CO_2 and its impact on the dynamic properties (e.g., viscosity, diffusivity, and ionic conductivity) on pure $[C_2C_1im][NTf_2]$ and CO_2 + $[C_2C_1im][NTf_2]$ and the role of cation comparing the latter with an $[C_4C_1pyr]$ $[NTf_2]$. Even though the experimental studies showed the solubility of CO_2 in pyrrolidinium ionic liquids are slightly higher than imidazolium-based ILs, the molecular simulation indicates that $[C_4C_1pyr][NTf_2]$ has less affinity for CO_2 compared to $[C_2C_1im][NTf_2]$.[46]

1.4.3. Ionic Liquids and Dihydroxy Alcohols

As new bioprocesses continue to produce diols, ILs may be useful for separation processes. The phase behavior of alcohols and ILs (i.e., monohydroxy alcohols + IL systems) have been extensively investigated[47–51]; however, studies of the phase behavior of dihydroxy or polyhydroxy alcohols and ILs are rather scarce.[52–57]

1.5. Dissertation Objectives

The fundamental goal of this dissertation is to investigate the phase behavior of ionic liquid binary mixtures with ammonia, carbon dioxide, and dihydroxy alcohols. Within the scope of the thesis, the sub-goals are as follows:

1- The main goal of ammonia and ionic liquid studies is to investigate the phase equilibrium and kinetics of the IL + ammonia binary system through both experimental and modeling studies. The accuracy of the phase equilibrium measurements is of critical importance in applications of ILs in processes. The novelty of this research is that the gravimetric method described in this work,

Table 1.1. Literature summary for the solubility of CO_2 in pyrrolidinium ILs

IL Abbreviation	Temperature Range	Pressure Max/ MPa	Experimental Method	Reference
$[C_4C_1pyr][NTf_2]$	283.15 K 298.15 K 323.15 K	1.3	Gravimetric Microbalance	41
$[C_4C_1pyr][NTf_2]$	303.78 K to 344.15 K with ~10 K increment	0.6 MPa	Isochoric Saturation Technique	42
$[C_4C_1pyr][FEP]$	283.2 K 298.6 K 323.3 K	1.8	Gravimetric Microbalance	58
$[C_4C_1pyr][NTf_2]$	293 to 413 K with 40 K increment	10	Synthetic High-Pressure View-Cell Technique	59
$[C_4C_1pyr][OTf]$	303.15 K 373.15 K	70	High-Pressure Variable-Volume View Cell	60
$[C_4C_1pyr][NTf_2]$ $[C_4C_1pyr]$ $[C_1SO_4]$	303.15 to 373.15 K with 10 K increment	100	High-Pressure Variable-Volume View Cell	43
$[C_6C_1pyr][NTf_2]$ $[C_8C_1pyr][NTf_2]$	303.15 K to 373.15 with 10 K increment	62	High-Pressure Variable-Volume View Cell	44,61
$[C_3C_1pyr]$ $[NTf_2]$ $[C_5C_1pyr][NTf_2]$ $[C_7C_1pyr][NTf_2]$ $[C_9C_1pyr][NTf_2]$	303.15 to 373.15 K with 10 K increment	~ 72	High-Pressure Variable-Volume View Cell	45
$[C_4C_1pyr][NTf_2]$	313.2K 323.2 K	22	Isochoric Saturation Technique	62
$[C_3C_1pyr][NTf_2]$ $[(C_1OC_1)C_1pyr][NTf_2]$ $[(C_1OC_1)C_1pyr]$ [FSA]	298.15 K 313.15 K 333.15 K	6	High-Pressure Cell	63
$[C_4C_1pyr][OAc]$	~353 K	0.08981	Isochoric Saturation Technique	64
$[C_4C_1pyr][DCA]$ $[C_4C_1pyr][NTf_2]$	303.2 K to 343.2 K with ~10 K increment	30	High-Pressure Variable-Volume View Cell	65
$[C_3C_1pyr][DCA]$	298 K	1	Gravimetric Microbalance	66

which is one of the most accurate techniques for measuring gas solubility[4], has not been previously utilized to measure the solubility of NH_3 in ILs. Therefore, to the best of my knowledge, this study is the most accurate phase equilibrium data for NH_3+IL mixtures to date. This study also provides an overview of the new gravimetric microbalance technique for measuring gas absorption in ionic liquids. In addition, the detailed kinetic analysis of NH_3+ IL mixtures was performed. Only Bedia et al. have reported the effective diffusivity of NH_3 in one imidazolium and four functionalized ILs[22] using the kinetics model developed previously developed for CO_2 + IL mixtures by Yokozeki and Shiflett.[67] Therefore, this study reports for the first time, the diffusivity of NH_3 in imidazolium-based ILs at various temperatures using both the 1-D model and the Stokes-Einstein model. In addition, the interaction between ammonia and imidazolium-based ILs were elucidated using proton NMR as a characterization tool, which is also not performed in the literature.

2- The main objective of the carbon dioxide and ionic liquid study is to investigate the dissolution kinetics and high-pressure phase equilibria of supercritical fluid-ionic liquids mixtures. This research provides very thorough and accurate solubility and diffusivity of carbon dioxide in 1-alkyl-1-methyl pyrrolidinium bis(trifluoromethylsulfonyl)imide ionic liquids ($[C_nC_1pyr][NTf_2]$ (n = 3,4,6)) over a wide range of temperature and pressure using three independent experimental methods. The novelty of the research is that the study provides the most comprehensive investigation of the pyrrolidinium-based ILs and CO_2 using various techniques at a very wide pressure range.

3- The main purpose of the binary mixtures of ionic liquid and dihydroxy alcohols are to provide accurate and reproducible phase equilibria data in three ionic liquids, and to model liquid-

liquid equilibria using an activity coefficient model. The novelty of this research is that it provides a detailed analysis of the diol+ILs mixtures that have not been reported in the literature.

1.6. Outline of Chapters

Chapter 2 describes the experimental methods used in this dissertation. The chapter explains phase equilibria measurements via volumetric and gravimetric methods. The liquid-liquid equilibria measurement using both volumetric and cloud point method is also described. The ionic liquid drying apparatus and water content measurement techniques are also described.

Chapter 3 discusses the phase equilibrium modeling used in this thesis. The equilibrium criteria for vapor-liquid and liquid-liquid equilibria are reported. Equation of State and activity coefficients models are explained.

Chapter 4 provides phase equilibria measurement and modeling results for binary mixtures. The thermodynamic modeling of ammonia + ionic liquid mixtures, as well as dihydroxy alcohol + ionic liquid mixtures, are discussed in detail.

In Chapter 5, the gas dissolution kinetics for ammonia and carbon dioxide in ionic liquids is discussed.

In Chapter 6, the interaction dynamics between ammonia and ionic liquids were investigated using proton NMR.

Chapter 7 provides the details about the safety procedures used for safely working with ammonia.

Chapter 8 completes this dissertation providing conclusions and giving some recommendations for future research activities.

Chapter 2. Experimental Methods

"Science, for me, gives a partial explanation for life.
In so far as it goes, it is based on fact, experience, and experiment."
Rosalind Franklin, A chemist and X-ray crystallographer

In this study, several apparatuses and measurement techniques have been used for phase equilibria measurements, water determination of ionic liquids, and ionic liquid drying. The following sections describe the details.

2.1. Gas Absorption Measurement Techniques

As described in the previous sections, the novel characteristics of ILs led to extensive research to explore the feasibility of ionic liquids in various applications due to its unique characteristics. All these applications require fundamental thermodynamic knowledge of ILs with other substances, one of which is the solubility of gases in ionic liquids. In this thesis, the term "the solubility of gases in ionic liquids" is used to describe the thermodynamic equilibrium between gas and liquid at constant temperature and pressure. Therefore, "the solubility of gases in ionic liquids" interchangeably used as "the gas absorption capacity in ionic liquids" or the "vapor-liquid-equilibrium of gases and ionic liquids."

Many experimental techniques have been evolved over the years for the measurement of gas solubilities in ionic liquids. Three main categories of gas absorption measurements are gravimetric methods, stoichiometric (synthetic) methods, and pressure drop methods.[35,68] Gravimetric methods[35,68,69] such as gravimetric microbalance, quartz crystal microbalance, and weight methods are based on measuring the change in weight of the sample during a sorption process. The synthetic methods are mainly based on measuring a known amount of liquid and gas in a high-pressure view

cell.[68] The pressure drop technique (pressure decay method or similarly isochoric saturation method) is based on a known amount of gas contacting with ionic liquid in an equilibrium cell.[35,68] Even though some chromatographic and spectroscopic methods can be utilized to assess gas sorption capacities of ILs, the techniques introduce additional complexity into the experiment.[69] Furthermore, the latter techniques are more direct.

2.1.1. Gravimetric Methods (GMs)

Gravimetric methods are one of the most common techniques used to measure gas solubilities in ILs. The simplest gravimetric method to measure the gas solubilities in ILs is to utilize the bench-scale balances.[68] In this simple method, the sample container is weighed before and after the gas is bubbled into an IL sample in a container. The method is very crude compared to the other measurement techniques; however, it can be used as a quick screening method or when a substantial amount of gas is dissolved in the IL where the error might be compensated due to large dissolution. On the other hand, the gas and vapor solubilities in ILs can be more accurately and precisely measured using gravimetric microbalances (GMs) such as Hiden gravimetric microbalances. GMs are advanced gas sorption analyzers that are originally designed to measure gas sorption on solid samples such as zeolites, alumina, membranes, carbon nanotubes (CNTs), and many more. However, GMs can also be utilized to measure gas and vapor sorption in ILs because ILs do not evaporate into a vapor phase due to their negligible vapor pressure. In fact, since Anthony, Maginn, and Brennecke utilized the microbalance to measure CO_2 solubility in IGA instrument in 2001[70], many gas sorption experiments were performed using GMs.[4]

Many different GMs are available in the market with various capabilities. However, the most commonly used microbalances are manufactured by Hiden Isochema such as IGA, XEMIS, and

IGAsorp.[4] In this thesis, XEMIS and IGA microbalances were utilized to measure gas solubilities in ionic liquids. The next few sections detail the instruments.

2.1.1.1. XEMIS Gravimetric Microbalance

XEMIS microbalance is a magnetically coupled advanced gas sorption instrument for high pressure, high temperature, and corrosive gas applications. The name XEMIS comes from the Greek goddess Themis who holds the scale of justice and whose name means "divine law." The fully symmetric design reduces buoyancy effects and improves measurement accuracy without compromising resolution or stability. Like other gravimetric balances, XEMIS is also designed to measure gas sorption on solids. However, GMs can be utilized to measure gas solubility in non-volatile ionic liquids. XEMIS is a unique microbalance with numerous weighing capabilities, one of which is to enable corrosive gas measurements.

2.1.1.1.1. XEMIS Working Range and Capabilities

The XEMIS can operate over a broad temperature (77 to 773 K) and pressure (0 to 170 bar) range. The balance can hold a maximum weight of 5 g. The maximum sorption capacity is 200 mg with a weighing resolution of 0.2 μg. The XEMIS can be operated in both "static" and "dynamic" modes. The static mode uses a pair of admit and exhaust valves to regulate the pressure setpoint. The instruments can also be set up to handle mixed gas streams with some modifications. In dynamic mode, a set of mass flow controllers regulate the pressure with automatic switching between inlets to adjust the composition of the mixture. In this mode of operation, the XEMIS can be connected to an on-line mass spectrometer to analyze the gas expelled from the system through the dynamic sampling port (DSP). The DSP comes with a pressure reduction option, which reduces pressure to 1 atm (0.1 MPa) when the XEMIS is operating at high pressures. The

balance can also be set up for vapor measurements (water or organic solvents). The XEMIS system is completely automated.

2.1.1.1.2. XEMIS Components

The XEMIS system consists of a balance cabinet, control system, vacuum pump, heating and cooling units, and computer (Figure 2.1). The cabinet houses the magnetic suspension balance and is held at a temperature of 313.15 K to maintain the balance stability. The cabinet is mounted to the floor on a frame to minimize vibration. Beneath the balance cabinet, two equal-size stainless steel vessels contain the sample cup (right side) and counterweight (left side). Gantries inside the vessels support the temperature sensors and protect the hangdown wires. The internal volume of each vessel and the overall volume of the system are ~80 cm^3 and ~450 cm^3, respectively. The small internal volume of the XEMIS balance reduces the amount of gas required for each experiment. The control system consists of a temperature control unit, computer interface, valve drivers, and gas handling system. A flow control system can also be added for dynamic mode operations. The control system provides the interface to Hiden's HIsorp software, which allows users to easily set up an individual isotherm or sequential experiments, including pre- and post-treatments (heat, vacuum, etc.). The interface has real-time processor functions, high-resolution graphics with user-specific display options, and simple task symbols for easy operation. The HIsorp software also provides warning messages to minimize errors during the experimental setup. Experimental data can also be analyzed using the HIsorp software even while the experiment is in progress.

The vacuum system consists of an oil-free backing pump and a turbo pump. For normal operations, the backing pump reduces the system pressure to about 10^{-2} MPa, and the turbo pump

can reduce the pressure down to 10^{-10} MPa. The XEMIS can be set up with a standard furnace (up to 773 K), cryo furnace (down to 77 K) and water bath (278 to 358 K) with temperature regulation accuracy from ±0.05 (water bath) to 0.1-1.0 K (furnaces).

Figure 2.1. XEMIS Microbalance in a ventilated enclosure at the University of Kansas

A schematic of the XEMIS is shown in Figure 2.2 with a description of the components which are used in the force balance equation provided in Table 2.1. Stainless steel and nichrome hangdown wires connect the sample cup and counterweight to the balance mechanism. The XEMIS has various size Pyrex® containers for liquid samples and stainless-steel micromesh cone containers for solid samples. Figure 2.3 shows an example of a counterweight and a sample cup in XEMIS microbalance.

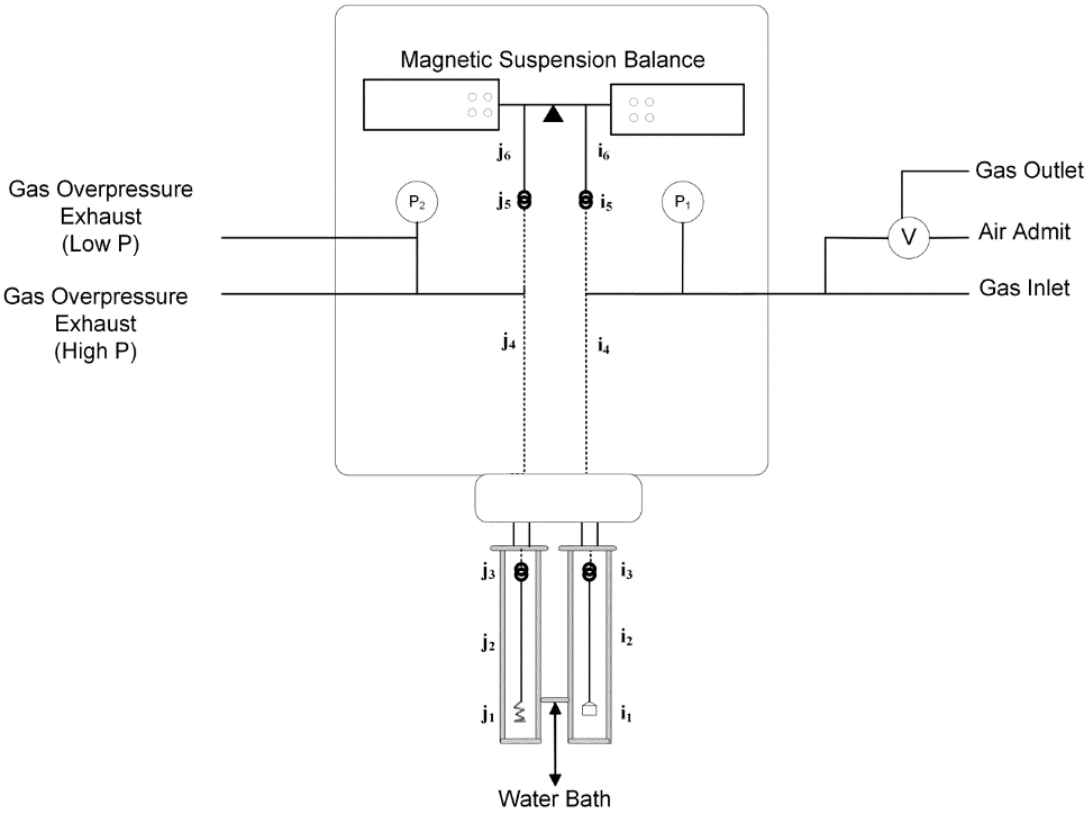

Figure 2.2. Hiden XEMIS gravimetric microbalance schematic with component labels.[71] Nomenclature is described in Table 2.1.

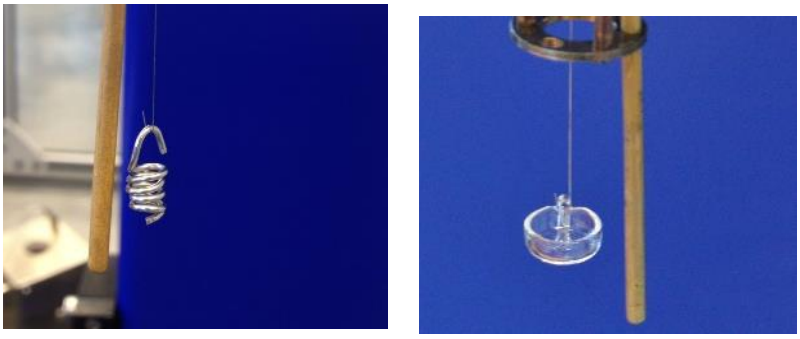

Figure 2.3. The XEMIS microbalance components. The left image shows a stainless-steel counterweight, and the right image shows the Pyrex® sample container used in this study.

Table 2.1. Standard XEMIS microbalance components included in buoyancy correction

Subscript	Component	Material	Weight (g)	Density (g/cm^3)	Temperature (K)
s	Sample	Variable	m_s	ρ_s	Sample Temp
a	Interacted Gas	Variable	m_a	ρ_a	Sample Temp
i_1	Sample container	Pyrex®	0.4769	2.23	Sample Temp
i_2	Hangdown	316 SS	0.0214	7.89	Cabinet Temp
i_3	Hook	316 SS	0.0465	7.89	Cabinet Temp
i_4	Hangdown	80% Ni/20% Cr	0.002	8.4	T Profile i
i_5	Hook	316 SS	0.04635	7.89	Cabinet Temp
i_6	Hangdown	316 SS	0.0209	7.89	Cabinet Temp
j_1	Counterweight	316 SS	0.5956	7.89	CW Temp
j_2	Hangdown	316 SS	0.0214	7.89	Cabinet Temp
j_3	Hook	316 SS	0.0462	7.89	Cabinet Temp
j_4	Hangdown	80% Ni/20% Cr	0.002	8.4	T Profile j
j_5	Hook	316 SS	0.04635	7.89	Cabinet Temp
j_6	Hangdown	316 SS	0.021	7.89	Cabinet Temp

2.1.1.1.3. XEMIS Working Principle

In XEMIS, the balance chamber holds the balance mechanism on a phosphor bronze ribbon. On the end of the beam on each side (counterweight side and sample side), as shown in Figure 2.4, there are gold magnets placed between copper solenoid coils where the magnetic field from electric current is generated. When the weight of the sample is changed due to sorption or desorption, the gold magnet on the sample side moves its position due to a change in magnetic field strength. The hall-effect sensor measures this change. Then, the magnetic field strength on the tare side altered to bring the beam back to the horizontal (tared) position. The force required to bring the beam back into the tared position is proportional to the weight change of the sample. This *Exosensor-Exodrive* system keeps the system in balance and placed under the Mu metal (nickel-iron soft magnetic alloy) magnetic shields to isolate the external magnetic fields, which might potentially affect the balance. The symmetric geometry of the XEMIS system provides high precision and minimizes the buoyancy effects during the measurements.

Figure 2.4. The XEMIS microbalance beam view.[72]

2.1.1.1.4. XEMIS Pressure and Temperature Transducers

The XEMIS is also equipped with two pressure sensors for accurately measuring pressure over both low (up to 2 MPa) and high (up to 20 MPa) ranges with an accuracy of 0.04% of transducer range. The low-pressure transducer can measure pressures as low as 10 to 20 mbar, which is useful when fine pressure regulation is required. Both pressure transducers within the XEMIS microbalance were calibrated against a NIST traceable Paroscientific Model 765-1K pressure transducer (range 0 to 6.89 MPa, serial no. 101314). This instrument is a NIST-certified secondary pressure standard with a traceable accuracy of ± 0.0008 MPa. Both transducers are accompanied by a burst disk to prevent damage in case of unexpected pressure elevation.

The sample and counterweight temperatures were measured with a K-type thermocouple with an accuracy of ± 0.1 K and calibrated against a NIST traceable standard platinum resistance thermometer (Hart Scientific SPRT model 5699 and readout Hart Scientific Blackstack model 1560 with an SPRT module 2560). The Blackstack instrument and SPRT module are also a certified secondary temperature standard with a NIST traceable accuracy to ± 0.005 K. The thermocouple in XEMIS cabinet is annually calibrated by Hiden Engineers.

The instrumental uncertainty in T is within ± 0.1 K, and P is within ± 0.0001 MPa for the low-pressure transducer and ± 0.001 MPa for the high-pressure transducer.

2.1.1.1.5. XEMIS Data Reduction

The measurement of the solubility of gases in ionic liquids using the gravimetric method (XEMIS gravimetric microbalance) involves several steps: (1) drying and degassing of ionic liquid in the microbalance at high T (348 K) and under high vacuum (10^{-12} MPa) to remove water and volatile impurities, (2) the equilibration of gas and ionic liquid at specified temperature and pressure, and (3) data analysis. The largest error in the data analysis is a result of neglecting the forces acting on the balance (buoyancy and aerodynamic), the balance sensitivity to temperature and pressure, and volume expansion of the sample due to gas solubility. The sum of these forces can lead to significant errors if not carefully accounted for during data reduction.

(a) Correction of Forces acting on the balance:

There are three forces acting on the components of the balance in a given state: (1) gravitational force is due to gravitational acceleration of given mass (Newton's Second Law) (2) buoyant force is due to the pressure exerted on the object by fluid and is equivalent to the mass of fluid displaced (Archimedes' Principle) and (3) drag force is due to flow of the gases (the force exerted on a particle as a result of relative motion between the particle and a surrounding fluid). The gravitational force acts downwards, the buoyant force acts upwards, and the drag force acts in the direction opposite to the gas flow.

- The gravitational force can be obtained using Newton's Second Law:

$$F_g = m_i\, g \tag{2.1}$$

where m_i is the mass of an object, and g is the gravitational acceleration.

- The buoyancy force is calculated using the Archimedes' Principle:

$$F_b = -V_i \, \rho_g \tag{2.2}$$

where *Vi* is the volume of the submerged object, ρ_g is the density of gas at a given *T* and *P*, and g is the gravitational acceleration. If the volume of the object remains constant, V_i can be calculated by knowing the mass (m_i) and density (ρ_i) of the object. The buoyancy correction using the XEMIS microbalance requires the weight of objects on both the sample and counterweight sides. The weight, material, density, temperature of these objects can be found in Table 2.

- The drag force can be calculated by a drag equation:

$$F_d = \pm \left(\frac{1}{2} C_d v^2 \, A \, \rho_g\right) \tag{2.3}$$

where C_d is a drag coefficient, *v* is the gas flow velocity, *A* is the cross-sectional area, and ρ_g is the density of the gas at a given *T* and *P*. In this study, aerodynamic forces due to flow of gases were eliminated by conducting the experiment in static mode.

The gravimetric measurement is the difference in these forces between the right (sample side) and the left (counterweight) arms of the balance. Because the gravitational acceleration is the same for all objects, the force balance leads to a mass balance shown in Equation 2.4. The correction factor (C_f) listed in Equation 2.4 is the result of the balance sensitivity to temperature and pressure. The correction factor (C_f) was determined as a function of *T* and *P* without sample load by calculating the least square fit to tare the balance.

$$\left(\sum_{i=1} m_i - \sum_{i=1} \frac{m_i}{\rho_i}\rho_g(T_i, P)\right) + \left(m_s - \frac{m_s}{\rho_s(T_s)}\rho_g(T_s, P)\right) + \left(m_a - \frac{m_a}{\rho_a(T_s)}\rho_g(T_s, P)\right)$$

$$-\left(\sum_{j=1} m_j - \sum_{j=1} \frac{m_j}{\rho_j}\rho_g(T_j, P)\right) - C_f(T_s, P) = \text{reading} \quad (2.4)$$

(b) Correction for Volume Expansion

Liquids can expand upon gas dissolution. The volume of the gas-expanded ionic liquid is assumed to be a mole fraction average of molar volumes of each constituent species:[67,69]

$$V_L = \tilde{\mathrm{V}}_1 \frac{w_1}{M_1} + \tilde{\mathrm{V}}_O \frac{w_0}{M_0} \quad (2.5)$$

where subscripts 1 and 0 represent a sample gas and an ionic liquid, respectively; w is the amount of weight in the liquid mixture; M is molar mass; and $\tilde{V}$ is the molar saturated-liquid volume at a given temperature T.

A liquid volume change δV_L due to the gas absorption amount δw_1 is:

$$\delta V_L = \frac{\tilde{\mathrm{V}}_1}{M_1}\delta w_1 \quad (2.6)$$

Then, the actual weight reading (w_1) in the microbalance can be corrected by adding the buoyancy effect (a small amount of weight, δw_1) attributed to δV_L:

$$\delta w_1 = \frac{\tilde{\mathrm{V}}_1}{M_1}\delta w_1\, \rho_g(T, P) = \tilde{\mathrm{V}}_1 \delta w_1\, \tilde{\rho}_g \quad (2.7)$$

where $\rho_g(T, P)$ is a superheated gas density at the system T and P, and $\tilde{\rho}_g$ is the corresponding molar density, which can be calculated as well as $\tilde{V}_1$ using the thermodynamic software package

from NIST called REFPROP V.9.1.[73] After some algebraic manipulations, Equation 2.7 can be converted to a molar correction term, δx_1:

$$\delta x_1 = x_1(1 - x_1)\,\tilde{\rho}_g \tilde{V}_1 \tag{2.8}$$

The volume change in the liquid solution can be corrected with Equation (2.8) as long as $\tilde{\rho}_g$ and $\tilde{V}_1$ are known. It is worth to note that $\tilde{V}_1$ can be calculated using this method for temperatures below the critical *T* of gaseous species.

2.1.1.2. Intelligent Gravimetric Analyzer (IGA) Microbalance

An Intelligent Gravimetric Analyzer (IGA) is the earliest gas sorption analyzer developed by Hiden. Despite some differences, both IGA and XEMIS work on the same force balance principle. The detailed description of the IGA balance can be found elsewhere[4]; however, the IGA balance is also briefly described here.

2.1.1.2.1. IGA Working Range and Capabilities

The IGA microbalance operates at pressures ranging from 10^{-10} MPa to 2 MPa, and temperatures between 77 and 1273 K. The balance can hold a maximum sample weight of 1 g. The maximum sorption capacity is 200 mg with a weighing resolution of 0.1 μg. Like XEMIS, the IGA can also be operated in both "static" and "dynamic" modes, and it can be set up to handle mixed gas streams. The measurements only require a small sample size (less than < 100mg). Sorption (adsorption or absorption) and desorption isotherms can be obtained. The system can handle both solid and liquid samples. An IGA microbalance can handle non-corrosive gases as the part of the control electronics (i.e., copper wiring) are exposed to gases in the balance during the experiment.

2.1.1.2.2. IGA Components

The IGA system consists of a balance cabinet, vacuum pumps, heating and cooling units, and computer interface. The cabinet houses the microbalance and is mounted in a thermostated heatsink to provide long-term stability. Beneath the balance cabinet, two vessels contain the sample cup (right side) and counterweight (left side). As depicted in the schematic in Figure 2.5, the IGA reactors are asymmetrically designed. The counterweight reactor is much smaller than the sample side reactor. In IGA, the temperature profile is zoned in three regions: IGA cabinet, counterweight side, and sample side. The cabinet temperature maintained at 318.2 K by a band heater. The sample side temperature is controlled using a heating device such as a water bath. The counterweight side is at room temperature without any temperature regulation. Even though the tare side temperature is not regulated, the temperature of the components in the tare side is also recorded along with the sample side and cabinet temperature. Like XEMIS, the gantry inside the sample vessel supports the temperature sensors and protect the hangdowns. The overall internal volume of the IGA balance is ~1.8 L. IGA is also operated through Hiden's user-friendly HIsorp software.

Figure 2.5. Intelligent Gravimetric Analyzer (IGA) Microbalance [74]

The vacuum system consists of an oil-free backing pump and a turbo pump. For normal operations, the backing pump reduces the system pressure to about 10^{-2} MPa, and the turbomolecular pump can reduce the pressure down to 10^{-10} MPa. The IGA can be set up with a furnace (up to 773 K), cryo furnace (down to 77 K) and water bath (278 to 358 K) with temperature regulation accuracy from ±0.05 (water bath) to 0.1-1.0 K (furnaces).

A schematic of the IGA is shown in Figure 2.6 with a description of the components which are used in the force balance equation provided in Table 2.2. In IGA, a balance beam is connected to the sample cup and counterweight by a series of tungsten or gold hangdown wires and hooks. The IGA has various size Pyrex®, quartz, or stainless-steel containers for liquid and solid samples.

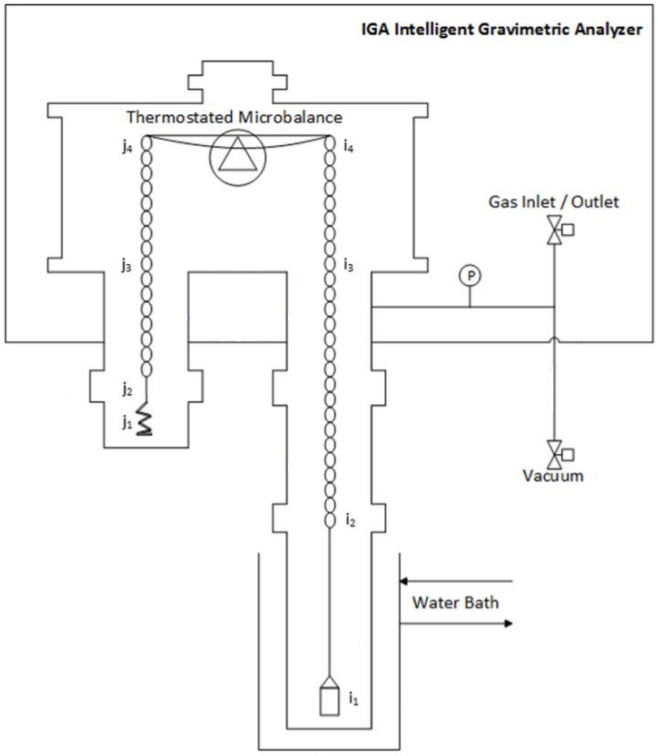

Figure 2.6. Hiden IGA gravimetric microbalance schematic with component labels.[4] Nomenclature is described in Table 2.2.

Table 2.2. Standard IGA microbalance components included in buoyancy correction[4]

Subscript	Component	Material	Weight (g)	Density (g/cm^3)	Temperature (K)
s	Sample	Variable	m_s	ρ_s	Sample Temp
a	Interacted gas	Variable	m_a	ρ_a	Variable
i_1	Sample container	Pyrex®	1.3915	2.23	Sample Temp
i_2	Lower hangdown wire	Tungsten	0.0572	19.04	Sample Temp
i_3	Upper hangdown chain	22 ct. gold	0.3028	11.10	T Profile Sample Side
i_4	Sample side balance hook	Tungsten	0.0059	19.04	Balance Temp
j_1	Counterweight (CW)	316 SS	1.5679	7.89	CW Temp
j_2	CW hook	Tungsten	0.0059	19.04	CW Temp
j_3	CW hangdown chain	22 ct. gold	0.2401	11.10	T Profile CW side
j_4	CW balance hook	Tungsten	0.0059	19.04	Balance Temp

2.1.1.2.3. IGA Working Principle

The IGA microbalance is a standard beam balance controlled by optical sensors. In the IGA, the beam balance is suspended in the center of the balance and is connected to the copper coil. When the balance arm moves due to sorption/desorption, the change in optical strength is measured by the optical sensors (an optical emitter on the counterweight side and optical receiver behind the balance mechanism). Based on the feedback on the optical sensor, an electric current is applied to the copper coil to bring the balance beam back to the horizontal ("tared" or "zero") position. The strength of the signal is related to how far the beam moving depending on the mass change in the system.

2.1.1.2.4. IGA Pressure and Temperature Transducers

The IGA can also be equipped with multiple sensors for accurately measuring pressure over both ultra-low (up to 0.1 MPa) and low pressures (up to 2 MPa) ranges with an accuracy of 0.05% of transducer range. The sample and counterweight temperatures were measured with a resistance

temperature detector (RTD) probes. The instrumental uncertainty in T is within ± 0.1 K, and P is within ± 0.0008 MPa for the.

2.1.1.2.5. IGA Data Reduction

Data reduction in IGA balance is the same as XEMIS. See Section 2.1.1.1.5.

2.1.1.3. The comparison of IGA and XEMIS Microbalances

Even though both IGA and XEMIS microbalances are based on the same force balance principle, the instruments differ in multiple ways. The comparison between the two instruments are listed here:

1- The maximum working pressure of the IGA microbalance is 2 MPa, whereas XEMIS can be operated as high as 20 MPa.

2- Both XEMIS and IGA microbalances can be operated using flammable gases. However, only XEMIS is suitable for corrosive gas applications because some IGA balance components such as copper wire and tungsten hangdown wires can corrode due to the incompatibility between balance components and working gas (i.e., H_2S and NH_3).

3- The overall internal volume of the IGA balance (~1.8 L) is larger than the overall internal volume of the XEMIS (~450 cm^3). XEMIS is preferred to IGA, where applications require low volumes of gas.

4- Once the microbalance is secured after the sample is set, XEMIS is fully controlled through the HIsorp system. The IGA system requires a researcher to open a valve to initiate air admittance or ultra-high vacuum. Even though the IGA HIsorp software guides the researcher to minimize user-related issues, the fully automated XEMIS system eliminates user-related issues.

5- Even though both instruments have a similar working principle, the sensors controlling the balance beams are different (see Section 2.1.1.1.3 for XEMIS working principle and 2.1.1.2.3 for IGA working principle).

Gravimetric microbalances are proven to be one of the most accurate methods to measure the gas solubilities in ionic liquids. However, the one major drawback of the system is that the maximum working pressure is limited to the saturation pressure of the gas at room temperature (*i.e.,* compressed gas cylinder pressure) because some balance components (gas lines from the gas cylinder to the control valve) are at room *T*.

2.1.2. Synthetic (Stoichiometric) Methods

The synthetic method involves loading a known amount of liquid and gas into a high-pressure view cell and determining the solubility of gases in several ways.[68] The high-pressure view cell technique used in this study is a volumetric method such that the solubility is obtained based on a mass balance in the entire system rather than based on the visual observation of the bubble point, as done in some synthetic methods.

2.1.2.1. High-Pressure View Cell

A high-pressure view cell is a stoichiometric method to conduct high-pressure and high-temperature phase equilibria measurements. The original and early design of high-pressure view cell[75–77] is modified by Ren and Scurto[78] to reduce the complexity of the design of the apparatus by excluding the use of mercury. The simplified, new version of the apparatus is described in detail elsewhere.[78] Therefore, the instrument is only briefly described here.

2.1.2.1.1. High-Pressure View Cell Working Range and Capabilities

A high-pressure view cell is an apparatus capable of measuring vapor-liquid equilibria, liquid-liquid equilibria, vapor-liquid-liquid equilibria, and solid-liquid equilibria under extreme temperature and pressure conditions. Extensive A method developed by Ren and Scurto[78] can calculate the solubility, molar volume, volume expansion, and molarity for such phase behavior.[78,79] For corrosive, flammable, and combustible gases, the design of the system can handle temperatures of 473 K and pressures 15 MPa. This limitation is due to the Teflon™ O-rings used in the high-pressure pump. The typical amount of ionic liquid loaded in the view cell varies between 1 to 3 grams.

2.1.2.1.2. High-Pressure View Cell Components

The apparatus consists of a high-pressure view cell, high precision syringe pump (Teledyne-Isco, Inc 100DM) and pressure gauge (Heise DXD Series 3711), a water bath, a cathetometer to read the height of the IL, and a computer data acquisition system (Figure 2.7). The line temperatures were measured using T-type thermocouples with an accuracy of ± 0.5 K. The pump temperature was measured using an ERTCO thermometer (Ertco-Eutechnic 5 digital thermistor, Model 4400) with an accuracy of ± 0.01 K in the range of 273.15-373.15 K. The cell temperature was calibrated against a NIST traceable standard platinum resistance thermometer (Hart Scientific SPRT model 5699 and readout Hart Scientific Blackstack model 1560 with an SPRT module 2560). The pressure gauge (Heise DXD Series 3711) was calibrated against a NIST Traceable Paroscientific Model 765-1K pressure transducer (range 0 to 6.89 MPa, serial no. 101314). The instrumental uncertainties in T and P are within ± 0.1 K and ± 0.01 MPa, respectively. The Eberbach 5160 cathetometer has a resolution of 0.01 mm and accuracy of ± 0.02+0.00005 L, where

L is the height of the ionic liquid from the starting point of the measurement to the given position (mm).

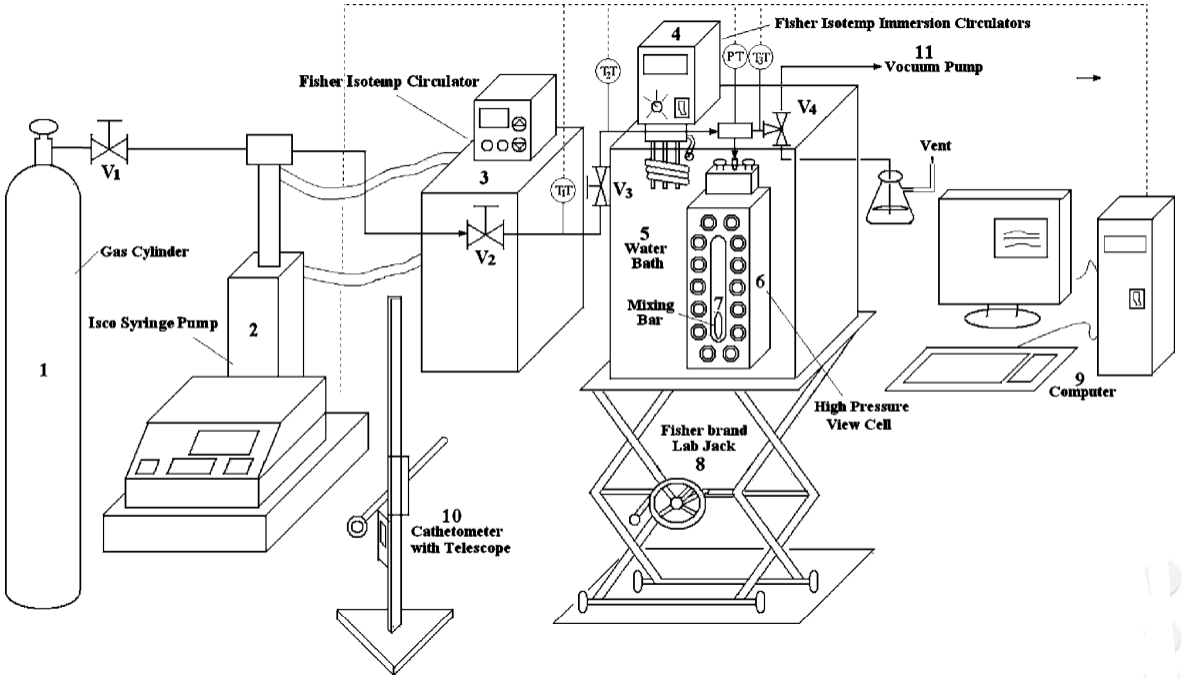

Figure 2.7. Diagram of experimental apparatus.[78] (1) Gas Cylinder (2) Syringe Pump (3) heater/circulator (4) Immersion heater/circulator (5) water bath (6) high-pressure view cell; (7) mixing bar; (8) laboratory jack; (9) computer; (10) cathetometer with telescope; (11) vacuum pump. *Reproduced from "Ren, W.; Scurto, A. M. High-Pressure Phase Equilibria with Compressed Gases. Rev. Sci. Instrum.* ***2007****, 78 (12), 125104 with the permission of AIP Publishing.*

2.1.2.1.3. High-Pressure View Cell Working Principle and Data Reduction

The measurement in high-pressure view cell is based on the mass balance by determining the amount of gas injected from the pump to the view cell, the amount of gas in the headspace above liquid sample, and the amount of gas in the tubing.[78] The gas solubility, density of the liquid

mixture, molar volume and volume expansion were also measured using the same apparatus [78] All calculations are completed in the REFPROP incorporated Excel spreadsheet developed by Scurto and Ren.[78]

2.1.3. Comparison of Gravimetric Microbalances and View Cell

Each gas absorption measurement technique has its strengths and weaknesses. In this section, GMs and high-pressure view cell are compared with various aspects:

1- Sample Size

The sample size for phase equilibria measurements in high-pressure view cell is much larger than the sample size for phase equilibria measurements in Hiden gravimetric microbalances. GMs can be more cost-effective for expensive samples such as ionic liquids.

2- Duration of an Experiment

A gas sorption measurement in an ionic liquid sample at a given temperature using GMs usually takes 3-10 hours for one pressure set point. Therefore, the gas sorption measurement for one isotherm can take as long as one week, depending on the number of *P,T* points, and whether the user desires both absorption and desorption data. On the other hand, an entire isotherm can be obtained using a high-pressure view cell in one day.

3- Operation

The gravimetric microbalances are either fully automated or required extremely minimal involvement of the researcher. With proper safety precautions, the microbalances can be set up for unattended operation. On the other hand, the high-pressure view cell requires a researcher during the entire operation. In the current design of the instrument, a researcher is responsible for continuously mixing the solution during the experimental procedure for 8-10 hours. This step is

extremely tedious and time-consuming. However, the system can be improved by automating mixing in the future.

4- Experimental Capabilities

In gravimetric microbalances, in addition to the absorption and desorption profile, the time-dependent behavior of gas dissolution can be obtained. On the other hand, with the current configuration, the desorption profile and kinetics information cannot be obtained using the high-pressure view cell.

As mentioned in the previous sections, the operating pressure of microbalances is limited to the vapor pressure of the gas at room temperature. On the other hand, a high-pressure view cell is only limited to the maximum operating pressure of the apparatus components, which is well above the desired experimental conditions.

5- Multi-gas adsorption

The instruments used in this study are limited to single gas absorption. However, a relatively simple modification could be made using the microbalances for multi-gas adsorption. The modification could also be made using the high-pressure view cell, which would include installing gas flow meters and analytical sampling capability (i.e., GC-MS).

6- Accuracy

Gravimetric microbalances are the most accurate and precise gas absorption measurement technique, especially at low pressures. The main sources of error in the experimental system are temperature and pressure sensors, mass variation during the experiment, and data reduction. As discussed in previous sections, the accuracy of the temperature and pressure sensors are very high. Furthermore, annual calibrations on temperature and pressure revealed that the sensors maintain

their calibrations. Therefore, their impact on the results is extremely negligible. The error in mass values (weight change with time) has the most measurable impact on the measured values when proper data reduction is conducted. The errors in mass values that were calculated by propagating the measured mass errors using the force balance equation are also found to be very small (less than 0.5 mol% and in many cases less than 0.2 mol%).

In a high-pressure view cell experiment, the major source of instrumental error comes from the ISCO pump, which is utilized to measure the amount of gas delivered to the system. Therefore, any minor inaccuracy in *T*, *P*, and the volume of the pump, or any leak from the pump has a significant impact on the measurement results. In addition, systematic error by the operator must also be carefully considered.

7- Visual Inspection

The high-pressure view cell design allows users to monitor phase transitions or visually inspect the interaction between gas and ionic liquid. Currently, the visual inspection of the sample is not possible in the IGA and XEMIS gravimetric microbalances. However, a custom reactor has been designed for the IGA to allow the sample to be viewed through quartz windows installed in the jacket.

8- Cost of the Instrument

The high-pressure view cell is an in-house designed apparatus. The manufacturing and maintenance costs of the high-pressure view cell are much lower compared to the manufacturing and maintenance cost of the gravimetric microbalances. The potential issues in the instrument can be handled and solved promptly by researchers or by technicians. On the other hand, the

maintenance issues for the gravimetric microbalances may require assistance from the manufacturer.

2.2. Liquid-Liquid Equilibria (LLE) Apparatus

2.2.1. LLE Apparatus Components

The experimental LLE apparatus shown in Figure 2.8 consisted of borosilicate sample tubes, a custom-made tube holder, a Plexiglas® water bath with a mixer, external temperature control, and a cathetometer. An external temperature control (VWR Polyscience Circulator, Model 1190s) regulated the temperature in the Plexiglas® water bath. The temperature of the water bath was measured by a thermocouple (Ertco Eutechnics Digital Thermometer, Model 4400). The Ertco thermometer was calibrated using a Fluke Standard Platinum Resistance Thermometer (S/N 1113), and the standard uncertainty was determined to be 0.04 K. A cathetometer (Mitutoyo Corp., model no. CD-6″ CS, code no. 500-19) was used to measure the height of the fluids in the sample tubes with a standard uncertainty of 0.01 mm. The sample holder can be set up to either mix the glass tubes via a rocking motion or set the tubes upright for phase separation and height measurements.

2.2.2. LLE Apparatus Working Principle and Data Reduction

The experimental liquid-liquid equilibria (LLE) measurement is based on a mass-volume technique which does not require any compositions be measured using analytical instruments.[3,80,81]

The experimental procedure was as follows[3]:

(1) The borosilicate glass tubes were cleaned with acetone and dried in a vacuum oven at 348.15 K for three hours before each experiment.

(2) Each tube was volumetrically calibrated with methanol as a reference fluid. The density of methanol was obtained using the REFPROP v.9.1 program.[73] A linear equation to calculate

volume (v) from height (h) was derived $v(cc) = a + b * h(mm)$, with individual a and b parameters for each tube. A correction factor (c) in the meniscus volume is necessary due to the variation in the capillary constant.[82] Therefore, the correction factor, $C = V_{ml} - V_{mm}$, was applied to each tube where V_{ml} is the meniscus volume of the liquid mixture and V_{mm} is the meniscus volume of the methanol.

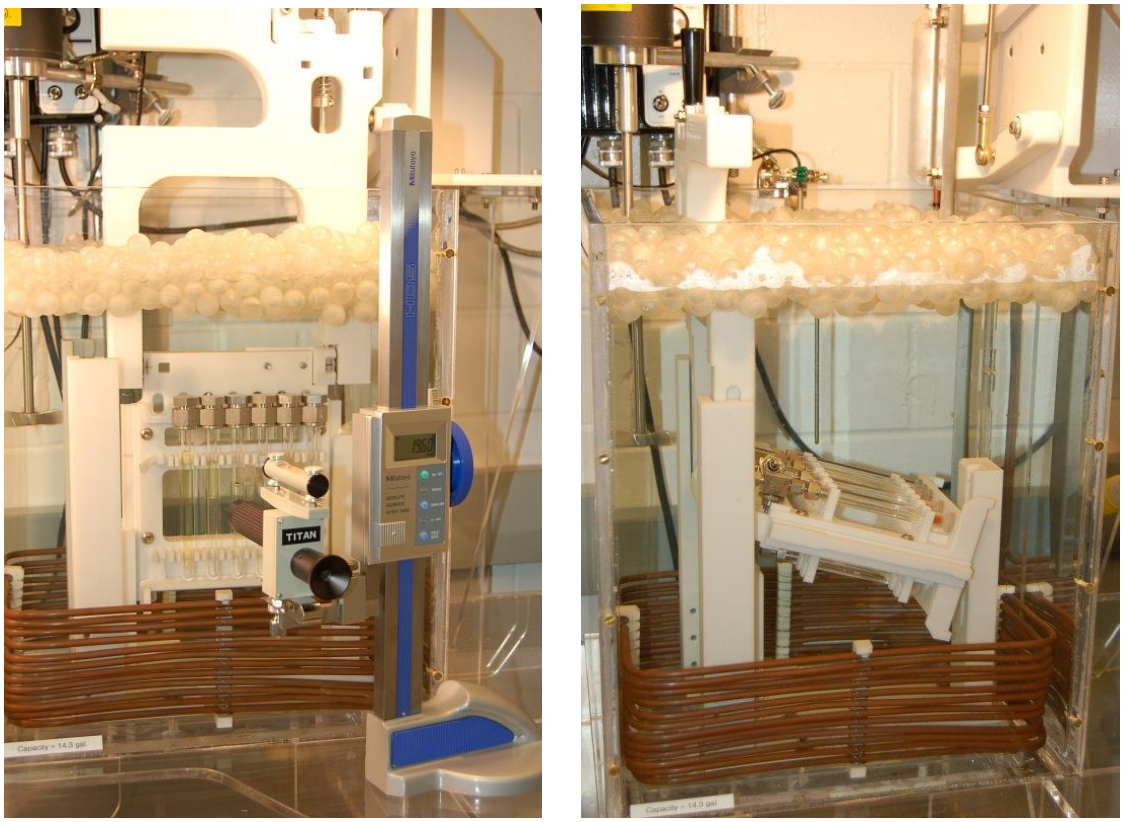

Figure 2.8. Liquid-Liquid Equilibria Apparatus. Picture in the left show experimental apparatus, tubes, and cathotemeter. The picture in the left demonstrates the mixing of the borosilicate tubes via the rocking movement. *This picture was taken at DuPont Experimental Station, Wilmington, Delaware, and used in this thesis with the permission of Dr. Mark B. Shiflett.*

(3) Two mixtures with different concentrations for each alcohol and IL system were prepared in borosilicate tubes by weighing each component on a balance with a standard uncertainty of 0.001 g in a nitrogen-purged glove box to reduce additional moisture uptake from the air.

(4) The sample containers were placed in a custom-made tube holder in a Plexiglas® water bath and mixed at a constant temperature for a minimum of 48 hours.

(5) The tubes were positioned upright for phase separation for a minimum of 12 hours, and the height of each liquid phase in each tube was measured three times using the cathetometer. The average value of the three measurements was recorded as the height of the corresponding liquid phase.

(6) The tubes were mixed again for at least 12 hours, and step (5) was repeated. The mixing, phase separation, and measurements were repeated until the heights of each liquid phase remained constant at the given temperature to ensure enough time given for thermodynamic equilibrium.

(7) The composition of each component in the alcohol-rich upper phase (x_1 and x_2) and the IL-rich lower phase (x'_1 and x'_2), as well as the molar volumes of each component in each phase, were calculated.

(8) The excess molar volume for each liquid phase ($V^{ex\prime}$or V^{ex}) was calculated using pure component molar volumes (V_1 and V_2): IL-rich lower phase with $V^{ex\prime} = V'_m - (x'_1 V_1 + x'_2 V_2)$ and alcohol-rich upper phase with $V^{ex} = V_m - (x_1 V_1 + x_2 V_2)$ where V_m is the measured volume of the mixture.

2.2.3. Cloud Point Measurement

In addition to the LLE measurements, the cloud point was measured to confirm the existence of the upper critical solution temperature (UCST) for each system. The samples that contained a known amount of components were prepared in borosilicate glass tubes in a nitrogen-purged glove box. The sample was placed in a silicone oil bath (Hart Scientific, Model 7341). The bath temperature was calibrated using a Fluke Standard Platinum Resistance Thermometer (S/N 1113), and the standard uncertainty was determined to be 0.03 K. Starting at a high temperature such as 370 K where only a single liquid phase exists, the temperature was slowly decreased at about 1 $K \cdot h^{-1}$ until a second liquid phase began to form. The cloud point experiment was also repeated to confirm the UCST by increasing the temperature from a two-liquid phase mixture until only one liquid phase was observed.

2.2.4. Uncertainty Estimation

The total uncertainties (combined uncertainty $u_c(x)$) were estimated by calculating both random and systematic errors present in the system. The overall random uncertainties were calculated using an error propagation method considering that the sample calibration constants (*a, b*), the mass of diols and ILs, the height of each phase, and the density of the pure components were experimental parameters which have an effect on the random uncertainties. The systematic uncertainties include properly correcting for the vapor phase composition and meniscus. The mass (or moles) of nitrogen in the vapor phase can be neglected and has a negligible change on the liquid composition as discussed in our previous report.[56]

2.3. Water Determination in Ionic Liquids

Water is one of the most abundant substances in the world, and it consequently and inevitably present everywhere. The quality of most products or processes today has strongly dependent on the presence of water because the water content has an impact on the chemical stability, purity of the substances, the efficiency, and more.[83] The presence of water in ionic liquids also has an impact on the thermophysical properties, which might ultimately impact how the process works with ILs. Therefore, it is quite important to measure the water content of ionic liquids as accurately as possible.

There are numerous direct and indirect methods to assess the water content of substances such as thermogravimetric methods, analytical methods, chromatographic methods, to name a few.[83]

The thermogravimetry method, also widely known as a loss on drying method, is a widely used technique to quantify the moisture content of substances based on the loss in weight via drying of the sample. The known amount of sample is heated to high temperature, and the weight change of the sample is monitored during the heating process. The loss on drying method works for solid samples. However, as most of the ionic liquids possess negligible vapor pressure, this technique can be utilized to measure the water content of the ionic liquids. Even though this technique is simple, the technique gives only a rough indication about the water content as a significant amount of other volatile compounds may have also been lost. Furthermore, the method only provides the amount of free water present in the sample.

One of the chromatography techniques used to determine water content is gas chromatography (GC), which is based on the volatilization of compounds without decomposition. The technique is not practical for ionic liquids due to their intrinsic low volatility. Additionally,

the GC technique is also limited for water determinations in other substances because of poor sensitivity of the detectors, and inefficiency and instability of the stationary phase.

Therefore, Karl Fisher titration is still the most common, practical, and simple analytical technique to measure the water content of ionic liquids.

2.3.1. Karl Fischer (KF) Titration

Karl Fischer titration is an easy and practical analytical technique to quantify the water content of a wide variety of solid and liquid samples when there is no chemical reaction between the sample and the reagents and where the water in the sample can be completely dissolved.[83,84] The KF technique might require additional steps for solid samples as the solid samples might initially require to be dissolved in the solution.[83] The water content obtained from KF consist of both free and bounded water.

The fundamental principle behind KF titration is based on the oxidation reaction where alcohol is reacted with sulfur dioxide and a base to form an intermediate alkyl sulfite salt, which is then oxidized by iodine to an alkyl sulfate salt.[84]

There are two main types of KF titrations available: volumetric and coulometric titration.[85] The differences between the two types are the source of titrant (iodine) in the reaction and the water measurement range. In the volumetric KF technique, iodine is mechanically added to the titration cell, and the technique usually works from 0.01 wt % to 100 wt %.[85] In the coulometric technique, iodine is electrolytically generated in the measurement cell, and the technique can determine the water content from 10 micrograms to 100 mg.[85]

Coulometric titrators are also divided into two main types: *fritted-cell* coulometric titrator or fritless-cell coulometric titrator.[85] In *fritted-cell*, a diaphragm separates the anode from the cathode.

The purpose of the diaphragm to prevent the iodine generated at the anode from being reduced back to iodide at the cathode instead of reacting with water. The *fritted-cell* is required for samples with a low water content, very accurate determinations, or unsaturated hydrocarbons. In *fritless-cell*, the measurement unit is designed without a diaphragm. Even though *fritless-cell* minimizes iodine being reduced back to iodide, the possibility of iodine reduction to iodine is not completely eliminated. The *fritless-cell* can be more advantageous when *fritted-cells* require two reagents. However, new KF solutions allow users to use one working solution for both anode and cathode in *fritted-cells*, as done in this study. On the other hand, *fritless-cells* might be ideal for the determination of water content of hydrocarbons, and petroleum oils.

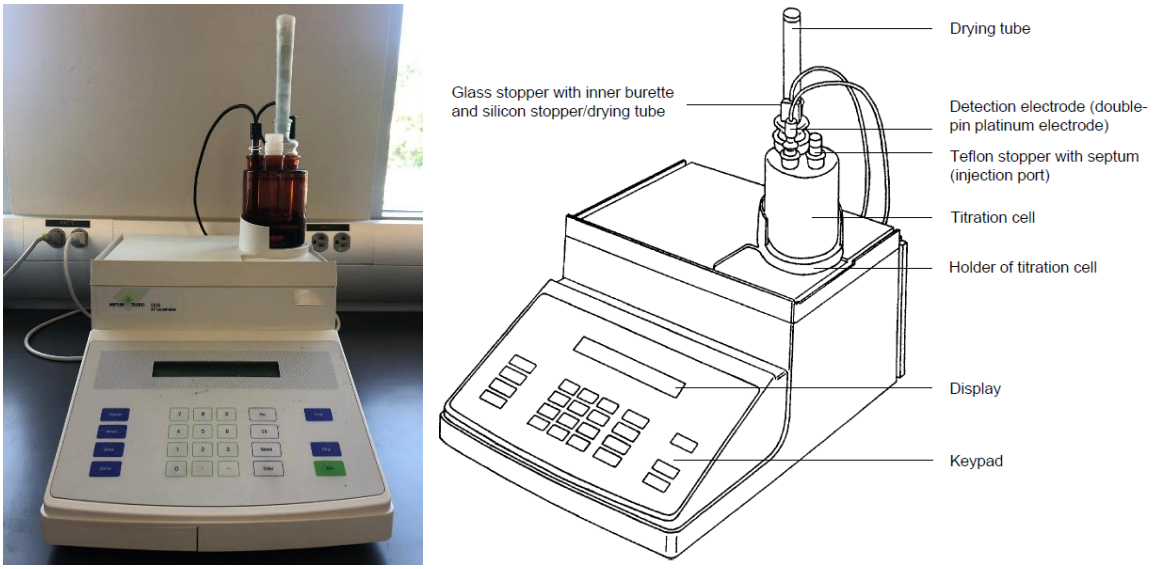

Figure 2.9. Mettler Toledo DL36 Coulometric Karl Fischer[86]

2.3.1.1. Mettler Toledo DL 36 Karl Fischer Coulometric Titration

Mettler Toledo DL 36 Karl Fischer is a coulometric titrator. The schematic diagram and the measurement unit of Mettler Toledo DL 36 Karl Fischer Coulometric Titration is shown in Figure 2.9 and Figure 2.10. respectively.[86] The experimental unit cell consists of titration cell, Teflon™

stopper, detection electrode, inner burette with a drying tube. The titration cell has a small size magnetic bar to stir the solution after sample injection. Both titration cell and inner burette contain Aquastar CombiCoulomat Fritless (EMD Chemicals, Product No. EM1092570500) KF reagent for coulometric water determinations for cells with and without diaphragm as an anolyte and catholyte, respectively.

2.3.1.1.1. Measurement Principle

In the KF technique, alcohol (ROH) is reacted with sulfur dioxide (SO_2) and base (R'N) to form an intermediate alkyl sulfite salt ([R'NH]SO_3R) which is then oxidized by iodine to an alkyl sulfate salt ([R'NH]SO_4R). When the water in the measurement cell is consumed, an excess of iodine left in the anolyte is detected by the double-pin platinum electrode, which signals the endpoint of the titration.

$$ROH + SO_2 + R'N \rightarrow [R'NH]SO_3R + H_2O + I_2 + 2R'N \rightarrow 2[R'NH]I + [R'NH]SO_4R \quad (2.9)$$

$$2\ I^- \rightarrow I_2 + 2e^- \quad (2.10)$$

The amount of water present in the system is calculated based on the total current passed using a microprocessor. According to Faraday's law, the amount of iodine generated is proportional to the total current flowed into the system. In the reaction (Equation 2.9), I_2 and H_2O react with each other in proportion 1:1.[84,86] One mole of water (18 g) thus corresponds to 2 x 96,500 coulombs, in other words, per mg H_2O a quantity of electricity of 10.72 coulombs is consumed. The total current consumption is a measure of the amount of moisture present.

2.3.1.1.2. Measurement Technique

There are a few important steps before an actual measurement. As both catholyte and anolyte solutions have a limited capacity for water determination, catholyte or anolyte solutions should be changed when their capacity is reached. However, it is also recommended to change the solution if drift is too high, or the membrane is contaminated.[86] If the volume of the titration cell reached 150 ml (upper marking on the titration cell), the anolyte solution should also be renewed even if the capacity is not reached.[86] When the KF system is ready for an experiment, the instrument should be left in an operation mode until a stable baseline (i.e., drift) is obtained. After the system is stable, a known amount of ionic liquid is injected into the titration cell through a Teflon™ stopper. The amount of sample should be adjusted to the expected amount of water present in the sample. For example, 0.5-1 g of sample is adequate for most ionic liquids and dihydroxy alcohols. The amount of sample should be less if the water content is expected to be high. During injections, it is important to keep the stopper in place to prevent an excessive amount of moisture entering into the cell. In this study, the Karl Fischer titration was tested with an Apura water standard (EMD Chemicals, Lot No. HC61276950) before and after each measurement to ensure accurate and reliable titration results.

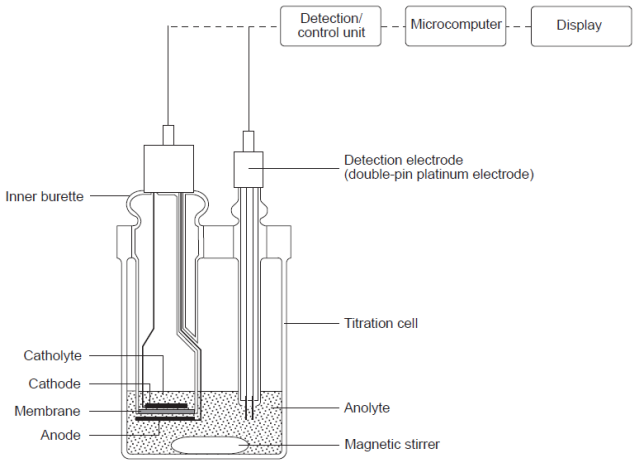

Figure 2.10. The measurement unit of Mettler Toledo Dl 36 Coulometer Karl Fischer Titrator[86]

2.4. Ionic Liquid Drying Apparatus

As discussed in Section 2.3, the water content of the ionic liquids has an impact on the thermophysical properties of the ionic liquids. Therefore, all ionic liquid samples used in this study were dried under vacuum for 24 to 48 h to remove water and volatile impurities. Since ionic liquids are exposed to air during sample the loading procedure for the microbalances, the IL sample was dried and degassed under high vacuum (10^{-12} MPa) at 348.15 K for 24 h to remove moisture and volatile impurities before each experiment in the microbalance. In other experiments, the samples are prepared under a nitrogen glove box.

The ionic liquid drying apparatus consists of a backing pump, a turbo pump, and a borosilicate glass tube. Ionic liquid from the manufacturer bottle is poured into a borosilicate glass tube. A small stirring bar is placed into the tube to increase mixing and the desorption of dissolved air, water, and volatile impurities from the liquid sample. The system is initially evacuated to 10^{-3} mbar with a backing pump. At this point, large bubbles can be seen coming out of the ionic liquid, which

is dissolved gases and water vapor. After 2-3 hours of purging and the pressure in the manometer stabilized, the turbo pump is started for removing (i.e., evacuating) the remaining gases and water vapor. In aprotic IL applications, the drying was conducted at 323.15 K. Protic ionic liquids were dried at room temperature (~293 K) for a longer period (4-5 days) as they are more sensitive to temperature and can decompose at higher temperatures (i.e., 323.15 K).

Chapter 3. Phase Equilibrium Modeling

"Nothing in life is to be feared, it is only to be understood.
Now is the time to understand more,
so that we may fear less."
Marie Curie,
The first woman to win the Nobel Prize, and the first person to win the Nobel Prize twice

Phase equilibrium is the state of the thermodynamic system of a pure component or mixtures at which no macroscopic changes occur in the system. Phase equilibrium knowledge is essential for the design of chemical processes such as separations, reactions, fluids flow, to name a few.[87] Phase equilibrium models are mathematical correlations that describe the relationship between temperature, pressure, volume, and composition of a pure component or mixtures at equilibrium. The merit of the phase equilibrium modeling is that the models estimate thermodynamic properties or relations at points beyond the limit of experimental measurements.

3.1. Criteria of Phase Equilibrium

The equilibrium condition between phases (vapor, liquid, or solid) for a closed pure component system at constant temperature and pressure is given as:

$$T^I = T^{II} \tag{3.1}$$

$$P^I = P^{II} \tag{3.2}$$

$$\mu^I = \mu^{II} \tag{3.3}$$

where I and II represent phases. The equilibrium conditions (Equation 3.1 - 3.3) state that temperature, pressure, and chemical potential of phases of a pure component must be equal if the system is at equilibrium.

Similarly, the equilibrium condition between two or more phases for a closed multi-component system at constant temperature and pressure result:

$$T^I = T^{II} = ... = T^n = T \tag{3.4}$$

$$P^I = P^{II} = \cdots = P^n = P \tag{3.5}$$

$$\mu^{\mathbf{I}} = \mu^{\mathbf{II}} = \cdots = \mu^{\mathbf{n}} = \mu \tag{3.6}$$

where *I, II,* and *n* represent phases. The equilibrium conditions (Equation 3.4 - 3.6) state that temperature, pressure, and chemical potential of each component in all phases must be equal if the system is at equilibrium.

The chemical potential describes the change in Gibbs energy with the amount of a component at a constant temperature, pressure, and amount of the other components. However, the chemical potential is relatively an abstract expression without direct physical translation into the real world.[88] Therefore, Lewis described a new function called *fugacity* to find a physical translation of chemical potential for any component in any system (solid, liquid, or gas, pure or mixed, ideal or not):[88]

$$\mu_i - \mu_i^0 = RT\ ln\frac{\overline{f}_i^I}{\overline{f}_i^o} \tag{3.7}$$

where $\overline{f}_i^o$ is a fugacity of component *i* in an arbitrary standard state. The translation of chemical potential to fugacity (Equation 3.7) shows that fugacity can replace the chemical potential term in an equilibrium condition. Contrary to chemical potential, fugacity can be rather easily understood. Fugacity, a measure of chemical potential, can be considered as a "corrected pressure" for gases. In summary, at equilibrium, the fugacity of each component in each phase must be equal.

$$\overline{f}_i^{I} = \overline{f}_i^{II} = \cdots = \overline{f}_i^{n} = \overline{f}_i \tag{3.8}$$

Equation 3.8, the so-called equilibrium criterion, is also a starting point of all phase equilibrium calculations such as liquid-liquid equilibria (LLE), vapor-liquid-equilibria (VLE), or vapor-liquid-liquid-equilibria (VLLE).

3.1.1. Criteria of Vapor-Liquid Equilibrium

In vapor-liquid equilibrium (VLE), the equilibrium criteria states the fugacity of each component in the liquid phase (L) must be equal to the fugacity of each component in the vapor phase (V):

$$\overline{f}_i^{L}(T, P, x) = \overline{f}_i^{V}(T, P, y) \tag{3.9}$$

In VLE, both phases can be described via the equation of state. In this case, the method is called the *Φ-Φ* method. In the *Φ-Φ* method,

Liquid phase fugacity is described as:

$$\overline{f}_i^{L}(T, P, x) = x_i P \overline{\Phi}_i^{L}(T, P, x) \tag{3.10}$$

where P is pressure and $\overline{\Phi}_i^{L}$ is the fugacity coefficient of component i in the liquid phase.

Vapor phase fugacity is described as:

$$\overline{f}_i^{V}(T, P, y) = y_i P \overline{\Phi}_i^{V}(T, P, y) \tag{3.11}$$

where $\overline{\Phi}_i^{L}$ is the fugacity coefficient of component i in a vapor phase.

Then, vapor-liquid equilibrium via the Φ-Φ method leads to the vapor-liquid equilibrium criterion:

$$x_i P \overline{\Phi}_i^{L}(T, P, x) = y_i P \, \overline{\Phi}_i^{V}(T, P, y) \tag{3.12}$$

Alternatively, at low to moderate pressures, the liquid phase can be described via the activity coefficient model, whereas the vapor phase is described with the equation of state model. In this case, the method is called γ-*Φ* method. In the γ-*Φ* method,

Liquid phase fugacity is described as:

$$\overline{f}_i^L(T,P,x) = x_i\,\gamma_i(T,P,x)\,P_i^s(T)\,\Phi_i^{L,sat}(T,P)exp\,[\int_{Ps}^{P}\frac{\overline{V}_i(T,P,x)}{RT}\,dP] \tag{3.13}$$

where x_i is mole fraction of component i, γ_i is an activity coefficient of component i, $P_i^s(T)$ is the saturation pressure of component *i* at temperature T, $\Phi_i^{L,sat}$ is the fugacity coefficient of component *i* at saturation T. $exp\,[\int_{Ps}^{P}\frac{\overline{V}_i}{RT}\,dP]$ is a Poynting correction.

Vapor phase fugacity is described as:

$$\overline{f}_i^V(T,P,y) = y_i P\overline{\Phi}_i^V(T,P,y) \tag{3.14}$$

Then, vapor-liquid equilibrium via the γ-*Φ* method leads to the vapor-liquid equilibrium criterion:

$$x_i\,\gamma_i(T,x)\,P_i^s(T)\,\Phi_i^{L,sat}(T,P)\,[\int_{Ps}^{P}\frac{\overline{V}_i}{RT}\,dP] = y_i P\overline{\Phi}_i^V(T,P,y) \tag{3.15}$$

For liquid phase modeling, some useful assumptions can be made. When the pressure is not significantly higher than the vapor pressure of component *i* at a given temperature, the Poynting correction can be assumed to be 1 when the pressure difference is relatively low. At relatively low pressures and far from the critical points, $\Phi_i^{L,sat}(T,P)$ can be assumed to be 1. Then, simplified vapor-liquid equilibrium criteria via the γ-*Φ* method can be written as:

$$x_i\,\gamma_i(T,P,x)\,P_i^s(T) = \,y_i P\overline{\Phi}_i^V(T,P,y) \tag{3.16}$$

3.1.2. Criteria for Liquid-Liquid Equilibrium (LLE)

The equilibrium criteria for liquid-liquid equilibria (LLE) states that the fugacity of each component in liquid phase (L1) and liquid phase (L2) must be equal:

$$\overline{f}_i^{L1}(T,P,x) = \overline{f}_i^{L2}(T,P,y) \qquad (i = 1,2,\dots,N) \tag{3.17}$$

$$x_i^{L1}\gamma_i^{L1}\, f_i^{L1} = x_i^{L2}\gamma_i^{L2}\, f_i^{L2} \tag{3.18}$$

If each pure component exist as a liquid at the system temperature, $f_i^{L1} = f_i^{L2} = f_i$.[89] Therefore, the equilibrium criteria for LLE can be described as:

$$x_i^{L1}\gamma_i^{L1} = x_i^{L2}\gamma_i^{L2} \tag{3.19}$$

3.2. Raoult's law

Raoult's law is the simplest thermodynamic model to describe gas solubility in liquids:

$$P_i = x_i P_i^S \tag{3.20}$$

where P_i is the partial pressure of component *i* in the gas phase, x_i is the mole fraction of component *i* in the liquid phase, and Pi^s (also shown as P_i^{vap} or P_i^{sat}) is the saturation (or vapor) pressure of a pure liquid at the temperature of the solution.

Raoult's law can be obtained by reducing the equilibrium criterion (Equation 3.9) with the following major assumptions:

1- The vapor phase is ideal.

2- The effect of pressure on the condensed phase (Poynting correction) is negligible.

3- The liquid phase is an ideal solution (e.g. $\gamma_i = 1$) for all components.

Raoult's law neglects any non-idealities caused by the solute-solvent interaction[88] assuming the molecular species of the mixtures are similar in size and chemical nature[89]. The law works reasonably well when the partial pressure of a gas is low; the temperature of the solution is below

the critical temperature of the solvent and not above the critical temperature of gaseous solute. In some cases, mixtures demonstrate ideal solubility. For example, a mixture of isomers (ortho-, meta-, and para- xylenes) or acetone-acetonitrile.[89] In reality, most of the mixtures result in deviations from ideal solubility (Raoult's law). In the ideal solubility, the activity coefficient of the solute is equal to 1. When the vapor pressure of a mixture is lower than Raoult's law predictions ($P < \sum x_i P_i^s$), the activity coefficient of one of the species is lower than unity. Therefore, the solubility shows "negative" deviation from ideal solubility. Negative deviation from Raoult's law is a result of significant indifference in nature and the size of the solute and solvent. When the vapor pressure of a mixture is higher than Raoult's law predictions ($P > \sum x_i P_i^s$), the activity coefficient of one of the species is higher than unity; therefore, the solubility shows "positive" deviation from ideal solubility. In this case, the solubility of a gas in a liquid is lower than the solubility predicted by Raoult's law. Positive deviation from Raoult's law indicates stronger attractive forces between the like molecules (molecule *i*-molecule *i*) than the attractive forces between dissimilar molecules (molecule *i*-molecule *j*).

Raoult's law has two pitfalls. First, the law states that the solubility of a gas in a liquid is independent of the solvent for a given gas at a constant temperature. On the other hand, many experimental studies have shown otherwise. Second, the solubility of the gas decreases with an increase in temperature. Even though this is often correct, exceptions are present such as the solubility of light gases in solvents.[88] Due to the extreme simplification of Raoult's law, its application to estimate the gas solubility is very limited.

3.3. Henry's law

Application of Raoult's law requires the value of the saturation pressure of species *i*. Therefore, it is not appropriate for the species that has a lower critical temperature than the working temperature. Therefore, Raoult's law cannot be used if one desires to measure the solubility of a gas at a temperature lower than the critical temperature of the solute. For a very dilute solution, Henry's law states the partial pressure of the species in the vapor phase is directly proportional to its liquid phase composition. The proportionality constant or Henry's law constants (H or k_H) is a function of temperature. Henry's law constants (k_H) are used for assessment of gas solubility in a solvent at dilute concentrations where the lower the k_H value indicates higher gas solubility in the solvent.

Henry's law constants can be obtained from experimental gas solubility (*PTx*) data using the thermodynamic definition of the Henry's constant at low pressures:

$$k_H = \lim_{x_1 \to 0} \frac{f_1^V(T, P, y_1)}{x_1} \approx \left(\frac{df_1^V}{dx_1}\right)_{x_1=0} \tag{3.21}$$

where f^V is the vapor phase fugacity of the pure gas (y_1=1) and can be calculated by a proper EOS model at a given condition (*T, P*).[73] The Henry's law constants are obtained calculating the limiting slope while x_1 approaches zero using the linear fit of experimental data including a theoretical zero point (zero pressure and zero composition).

3.3.1. Effect of Pressure on Henry's constants

At high pressures, the effect of pressure on Henry's constants is not negligible. Therefore, the pressure dependence of k_H should be corrected for pressure dependence using the Krichevsky-

Kasarnovsky equation. The Krichevsky-Kasarnovsky equation has two assumptions. First, the solubility of gas should be small at high pressures so that the activity coefficient of the solute is close to unity. Second, the dilute liquid phase is incompressible, and the temperature of the solution is far from the critical temperature. At very high pressures and relatively higher gas solubilities, the activity coefficient of the solute can be included to estimate the solubility of gases in liquids using Henry's law. In this study, Henry's law constant was obtained at such low pressures that Krichevsky-Kasarnovsky was not needed.

3.3.2. Effect of Temperature on Henry's constants

In general, the gas solubility in liquids is inversely proportional to increases in temperature such that the solubility decreases with an increase in temperature. However, in some cases (e.g., the solubility of light gases in liquids), the temperature dependence of gas solubility is directly proportional to temperature variations. If one can obtain the enthalpy ($\Delta\overline{H}_{sol}$) and entropy ($\Delta\overline{S}_{sol}$) of a solution, the effect of temperature on the solubility can be properly discussed. The enthalpy ($\Delta\overline{H}_{sol}$) and entropy ($\Delta\overline{S}_{sol}$) of solution per mole of gas at infinite dilution can be obtained the following relations[90]:

$$\left(\frac{\partial \ln k_H}{\partial T}\right)_p = -\frac{\Delta\overline{H}_{sol}}{RT^2} \tag{3.22}$$

$$\left(\frac{\partial \ln k_H}{\partial T}\right)_p = -\frac{\Delta\overline{S}_{sol}}{RT} \tag{3.23}$$

The $\Delta\overline{H}_{sol}$ and $\Delta\overline{S}_{\mathrm{sol}}$ can be obtained by calculating the slope from equations (3.22) and (3.23) and using Henry's law constants. The negative $\Delta\overline{H}_{sol}$ indicates gas sorption in liquids is exothermic,

indicating an inverse relationship between the temperature and the solubility of gases. The positive $\Delta\overline{H}_{sol}$ indicates gas sorption in liquids endothermic process, which means the solubility of the gases would increase with an increase in temperature. The negative $\Delta\overline{S}_{sol}$ indicates the absorption of gases leads to an increase in molecular ordering.[90]

3.4. Equation of State Models

Equation of State (EoS) is a thermodynamic function related to temperature, pressure, or molar volume. Equations of state can be applied to pure components or multicomponent systems by incorporating mixing rules. The success of the phase equilibrium predictability of EoS is strongly associated with the mixing rules.

3.4.1. Cubic Equation of States

The first well-known Equation of State is proposed by Johannes Diderik van der Waals[91] to describe the relationship between pressure, temperature, and volume. In this cubic form of the equation, van der Waals included two terms (*a* and *b)* to improve the prediction ability of the equation. The attraction parameter (*a*) was introduced to consider the attraction between molecules, whereas the co-volume parameter (*b*) was to correct the volume occupied by molecules.[91] Later in 1949, Otto Redlich and Joseph Neng Shun Kwong modified the van der Waals equation to accurately correlate *PVT* properties of gases by adding a temperature dependence on the attractive term.[92] Giorgio Soave[93] improved the Redlich and Kwong equation including a more complex temperature-dependent term, which is a function of the acentric factor.[94] In 1985, Ding-Yu Peng and Donald B. Robinson developed a new equation on the base of the Redlich-Kwong equation to overcome the limitations of the inaccurate prediction of some properties (e.g., liquid density) in the near-critical region.

3.4.1.1. Peng-Robinson Equation of State

A new form of EoS was developed by Ding-Yu Peng and Donald B. Robinson by modifying the attractive term and introduced a *b(V-b)* term to represent attractive pressure forces, consequently, to have a better prediction of liquid densities. The Peng-Robinson equation of state (PR-EoS) has been one of the most commonly used thermodynamic models to estimate vapor-liquid equilibrium data in both academic and industrial fields.[95] Today, there are more than 220 modifications to the PR-EoS for pure compounds and a significant amount of work on parameter adjustments for mixtures.[95]

The PR-EoS for mixtures is given as:[96]

$$P = \frac{R\,T}{\underline{V} - b_m} - \frac{a_m}{\underline{V}\left(\underline{V} - b_m\right) + b(\underline{V} - b_m)} \tag{3.24}$$

where a_m and b_m are the mixture attractive term and co-volume parameters, respectively. In this thesis, the a_m and b_m parameters are computed with the one-parameter van der Waals mixing rule with Boston-Mathias extension for the attractive term and the standard PR-EoS alpha function. Pure component parameters (a_i and b_i) are computed based on the critical temperature (T_c), critical pressure (P_c) and acentric factor (ω). The binary parameters k_{ij} and l_{ij} can be determined from the regression of the VLE data by minimizing the objective function of the average absolute relative deviation (% AARD $= (100/n)\sum_{i=1}^{n}|(P^{exp} - P^{regressed})/P^{exp})|$). The critical properties of the ionic liquids cannot be experimentally determined (i.e., the critical temperature is above the decomposition temperature). Therefore, the critical properties used in this dissertation were obtained from the literature where the critical properties were estimated using a Group Contribution Method.[37]

Pure component parameters:

$$a_i = \frac{0.45724\ R^2\ T_{c_i}^2}{P_{c_i}}\ \ \alpha_i(T) \tag{3.25}$$

$$b_i = \frac{0.07780\ R\ T_{c_i}}{P_{c_i}} \tag{3.26}$$

Alpha Function:

$$\alpha_i(T) = \left(1 + m_i\left(1 - \sqrt{T_r}\right)\right)^2 \tag{3.27}$$

$$m_i = 0.037464 + 1.54226\ \omega_i - 0.26992\ \omega_i^2 \tag{3.28}$$

Mixing rule:

$$T_{r_i} = \frac{T_i}{T_{c_i}} \tag{3.29}$$

$$a_m = \sum_i \sum_j x_i\, x_j\left(1 - k_{ij}\right)\left(a_i a_j\right)^{1/2} + \sum_i x_i \left(\sum_j x_j \left(\left(a_i a_j\right)^{1/2} l_{ij}\right)^{1/3}\right)^3 \tag{3.30}$$

$$k_{ij} = k_{ij}^{(1)} + k_{ij}^{(2)} T + \frac{k_{ij}^{(3)}}{T} \quad \text{and} \quad l_{ij} = l_{ij}^{(1)} + l_{ij}^{(2)} T + \frac{l_{ij}^{(3)}}{T} \tag{3.31}$$

$$b_m = \sum_i x_i b_i \tag{3.32}$$

3.4.2. Virial Equation of State

Ideal gas law assumes gas molecules do not interact with each other, which is not valid for real gases. To describe the real behavior of gases, H. Kamerlingh Onnes developed the virial equation of state (VEoS) on the strong foundation of statistical thermodynamics and molecular theory.[94,97] In the model, molecules are assumed as rigid bodies that obey classical Newtonian mechanics.[94] Also, it is assumed that "the intermolecular potential energy of a pair of molecules depends only upon the separation of mass."[94] For the virial equation, for orders of more than third or higher, it is assumed that "the intermolecular potential energy of a cluster of molecules is the sum of that calculated for each unique pair in the cluster considered in isolation." [94]

The VEoS is a power series expansion for the pressure *P* of a real gas in terms of the molar volume. The virial series can also be more conveniently written in terms of the compressibility factor (Z). The virial coefficients are the only function of temperature and describe the interaction between the number of molecules. For example, the second virial coefficient (B(*T*)) accounts for the interaction between two molecules, and the third virial coefficient accounts (C(*T*)) for the interaction between three molecules, and so on.

3.4.2.1. Second Virial Coefficient Equation of State

At low and moderate densities, the mean distance between gas molecules significantly increases, and the intermolecular forces between the molecules decrease. Therefore, only a few virial coefficients could yield high accuracy results. At higher densities, the higher terms cannot be ignored[98] because the intermolecular forces between the molecules increase as a result of the decreased mean distance between the molecules. The second virial coefficient, therefore, can be accurately used to describe the gas densities at low to moderate pressures.

The translation of second virial correction on the fugacity of gas can be given as[1]:

$$\phi_1 = exp\left[\frac{(B_1(T) - \tilde{V}_1)(P - P_1^s)}{RT}\right] \tag{3.33}$$

where $B_1(T)$ is the second virial coefficient of gas at system T, $\tilde{V}_1$ is the saturated molar liquid volume at system T, and R is the universal gas constant. The $B_1(T)$ is obtained using the NIST REFPROP computer code *v.9.1*.[73] $\tilde{V}_1$ can be calculated as described in the previous section, and P_1^s can be obtained using the Extended Antione vapor pressure model where A, B, C, D, E, and F are constants:

$$lnP_i^s = A + \frac{B}{T + C} + D\ T + E\ lnT + F\ T^G \tag{3.34}$$

3.5. Activity Coefficient Models

At low to medium pressures, EoS models can be used to estimate the vapor phase fugacity as non-idealities in the vapor phase is usually small. On the other hand, non-idealities in the liquid phase can be large; therefore, the EoS with van der Waals one fluid mixing rules may not reasonably predict the liquid phase fugacities.[99] EoS models with excess free energy-based mixing rules can be used to estimate the liquid phase fugacities at all temperatures and pressures.[99] However, modeling the experimental data with EoS models is usually more tedious, while activity coefficient models are simple to estimate the liquid phase fugacities at low pressures. When two different models are used in phase equilibria modeling (an activity coefficient model for the liquid phase and an EoS model for the vapor phase), the critical point of the mixture might be incorrectly predicted because of the properties of the two phases might not be identical.[99] However, using two different models can accurately estimate the VLE when the critical point of the pure components is far from the critical point of the mixtures.

3.5.1. Non-Random Two-Liquid Model

Non-Random Two-Liquid (NRTL) model is an activity coefficient model to predict the activity coefficients of compounds in a liquid mixture. The NRTL model was developed by Henri Renon and John M, Prausnitz in 1968[100] based on Wilson's local composition theory[101] and Scott's two-liquid theory of binary mixtures[102]. The local composition theory of Wilson hypothesizes that the local concentration around each molecule is different than the bulk concentration, which is due to the difference in interaction energy of the central molecule (*i*) with the same kind of molecules (*i*) and the other molecules (*j*). The local composition theory introduces a non-randomness at a molecular level. To take into account non-randomness of mixing, Renon and Prausnitz redefined Wilson's relation among the local mole fractions introducing the term of α as a constant characteristic of the non-randomness of the mixture.[100] Renon and Prausnitz also used the two-liquid theory of Scott, which assumes the binary mixtures can be described with the average of two hypothetical fluids. The two hypothetical fluids are fluid (1) at which molecules *i* are at the center of a molecule's cell and are fluid (2) at which molecule *j* at the center of the molecule's cell. The residual Gibbs energy is assumed to be the sum of all the residual Gibbs energies for two-body interactions experienced by the center molecule.

The NRTL has a good prediction ability for highly non-ideal vapor-liquid or liquid-liquid equilibria systems. The model has adjustable interaction parameters that account for the interactions between alike and like molecules along with a non-randomness factor.[103] The non-randomness factor(α) usually varies from 0.2-0.47. The value of 0.2 is commonly used for many IL systems. Alternatively, the α parameter can be regressed along with binary interaction parameters.

The NRTL activity coefficient for a binary system is given as:

$$\ln \gamma_1 = {x_2}^2 \left[\tau_{21} \left(\frac{G_{21}}{x_1 + x_2 G_{21}} \right)^2 + \frac{\tau_{12}\, G_{12}}{(x_2 + x_1 G_{12})^2} \right] \tag{3.35}$$

$$\ln \gamma_2 = {x_1}^2 \left[\tau_{12} \left(\frac{G_{12}}{x_2 + x_1 G_{12}} \right)^2 + \frac{\tau_{21}\, G_{21}}{(x_1 + x_2 G_{21})^2} \right] \tag{3.36}$$

where G_{12} and G_{21} are defined by three interaction parameters $(\tau_{12}, \tau_{12}, \alpha)$:

$$G_{12} \equiv \exp(-\alpha \tau_{12}) \quad \text{and} \quad G_{21} \equiv \exp(-\alpha \tau_{21}) \tag{3.37}$$

The binary interaction parameters for a binary system can be obtained using temperature-dependent terms:

$$\tau_{ij} = \tau_{ij}^{(0)} + {\tau_{ij}^{(1)}}\Big/_{T(K)} + \tau_{ij}^{(2)} ln T(K) + \tau_{ij}^{(3)} T(K) \tag{3.38}$$

For most IL systems, only one temperature-dependent term is used in the literature. Therefore, the binary interaction parameters for a binary IL system is obtained using one temperature-dependent term in this study:

$$\tau_{12} = \tau_{12}^{(0)} + {\tau_{12}^{(1)}}\Big/_{T(K)} \quad \text{and} \quad \tau_{21} = \tau_{21}^{(0)} + {\tau_{21}^{(1)}}\Big/_{T(K)} \tag{3.39}$$

3.5.2. Flory-Huggins Model

The Flory-Huggins solution theory is based on a lattice model where a liquid is considered as a solid-like state where each molecule stays in a relatively fixed position and vibrates back and forth.[88] Paul J. Flory[104–106] and Maurice L. Huggins[107] independently developed an expression for solution of molecules are chemically similar but greatly differ in size based on statistical arguments

and well-defined assumptions.[88,108] This combinatorial entropy of mixing theory developed by Flory and Huggins represents an athermal solution where no heat evolved from the system upon mixing at constant temperature and pressure. For an athermal solution, the activity coefficient for component 1 in a binary mixture can be described as[29,37,88,109–111]:

$$\ln\gamma_1 = ln\frac{\phi_1}{x_1} + \left(1 - \frac{\phi_1}{x_1}\right) \tag{3.40}$$

Here

$$\phi_1 = \frac{x_1 v_1}{x_1 v_1 + x_2 v_2} = \frac{x_1}{x_1 + m x_2} \tag{3.41}$$

is the volume fraction, with v_i being some measure of the volume of species *i* of molecules, and $m = {}^{v_2}/_{v_1}$.[111]

Even though athermal behavior was never particularly observed[112], the behavior can be approximated for mixed components that differ significantly in size, such as polymer and solvent mixtures.[88] To apply the Flory-Huggins theory to real solutions, a residual contribution is added to the combinatorial term.[88] Then, the extended Flory-Huggins equation for real polymer solutions becomes[111]:

$$\frac{\underline{G}^{ex}}{RT} = \frac{\underline{H}^{ex} - T\underline{S}^{ex}}{RT} = \chi\,(x_1 + m x_2)\phi_1\phi_2 + \left[x_1\, ln\frac{\phi_1}{x_1} + x_2\, ln\frac{\phi_2}{x_2}\right] \tag{3.42}$$

Here

$$\phi_2 = \frac{x_2 v_2}{x_1 v_1 + x_2 v_2} = \frac{m x_2}{x_1 + m x_2} \tag{3.43}$$

Whereas χ is the dimensionless semi-empirical interaction parameter that characterizes the difference in interaction energy of solvent molecules immersed in pure polymer compared with one in pure solvent.[108,113] The original Flory theory considers the χ interaction parameter to be

constant ($\chi = 0$), which means the solvent and polymer are chemically similar. If the χ interaction parameter is greater than zero ($\chi > 0$), then the solvent and polymer "dislike" each other. If the χ interaction parameter is less than zero ($\chi < 0$), then the solvent and polymer attract each other.[108] In the field of polymers, the critical value for polymer solubility of χ is 0.5, and good solvents have a low χ value.[113]

The first term on the left side of the Equation 3.42 is an enthalpic contribution to excess Gibbs energy and the so-called residual term, and the second term is an entropic contribution to excess Gibbs energy and the so-called combinatorial term. When the attractive forces between unlike molecules are quantitatively different, this results in enthalpy of mixing. When unlike molecules in the solution are greatly different in size or shape, molecular arrangements of the molecules might be different than pure liquids resulting in entropy of mixing deviating from the ideality.

The activity coefficients in the new form of the Flory-Huggins model are then described as:

$$\ln\gamma_1 = ln\frac{\phi_1}{x_1} + \left(1 - \frac{1}{m}\right)\phi_2 + \chi\phi_2^2 \tag{3.44}$$

$$\ln\gamma_2 = ln\frac{\phi_2}{x_2} - (m-1)\phi_1 + m\chi\phi_1^2 \tag{3.45}$$

The Flory-Huggins model is widely used to model the solubility of water or gas solubility in polymers due to the significant difference between large polymer molecules and other solutes and solvents. Considering the solutions consist of ionic liquids and gas where the two molecules are significantly different in size (e.g., ionic liquid and ammonia), the Flory-Huggins model can be used to model the mixtures of ionic liquids at low to moderate pressures.

Chapter 4. Phase Behavior of Binary Ionic Liquid Systems

"In life, you should never give up, surrender to mediocrity,

but leave the "gray zone" where everything is a habit and passive resignation,

we must cultivate the courage to rebel."

Rita Levi-Montalcini,

Italian American neurologist and the Nobel Prize winner in 1986

The phase behavior of IL systems is of great importance for many applications, as discussed in Chapter 1. The phase behavior of binary ionic liquid systems in this chapter is divided into two main categories: ionic liquid with gases such as ammonia and carbon dioxide and ionic liquid with organic solvents such as dihydroxy alcohols. The phase behavior of ionic liquids and gas system involves vapor-liquid equilibria data, whereas the phase behavior of ionic liquids and organic solvents involves liquid-liquid equilibria.[114]

4.1. Phase Behavior of Ionic Liquid and Gas Mixtures

4.1.1. Assessment of Experimental Methods of XEMIS, IGA and High-Pressure View Cell

The reliability and accuracy of the gravimetric and synthetic methods used in this work were assessed by measuring the solubility of CO_2 in 1-hexyl-3-methylimidazolium bis(trifluoromethylsulfonyl)imide ($[C_6C_1im][NTf_2]$) which is a reference measurement recommended and sponsored by IUPAC in 2007.[115] Carbon dioxide (CAS:124-38-9, purity of 0.9999) was obtained from Matheson Tri-Gas, Inc. $[C_6C_1im][NTf_2]$ (CAS: 382150-50-7, EQ500831 632, purity of >0.99) was obtained from EMD Chemicals, Inc. The IL sample was dried, as described in Chapter 2. In order to account for buoyancy effects in data analysis in gravimetric methods, the CO_2 gas density as a function of T and P and the liquid density for the

ionic liquids as a function of *T* is required. Density for CO_2 was obtained using the National Institute of Standards and Technology (NIST) REFPROP V.9.1 Database[73]. The density of $[C_6C_1im][NTf_2]$ was calculated using the recommended IUPAC correlation.[115] The CO_2 + $[C_6C_1im][Tf_2N]$ solubility data are provided in Table 4.1.

Table 4.1. Experimental Vapor-Liquid Equilibrium (VLE) Data for CO_2 (1) + $[C_6C_1im][NTf_2]$

T/K	*P*/MPa	x_1	Method[a]	*T*/K	*P*/MPa	x_1	$u_c(x_1)$	Method[a]
293.15	0.1000	0.0270	3	333.15	1.018	0.1483	0.0097	2
293.15	0.5000	0.1563	3	333.15	2.025	0.2653	0.0076	2
293.15	1.000	0.2781	3	333.15	2.515	0.2972	0.0070	2
293.15	2.000	0.4552	3	333.15	3.009	0.3424	0.0063	2
293.15	3.000	0.5743	3	333.15	3.51	0.3784	0.0059	2
293.15	4.000	0.6596	3	333.15	4.01	0.4098	0.0055	2
293.15	5.000	0.7253	3	333.15	5.108	0.4908	0.0046	2
				333.15	6.048	0.5459	0.0041	2
297.4	0.0100	0.0027	4	333.15	7.502	0.5999	0.0041	2
297.4	0.0500	0.0151	4	333.15	10.045	0.6871	0.0063	2
297.4	0.1000	0.0301	4	333.15	12.479	0.7363	0.0050	2
297.4	0.3900	0.1139	4	333.15	14.92	0.7444	0.0030	2
297.4	0.6900	0.1890	4					
297.4	0.9900	0.2560	4					
297.4	1.2800	0.3153	4					
297.4	1.4800	0.3510	4					
297.4	1.9800	0.4291	4					
297.4	0.0100	0.0017	1					
297.4	0.0500	0.0143	1					
297.4	0.1000	0.0301	1					
297.4	0.3900	0.1166	1					
297.4	0.6900	0.1919	1					
297.4	0.9900	0.2581	1					
297.4	1.2800	0.3165	1					
297.4	1.4800	0.3512	1					
297.4	1.9800	0.4285	1					

T: Temperature; *P*: Pressure; x_1: Mole fraction of CO_2 in Ionic Liquids; [a] Experimental Method: 1) IGA-II Microbalance Standard Uncertainties u(T) = 0.01 K and u(P) = 0.0008 MPa, and Combined Standard Uncertainty $u_c(x_1)$ = 0.005; 2) High-pressure Viewcell Stand Uncertainties u(T) = 0.1 K and u(P) = 0.01 MPa, and Combined Standard Uncertainty $u_c(x_1)$ = reported at each point; 3) XEMIS Microbalance Standard Uncertainties u(T) = 0.1 K T and u(P) = 0.001 MPa and Combined Standard Uncertainty $u_c(x_1)$ = 0.005; 4) IGA-I Microbalance Standard Uncertainties u(T) = 0.01 K and u(P) = 0.0008 MPa, and Combined Standard Uncertainty $u_c(x_1)$ =0.005.

The experimental data for CO_2 + $[C_6C_1im][NTf_2]$ measured in this work were compared with the values reported in the IUPAC study by Shiflett et al.[116], Kumelan et al.[117] and Raeissi et al.[118] instead of the generalized IUPAC correlation because the data reported by these groups are in excellent agreement with each other and are high accuracy measurements. The solubility of CO_2 in $[C_6C_1im][NTf_2]$ was measured using two IGA microbalances (IGA-I and IGA-II) at 297.4 K from 0.01 to 2 MPa, the XEMIS microbalance at 293.15 K from 0 to 5 MPa, and the high-pressure view cell apparatus at 333.15 K up to 15 MPa.

The difference in the solubility data measured with the two IGA microbalances showed an average deviation of less than 1 mole % compared to Shiflett et al.[116] and Raessi et al.[118]. The average deviation between the two IGA microbalances for CO_2 absorption in $[C_6C_1im][NTf_2]$ was approximately 0.1 mole %. The average deviation for the XEMIS balance and high-pressure view cell compared to Kumelan et al.[117] and Raessi et al.[118] were 0.3 to 1.3 mole % and 1.9 to 2.3 mole %, respectively. Remarkable agreement between the IUPAC literature values and this study confirms the high accuracy and reproducibility in the experimental methods used herein.

4.1.2. Phase Behavior of Ionic Liquids and Ammonia

As discussed in Chapter 1, the need for accurate thermodynamic analysis of NH_3 in ILs is essential for developing existing and new applications. Up to now, phase behavior measurements for NH_3 in ILs have been conducted using either volumetric or semi-gravimetric methods in the literature. The gravimetric method described in this work, which is one of the most accurate techniques for measuring gas solubility,[4] has not been previously utilized to measure the solubility of NH_3 in ILs.

In this section, the vapor-liquid equilibrium of the binary systems of NH_3 and a series of ILs have been measured using a gravimetric microbalance. Initially, the ILs 1-butyl-3-methylimidazolium hexafluorophosphate ($[C_4C_1im][PF_6]$), 1-butyl-3-methylimidazolium tetrafluoroborate ($[C_4C_1im][BF_4]$), and 1-ethyl-3-methylimidazolium bis(trifluoromethylsulfonyl)imide ($[C_2C_1im][NTf_2]$) were studied. This very first gravimetric VLE data were correlated using the PR-EoS, NRTL, and Flory-Huggins. Then, the NH_3 sorption capacity of another imidazolium-based IL, namely 1-ethyl-3-methylimidazolium 1,1,2,2-tetrafluoroethanesulfonate ($[C_2C_1im][TFES]$), was investigated, and the VLE data was solely modeled via activity coefficient models (NRTL and FH) due to the success of these models. The VLE and modeling results of these four aprotic ionic liquids were collectively reported in Section 4.1.2.2. In addition to the imidazolium-based ILs, the NH_3 sorption capacities of protic ionic liquids are also examined for NH_3 sorption capacities and reported in Section 4.1.2.3.

4.1.2.1. Materials

The chemicals used in section 4.1.2 are listed in Table 4.2. The ILs were stored under nitrogen to prevent moisture contamination. The as-received ILs were dried under vacuum before conducting gas solubility measurements, and the water content was measured using Karl Fischer Coulometer. In order to account for buoyancy effects in the experimental method, the gas density as a function of *T* and *P* as well as the liquid density of the pure ILs as a function of *T* are required. The density of NH_3 was obtained using the NIST REFPROP V.9.1 database.[73] The density of $[C_4C_1im][PF_6]$, $[C_4C_1im][BF_4]$, $[C_2C_1im][NTf_2]$, $[C_2C_1im][TFES]$, and $[C_2im][NTf_2]$ were obtained from the literature.[28,119–122]

Table 4.2. Description of Ionic Liquids used in Ammonia Studies

Name	Acronym	CAS Number	Initial Mole Fraction Purity	Water Content (ppm)	Source, Product Number and Lot Number
Ammonia	NH_3	7664-41-7	0.999992	N/A	Matheson Tri-Gas,Inc
1-butyl-3-methylimidazolium hexafluorophosphate	$[C_4C_1im][PF_6]$	174501-64-5	≥0.96	500*	Fluka, Lot and Filling Code No. 1242554 304070904
1-butyl-3-methylimidazolium tetrafluoroborate	$[C_4C_1im][BF_4]$	174501-65-6	≥0.97	249 ± 16	Fluka, Lot and Filling Code No. 1116280 23404335
1-ethyl-3-methylimidazolium bis(trifluoromethyl-sulfonyl)imide	$[C_2C_1im][NTf_2]$	174899-82-2	0.99	158 ± 34	Iolitec,IL-0023-HP-1000 H00620.1
1-ethyl-3-methylimidazolium 1,1,2,2-tetrafluoroethane-sulfonate	$[C_2C_1im][TFES]$	880084-63-9	0.99	512 ± 44	Io-li-tec, Lot no. I00113.1.3
Ethylammonium nitrate	EAN	22113-86-6	>0.97	4712 ± 170	Io-li-tec, K00531.3.lnc
1-ethly imidazolium bis(trifluoromethyl-sulfonyl)imide	$[eim][NTf_2]$	353239-10-8	0.97	97 ± 31	Io-li-tec, P00170.1.Inc-IL-0269

4.1.2.2. Phase Behavior of Imidazolium-based Ionic Liquids and Ammonia

The solubility of NH_3 in four imidazolium-based ILs,$[C_4C_1im][PF_6]$, $[C_4C_1im][BF_4]$, $[C_2C_1im][NTf_2]$, and $[C_2C_1im][TFES]$ were measured at temperatures of 283.15, 298.15, 323.15 and 348.15 K and at pressures up to 0.7 MPa using XEMIS gravimetric microbalance. The experimental apparatus has been discussed in Section 2.1.1.1; therefore, only a brief description

of the measurement procedure is provided here. A small amount of IL sample (~40-60 mg) was loaded into a flat bottom Pyrex® sample container. The sample was dried and degassed under high vacuum (10^{-12} MPa) at 348.15 K for 24 h to remove moisture and volatile impurities before each experiment in the balance. The balance was operated in a static mode to eliminate drag forces by introducing NH_3 to the top of the balance away from the sample and by controlling the set-point pressure with simultaneous adjustments to the admit and exhaust valves. In order to ensure enough time for thermodynamic equilibrium, the IL sample was maintained at each setpoint pressure for a minimum of 8 h to a maximum of 20 h. NH_3 experiments were conducted using the low-pressure transducer due to the required fine pressure control at low pressures. The gas sorption data were corrected for buoyancy and volume expansion using the procedure described in Section 2.1.1.1.5. The total uncertainties in the solubility data have been estimated by propagating the measured mass errors using the force balance equation and found to be less than ± 0.5 mol % at any given *T* and *P*.

The present experimental solubility (*PTx*) data are summarized in Appendix A1, A2, A3, and A4. Yokozeki and Shiflett previously demonstrated high NH_3 sorption in $[C_4C_1im][PF_6]$, $[C_4C_1im][BF_4]$, and $[C_2C_1im][NTf_2]$; however, the inaccuracy due to weighing small amounts of NH_3 using a semi-gravimetric method resulted in large uncertainties in compositions, especially at low NH_3 concentrations (i.e., low pressures).[15] The comparison of the results in this study and our previous results (Appendix A5) indicate that the NH_3 solubility in these ILs was originally underestimated, particularly at low pressures. As described in Chapter 2, the XEMIS balance provides highly accurate solubility measurements, even at very low pressures. Therefore, this study reports the most accurate vapor-liquid equilibria data for mixtures of NH_3 and $[C_4C_1im][PF_6]$, NH_3

and $[C_4C_1im][BF_4]$, NH_3 and $[C_2C_1im][NTf_2]$, and NH_3 and $[C_2C_1im][TFES]$ at temperatures from 283.15 to 348.15 K and pressures up to 0.7 MPa.

4.1.2.2.1. Henry's Law Constants at Infinite Dilution

Henry's law constants (k_H) are used for assessment of gas solubility in a solvent at dilute concentrations where the lower the k_H value, the higher the gas solubility in the solvent. In this study, the NH_3 solubility linearly increases at pressures up to about 0.15 MPa indicating Henry's law regime. The results suggest the partial pressure of NH_3 ($P_{NH3} \approx P$ as $P_{IL}^{vap} \approx 0$) is directly proportional to its liquid phase concentration in the dilute regime. The Henry's law constants were obtained calculating the limiting slope while x_{NH_3} approaches zero using the linear fit of experimental data up to 0.15 MPa including a theoretical zero point (zero pressure and zero composition) as described in Section 3.3. Henry's law constants obtained for this study are shown in Table 4.3. Henry's law constants increase with an increase in *T* for the four imidazolium-based ILs indicating that the solubility of NH_3 decreases with an increase in *T*.

Table 4.3. Henry's law constants for the mixtures of NH_3 + $[C_4C_1im][PF_6]$, NH_3 + $[C_4C_1im][BF_4]$, NH_3 + $[C_2C_1im][NTf_2]$, NH_3 + $[C_2C_1im][TFES]$ and at 283.15, 298.15, 323.15 and 348.15 K

	Henry's law constants, k_H (MPa)[a]			
Binary System	T = 283.15 K	T = 298.15 K	T = 323.15 K	T = 348.15 K
NH_3 + $[C_4C_1im][PF_6]$	0.31 ± 0.02	0.46 ± 0.03	0.83 ± 0.03	1.4 ± 0.16
NH_3+ $[C_4C_1im][BF_4]$	0.29 ± 0.02	0.41 ± 0.04	0.64 ± 0.07	1.3 ± 0.17
NH_3+$[C_2C_1im][NTf_2]$	0.31 ± 0.02	0.46 ± 0.03	0.81 ± 0.04	1.1 ± 0.14
NH_3+$[C_2C_1im][TFES]$	0.34 ± 0.02	0.50 ± 0.06	0.96 ± 0.16	1.0 ± 0.22

[a]The uncertainties are the standard error of the coefficient obtained in the linear regression.

Henry's law constants are also used to estimate the enthalpy ($\Delta\overline{H}_{sol}$) and entropy ($\Delta\overline{S}_{sol}$) of gas dissolution that accompanies the absorption of a mole of gas into a solution at infinite dilution using Equations 3.22 and 3.23. The $\Delta\overline{H}_{sol}$ and $\Delta\overline{S}_{sol}$ of NH_3 absorption in $[C_4C_1im][PF_6]$, $[C_4C_1im][BF_4]$, $[C_2C_1im][NTf_2]$, and $[C_2C_1im][TFES]$ are reported in Table 4.4. The negative $\Delta\overline{H}_{sol}$ indicates the NH_3 sorption in imidazolium-based ILs is exothermic. Also, the magnitude of $\Delta\overline{H}_{sol}$ indicates a relatively weak association of NH_3 in IL, which suggests only physical sorption (i.e., gas solubilities) at low NH_3 compositions. The negative $\Delta\overline{S}_{sol}$ indicates NH_3 absorption in imidazolium-based ILs increases in molecular ordering. The $\Delta\overline{H}_{sol}$ and $\Delta\overline{S}_{sol}$ results are very similar to SO_2 in $[C_4C_1im][BF_4]$[17] and CO_2 in $[C_4C_1im][PF_6]$[90]. This suggests there is no regular bonding between the solvent (ILs) and solute molecules (NH_3, SO_2, or CO_2) at infinite dilution. It is worth emphasizing that the $\Delta\overline{H}_{sol}$ and $\Delta\overline{S}_{sol}$ results are only instructive at low NH_3 compositions (i.e., below 0.15 MPa).

Table 4.4. Enthalpy of solution ($\Delta\overline{H}_{sol}$) and entropy of solution ($\Delta\overline{S}_{sol}$) of NH_3 absorption in $[C_4C_1im][PF_6]$, $[C_4C_1im][BF_4]$, $[C_2C_1im][NTf_2]$, and $[C_2C_1im][TFES]$ at infinite dilution

Ionic Liquid	$\Delta\overline{H}_{sol}$ (kJ·mol^{-1})[a]	$\Delta\overline{S}_{sol}$ (J·mol^{-1}·K^{-1})[a]
$[C_4C_1im][PF_6]$	-18.7 ± 0.4	-59.7 ± 1.7
$[C_4C_1im][BF_4]$	-18.1 ± 1.8	-57.9 ± 4.6
$[C_2C_1im][NTf_2]$	-16.1 ± 1.2	-51.3 ± 4.8
$[C_2C_1im][TFES]$	-14.4 ± 3.0	-45.4 ± 10.4

[a] The uncertainties are the standard error of the coefficient obtained in the linear regression.

4.1.2.2.2. PR-EoS Modeling of Imidazolium-based Ionic Liquids and Ammonia

The Peng-Robinson Equation of State (PR-EoS) was selected to model vapor-liquid equilibrium data as it has been used extensively in academic evaluations and industrial

applications[95] and has been previously applied to NH_3+ IL mixtures[31]. In the PR-EoS (Equation 3.24), the a_m and b_m parameters are computed with the one-parameter van der Waals mixing rule with Boston-Mathias extension for the attractive term and the standard PR-EoS alpha function. Pure component parameters (a_i and b_i) are computed based on the critical temperature (T_c), critical pressure (P_c), and acentric factor (ω). The PR-EoS parameters (a_i, b_i, $\alpha_i(T)$, m, a_m, b_m, k_{ij}, *and* l_{ij}) used for this analysis are shown in Equations 3.25 - 3.32. Table 4.5 provides the EoS constants used for NH_3 and ILs. The binary parameters k_{ij} and l_{ij} were determined from the regression of the VLE data using ASPEN Plus v.10[123] by minimizing the objective function of the average absolute relative deviation ($\%\,\mathrm{AARD} = (100/n)\sum_{i=1}^{n}|(P^{exp} - P^{regressed})/P^{exp})|$). The binary interaction parameters obtained for the PR-EoS results are listed in Table 4.6. The experimental results along with the PR-EoS models are shown in Figures 4.1-4.3. The difference between the experimental and estimated VLE data for the three binary mixtures of NH_3-ILs was less than 5% AARD except in the case of NH_3 + $[C_4C_1im][PF_6]$ at 298.15 K where the model underestimates the VLE behavior by 6.5% AARD. The critical properties of the ILs cannot be experimentally determined (i.e., the critical temperature is above the decomposition temperature). Therefore, the critical properties used in this study were obtained from the literature where the critical properties were estimated using a Group Contribution Method.[37] As the ILs have very low vapor pressure, one might expect to observe the T_c of $[C_4C_1im][PF_6]$ or $[C_4C_1im][BF_4]$ to be higher than what is reported in Table 4.5. Therefore, to investigate the impact of T_c of the ILs on the PR-EoS fit, the PR-EoS models for the systems NH_3 + $[C_4C_1im][PF_6]$ and NH_3 + $[C_4C_1im][BF_4]$ systems were also computed using an arbitrary high T_c (*i.e.* 1245 K). For both $[C_4C_1im][BF_4]$+NH_3 and $[C_4C_1im][PF_6]$+NH_3 systems, the impact of T_c on the fit (AARD%) was ±~1% and ± 2 %,

respectively; therefore, the results indicate that the T_c calculated in Table 4.5.can be used to correlate NH_3+IL systems using the PR-EoS model.

Table 4.5. Pure component EoS constants used in this study

Compound	**Molar Mass (g·mol^{-1})**	T_c **(K)** [a]	P_c **(MPa)** [a]	ω [a]
NH_3	17.03	405.7	11.3	0.253
$[C_4C_1im][PF_6]$	284.18	708.9	1.73	0.755
$[C_4C_1im][BF_4]$	226.03	632.3	2.04	0.849
$[C_2C_1im][NTf_2]$	391.31	1244.9	3.26	0.182

[a] The critical properties and acentric factor of the ILs were taken from Ref ([124]).

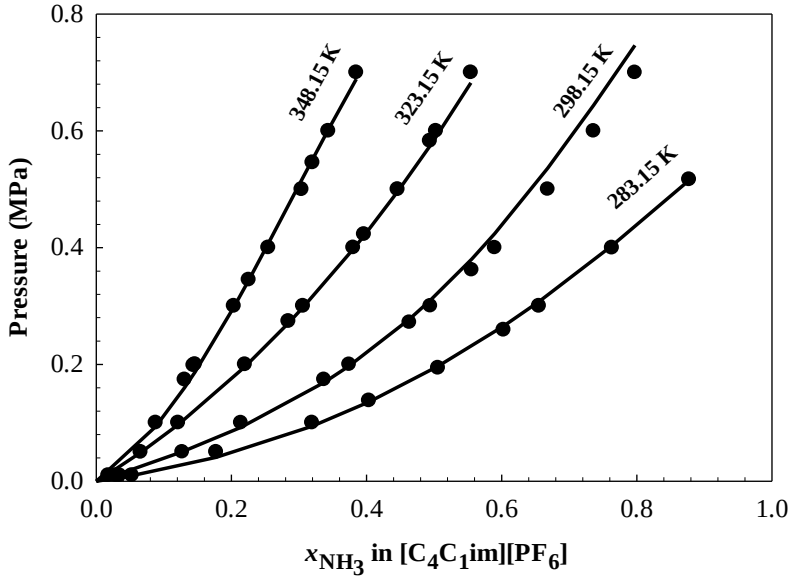

Figure 4.1. *PTx* phase diagram for NH_3 and $[C_4C_1im][PF_6]$ at 283.15, 298.15, 318.15, and 338.15 K. Symbols represent experimental data, and solid lines represent PR-EoS model.

Table 4.6. Binary interaction parameters for the Peng Robinson EoS Model

NH_3-ILs	Temperature (K)	k_{12}	l_{12}	AARD %
NH_3+[C_4C_1im][PF_6]	283.15	-0.1962	0.1361	4.4
	298.15	-0.2090	0.0039	6.5
	323.15	-0.1729	0.0914	3.4
	348.15	-0.0785	0.4920	3.4
NH_3+[C_4C_1im][BF_4]	283.15	-0.2034	-0.1648	3.3
	298.15	-0.2189	0.0512	2.3
	323.15	-0.2084	0.1420	2.3
	348.15	-0.1774	0.1300	4.0
NH_3+[C_2C_1im][NTf_2]	283.15	-0.1320	0.0520	1.9
	298.15	-0.1340	0.0457	1.9
	323.15	-0.1345	0.0882	1.9
	348.15	-0.1338	0.1694	2.9

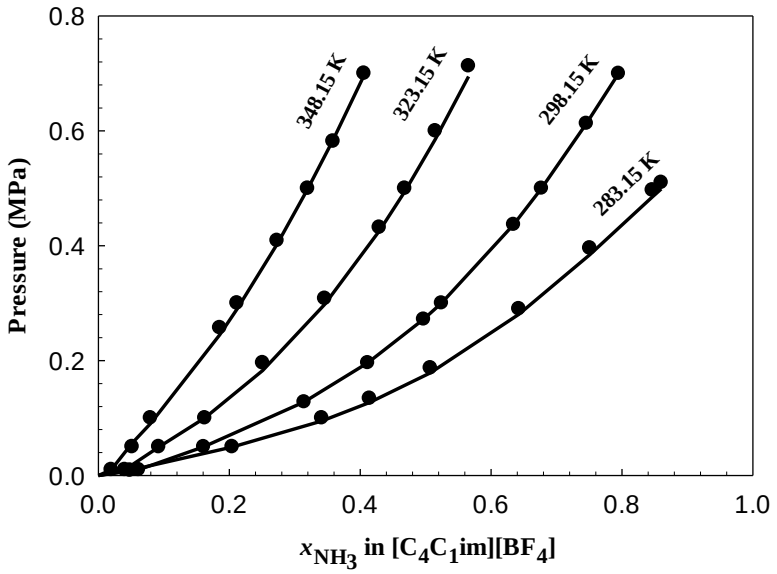

Figure 4.2. *PTx* phase diagram for NH_3 and [C_4C_1im][BF_4] at 283.15, 298.15, 318.15, and 338.15 K. Symbols represent experimental data, and solid lines represent PR-EoS model.

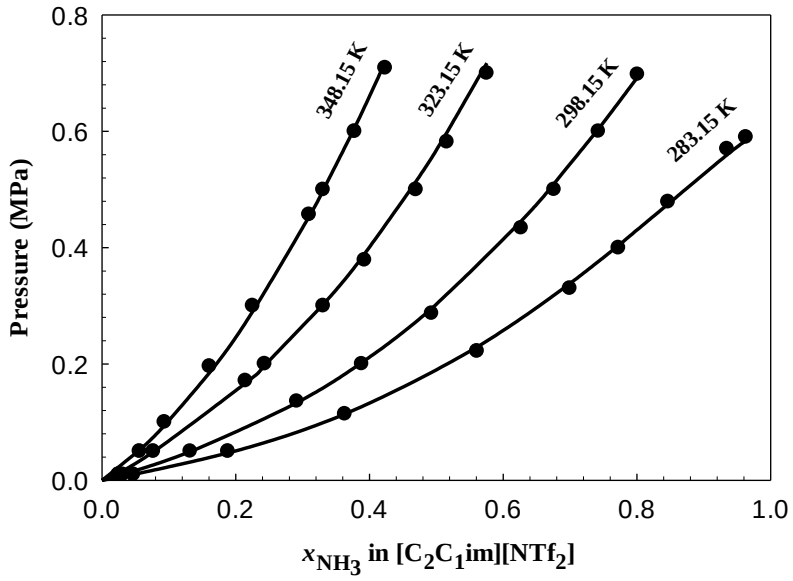

Figure 4.3. *PTx* phase diagram for NH_3 and [C_2C_1im][NTf_2] at 283.15, 298.15, 318.15, and 338.15 K. Symbols represent experimental data, and solid lines represent PR-EoS model.

4.1.2.2.3. Activity Coefficient Modeling of Imidazolium-based Ionic Liquids and Ammonia

Considering the critical point of the mixture is considerably high, using two different models can accurately estimate the VLE of NH_3 and IL mixtures. Therefore, in this study, the vapor-liquid equilibria of NH_3+ IL mixtures were also modeled using the NRTL and Flory-Huggins model for the liquid phase, and the Second Virial Coefficient correction for the vapor phase.

For low- and medium- pressure, VLE for an *N*-component system can be described with Equation 3.16. For a binary system of NH_3 + IL mixtures, it is reasonable to assume that the solubility of IL in NH_3 is negligible ($P_{IL}^{vap} \approx 0$) so y_{NH_3}=1 (or y_{IL}= 0). The activity coefficient of NH_3 (1) is given by

$$\gamma_1 = \frac{P\,\Phi_1}{x_1 P_1^s} \tag{4.1}$$

The correction factor (ϕ_1) for NH_3 in the present case is calculated using Equation 3.33, and the vapor pressure of ammonia Equation 3.34 with coefficients as A = 83.58, B = -4669.70, C = 0, D = 0, E = -11.61, F = 0.02, and G = 1[123]. The activity coefficients were calculated using the NRTL equations 3.35-3.38. The regressed binary interaction parameters are summarized in Table 4.7.

Table 4.7 Binary interaction parameters for the NRTL activity coefficient model

System (1)/(2)	$\tau_{12}^{(0)}$	$\tau_{12}^{(1)}$ (K)	$\tau_{21}^{(0)}$	$\tau_{21}^{(1)}$ (K)
NH_3+[C_4C_1im][PF_6]	-2.439	1350.8	0.3428	-815.96
NH_3+[C_4C_1im][BF_4]	-4.871	2634.5	-0.1423	-891.45
NH_3+[C_2C_1im][NTf_2]	-3.306	1669.7	-0.1201	-730.79
NH_3+[C_2C_1im][TFES]	-3.221	1659.4	1.3067	-1193.41

The experimental VLE results and NRTL models are shown in Figures 4.4-4.7. The models accurately predict the VLE for each of the NH_3+[C_4C_1im][PF_6], NH_3+[C_4C_1im][PF_6], and NH_3+[C_2C_1im][NTf_2] systems with an average overall difference of less than 5 % AARD. However, the average difference between the NRTL model and experimental results in the NH_3+[C_2C_1im][TFES] system was 15 % AARD. The activity coefficient model for the NH_3 and [C_4C_1im][PF_6] system is also compared with the results reported by Tomida et al.[20] The activity coefficient model accurately estimated the NH_3 composition at high pressures using only low pressure (up to 0.7 MPa) VLE measurements. The average absolute relative deviation between this study and Tomida et al.[20] was 5.1, 3.5, 2.5, and 2.8 % AARD at 283.15, 298.15, 323.15, and 348.15 K, respectively. The excellent agreement between the model obtained in this study and the high-pressure experimental data obtained by Tomida et al.[20] indicates the low-pressure solubility

measurements were highly accurate. The models also do not predict any liquid-liquid phase separation at high NH_3 concentration.

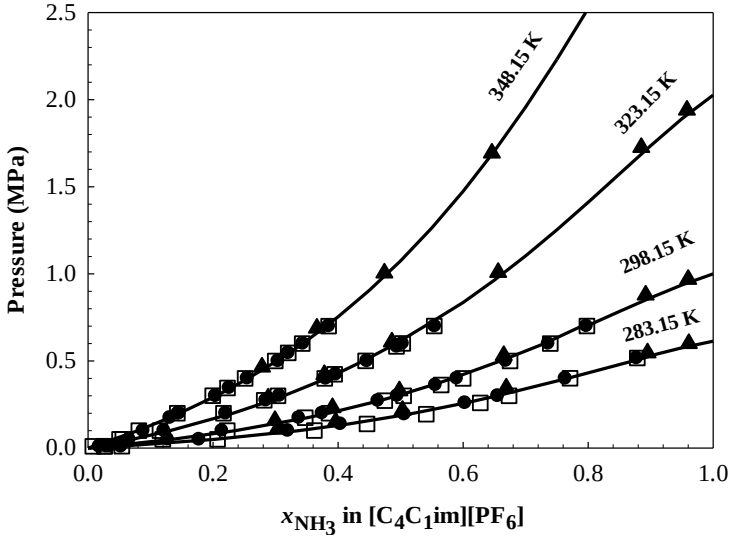

Figure 4.4. *PTx* phase diagram for NH_3 and [C_4C_1im][PF_6] at 283.15, 298.15, 318.15, and 338.15 K. Solid Symbols: ●, absorption data; Open Symbols □, desorption data; ▲, Tomida et al.[20] Solid lines: NRTL model in this study.

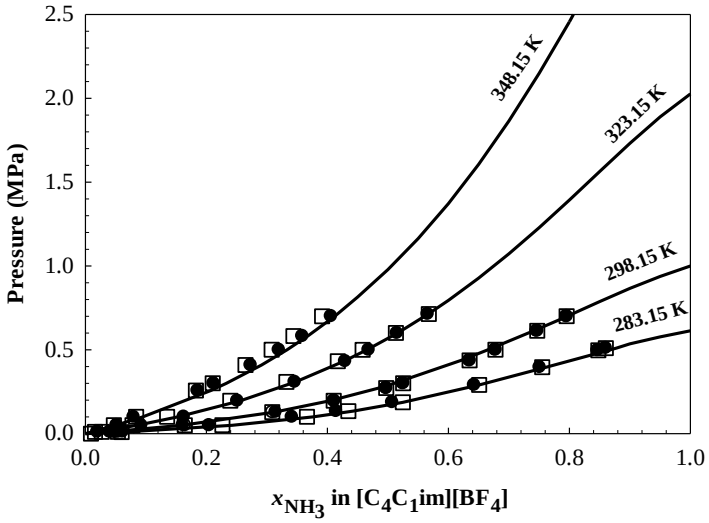

Figure 4.5. PTx phase diagram for NH_3 and [C_4C_1im][BF_4] at 283.15, 298.15, 318.15, and 338.15 K. Solid Symbols ●, absorption data; Open Symbols □, desorption data. Solid lines represent the NRTL model.

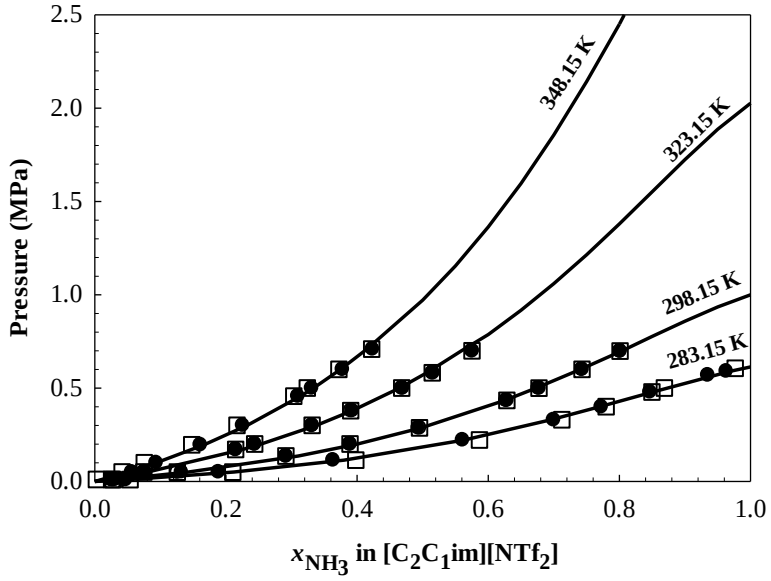

Figure 4.6. *PTx* phase diagram for NH_3 and [C_2C_1im][NTf_2] at 283.15, 298.15, 318.15, and 338.15 K. Solid Symbols ●, absorption data; Open Symbols □ , desorption data. Solids lines represent the NRTL model.

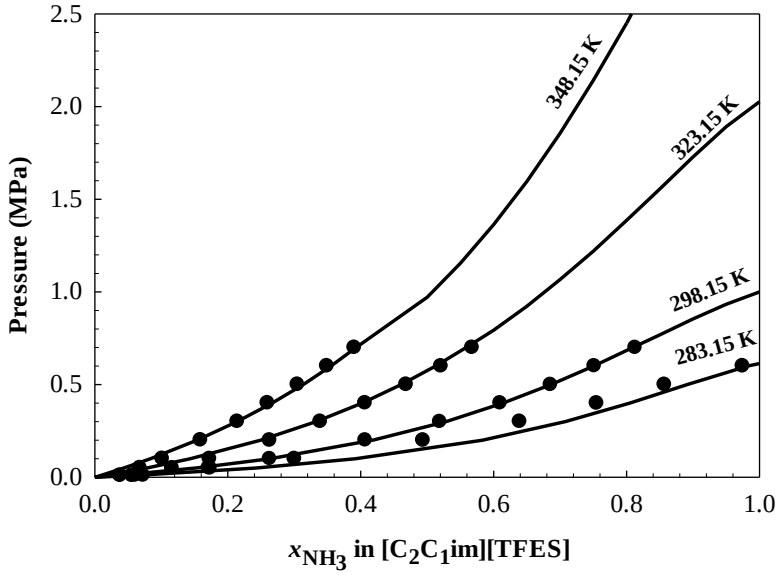

Figure 4.7. *PTx* phase diagram for NH_3 and [C_2C_1im][TFES] at 283.15, 298.15, 318.15, and 338.15 K. Solid Symbols (●) represent absorption data. Solids lines represent the NRTL model.

The vapor-liquid equilibria of NH_3 + IL mixtures were also modeled using the Flory-Huggins model for the liquid phase and the Second Virial Coefficient correction for the vapor phase. The original model developed by Flory and Huggins only considers the entropic effects on the non-idealities, as discussed in Chapter 2. Since ILs and NH_3 molecules greatly differ in size and shape, the experimental data are initially modeled only considering the combinatorial contribution to the non-ideality. Then, the experimental data are modeled using the extended Flory-Huggins model by including both the combinatorial and residual terms. The experimental VLE results and the extended Flory-Huggins models are shown in Figures 4.8 - 4.11. The comparison of Raoult's law, the Flory-Huggins model that has the combinatorial term only, and the extended Flory-Huggins model that has both combinatorial and residual terms are shown in Figures 4.12 – 4.15.

Figures 4.8 – 4.11 showed that the extended Flory-Huggins models accurately predict the VLE for the NH_3+[C_4C_1im][PF_6], NH_3+[C_4C_1im][BF_4], and NH_3+[C_2C_1im][NTf_2] systems with an average overall difference of less than 6 % AARD. The average difference between the model and experimental results in the NH_3+[C_2C_1im][TFES] system was 14 % AARD. The Flory-Huggins model for the NH_3 and [C_4C_1im][PF_6] system is also compared with results reported by Tomida et al.[20] The average absolute relative deviation between this study and Tomida et al.[20] was 4.3, 2.9, 3.2 and 2.8 % AARD at 283.15, 298.15, 323.15, and 348.15 K, respectively. In the extended Flory-Huggins model, χ is introduced into the equation to extend the original Flory and Huggins theory of athermic processes to non-athermic processes of mixing. Therefore, in the extended Flory-Huggins model, the χ parameter is obtained via regression. The χ parameter is usually a function of both temperature and composition.[125] For poor solvents, the χ depends on

the composition. For good solvents, the χ is nearly independent of the composition. As ILs are good solvents for NH_3, in this study, the χ term is assumed to be independent of composition and is calculated only dependent on temperature variation. The temperature dependence of χ is usually given as $\chi(T) = a + \frac{b}{T}$. In some cases where significant non-linearity is observed, the temperature dependence of χ can be given in quadratic or cubic forms. Here, the linear form of temperature dependence is used. For the systems of NH_3+[C_4C_1im][PF_6], NH_3+[C_4C_1im][BF_4], and NH_3+[C_2C_1im][NTf_2], the linear form of χ - 1/T correlation worked very well. In the system of NH_3+[C_4C_1im][BF_4], the cubic form of the temperature dependence resulted in a better fit for the model, whereas the linear fit also gives a reasonable fit. In order to safely assume the temperature dependence of χ is really in cubic form, the additional isotherms might be necessary. In the system of NH_3+[C_2C_1im][TFES], the solubility estimation using the linear form of χ - 1/T correlation was very poor. Therefore, the data is fitted to the cubic form function of $\chi(T) = a + b / T + C / T^2 + D / T^3$. In the extended Flory-Huggins modeling, χ parameter was regressed satisfying the equilibrium condition simultaneously for all isotherms. The χ parameters of NH_3 + [C_4C_1im][PF_6], NH_3 + [C_4C_1im][BF_4], NH_3 + [C_2C_1im][NTf_2], and NH_3 + [C_2C_1im][TFES] systems are summarized in Table 4.8.

Table 4.8. Flory-Huggins Parameters (χ) obtained for NH_3+[C_4C_1im][PF_6], NH_3+[C_4C_1im][BF_4], NH_3+[C_2C_1im][NTf_2], and NH_3+[C_2C_1im][TFES] Systems

System (1)/(2)	*a*	*b*	*c*	*d*
NH_3+[C_4C_1im][PF_6]	-0.42	229.93	-	-
NH_3+[C_4C_1im][BF_4]	-0.47	276.06	-	-
NH_3+[C_2C_1im][NTf_2]	-0.80	375.54	-	-
NH_3+[C_2C_1im][TFES]	-42.10	42585.0	-1.43×10^7	1.59×10^9

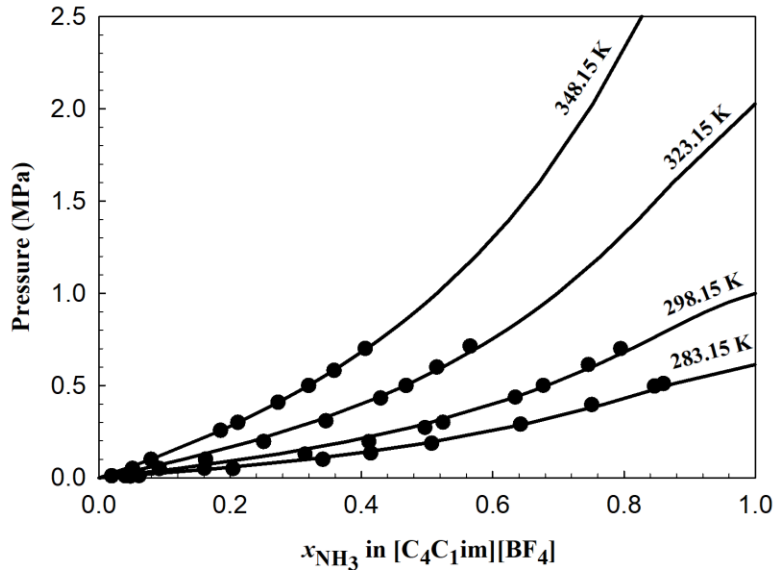

Figure 4.8. *PTx* phase diagram for NH_3 and $[C_4C_1im][BF_4]$ at 283.15, 298.15, 318.15, and 338.15 K. Solid symbols represent experimental measurements. Solid lines represent the Flory-Huggins model in this study.

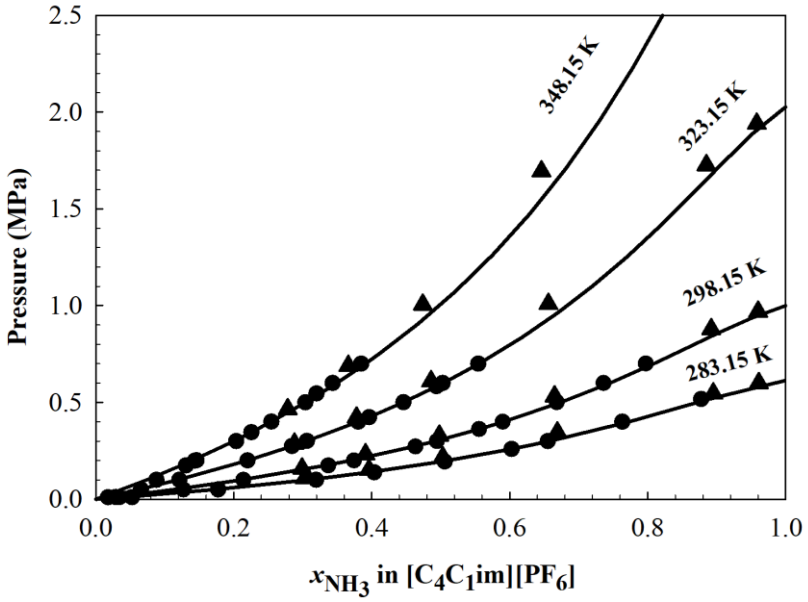

Figure 4.9. *PTx* phase diagram for NH_3 and $[C_4C_1im][PF_6]$ at 283.15, 298.15, 318.15, and 338.15 K. Solid symbols represent experimental measurements. Solid lines represent the Flory-Huggins model in this study.

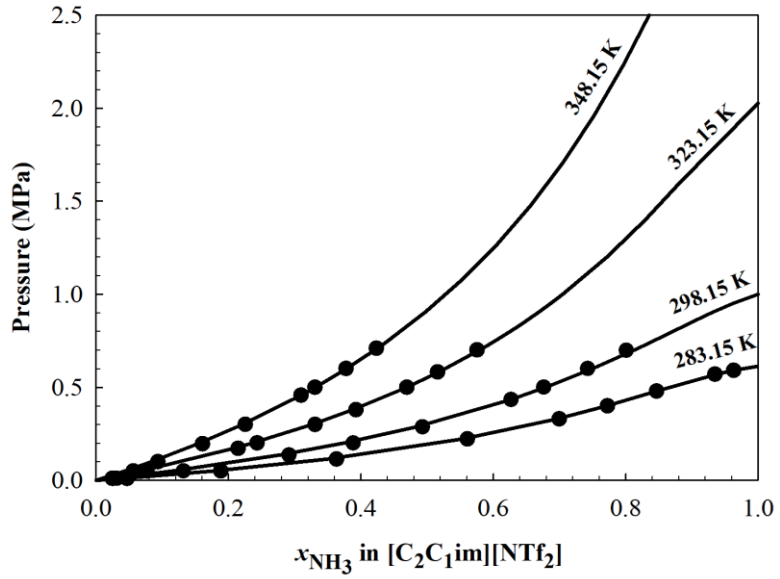

Figure 4.10. *PTx* phase diagram for NH_3 and [C_2C_1im][NTf_2] at 283.15, 298.15, 318.15, and 338.15 K. Solid symbols represent experimental measurements. Solid lines represent the Flory-Huggins model in this study.

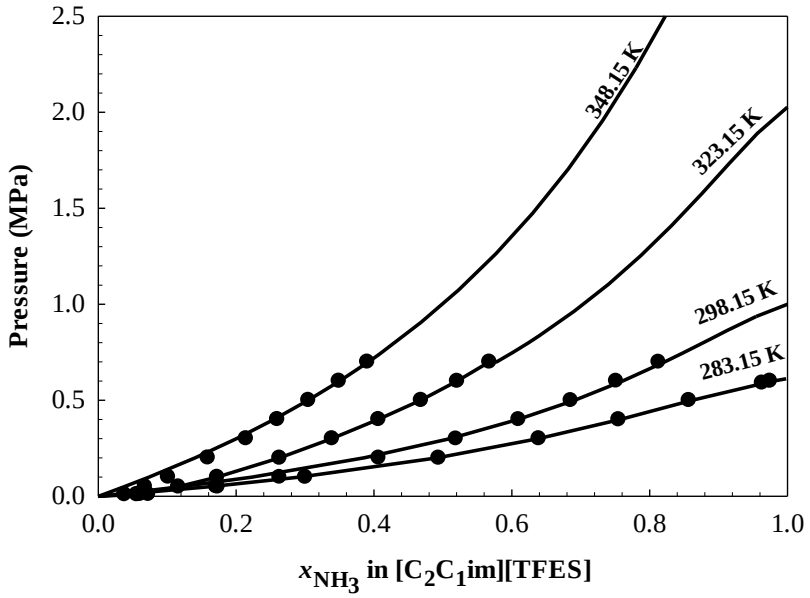

Figure 4.11. *PTx* phase diagram for NH_3 and [C_2C_1im][TFES] at 283.15, 298.15, 318.15, and 338.15 K. Solid symbols represent experimental measurements. Solid lines represent the Flory-Huggins model in this study.

Figures 4.12 – 4.15 compares Raoult's law, the Flory-Huggins model with the combinatorial term only, and the extended Flory-Huggins model with both combinatorial and residual terms. As shown in Figures 4.12 – 4.15, the NH_3+ILs system shows a strong negative deviation from the ideal solubility. The results clearly indicate that the solubility of NH_3 in ionic liquids cannot be solely described with entropic impacts. Carvalho and Countho[29] modeled experimentally available NH_3+IL data using the Flory-Huggins model including the combinatorial term only. Their results showed a strong negative deviation from the non-ideality in the entire NH_3 composition range, and their model overestimated the NH_3 solubility in the ILs compared to the experimental results. In their study, they concluded that the interaction between the NH_3 and IL is mostly driven by entropic effects. Regardless of their crude conclusion, the significant deviation between their Flory-Huggins model and the experimental data can be seen in their given comparison graphs. The findings in this study showed that the Flory-Huggins model predicts experimental results well if both combinatorial and residual term are considered. If the non-idealities are truly a result of entropy effects or dominated by entropy effects as Carvalho and Countho[29] suggested, then all ionic liquids should have the same solubilities when the impact of molecular weight is eliminated. However, when the NH_3 absorption is reported in molality (moles of NH_3 per kg of ionic liquid) at selected pressures of 0.1, 0.3, and 0.5 MPa and temperatures of 283.15, and 348.15 K, the imidazolium-based ionic liquids have different solubilities, which indicates the non-idealities are not dominated by entropic effects. The non-idealities in NH_3+IL mixtures here are results of both entropic and enthalpic contributions.

Table 4.9. Experimental Vapor-Liquid Equilibrium (VLE) Data for NH_3 and imidazolium-based ILs reported in molality.

		m_{NH_3} (mol·kg^{-1})		
Ionic Liquid	T/K	P = 0.1 MPa	P = 0.3 MPa	P=0.5 MPa
$[C_4C_1im][PF_6]$	283.15	1.6503	6.6888	25.1861
	348.15	0.3388	0.8987	1.5354
$[C_4C_1im][BF_4]$	283.15	2.2902	7.9519	27.2123
	348.15	0.3819	1.6256	2.0779
$[C_2C_1im][NTf_2]$	283.15	1.4569	5.9566	14.1042
	348.15	0.2631	0.7431	1.2617
$[C_2C_1im][TFES]$	283.15	1.4676	6.0615	20.4892
	348.15	0.3850	0.9325	1.4999

4.1.2.2.4. Absorption and Desorption Comparison

Chemical interaction between NH_3 and imidazolium-based ILs was also considered by measuring the desorption of $[C_4C_1im][PF_6]$, $[C_4C_1im][BF_4]$, and $[C_2C_1im][NTf_2]$, at temperatures of 283.15, 298.15, 323.15, and 348.15 K and at pressures ranging from 0.010 to 0.7 MPa. In the desorption experiment, NH_3 was gradually desorbed from NH_3+IL mixtures at any given isotherm from higher P to lower P with a fine adjustment between admit and exhaust valves in the microbalance. The samples were maintained at the new setpoint pressure for a minimum of 3 h to a maximum of 12 h until thermodynamic equilibrium is achieved (i.e., no mass decrease occurs with respect to time). The desorption data are shown in Figures 4.1, 4.2, and 4.3. At some conditions, particularly at low T and low P, the difference between absorption and desorption solubility was as high as ~ 3 mole %. This difference between the equilibrium concentrations for

the given isotherms during absorption and desorption suggests the interaction between NH_3 and imidazolium-based ILs maybe both chemical and physical.

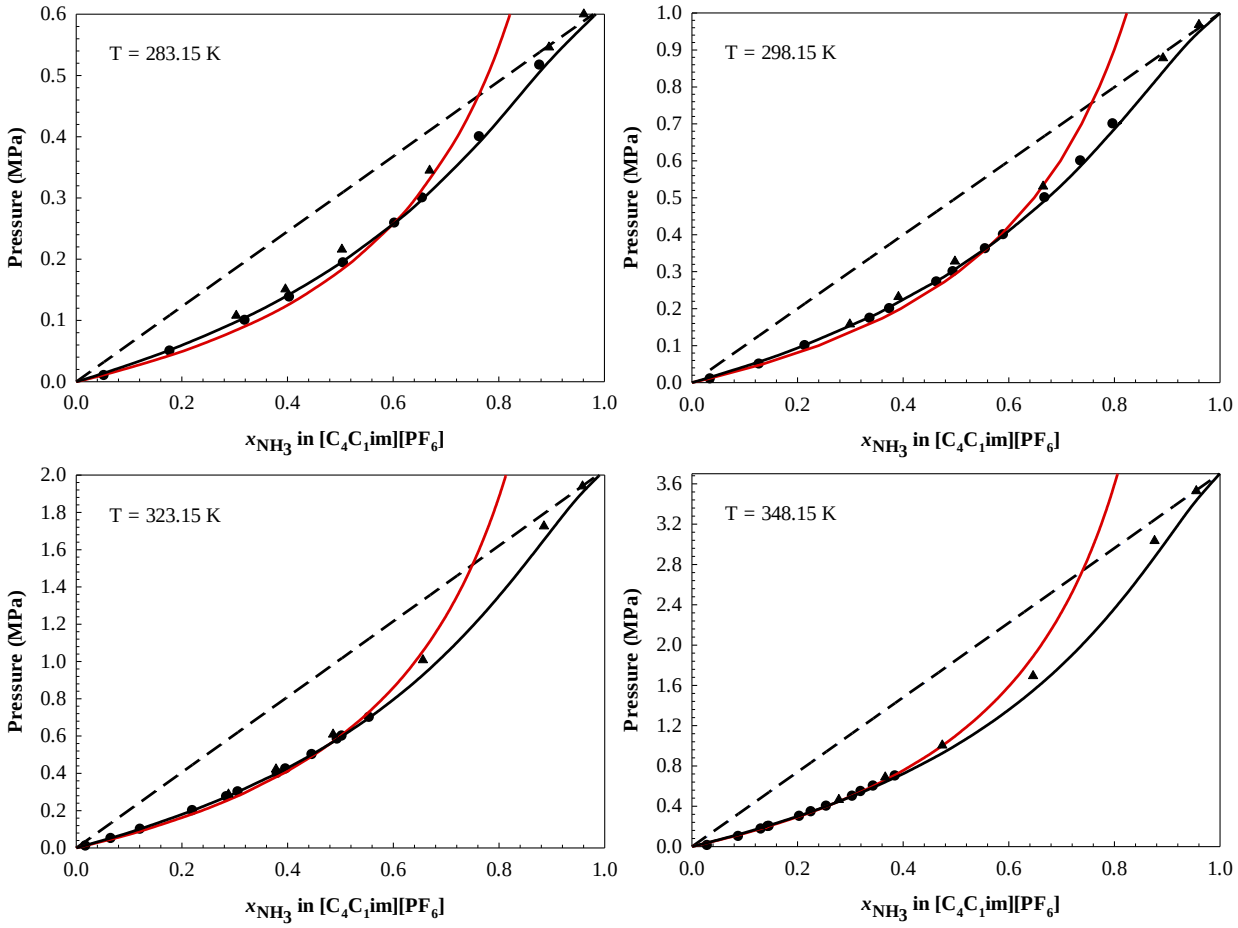

Figure 4.12. *PTx* phase diagram for NH_3 and [C_4C_1im][PF_6] at 283.15, 298.15, 318.15, and 338.15 K. Solid symbols represent experimental measurements. Black dashed lines represent the Raoult's law. Black solid lines represent the Flory-Huggins model with both combinatorial and residual terms. Red solid lines represent the Flory-Huggins model with the combinatorial term only.

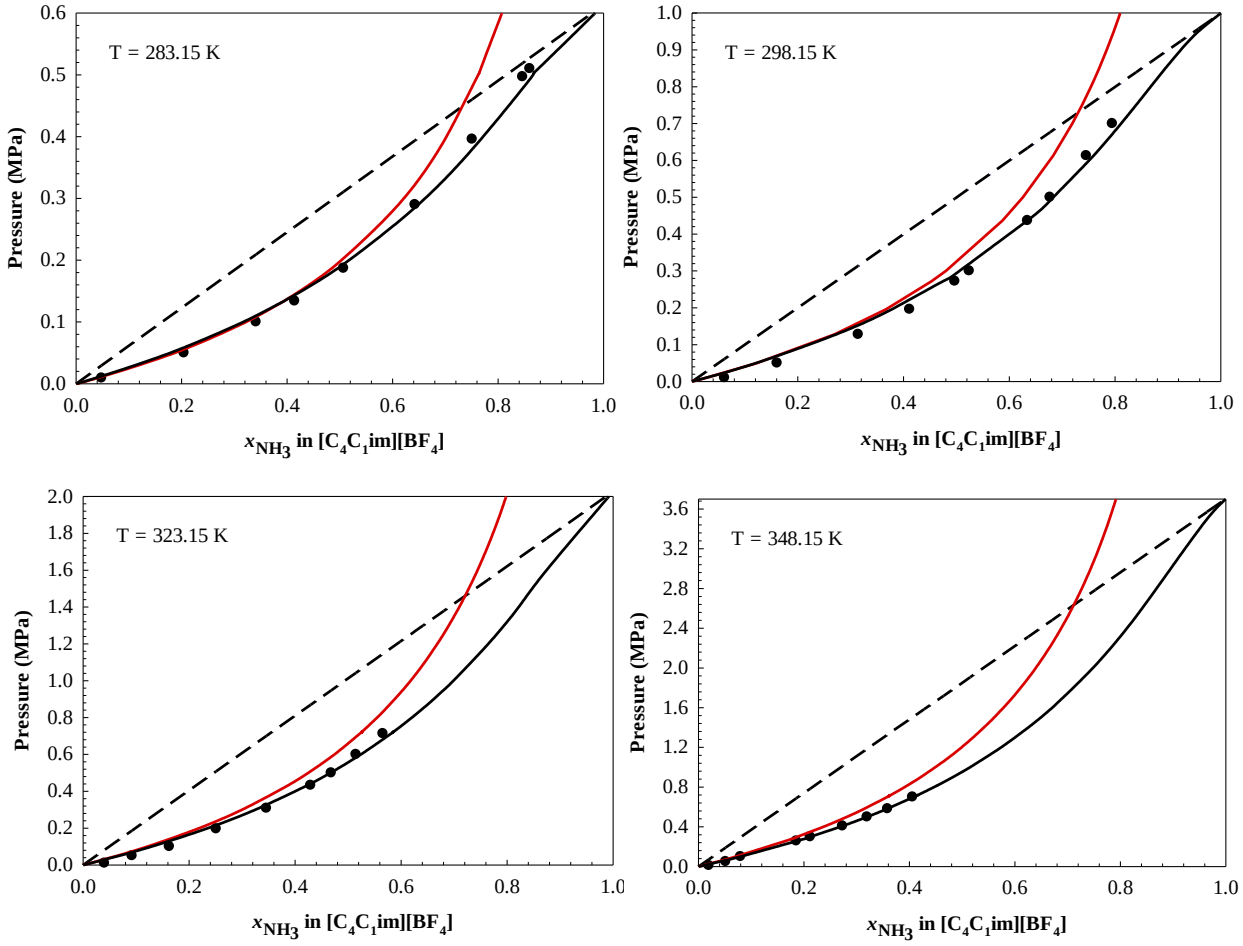

Figure 4.13. *PTx* phase diagram for NH_3 and [C_4C_1im][BF_4] at 283.15, 298.15, 318.15, and 338.15 K. Solid symbols represent experimental measurements. Black dashed lines represent the Raoult's law. Black solid lines represent the Flory-Huggins model with both combinatorial and residual terms. Red solid lines represent the Flory-Huggins model with the combinatorial term only.

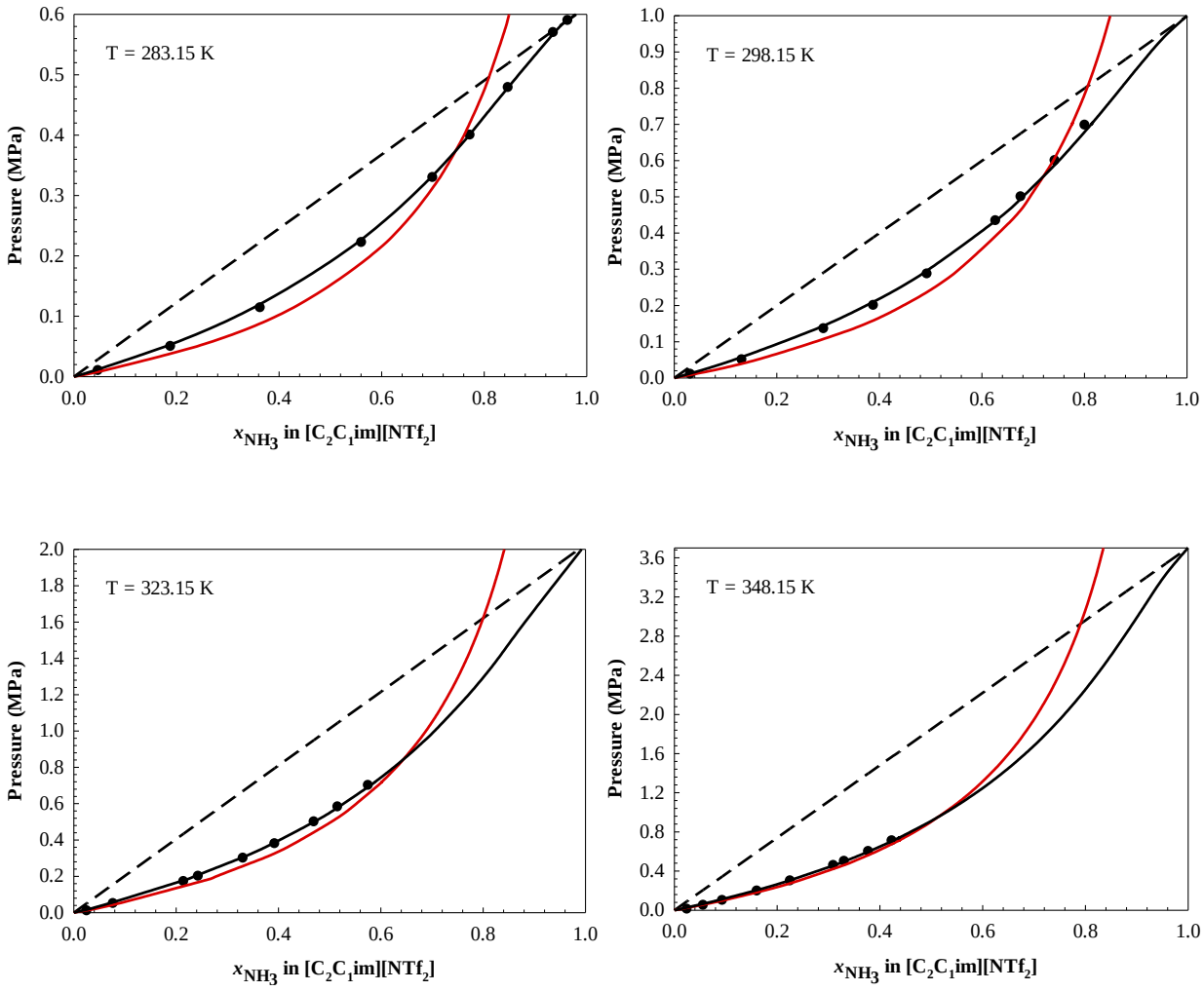

Figure 4.14. *PTx* phase diagram for NH_3 and $[C_4C_1im][NTf_2]$ at 283.15, 298.15, 318.15, and 338.15 K. Solid symbols represent experimental measurements. Black dashed lines represent the Raoult's law. Black solid lines represent the Flory-Huggins model with both combinatorial and residual terms. Red solid lines represent the Flowy-Huggins model with the combinatorial term only.

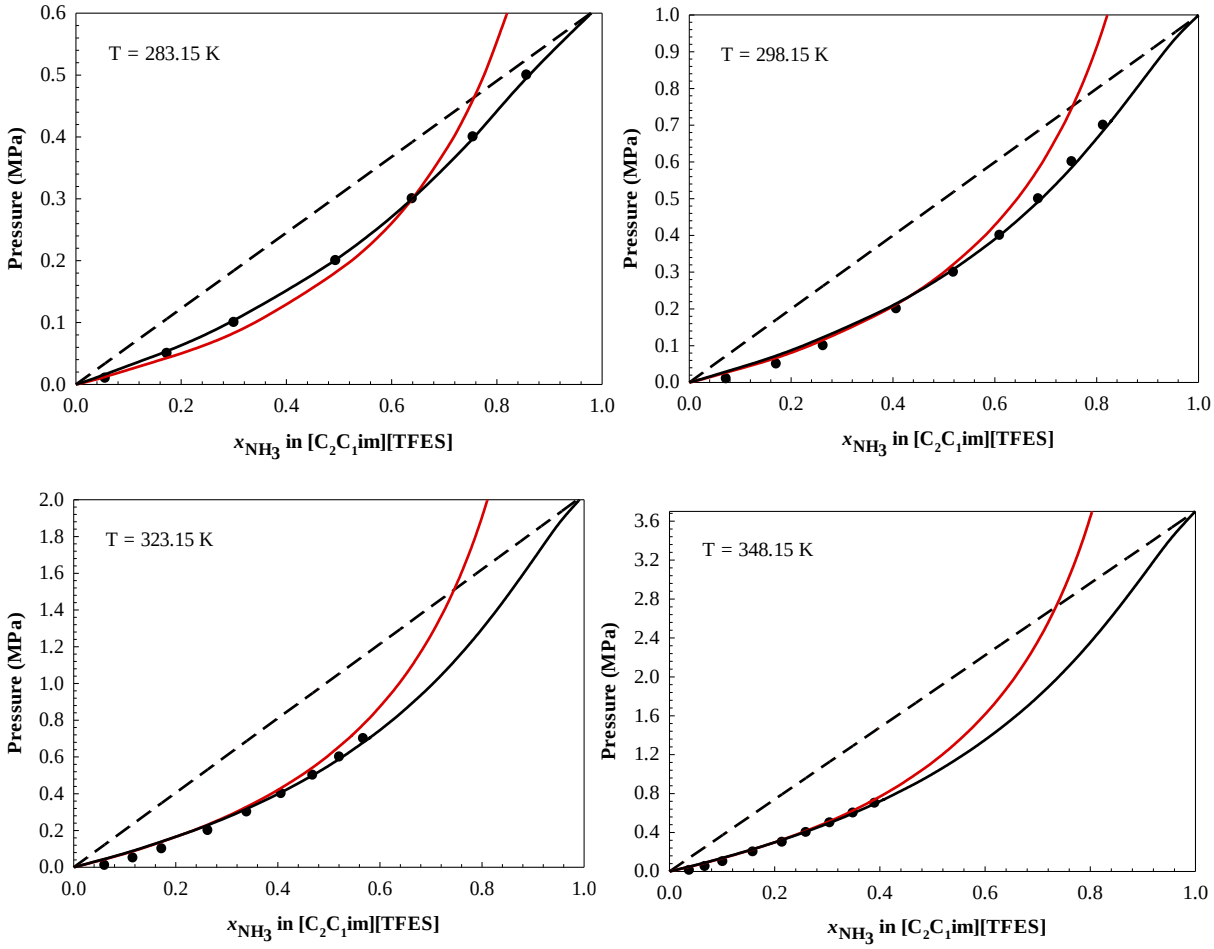

Figure 4.15. *PTx* phase diagram for NH_3 and [C_4C_1im][TFES] at 283.15, 298.15, 318.15, and 338.15 K. Solid symbols represent experimental measurements. Black dashed lines represent the Raoult's law. Black solid lines represent the Flory-Huggins model with both combinatorial and residual terms. Red solid lines represent the Flowy-Huggins model with the combinatorial term only.

4.1.2.3. Phase Equilibria of Ammonia and Protic Ionic Liquids

Protic ionic liquids are reported as promising sorbents with very high ammonia sorption capacities.[27,28] To explore protic ionic liquids as potential absorbents, the solubility of ammonia in two protic ionic liquids , namely ethyl ammonium nitrate (EAN) and 1-ethyl imidazolium ([eim][NTf_2], were also investigated in this study.

EAN is the first truly room-temperature ionic liquid discovered by Walden in 1914.[126] It is selected in this study because EAN mostly stands out from other ILs with its water-like properties and high NH_3 sorption capacities might be expected.[126]. Since protic ionic liquids are more prone to vaporization, the sample was slowly degassed at room temperature in the XEMIS microbalance. After the gas evacuation, the ammonia pressure is set to 100 mbar at room temperature for the initial investigation. Shortly after NH_3 was introduced into the balance, the experiment was ceased due to unusual and inconsistent mass change. When the balance was opened for inspection, white solid particles were found in and around the sample cup and in the balance, as shown in Figure 4.16 (a). The white powder is found to be insoluble in acetone, and partially soluble in methanol. The solubility behavior of the white particulate might suggest that the reaction between EAN and NH_3 may result in ammonium nitrate, which is a chemical used in agricultural industry or used as explosives. Further tests were not performed to test this hypothesis as it is beyond of the scope of this study.

In order to validate protic ILs might be really a promising class of solvents, the study on the solubility of ammonia in [eim][NTf_2] from the literature[28] is replicated at temperatures of 283.15, 298.15, and 323.15 K and at pressures up to 7 MPa. The results are shown in Figure 4.17. As can be seen in Figure 4.17, [eim][NTf_2] quickly reached high NH_3 saturations at very low pressures

(less than 0.1 MPa). Similar observations were made in some CO_2 + IL systems where CO_2 chemically interacted with a given IL (i.e., [C_4C_1im][acetate]). In fact, even though the solubility results obtained in this study are in good agreement with the results obtained from the literature, Figure 4.16 (b) also shows some small white particles formed in [eim][NTf_2] similar to the white particles formed in the EAN+NH_3 system. The rapid ammonia saturation at low pressures and small white particles in the IL after the experiment suggest that chemical interaction between the protic ionic liquid and NH_3 exists contrary to the findings reported in the literature. As protic ionic liquids chemically interact with ammonia, possess noticeable vapor pressure, and are expensive compared to traditional aprotic ionic liquids, it might not be feasible to utilize them in industrial processes. For these reasons, the protic ILs are not further investigated in this study.

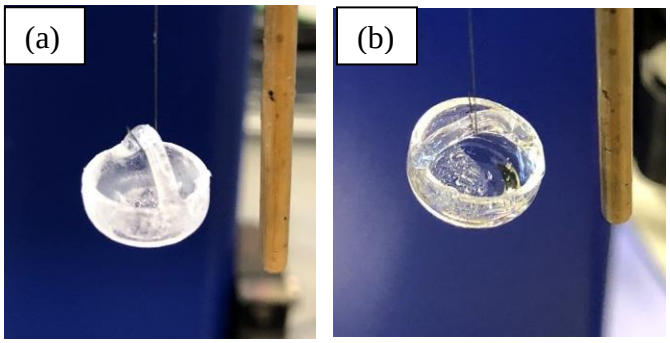

Figure 4.16. The sample cup in XEMIS microbalance after protic ionic liquids have interacted with NH_3. (a) NH_3 + EAN system, and (b) NH_3 + [C_2im][NTf_2] system.

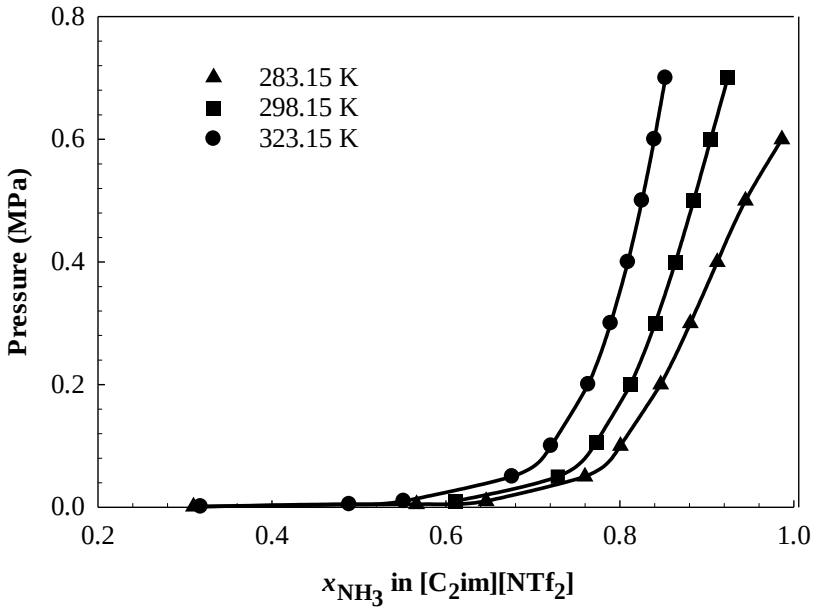

Figure 4.17. *PTx* phase diagram for NH_3 and [C_2im][NTf_2] at 283.15, 298.15, and 323.15 K. Solid Symbols represent the experimental point. Solid lines are guided to the eye.

4.1.3. Phase Behavior of Ionic Liquids and Carbon dioxide

In this section, the high-pressure vapor-liquid equilibrium for the binary systems of CO_2 and a series of 1-alkyl-1-methyl pyrrolidinium bis(trifluoromethylsulfonyl)imide ionic liquids ([$C_nC_1$pyr][NTf_2] (n = 3,4,6)) are measured at pressures up to 20 MPa. Experiments were conducted using gravimetric (IGA and XEMIS microbalances) and synthetic (high-pressure view cell) methods. The impact of temperature, pressure, and the alkyl chain length of cation on the solubility of CO_2 in the pyrrolidinium-based ILs with [NTf_2] were considered. In addition, molar volume and volume expansion of CO_2 + IL mixtures are discussed.

4.1.3.1. Phase Behavior of Pyrrolidinium-based Ionic Liquids and Carbon dioxide

The vapor-liquid equilibrium for the binary systems of CO_2 and a series of pyrrolidinium-based ILs, namely 1-propyl-1-methylpyrrolidinium bis(trifluoromethylsulfonyl)imide

([C_3C_1pyr][NTf_2]), 1-butyl-1-methylpyrrolidinium bis(trifluoromethylsulfonyl)imide ([C_4C_1pyr][NTf_2]) and 1-hexyl-methylpyrrolidinium bis(trifluoromethylsulfonyl)imide ([C_6C_1pyr][NTf_2]), are measured at 298.15, 318.15, and 338.15 K and at pressures up to 20 MPa using three independent experimental methods such as gravimetric (IGA and XEMIS microbalances) and synthetic (high-pressure view cell) methods.

4.1.3.1.1. Materials

The pyrrolidinium-based ionic liquids used in this study were purchased from Iolitec, Inc. The IL samples were stored under nitrogen and dried at 348.15 K in a high vacuum for 24 h to remove moisture before each experiment. The water content of each ionic liquid was measured upon delivery using a Karl Fisher Titrator, as described in Section 2.3.1. The specifications for all the chemicals used in this study, including the CO_2 are provided in Table 4.10. All chemicals were used as received. In order to account for buoyancy effects, the CO_2 gas density as a function of *T* and *P* and the liquid density for the ionic liquids as a function of *T* is required. Density for CO_2 was obtained using the NIST REFPROP V.9.1 Database[73]. The density of [C_3C_1pyr][NTf_2], [C_4C_1pyr][NTf_2], and [C_6C_1pyr][NTf_2] were obtained from the literature.[127–130]

4.1.3.1.2. Vapor-Liquid Equilibrium of CO_2 + [$C_nC_1$pyr][NTf_2] Mixtures at Low Pressures

The solubility of carbon dioxide was measured in the ionic liquids [C_3C_1pyr][NTf_2], [C_4C_1pyr][NTf_2], and [C_6C_1pyr][NTf_2] at 298.15, 318.15, and 338.15 K and at pressures ranging from 0.0250 to 2 MPa using two IGA gravimetric microbalances. The data are shown in Figures 4.18 - 4.20 and listed in Appendices B1, B2, and B3. The solubility of CO_2 increased in the three pyrrolidinium-based ionic liquids as temperature decreased.

Table 4.10. Description of Chemical Components

Name	**Acronym**	**CAS Number**	**Initial Mole Fraction Purity**	**Water Content (ppm)**	**Source, Product Number and Lot Number**
Carbon dioixide	CO_2	124-38-9	0.99999	N/A	Matheson Tri-Gas,Inc
1-propyl-1-methylpyrrolidinium bis(trifluoromethyl-sulfonly)imide	$[C_3C_1pyr][NTf_2]$	223437-05-6	>0.995	38 ± 3	Iolitec, IL-0044-UP-0100 and P00369.1-IL-0044
1-butyl-1-methylpyrrolidinium bis(trifluoromethyl-sulfonyl)imide	$[C_4C_1pyr][NTf_2]$	223437-11-4	>0.995	110 ± 1	Iolitec, IL-0035-UP-0100 and N00352.7.1-IL-0035
1-hexy-l-methylpyrrolidinium bis(trifluoromethylsulfonyl)imide	$[C_6C_1pyr][NTf_2]$	380497-19-8	>0.995	23 ± 2	Iolitec, IL-0092-UP-0100 and P00269.1-IL-0092

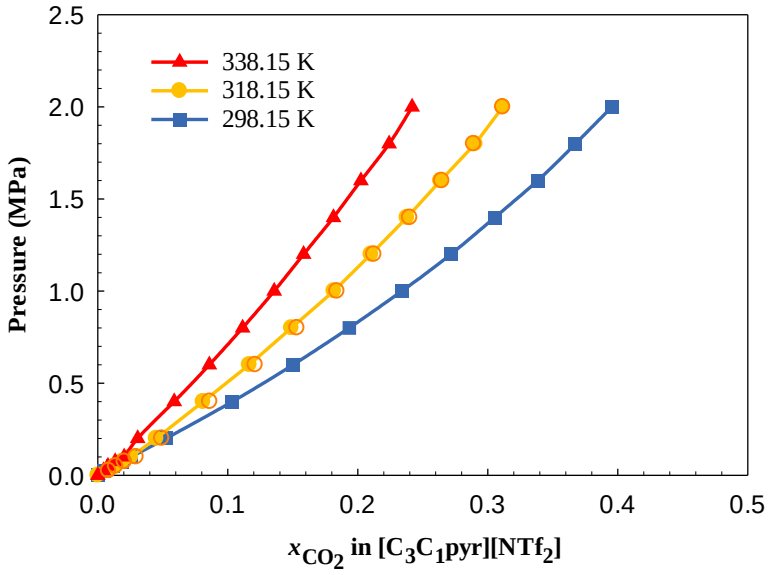

Figure 4.18. PTx diagram for CO_2 solubility in $[C_3C_1pyr][NTf_2]$ at 298.15, 318.15, and 338.15 K at pressures up to 2 MPa. Symbols: solid symbols, absorption data; open symbols, desorption data. Lines added to guide the eye.

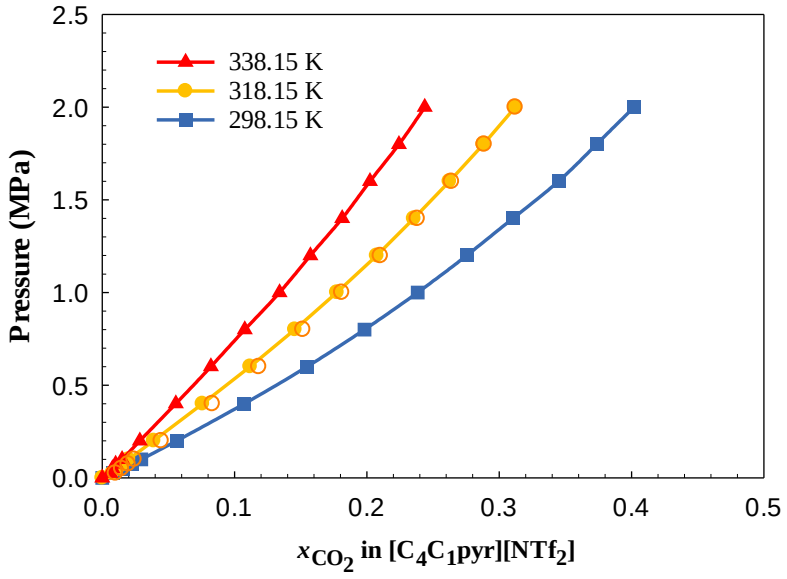

Figure 4.19. *PTx* diagram for CO_2 solubility in [C_4C_1pyr][NTf_2] at 298.15, 318.15, and 338.15 K at pressures up to 2 MPa. Symbols: solid symbols, absorption data; open symbols, desorption data. Lines added to guide the eye.

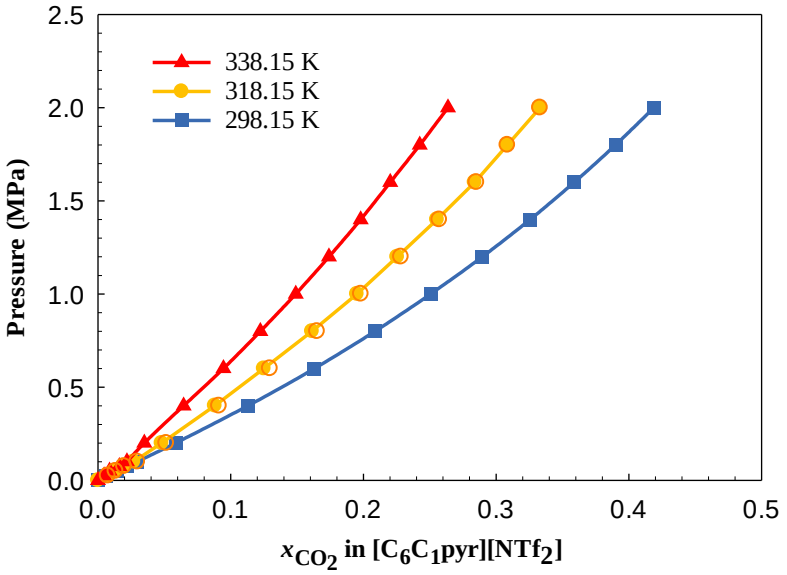

Figure 4.20. *PTx* diagram for CO_2 solubility in [C_6C_1pyr][NTf_2] at 298.15, 318.15, and 338.15 K at pressures up to 2 MPa. Symbols: solid symbols, absorption data; open symbols, desorption data. Lines added to guide the eye.

4.1.3.1.2.1. Henry's Law Application

The CO_2 solubility increased linearly at low pressures up to about 0.1 MPa. Henry's law constants (k_H) are useful for quick assessment of gas solubility in a solvent as the lower k_H values mean higher gas solubility in the solvent.[90,131] The Henry's law constants were obtained from experimental gas solubility (*PTx*) data using Equation 3.21, assuming the hydrostatic pressure correction (Krichevsky-Kasarnovsky equation) is not required.[90] Henry's law constants were obtained by calculating the limiting slope while x_{CO_2} approached zero using the linear fit of experimental data up to 0.1 MPa including the theoretical zero point (zero pressure and zero composition). As can be seen in Table 4.11, Henry's law constants increased with an increase in *T* for any given pyrrolidinium-based IL indicating that the solubility of CO_2 decreased with increase in *T*. The constants obtained in this study for CO_2 in $[C_4C_1pyr][NTf_2]$ were compared with previously published data.[41,42,58,59] The k_H obtained in this study at 298.15 K (3.30 ± 0.06 MPa) was comparable with k_H value obtained by Anthony et al. (3.86 ± 0.14 MPa)[41] at 298.15, the k_H value predicted via COSMO-RS method by Zhang et al. (3.1 MPa)[58] at 298.15 K, and the k_H value obtained by Hong et al (3.27 MPa)[42]. Kumelan et al. also reported a correlation between temperature and Henry's constants on the molality scale.[59] The k_H values are calculated using their molality scaled correlation at our experimental temperatures and converted to the mole fraction scale to make a comparison. The k_H values obtained via the correlation[59] of 3.17 MPa at 298.15 K, 4.49 MPa at 318.15 K, and 6.05 MPa at 338.15 K are also in good agreement with the k_H values calculated in this study (3.30 ± 0.06 MPa) at 298.15 K, (4.76 ± 0.58 MPa) at 318.15 K, and (7.19 ± 1.53 MPa) at 338.15 K. The Henry's law constants are also used to estimate the enthalpy ($\Delta\overline{H}_{sol}$) and entropy ($\Delta\overline{S}_{sol}$) of solution per mole of gas at infinite dilution using Equation 3.22 and 3.23.

The $\Delta\overline{H}_{sol}$ and $\Delta\overline{S}_{sol}$ for CO_2 absorption in ($[C_nC_1pyr][NTf_2]$ (n = 3,4,6)) are reported in Table 4.12. The negative $\Delta\overline{H}_{sol}$ indicates the CO_2 sorption in pyrrolidinium-based ILs is exothermic. The negative $\Delta\overline{S}_{sol}$ indicates the absorption of CO_2 in the pyrrolidinium-based ionic liquids leads to an increase in molecular ordering.[90] The estimated solvation enthalpy for CO_2 in $[C_4C_1pyr][NTf_2]$ obtained in this study (-16.0 ± 1.1 kJ·mol^{-1}) was comparable with previous literature values for CO_2 in $[C_4C_1pyr][NTf_2]$, (-13.94 ± 0.21 kJ·mol^{-1})[59], (-11.9 ± 1.1 kJ·mol^{-1})[41], and (-13.2 kJ·mol^{-1})[42]. Entropy of dissolution obtained in this study (-50.4 ± 2.5 J·mol^{-1}·K^{-1}) is within the range of the data reported by Anthony *et al* (-38.7 ± 3.5 J·mol^{-1}·K^{-1})[41] , Kumelan *et al* (-68.74 ± 0.71 J·mol^{-1}·K^{-1})[59], and Hong *et al* (-73.4 J·mol^{-1}·K^{-1})[42].

Table 4.11. Henry's law constants for CO_2 + $[C_3C_1pyr][NTf_2]$ mixtures at 298.15, 318.15, and 338.15 K

	Henry's law Constants (k_H)/MPa		
Binary System	T= 298.15 K	T=318.15 K	T= 338.15 K
CO_2 + $[C_3C_1pyr][NTf_2]$	3.94 ± 0.26	4.02 ± 0.29	5.67 ± 0.39
CO_2 + $[C_4C_1pyr][NTf_2]$	3.30 ± 0.06	4.76 ± 0.58	7.19 ± 1.53
CO_2 + $[C_6C_1pyr][NTf_2]$	3.41 ± 0.12	3.78 ± 0.23	4.68 ± 0.48

The uncertainties are the standard error of the coefficient obtained in the linear regression.

Table 4.12. Enthalpy of solution ($\Delta\overline{H}_{sol}$) and Entropy of solution ($\Delta\overline{S}_{sol}$) of CO_2 absorption in ($[C_nC_1pyr][NTf_2]$ (n = 3,4,6)) at Infinite Dilution

Ionic Liquid	$\Delta\overline{H}_{sol}$ / kJ·mol^{-1}	$\Delta\overline{S}_{sol}$/ J·mol^{-1}·K^{-1}
$[C_3C_1pyr][NTf_2]$	-7.5 ± 4.2	-23.8 ± 12.8
$[C_4C_1pyr][NTf_2]$	-16.0 ± 1.1	-50.4 ± 2.5
$[C_6C_1pyr][NTf_2]$	- 6.5 ± 1.6	-20.6 ± 4.5

The uncertainties are the standard error of the coefficient obtained in the linear regression.

4.1.3.1.2.2. Absorption and Desorption

Chemical interaction between CO_2 and pyrrolidinium-based ionic liquids was also considered by measuring the absorption and desorption of CO_2 in $[C_3C_1pyr][NTf_2]$, $[C_4C_1pyr][NTf_2]$, and $[C_6C_1pyr][NTf_2]$ at 318.15 K and pressures from 0.025 MPa to 2 MPa. The desorption data are shown in Figures 4.18 – 4.20 (open circles) and provided in Appendix B4. The average deviation, in terms of mole percent, between the absorption and desorption studies for all three ionic liquids was less than 0.4 mole % and within the error range of the balance. Therefore, obtaining the same equilibrium concentrations for the given isotherms during absorption and desorption suggests that the interaction between CO_2 and pyrrolidinium ionic liquids are physical.

4.1.3.1.3. Vapor-Liquid Equilibrium of CO_2 + $[C_nC_1pyr]$ mixtures at High Pressures

The solubility of CO_2 in $[C_3C_1pyr][NTf_2]$, $[C_4C_1pyr][NTf_2]$, and $[C_6C_1pyr][NTf_2]$ was measured using a high-pressure view cell apparatus at 298.15, 318.15, and 338.15 K, and at pressures up to approximately 20 MPa. The data are provided in Appendices B1, B2, and B3, and shown in Figures 4.21 - 4.23 along with lower pressure data.

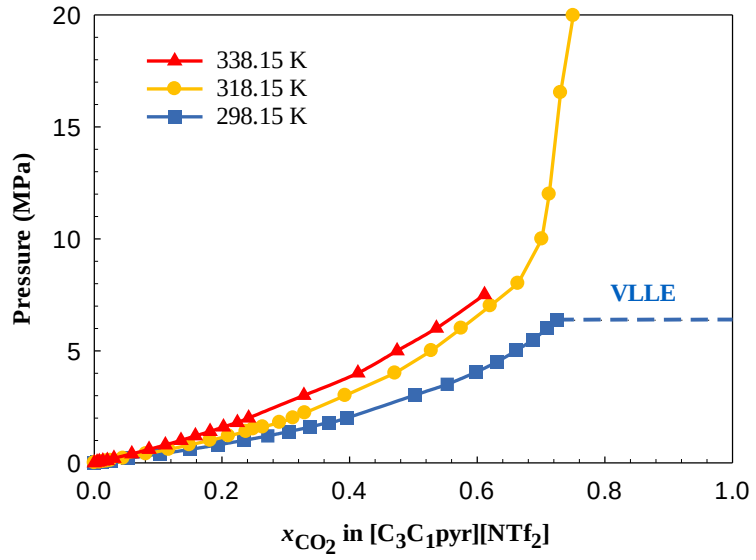

Figure 4.21. *PTx* diagram for CO_2 solubility in [C_3C_1pyr][NTf_2] at 298.15, 318.15, and 338.15 K at pressures up to 20 MPa. Lines added to guide the eye

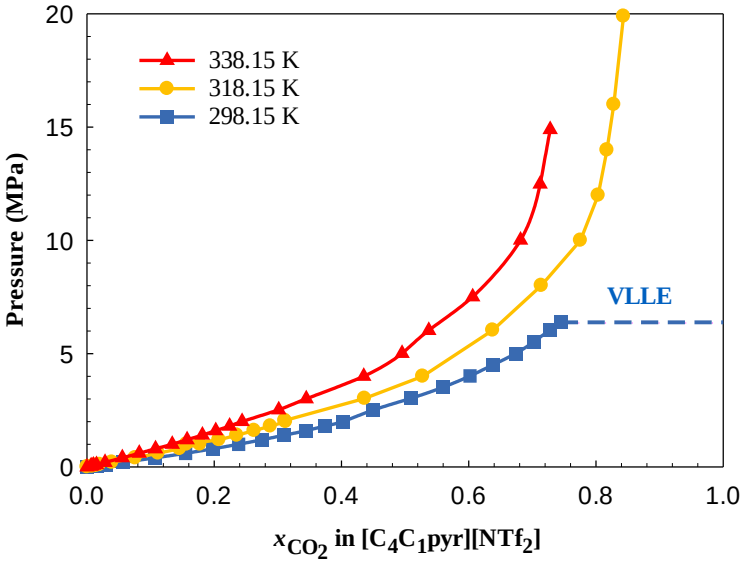

Figure 4.22. *PTx* diagram for CO_2 solubility in [C_4C_1pyr][NTf_2] at 298.15, 318.15, and 338.15 K at pressures up to 20 MPa. Lines added to guide the eye.

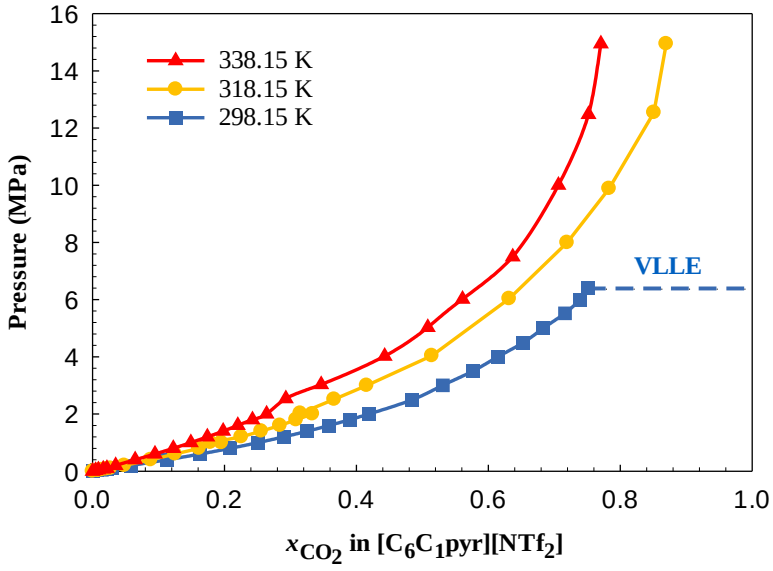

Figure 4.23. *PTx* diagram for CO_2 solubility in [C_6C_1pyr][NTf_2] at 298.15, 318.15, and 338.15 K at pressures up to 15 MPa. Lines added to guide the eye.

4.1.3.1.3.1. Effect of Temperature

Over the pressure range measured at experimental temperatures (318.15 and 338.15 K) above the critical temperature of CO_2 (304.25 K), only VLE exists between the CO_2 vapor phase and the ionic liquid-rich liquid phase as shown in Figures 4.21-4.23. However, 298.15 K is below the critical temperature for CO_2; therefore, VLE between the CO_2 vapor phase and the ionic liquid-rich liquid phase is followed by vapor-liquid-liquid equilibrium (VLLE) between the ionic liquid-rich liquid phase, the CO_2-rich liquid phase and the pure CO_2 vapor phase assuming that the IL solubility in the vapor phase is immeasurably small. The phase transition from VLE to VLLE occurs at the vapor pressure of pure CO_2 (~6.4 MPa at 298.15 K) within experimental uncertainty, which also indicates that the solubility of the IL in CO_2 liquid phase is very small.

4.1.3.1.3.2. Effect of Pressure

Figures 4.21-4.23 shows that the solubility of CO_2 in pyrrolidinium-based ILs increased with an increase in pressure. The high-pressure behavior (above 10 MPa) approaches almost a vertical slope ($\Delta P/\Delta x$), which indicates the CO_2 solubility only slightly increases despite large increases in pressure. Similar observations are made for both imidazolium[132] and pyrrolidinium ionic liquids[45]. This behavior can be attributed to the large reduction in free volume in the IL phase. As shown in Figure 4.24, the CO_2 solubility in all three pyrrolidinium-based ionic liquids at 298.15 K ($T<T_c$ of CO_2) has slight negative deviations from Raoult's Law at lower compositions (below 0.4 mole fraction). However, above approximately 0.4 mole fraction, positive deviations are observed in any of the ionic liquids studied, especially as the VLLE conditions are approached (Figure 4.24). The positive deviation from Raoult's Law may indicate that the CO_2-IL interactions are not as favorable as the CO_2-CO_2 or IL-IL interactions at high CO_2 compositions.

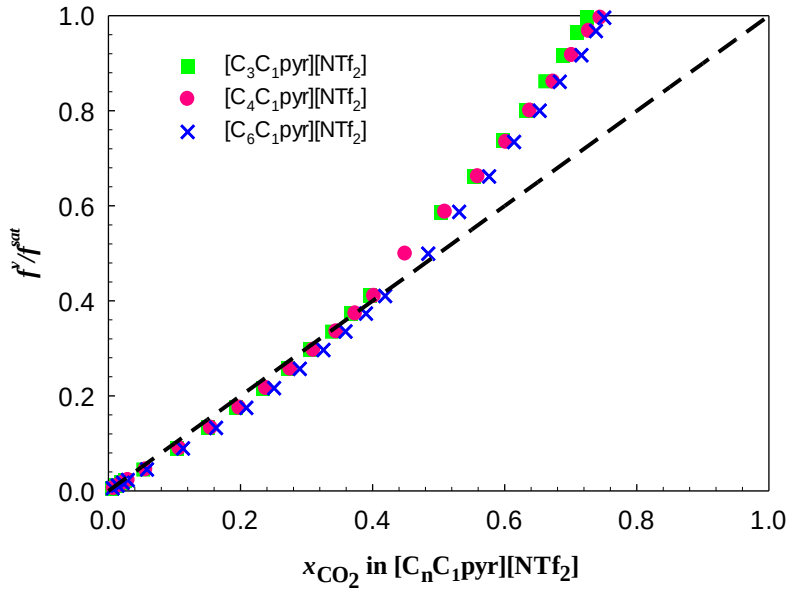

Figure 4.24. Normalized fugacity of CO_2 in $[C_nC_1pyr][NTf_2]$ (n = 3,4,6) at 298.15 K. The dashed line represents the Raoult's Law.

4.1.3.1.3.3. Effect of Cation Alkyl Chain Length

Increasing the length of the alkyl chain on the pyrrolidinium cation was found to slightly increase the CO_2 solubility at any given temperature: $[C_3C_1pyr][NTf_2]$ < $[C_4C_1pyr][NTf_2]$ < $[C_6C_1pyr][NTf_2]$. This behavior is depicted in Figure 4.24 as an example at 298.15 K. Kim et al. also observed that the longer the alkyl chain length leads to slightly higher CO_2 solubility: $[C_3C_1pyr][NTf_2]$ < $[C_5C_1pyr][NTf_2]$ < $[C_7C_1pyr][NTf_2]$<$[C_9C_1pyr][NTf_2]$.[45] Hou and Boltus[133] and Aki et al[134] observed an increase in the solubility of CO_2 in imidazolium-based ILs with longer cation alkyl chain length. The higher dissolution of CO_2 was attributed to larger free volume in the imidazolium ILs with longer alkyl chain.[133,134] Aki et al. discussed that this steric impact might be explained by entropic arguments rather than enthalpic.[134] Therefore, similar to imidazolium-based ILs, the increase in solubility of CO_2 in pyrrolidinium-based ILs with an increase in alkyl chain length could also be explained by the entropic contribution due to increased free volume rather than enthalpic contribution. Hou and Boltus discussed that the large cation (i.e., pyridinium compared to imidazolium) could distribute and stabilize the charge better resulting in weaker cation-anion interactions, which lead to stronger CO_2-anion interactions and consequently higher CO_2 dissolution.[133] However, the marginally larger alkyl groups in this study might not create such significant alterations in charge distribution and, consequently, the solubility. Therefore, the solubility of CO_2 in pyrrolidinium ILs with $[NTf_2]$ anion might be dominated by the steric impacts.

4.1.3.1.4. Vapor-Liquid Equilibrium of CO_2 + $[C_3C_1pyr][NTf_2]$ mixtures from Low to High Pressures

In the previous two sections, the low- and high-pressure vapor-liquid equilibrium data were measured using the IGA microbalances and high-pressure view cell. Even though the apparatuses

have shown high reproducibility and accuracy, as discussed in Section 4.1.1, the repeatability of the experimental results was tested with two additional experiments. First, the solubility of CO_2 in $[C_3C_1pyr][NTf_2]$ at 298.15 K and at pressures up to 2 MPa was measured using both IGA microbalances (IGA-I and IGA-II). The gas solubility results in both IGA balances were within 0.1 mole % deviation. Second, a Hiden XEMIS gravimetric microbalance was used to measure the solubility of CO_2 in $[C_3C_1pyr][NTf_2]$ at 318.15 K at pressures up to 5 MPa to compare with both low- and high-pressure CO_2 solubility results. The XEMIS microbalance results were within 0.1 mole % on average compared with the IGA and high-pressure view cell measurements. Considering the independence of each method and experimental apparatuses, the gas solubility data measured using the IGA, XEMIS, and high-pressure view cell are in excellent agreement, as shown in Figure 4.25.

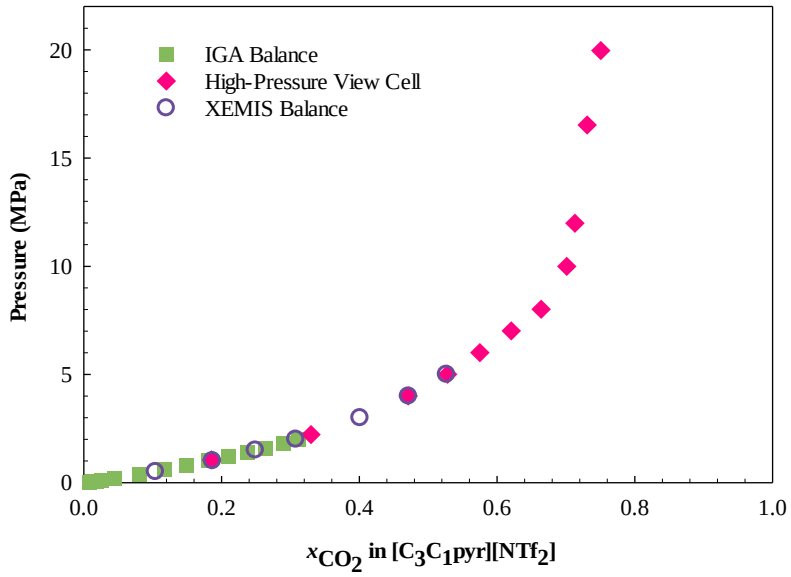

Figure 4.25. Comparison of experimental methods (IGA microbalance, XEMIS microbalance, and high-pressure view cell) on the *Px* diagram for CO_2 solubility in $[C_3C_1pyr][NTf_2]$ at 318.15 K and at pressures up to 20 MPa.

4.1.3.1.5. Literature Comparison

The solubility of CO_2 in $[C_3C_1pyr][NTf_2]$, $[C_4C_1pyr][NTf_2]$, and $[C_6C_1pyr][NTf_2]$ have also been measured by other research groups.[5,11–14,17–24]. The solubility of CO_2 in $[C_4C_1pyr][NTf_2]$ by Kumelan et al.[59] and Anthony et al.[41] at any given temperature (298.15, 318.15 and 338.15 K) and low pressures are shown in Figure 4.26 and consistent with this study. Experimental data by Lee and Nam[65] and Yim et al.[43] are not in good agreement with either study or other data in the literature. Kim et al.[45] and Yim et al.[44,61] investigated the solubility of $[C_3C_1pyr][NTf_2]$[45] and $[C_6C_1pyr][NTf_2]$ [44,61] which also is not in agreement with this study as shown in Figures 4.27 and 4.28. Their solubility data appears to be higher than our data (using either the microbalance or high-pressure technique) at a lower pressure (composition), and lower solubility than our data at higher pressure.

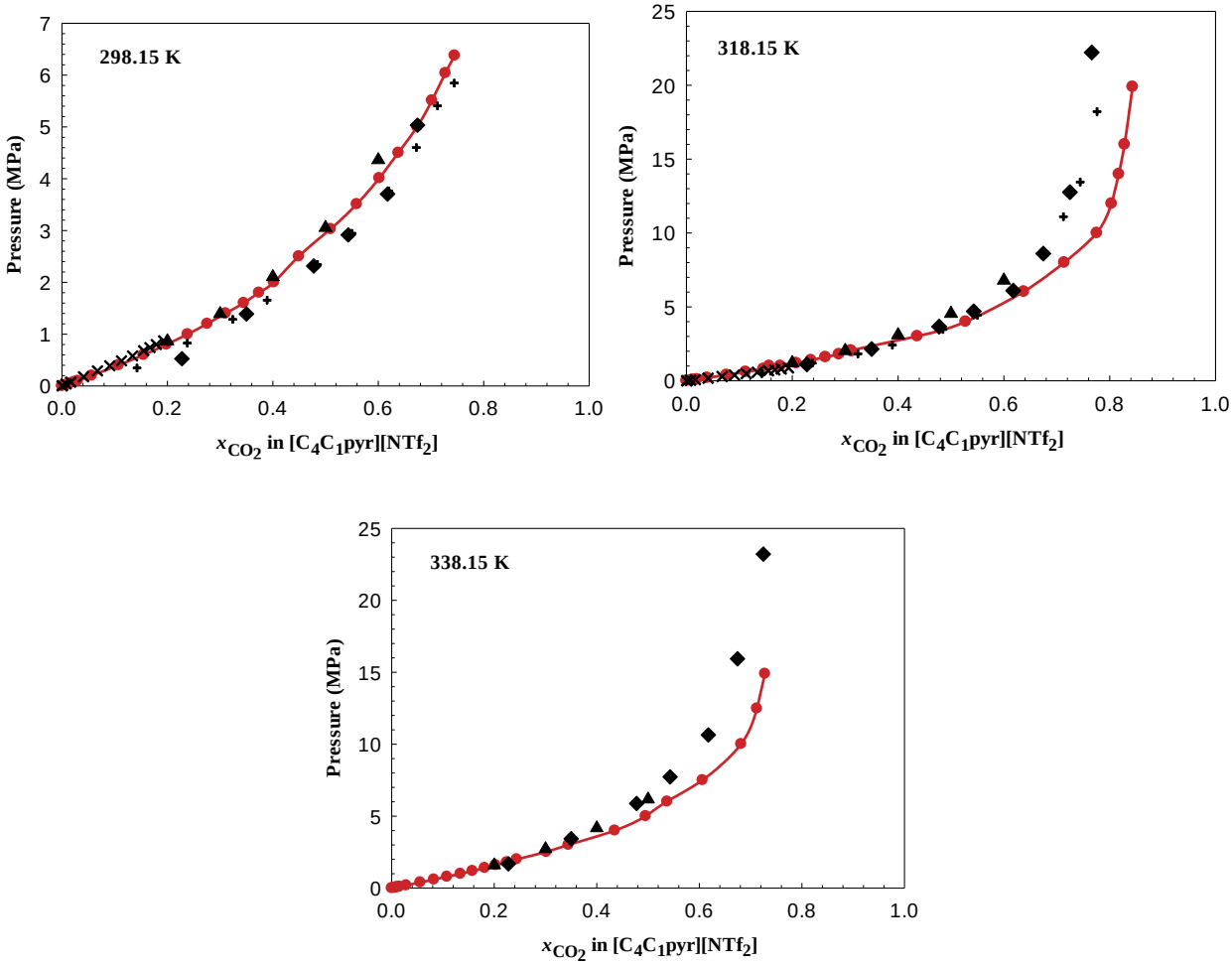

Figure 4.26. Comparison of the experimental PTx diagram of CO_2 solubility in [C_4C_1pyr][NTf_2] at 298.15 K , 318.15 K, and 338.15 K. Symbols: ●, this study; x, Anthony et al[41]; ▲, Kumelan et al.[59]; ♦, Yim et al.[43]; + , Lee and Nam[65]. Solid lines added to guide the eye. The literature data (except Anthony et al. at 298.15 K[41]) has been interpolated or extrapolated to compare with our experimental measurements at different temperatures.

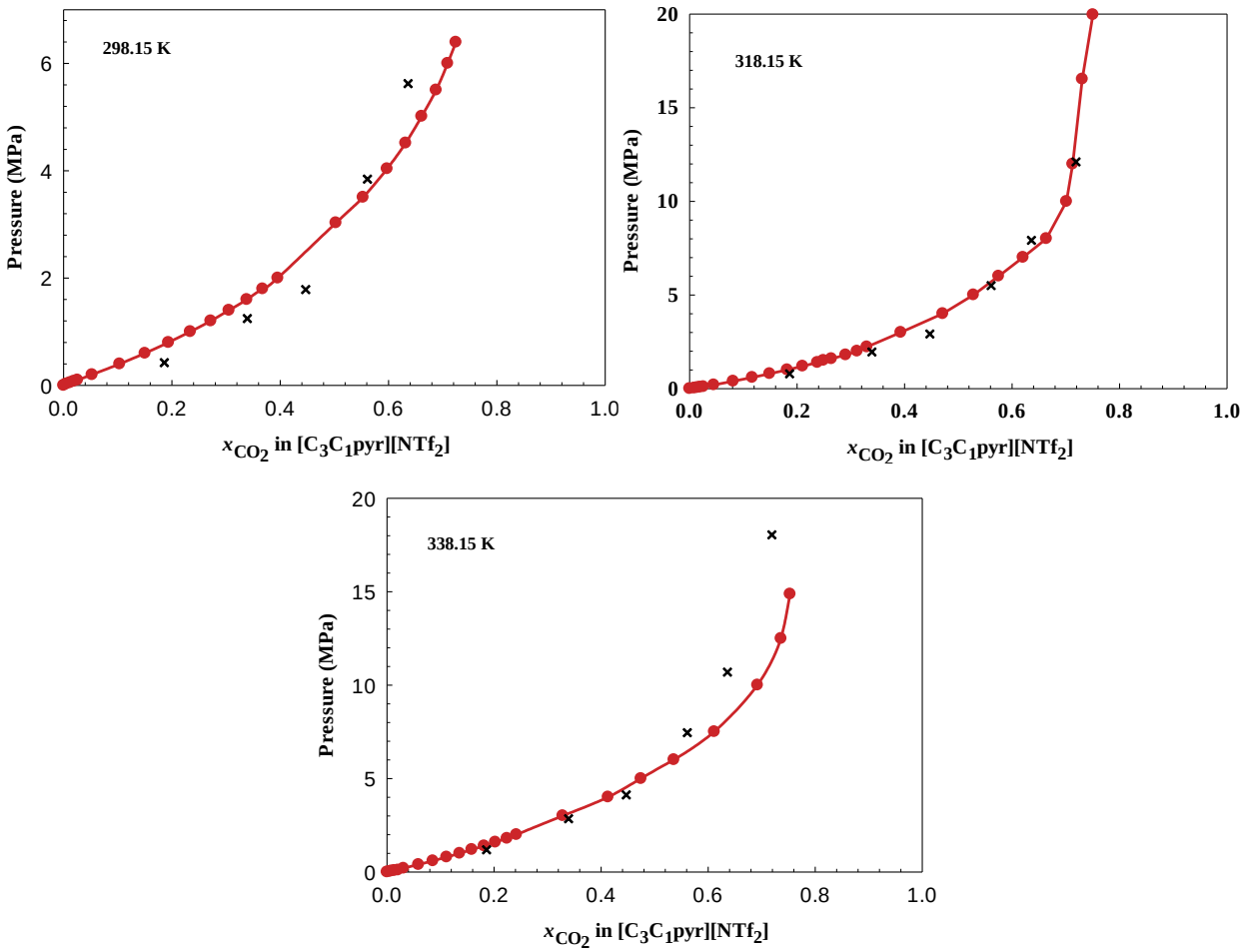

Figure 4.27. Comparison of the experimental *PTx* diagram of CO_2 solubility in [C_3C_1pyr][NTf_2] at 298.15 K, 318.15 K, and 338.15 K. Symbols: ●, this study; x, Kim et al[14]. Solid lines added to guide the eye. In some cases, the literature data has been interpolated or extrapolated to compare with our experimental measurements.

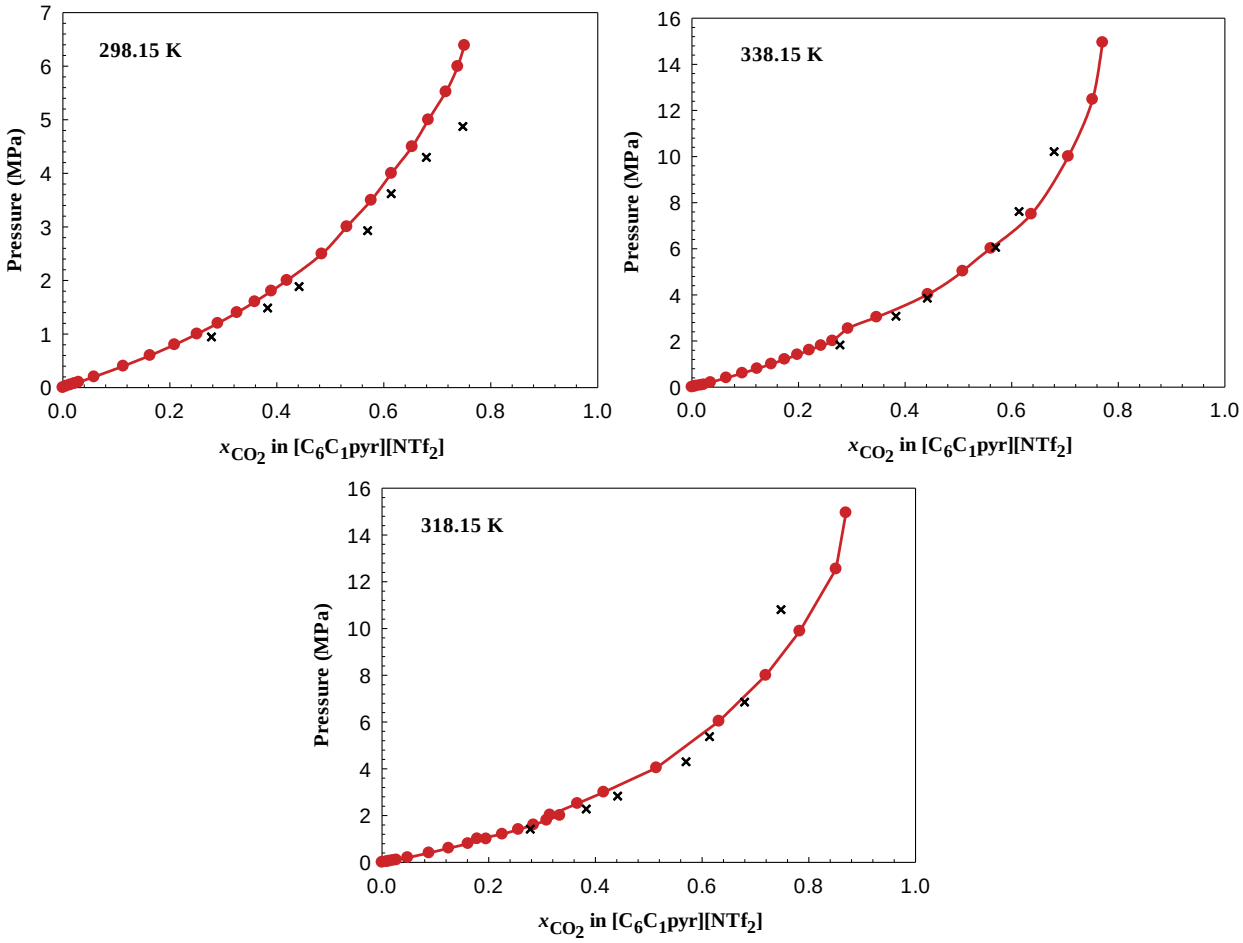

Figure 4.28. Comparison of the experimental *PTx* diagram of CO_2 solubility in [C_6C_1pyr][NTf_2] at 298.15 K, 318.15 K, and 338.15338.15 K. Symbols: ●, this study; x, Yim et al[13,20]. Solid lines added to guide the eye. In some cases, the literature data has been interpolated or extrapolated to compare with our experimental measurements.

4.1.3.1.6. Molar Volume, Density and Volume Expansion of CO_2 + [$C_nC_1$pyr] mixtures at High Pressures

In this study, the molar volume ($\underline{V}$), density, and volume expansion of CO_2+[C_3C_1pyr][NTf_2], CO_2+[C_4C_1pyr][NTf_2], and CO_2+[C_6C_1pyr][NTf_2] mixtures were measured at 298.15, 318.15, and 338.15 K, and pressures up to approximately 20 MPa using the high-pressure view cell. The data are provided in Appendices B1, B2, and B3. The fractional volume expansion is calculated based on the difference in the pure liquid volume (V_0) and the expanded liquid volume (V_1) with respect to the pure liquid volume using Equation 4.2:

$$\frac{\Delta V}{V_o} = \frac{V_1(T,P,x) - V_o(T,P = 0.1\ MPa)}{V_o\ (T,P = 0.1\ MPa)} \tag{4.2}$$

Most organic liquids exhibit a large volume expansion with dissolved CO_2 (i.e., 281% in dimethylformamide (DMF)).[135] On the other hand, ILs typically exhibit only modest volume expansion with CO_2 dissolution (i.e., 17% for [C_4C_1im][BF_4]).[135] The maximum volume expansion in this study compared to ambient pressure was for CO_2 + [C_4C_1pyr][NTf_2] and CO_2 + [C_6C_1pyr][NTf_2] mixtures at 298.15 K and ~ 6.4 MPa, and was about 37%. At any given temperature, the volume of the liquid mixture expanded with an increase in pressure and reached a plateau at high pressures due to the limited solubility as a result of the free volume occupied by CO_2 molecules in the ILs. The temperature change resulted in a change in volume expansion due to lower CO_2 dissolution for any given IL. Shiflett and Yokozeki showed that the change in molar volume can be estimated at low pressures (below 2 MPa) using a mole fraction average of the pure component molar volumes, and is insensitive to the temperature variation between 298 and 333 K for CO_2 + [C_4C_1im][PF_6] and CO_2 + [C_4C_1im][BF_4] systems.[136] The findings in this study suggests

a simple mole fraction average is not recommended at higher pressures, and experimental measurements are needed to calculate the volume expansion properly. The increase in the length of the alkyl group on the cation led to only a slight increase in volume expansion at a given pressure (~1-2 %) as a result of only a slight increase in CO_2 dissolution.

The liquid mixture molar volume decreased with CO_2 pressure due to the increased solubility of CO_2 in $[C_3C_1pyr][NTf_2]$ at 298.15, 318.15, and 338.15 K as shown in Figure 4.29 (a). At low pressures (up to 2 MPa), the molar volume linearly decreased with an increase in pressure, and the slope of the liquid molar volume with pressure increased with a decrease in temperature. Considering the inverse molar volume equals the molar density, the molar density increased with increasing CO_2 solubility. At high pressures, the significant decrease in liquid mixture molar volume with pressure was observed at each temperature with any given IL. The molar volume of the liquid mixture is also independent of temperature and demonstrates nearly a linear decrease with increasing CO_2 composition for each temperature, as shown in Figure 4.29 (b). This trend is similar to other IL systems in the literature.[79] The results showed the molar volume of the liquid mixtures increased with an increase in cation alkyl chain length at any given temperature, which is depicted for CO_2 and $[C_nC_1pyr][NTf_2]$ at 338.15 K in Figure 4.30. The molar volume data for the mixtures of CO_2 and $[C_nC_1pyr][NTf_2]$ (n=4,6) are also qualitatively similar to CO_2 in $[C_3C_1pyr][NTf_2]$ as shown in Figures 4.31 and 4.32.

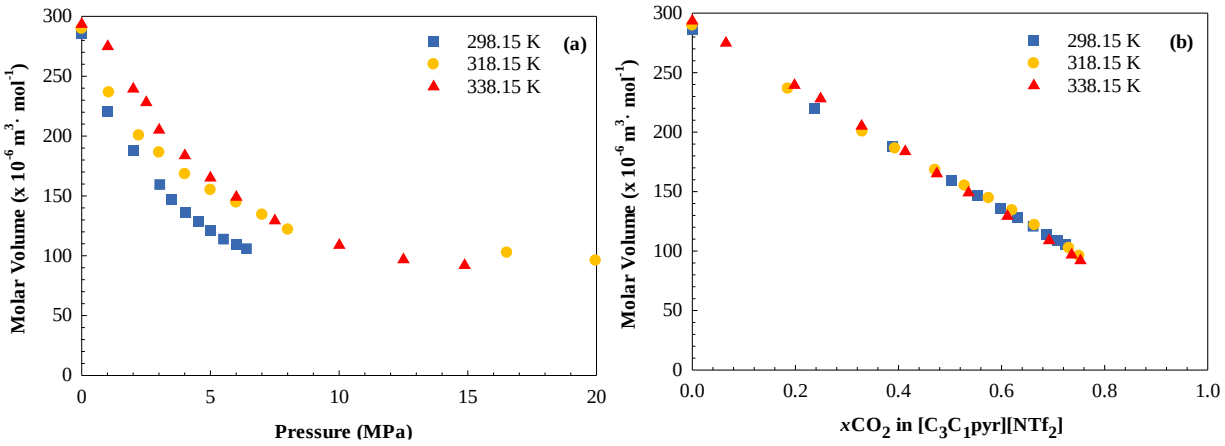

Figure 4.29. Experimental molar volume data for CO_2 and $[C_3C_1pyr][NTf_2]$ mixture at 298.15, 318.15, and 338.15 K with respect to (a) pressure and (b) CO_2 composition

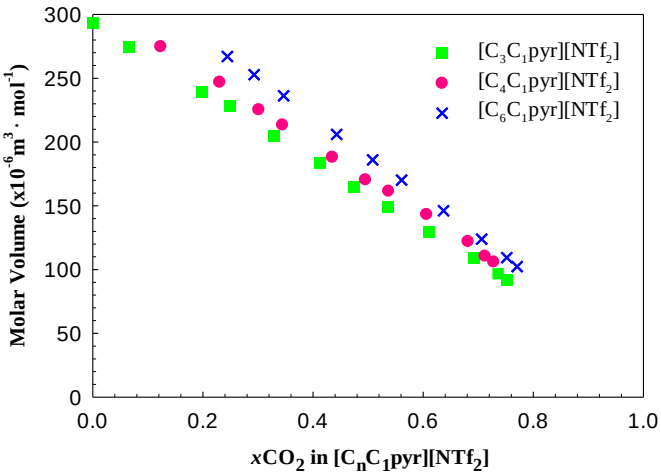

Figure 4.30. Experimental molar volume data of CO_2 and $[C_nC_1pyr][NTf_2]$ mixtures (n = 3,4,6) at 338.15 K.

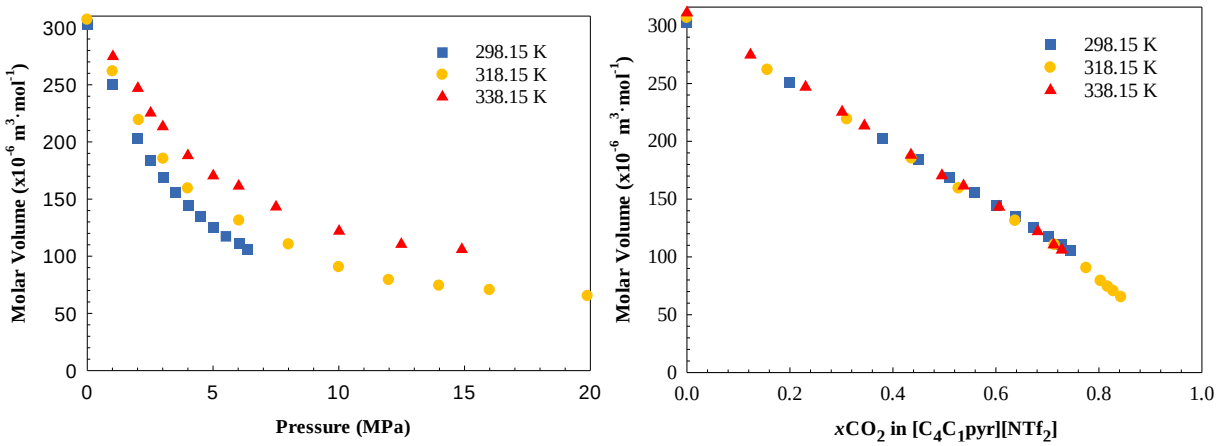

Figure 4.31. Experimental molar volume data for CO_2 and $[C_4C_1pyr][NTf_2]$ at 298.15, 318.15, and 338.15 K

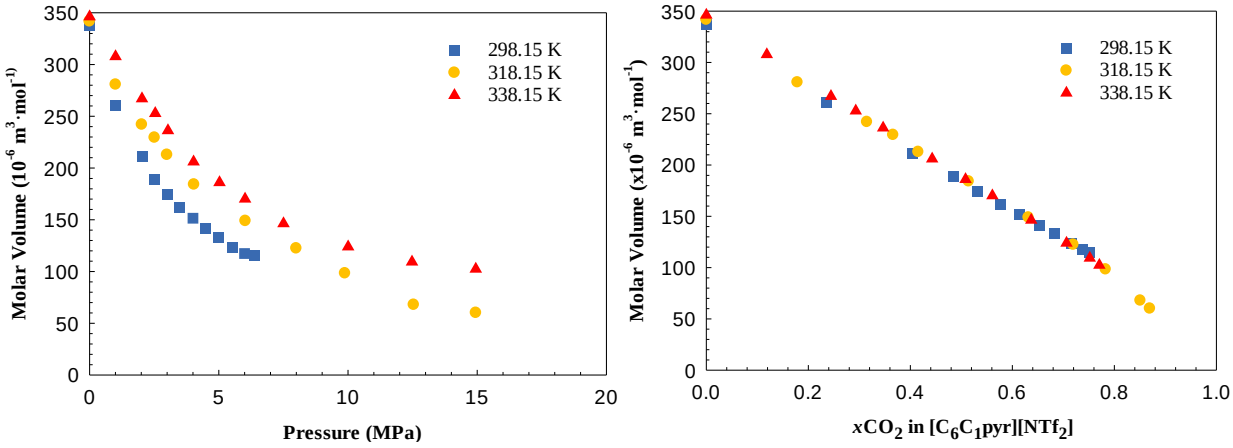

Figure 4.32. Experimental molar volume data for CO_2 and $[C_6C_1pyr][NTf_2]$ at 298.15, 318.15, and 338.15 K

4.1.3.1.7. Density of the CO_2 + $[C_nC_1pyr]$ mixtures

The liquid density of the CO_2 + $[C_3C_1pyr][NTf_2]$ mixture at CO_2 mole fractions less than about 0.6 is almost independent of concentration (i.e., CO_2 pressure) as shown in Figure 4.33. However, at higher CO_2 concentrations (i.e., higher pressures), the density increased at 318.15 K and 338.15 K, whereas the density decreased at 298.15 K. At 298.15 K, the decrease in molar

volume of the mixture was larger than the decrease in the average molecular weight; therefore, the density of the mixture at 298.15 K decreased with an increase in pressure. On the other hand, at 318.15 K and 338.15 K, the decrease in average molecular weight was larger than the decrease in the molar volume; therefore, the density at 318.15 K and 338.15 K increased with an increase in pressure. The density data for the mixtures of CO_2 and $[C_nC_1pyr][NTf_2]$ (n=4,6) are also qualitatively similar to CO_2 in $[C_3C_1pyr][NTf_2]$, and shown in Figures 4.34 and 4.35. When alkyl chain length increases, the density of the mixture decreases, as shown in 4.36.

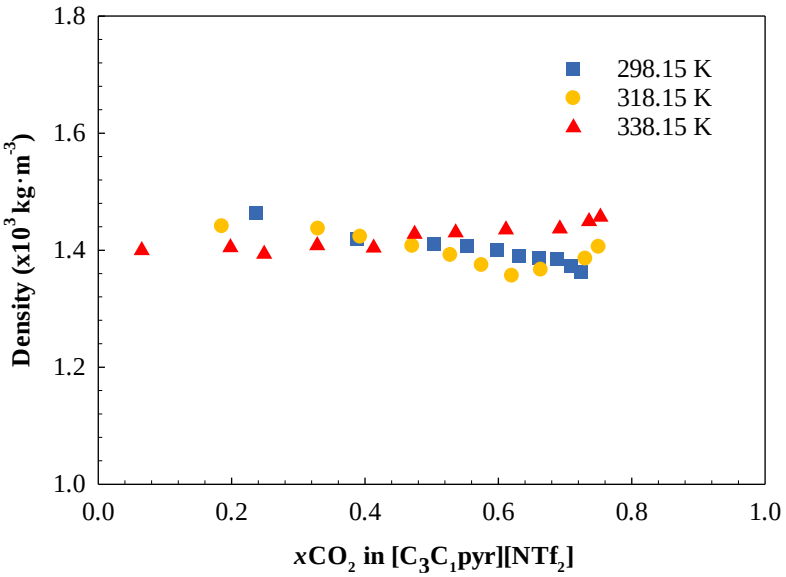

Figure 4.33. The experimental density data for CO_2 and $[C_3C_1pyr][NTf_2]$ mixtures at 298.15, 318.15, and 338.15 K

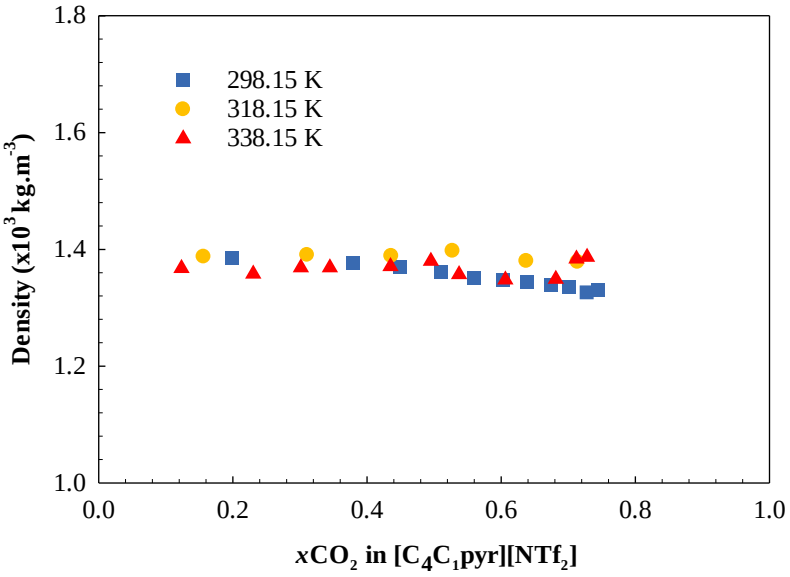

Figure 4.34. The experimental density data for CO_2 and [C_4C_1pyr][NTf_2] mixtures at 298.15, 318.15, and 338.15 K

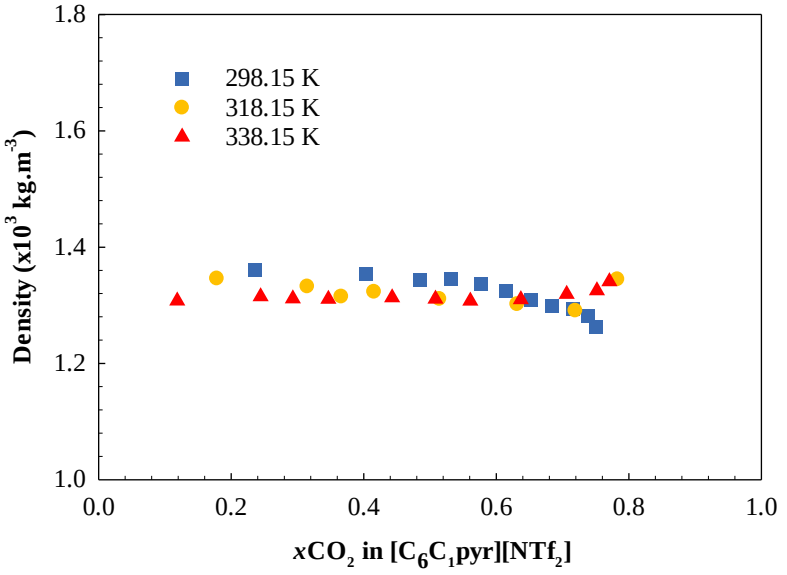

Figure 4.35. The experimental density data for CO_2 and [C_6C_1pyr][NTf_2] mixtures at 298.15, 318.15, and 338.15 K

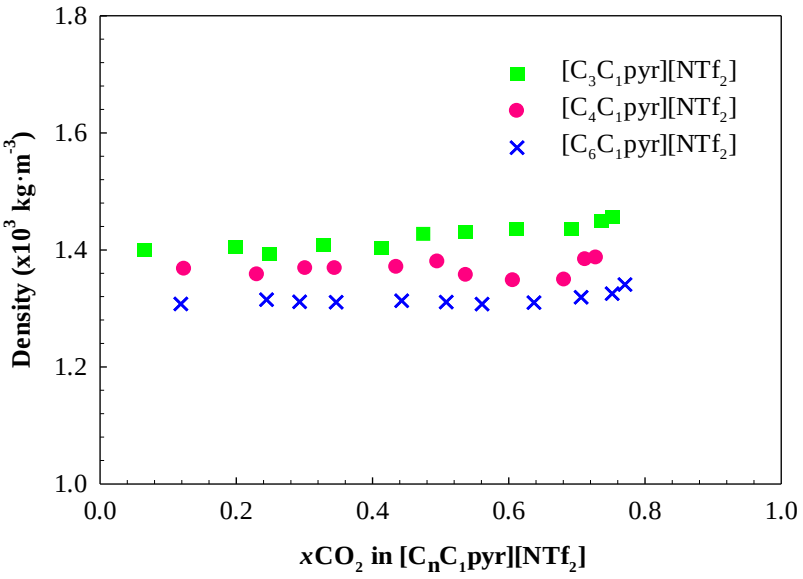

Figure 4.36. The experimental density data for CO_2 and [$C_nC_1$pyr][NTf_2] mixtures 338.15 K.

4.2. Phase Behavior of Ionic Liquid and Alcohols

4.2.1. Assessment of the Experimental Method

The reliability and accuracy of the experimental method used in this study were verified by measuring the liquid-liquid equilibria of 2-butanol and water mixture at 298.15 K. Two samples of a 2-butanol and water mixture were prepared as described in Section 2.2. 2-butanol (CAS:78-92-2, Lot no. SHBJ2337) and water (CAS:7732-18-5, Lot no. SHBH9984) were obtained from Sigma Aldrich.

The LLE compositions for the 2-butanol in the water-rich liquid phase (lower phase) and in the 2-butanol-rich liquid phase (upper phase) were 5.91 and 30.36 mol %, respectively. The composition of 2-butanol in the lower (5.91 mol %) and upper (30.36 mol %) phases was within about 1 mol % compared with previously reported values by Shiflett and Yokozeki (5.5 and 31.7 mol %) [56], Hefter et al. (5.99 and 30.56 mol %),[137] and Ochi et al. (4.91 and 31.5 mol %)[138]. The good agreement between the experimental results and the literature data verify that the

experimental method used in this study is an accurate method to measure the LLE for ILs and diols.

4.2.2. Liquid-Liquid Equilibria of Ionic Liquids and Dihxdroxy Alcohols

In the discussed in Section 1.4.3, ILs might be useful for separation processes in the new sustainable bio-based plants where diols are produced. Like many other processes, these processes also require the fundamental thermodynamic knowledge of IL binary mixtures. In this section, the binary LLE for the mixtures of dihydroxy alcohols and three imidazolium-based ionic liquids was measured. The dihydroxy alcohols were 1,3-propanediol, 1,4-butanediol, and 1,5-pentanediol and the ionic liquids were 1-ethyl-3-methylimidazolium tetrafluoroborate ($[C_2C_1im][BF_4]$), 1-ethyl-3-methylimidazolium bis(trifluoromethylsulfonyl)imide ($[C_2C_1im][NTf_2]$), and 1-ethyl-3-methylimidazolium 1,1,2,2-tetrafluoroethanesulfonate ($[C_2C_1im][TFES]$).

4.2.2.1. Materials

All chemicals used in the LLE of ILs and diols are listed in Table 4.13. The ILs ($[C_2C_1im][BF_4]$, $[C_2C_1im][BF_4]$, and $[C_2C_1im][TFES]$) and dihydroxy alcohols (1,3-propanediol, 1,4-butanediol, and 1,5-pentanediol) were used in the LLE and/or cloud point measurements. Methanol was used as a reference fluid for volumetric calibration of the test tubes. Anhydrous 2-butanol and high purity water were used to check the experimental method. All chemicals except the ILs were used as received. The ionic liquids were dried and degassed at 323.15 K under a high vacuum (10^{-9} MPa) to remove water and volatile impurities for 24 h to 48 h. After drying, the water content of the ILs was measured using Karl Fischer titration. The water content of the ILs after drying is shown in Table 4.13.

Table 4.13. Description of Materials used in this study

Name	Acronym	CAS Number	Initial Mole Fraction Purity[a]	Water Content ($mg \cdot kg^{-1}$)[b]	Source and Lot Number
1-ethyl-3-methyimidazolium tetrafluoroborate	$[C_2C_1im][BF_4]$	143314-16-3	0.985	249 ± 16	Fluka, Lot no. 1084445
1-ethyl-3-methylimidazolium bis(trifluoromethylsulfonyl)imide	$[C_2C_1im][Tf_2N]$	174899-82-2	0.99	158 ± 34	Iolitec, Lot no. H00620.1
1-ethyl-3-methylimidazolium 1,1,2,2-tetrafluoroethanesulfonate	$[C_2C_1im][TFES]$	880084-63-9	0.99	512 ± 44	Io-li-tec, Lot no. I00113.1.3
Methanol	CH_3OH	67-56-1	0.999	-	Fischer Chemicals, A452-2 4L, Lot no. 170785
2-butanol	-	78-92-2	0.995	179 ± 15	Sigma Aldrich, 294810-100ml, Lot no. SHBJ2337
1,3-propanediol	$C_3(1,3)(OH)_2$	504-63-2	0.98	7143 ± 105	Aldrich, Lot no. STBD6490V
1,4-butanediol	$C_4(1,4)(OH)_2$	110-03-4	0.99	633 ± 16	Sigma-Aldrich, Lot no. MKCD7755
1,5-pentanediol	$C_5(1,5)(OH)_2$	111-29-5	0.98	598 ± 6	Acros Organics, Lot no. A0366238
Water	H_2O	7732-18-5	-	-	Sigma Aldrich, 270733-1L, Lot no. SHBH9984
Apura® Water Standard	-		-	100	EMD, Lot No. HC61276950

[a] The purity is reported by the supplier. [b] The water content was measured with Karl Fischer as described in Section 2.3.1.

4.2.2.2. Liquid-Liquid Equilibria Measurement and Thermodynamic Modeling

The liquid-liquid equilibria for the mixtures of 1,4-butanediol + $[C_2C_1im][BF_4]$, 1,5-pentanediol + $[C_2C_1im][BF_4]$, 1,3-propanediol+ $[C_2C_1im][NTf_2]$, 1,4-butanediol + $[C_2C_1im][NTf_2]$, and 1,5-pentanediol + $[C_2C_1im]$ $[NTf_2]$ were measured at temperatures from 298.15 to 318.15 K and at atmospheric pressure using a volumetric method. The experimental results in this study are reported together with our previous result for 1,3-propanediol + $[C_2C_1im][BF_4]$[56] in Tables 4.14-4.19. The LLE results of the 1,3-propanediol + $[C_2C_1im][BF_4]$ system in Table 4.14 are reproduced here to provide a more thorough discussion while making a comparison with other diol + IL systems. The LLE results show low solubility of ILs in the alcohol and high solubility of alcohols in the ILs. For example, at 298.15 K, the solubility of $[C_2C_1im][BF_4]$ in the 1,4-butanediol-rich phase is 2.2 mol% whereas the solubility of 1,4-butanediol in the $[C_2C_1im][BF_4]$-rich phase (x'_1) is 19 mol %. The equimolar mixtures of 1,3-propanediol, 1,4-butanediol, and 1,5-pentanediol with $[C_2C_1im]$[TFES] have also been investigated and were found to be completely miscible from ~293 to 373 K. This result was surprising, but the miscibility over the range of temperatures measured is likely due to strong hydrogen bonding between the [TFES] anion ($CHF_2CF_2SO_3^-$) and the diols.

The volumetric LLE measurement also provides information about the molar volume and excess molar volume for each liquid phase. Excess molar volume in binary mixtures can be due to the differences in size and shape of the components and/or intermolecular interactions between the components[139,140]. The findings in this study suggest that the presence of the higher IL concentration in the diol-rich phase increases the intermolecular interaction between IL and diol. The choice of the anion impact on excess molar volumes for the upper and lower phases is

inconclusive as the values are similar. However, the excess molar volume for the IL-rich phase appears to be slightly lower for the diol + $[C_2C_1im][NTf_2]$ systems compared to the diol + $[C_2C_1im][BF_4]$ systems. This is rather interesting because the increase in the size of the $[NTf_2^-]$ anion, which in turn corresponds to an increase in free volume, could have been expected to result in a larger negative excess molar volume. Furthermore, the excess molar volume for the diol-rich phase for both the $[C_2C_1im][NTf_2]$ and $[C_2C_1im][BF_4]$ systems are about the same. These results indicate the excess molar volume of diols + ILs system is a complex function of the free volume of the molecules and inter/intramolecular interactions.

For ordinary binary alcohol mixtures, the excess molar volume is generally reported to be 0 ± 2 $cm^3 \cdot mol^{-1}$.[112,141–143] The excess molar volume for 1,3-propanediol, 1,4-butanediol, and 1,5-pentanediol with $[C_2C_1im][BF_4]$ and $[C_2C_1im][NTf_2]$ are slightly larger than those of ordinary solutions. In this study, the relatively large error in certain excess volumes is due to the propagating error measurements, as discussed in Section 2.2.4.

A few comments should be made about the potential degradation of the $[BF_4^-]$ anion. As discussed by Freire et al[144], in the presence of water as a function of temperature, pH, and time, the $[BF_4^-]$ anion can undergo hydrolysis to form hydrofluoric acid (HF). However, in this study, a visual inspection of the sample tubes was made after containing the samples for several months, and no frosting of the glass was detected. Even if minor (ppm) levels of HF are produced, the borosilicate glass tubes would frost (i.e., turn white).[145] In addition to the visual inspection of the glass tubes, the pH of equimolar mixtures of diols and $[C_2C_1im][BF_4]$ have also been measured to confirm the $[BF_4]$ anion has not degraded. Equimolar mixtures of diols and $[C_2C_1im][BF_4]$ were prepared in glass vials under the atmospheric conditions and vigorously mixed at room

temperature. The initial pH of the diols + $[C_2C_1im][BF_4]$ was about 3 which was expected because the pH of neat diol is about 4 and the pH of the $[C_2C_1im][BF_4]$ is about 2. The pH was checked after one week and remained the same indicating again no degradation of the $[BF_4^-]$ anion. Furthermore, even if minor degradation (ppm) of the IL occurs, it would not have any impact on the thermodynamic measurements.[144]

Table 4.14. 1,3 Propanediol (1) + $[C_2C_1im][BF_4]$ (2) System[14,a]

T /K	x'_1	x_1	V' /cm^3·mol^{-1}	V /cm^3 · mol^{-1}	$V^{ex\prime}$ /cm^3·mol^{-1}	V^{ex} /cm^3·mol^{-1}
286.6 ± 0.2	0.238 ± 0.005	0.970 ± 0.002	129.5 ± 0.4	72.5 ± 0.2	-4.7 ± 0.4	-1.9 ± 0.2
287.8 ± 0.2	0.245 ± 0.005	0.970 ± 0.002	129.2 ± 0.4	72.7 ± 0.2	-4.5 ± 0.4	-1.8 ± 0.2
288.2 ± 0.2	0.249 ± 0.004	0.968 ± 0.002	128.9 ± 0.4	72.9 ± 0.2	-4.4 ± 0.4	-1.7 ± 0.2
291.9 ± 0.2	0.309 ± 0.004	0.958 ± 0.002	123.9 ± 0.3	74.7 ± 0.2	-4.9 ± 0.3	-1.0 ± 0.2
298.3 ± 0.2	0.358 ± 0.004	0.945 ± 0.002	120.8 ± 0.3	76.0 ± 1.2	-4.4 ± 0.3	-0.9 ± 1.2
303.3 ± 0.2	0.435 ± 0.003	0.922 ± 0.001	114.6 ± 0.2	77.5 ± 0.2	-4.6 ± 0.2	-1.6 ± 0.1

[a] Combined uncertainties $u_c(x'_1)$, $u_c(x_1)$, $u_c(x'_1)$, $u_c(V')$, $u_c(V)$, $u_c(V^{ex\prime})$ and $u_c(V^{ex})$ are reported at each point next to their corresponding values.

Table 4.15. 1,4-Butanediol (1) + $[C_2C_1im][BF_4]$ (2) System [a]

T /K	x'_1	x_1	V' /cm^3·mol^{-1}	V /cm^3 · mol^{-1}	$V^{ex\prime}$ /cm^3·mol^{-1}	V^{ex} /cm^3·mol^{-1}
298.15	0.190 ± 0.004	0.978 ± 0.003	136.8 ± 0.3	91.8 ± 0.2	-5.4 ± 0.8	1.4 ± 0.6
303.15	0.240 ± 0.007	0.962 ± 0.002	134.6 ± 0.3	92.6 ± 0.2	-4.7 ± 1.3	0.9 ± 0.4
308.15	0.251 ± 0.005	0.957 ± 0.001	134.5 ± 0.3	93.3 ± 0.2	-4.5 ± 0.9	0.9 ± 0.3
313.15	0.326 ± 0.005	0.944 ± 0.002	128.6 ± 0.4	90.4 ± 0.2	-5.9 ± 1.0	-3.1 ± 0.4

[a] Combined uncertainties $u_c(x'_1)$, $u_c(x_1)$, $u_c(x'_1)$, $u_c(V')$, $u_c(V)$, $u_c(V^{ex\prime})$ and $u_c(V^{ex})$ are reported at each point next to their corresponding values.

Table 4.16. 1,5-Pentanediol (1) + $[C_2C_1im][BF_4]$ (2) System [a]

T /K	x'_1	x_1	V' /cm^3·mol^{-1}	V /cm^3 · mol^{-1}	$V^{ex\prime}$ /cm^3·mol^{-1}	V^{ex} /cm^3·mol^{-1}
303.15	0.129 ± 0.005	0.982 ± 0.001	142.3 ± 0.2	106.9 ± 0.4	-6.5 ± 1.0	0.1 ± 0.5
308.15	0.151 ± 0.005	0.977 ± 0.001	141.6 ± 0.2	107.5 ± 0.4	-6.6 ± 1.0	0.1 ± 0.5
313.15	0.183 ± 0.003	0.970 ± 0.001	141.2 ± 0.2	106.2 ± 0.4	-5.8 ± 0.6	-1.8 ± 0.5
318.15	0.231 ± 0.009	0.969 ± 0.001	138.1 ± 0.3	106.4 ± 0.4	-7.0 ± 1.7	-2.0 ± 0.5

[a] Combined uncertainties $u_c(x'_1)$, $u_c(x_1)$, $u_c(x'_1)$, $u_c(V')$, $u_c(V)$, $u_c(V^{ex\prime})$ and $u_c(V^{ex})$ are reported at each point next to their corresponding values.

Table 4.17. 1,3-propanediol (1) + $[C_2C_1im][NTf_2]$(2) System [a]

T /K	x'_1	x_1	V' /cm^3·mol^{-1}	V /cm^3 · mol^{-1}	$V^{ex\prime}$ /cm^3·mol^{-1}	V^{ex} /cm^3·mol^{-1}
298.15	0.208 ± 0.012	0.977 ± 0.001	215.3 ± 0.2	74.8 ± 0.3	-3.8 ± 3.2	-1.9 ± 0.4
303.15	0.226 ± 0.012	0.974 ± 0.001	212.4 ± 0.2	75.5 ± 0.3	-4.1 ± 3.2	-2.0 ± 0.4
308.15	0.234 ± 0.008	0.971 ± 0.002	211.4 ± 0.2	76.1 ± 0.3	-4.3 ± 2.2	-2.2 ± 0.6
313.15	0.259 ± 0.013	0.971 ± 0.007	206.3 ± 0.3	76.0 ± 0.4	-5.4 ± 3.5	-2.5 ± 1.9

[a] Combined uncertainties $u_c(x'_1)$, $u_c(x_1)$, $u_c(x'_1)$, $u_c(V')$, $u_c(V)$, $u_c(V^{ex\prime})$ and $u_c(V^{ex})$ are reported at each point next to their corresponding values.

Table 4.18. 1,4-Butanediol (1) + $[C_2C_1im][NTf_2]$(2) System[a]

T /K	x'_1	x_1	V' /cm^3·mol^{-1}	V /cm^3 · mol^{-1}	$V^{ex\prime}$ /cm^3·mol^{-1}	V^{ex} /cm^3·mol^{-1}
298.15	0.177 ± 0.010	0.971 ± 0.001	225.3 ± 0.2	92.3 ± 0.3	-2.4 ± 2.7	-1.6 ± 0.4
303.15	0.189 ± 0.014	0.968 ± 0.004	224.1 ± 0.3	93.1 ± 0.7	-2.4 ± 3.8	-1.5 ± 1.3
308.15	0.217 ± 0.018	0.962 ± 0.002	220.0 ± 0.3	93.6 ± 0.7	-2.5 ± 4.9	-2.4 ± 0.9
313.15	0.233 ± 0.007	0.958 ± 0.000	218.1 ± 0.2	92.9 ± 0.7	-2.4 ± 1.9	-4.0 ± 0.7

[a] Combined uncertainties $u_c(x'_1)$, $u_c(x_1)$, $u_c(x'_1)$, $u_c(V')$, $u_c(V)$, $u_c(V^{ex\prime})$ and $u_c(V^{ex})$ are reported at each point next to their corresponding values.

Table 4.19. 1,5-Pentanediol (1) + $[C_2C_1im][Tf_2N]$ (2) System[a]

T/K	x'_1	x_1	V' /cm^3·mol^{-1}	V /cm^3 · mol^{-1}	$V^{ex\prime}$ /cm^3·mol^{-1}	V^{ex} /cm^3·mol^{-1}
298.15	0.142 ± 0.016	0.995 ± 0.001	229.7 ± 0.5	107.5 ± 1.8	-6.3 ± 1.8	1.1 ± 4.5
303.15	0.160 ± 0.005	0.992 ± 0.001	225.3 ± 0.5	108.6 ± 1.8	-8.7 ± 1.8	1.5 ± 1.5
308.15	0.175 ± 0.006	0.987 ± 0.002	225.1 ± 0.5	108.8 ± 1.8	-7.5 ± 1.9	0.6 ± 1.8
313.15	0.193 ± 0.003	0.982 ± 0.001	223.9 ± 0.5	109.5 ± 1.8	-6.6 ± 1.8	0.2 ± 1.0

[a] Combined uncertainties $u_c(x'_1)$, $u_c(x_1)$, $u_c(x'_1)$, $u_c(V')$, $u_c(V)$, $u_c(V^{ex\prime})$ and $u_c(V^{ex})$ are reported at each point next to their corresponding values.

Table 4.20. Binary Interaction Parameters

System (1)/(2)	$\tau_{12}^{(0)}$	$\tau_{12}^{(1)}$/K	$\tau_{21}^{(0)}$	$\tau_{21}^{(1)}$/K
1,3-propanediol / $[C_2C_1im][BF_4]$	-3.0630 [a]	1908.25 [a]	-8.1996 [a]	2397.28 [a]
1,4-butanediol / $[C_2C_1im][BF_4]$	-6.9896	3178.58	-5.8727	1849.51
1,5-pentanediol / $[C_2C_1im][BF_4]$	-3.2687	2072.70	-7.1816	2393.01
1,3- propanediol / $[C_2C_1im][NTf_2]$	-2.7340	2003.3	-4.2074	1336.77
1,4-butanediol / $[C_2C_1im][NTf_2]$	-2.5080	1786.6	-2.5717	898.2
1,5-pentanediol / $[C_2C_1im][NTf_2]$	-3.4525	2320.8	-4.6942	1550.98

[a] Data is taken from Reference [56].

The experimental LLE data was correlated with the Non-Random Two Liquids (NRTL) solution model. The non-randomness parameter (α) is assumed to be constant at 0.2. The temperature-dependent binary interaction parameters were modeled using a two-term empirical equation. Temperature-dependent parameters ($\tau_{12}^{(0)}$, $\tau_{12}^{(1)}$, $\tau_{21}^{(0)}$, and $\tau_{21}^{(1)}$) were determined by evaluating the volumetric temperature-composition data at a given equilibrium condition ($\gamma_i^I x_i^I = \gamma_i^{II} x_i^{II} (i =$

1,2)) (Table 4.20). The binary interaction parameters were obtained, and the entire *T-x* diagram was calculated using the regressed binary interaction parameters for each system. The absolute average deviation between the experiment and the model was less than 1 mol % in all cases. Figures 4.37 and 4.38 show the *T-x* diagram of dihydroxy alcohols with $[C_2C_1im][BF_4]$ and $[C_2C_1im][NTf_2]$, respectively. The UCST was measured for each system using the cloud point method, and the results are summarized in Table 4.21.

Table 4.21. Upper Critical Solution Temperature (UCST) and composition

System (1) / (2)	UCST (K)	x_1
1,3-propanediol / $[C_2C_1im][BF_4]$	308.2 [a]	0.701 [a]
1,4-butanediol / $[C_2C_1im][BF_4]$	327.5	0.702
1,5-pentanediol / $[C_2C_1im][BF_4]$	344.8	0.674
1,3- propanediol / $[C_2C_1im][NTf_2]$	354.7	0.703
1,4-butanediol / $[C_2C_1im][NTf_2]$	341.2	0.503
1,4-butanediol / $[C_2C_1im][NTf_2]$	352.6	0.701
1,5-pentanediol / $[C_2C_1im][NTf_2]$	361.1	0.750

[a] The data is taken from Reference [56], and the standard uncertainty on the UCST is reported $u(T) = 2$ K. The standard uncertainty on the UCST in this study $u(T) = 1$ K.

As can be seen from Figures 4.37 and 4.38, all diol + IL systems exhibit an UCST, which means the solubility of the IL in the alcohols increased with an increase in temperature up to the UCST above, which the two components become completely miscible. The existence of the UCST has also been verified by cloud point measurements. The NRTL model results based on the LLE are in excellent agreement with the UCST measurements, as shown in Figures 4.37 and 4.38. The longer the length of the alkyl chain for the diol resulted in higher UCST for both $[C_2C_1im][BF_4]$ as shown in Figure 4.37 and $[C_2C_1im][NTf_2]$ as shown in Figure 4.38 which may be due to an

increase in intermolecular interactions (hydrogen bonding, dipolar, or columbic forces).[50] Figures 4.37 and 4.38 also illustrate that the miscibility of 1,3-propanediol, 1,4-butanediol, and 1,5-pentanediol with $[C_2C_1im][BF_4]$ and $[C_2C_1im][NTf_2]$ decreases with an increase in the length of the alkyl chain for the diols.

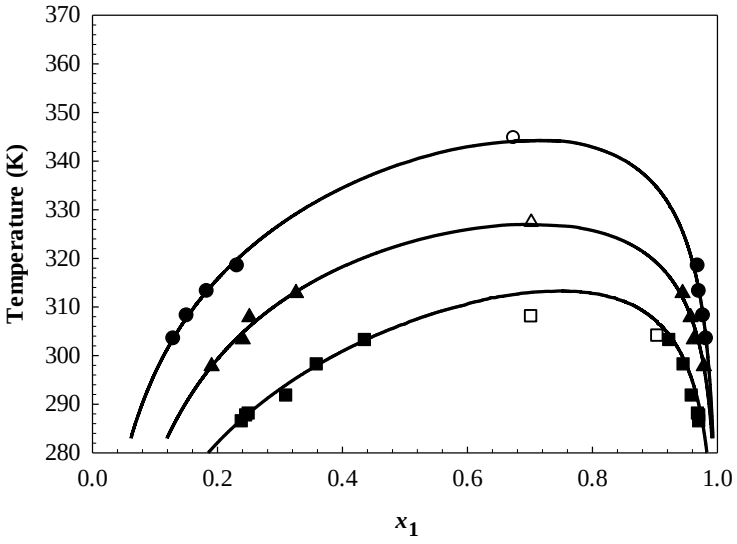

Figure 4.37. Temperature-Composition Diagram of dihydroxy alcohols (1) and $[C_2C_1im][BF_4]$ (2) mixtures. Solid symbols represent experimental LLE measurements: ■, 1,3-propanediol + $[C_2C_1im]$ $[BF_4]$ (Shiflett and Yokozeki[56]); ▲, 1,4-butanediol + $[C_2C_1im][BF_4]$; ●, 1,5-pentanediol + $[C_2C_1im][BF_4]$. Empty symbols represent experimental cloud point measurements: □, 1,3-propanediol + $[C_2C_1im][BF_4]$ (Shiflett and Yokozeki[56]); Δ, 1,4-butanediol + $[C_2C_1im]$ $[BF_4]$; ○, 1,5-pentanediol + $[C_2C_1im][BF_4]$. Solid lines represent the NRTL model.

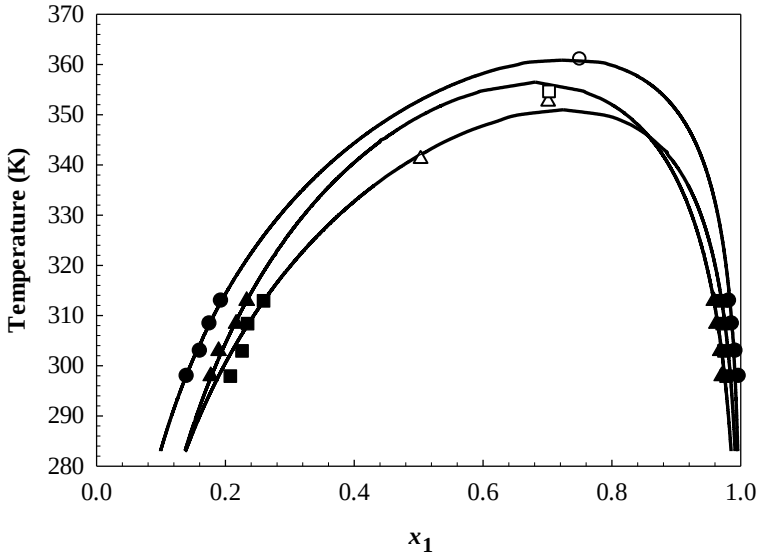

Figure 4.38.Temperature-Composition Diagram of dihydroxy alcohols (1) and $[C_2C_1im][NTf_2]$ (2) mixtures. Solid symbols represent experimental LLE measurements: ■, 1,3-propanediol + $[C_2C_1im][NTf_2]$; ▲, 1,4-butanediol + $[C_2C_1im][NTf_2]$; ●, 1,5-pentanediol + $[C_2C_1im][NTf_2]$. Empty symbols represent experimental cloud point measurements: □, 1,3- propanediol + $[C_2C_1im][NTf_2]$; Δ, 1,4-butanediol + $[C_2C_1im][NTf_2]$; ○ , 1,5-pentanediol + $[C_2C_1im][NTf_2]$. Solid lines represent the NRTL model.

The type of anion also had a significant impact on miscibility behavior. Figures 4.39, 4.40, and 4.41 demonstrate the miscibility of 1,3-propanediol, 1-4, butanediol, and 1,5-pentanediol in $[C_2C_1im][BF_4]$ and $[C_2C_1im][NTf_2]$ with the same cation $[C_2C_1im]$. Makowska et al. also reported that the miscibility of dihydroxy alcohols such as 1,2-ethanediol, 1,2-propanediol, and 1,3-propanediol with a similar cation $[C_4C_1im]$. In both cases, the ionic liquids with the $[BF_4^-]$ anion have a lower UCST (i.e., smaller immiscibility gap) compared with the $[NTf_2^-]$ anion (i.e., larger immiscibility gap).[12] However, it is important to point out that this is contrary to monohydroxy alcohols where the miscibility (i.e., alcohol affinity) was observed to follow:

[NTf_2^-] > [BF_4^-] > [PF_6^-], which is attributed to increased hydrogen bonding between the anion and 1-butanol [47].

The results obtained in this study are also compared with Trindade et al.[16] and Forte et al.[14] (same research group) who measured the LLE behavior for mixtures of 1,3-propanediol + [C_2C_1im][NTf_2] and 1,4-butanediol + [C_2C_1im][NTf_2], respectively. In both cases, their visual measurements are 1 to 10 K lower than our NRTL calculations, which are based on LLE measurements and confirmed by UCST measurements. We believe the visual observation technique (i.e., cloud point measurement) for the phase separation should not be used solely, but rather a combination of LLE and UCST measurements and NRTL modeling is preferable in order to check the consistency of the results.

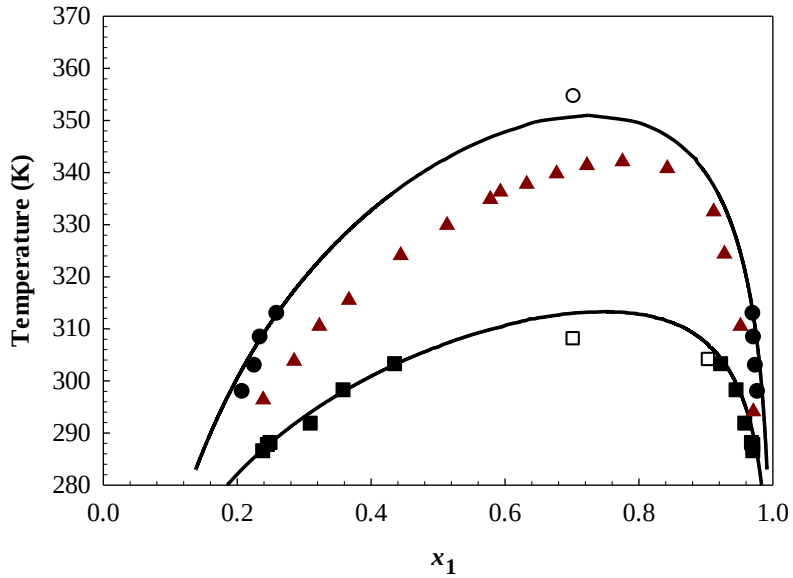

Figure 4.39. Temperature-Composition Diagram of 1,3-propanediol (1) and imidazolium-based ionic liquids (2). Solid symbols represent experimental LLE measurements: ●, 1,3-propanediol + [C_2C_1im][NTf_2] (this study); ▲, 1,3-propanediol + [C_2C_1im][NTf_2] (Trindade et al[57]) ■, 1,3-propanediol + [C_2C_1im][BF_4] (this study). Empty symbols represent experimental cloud point

measurements: ○, 1,3-propanediol + [C_2C_1im][NTf_2]; □, 1,3-propanediol + [C_2C_1im][BF_4]. Solid lines represent the NRTL model.

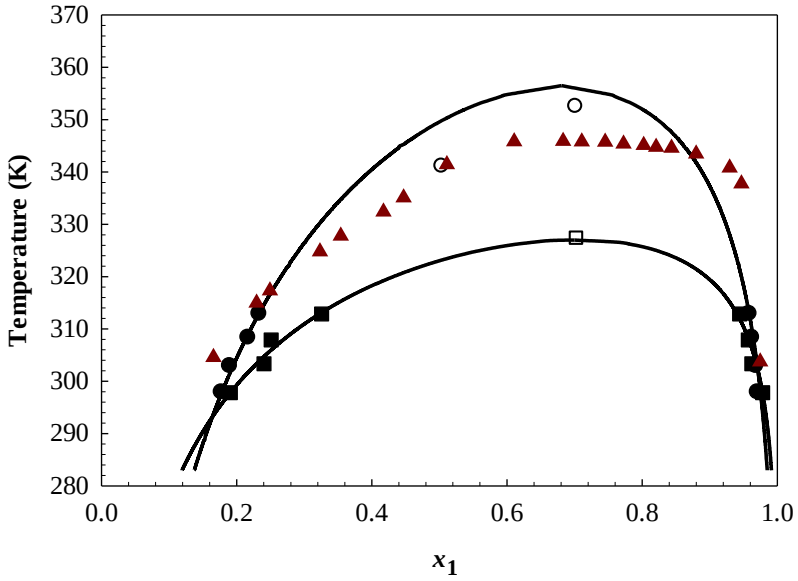

Figure 4.40. Temperature-Composition Diagram of 1,4-butanediol (1) and imidazolium-based ionic liquids (2). Solid symbols represent experimental measurements: ●, 1,4-butanediol + [C_2C_1im][NTf_2] (this study); ▲, 1,4-butanediol + [C_2C_1im][NTf_2] (Forte et al[55]); ■, 1,4-butanediol + [C_2C_1im][BF_4] (this study). Empty symbols represent experimental cloud point measurements: ○, 1,4-butanediol + [C_2C_1im][NTf_2]; □, 1,4- butanediol + [C_2C_1im][BF_4]. Solid lines represent NRTL model.

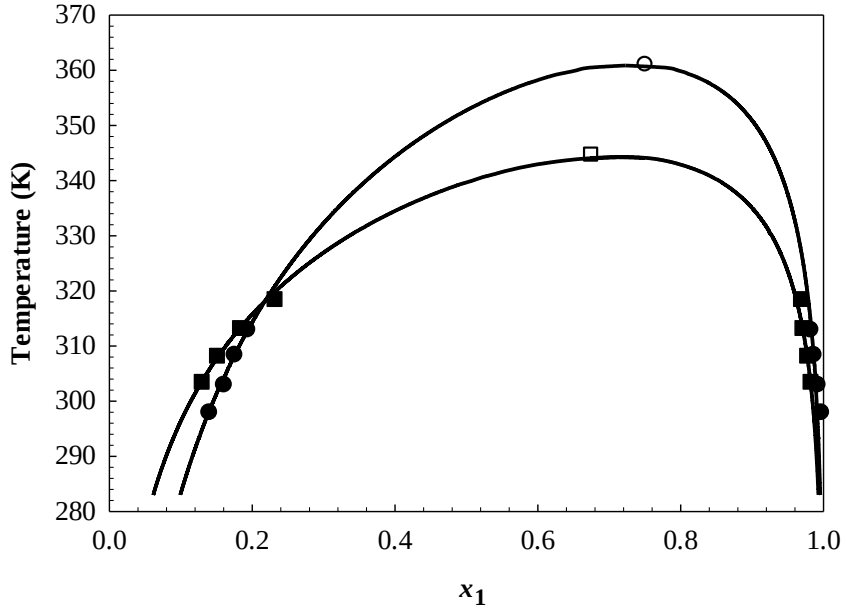

Figure 4.41. Temperature-Composition Diagram of 1,5-pentanediol (1) and imidazolium-based ionic liquids (2). Solid symbols represent experimental LLE measurements: ●, 1,5-pentanediol + $[C_2C_1im][NTf_2]$; ■, 1,5-pentanediol + $[C_2C_1im][BF_4]$. Empty symbols represent experimental cloud point measurements: ○, 1,5-pentanediol + $[C_2C_1im][NTf_2]$; □, 1,5-propanediol + $[C_2C_1im][NTf_2]$. Solid lines represent the NRTL model for this study.

Chapter 5. Gas Absorption Kinetics

"If you know you are on the right track, if you have this inner knowledge, then nobody can turn you off, no matter what they say."

Barbara McClintock,

Cytogeneticist and winner of the 1983 Nobel Prize in Physiology or Medicine

As discussed in the previous sections, the knowledge of the solubility of gases in the ILs at various temperatures and pressures is fundamentally important for various applications. In addition to the thermodynamics of the binary IL systems, the rate of gas dissolution in ILs also comes into prominence for potential use in industrial applications as the viscosity of ILs is usually one to three orders of magnitude higher than most traditional solvents.[146] Therefore, in this chapter, the diffusivity of ammonia and carbon dioxide in ILs is measured and calculated.

5.1. Fickian Diffusion of Gases in Ionic Liquids

As described in Chapter 2, IGA and XEMIS gravimetric microbalances are utilized to measure the equilibrium gas concentrations in ILs. In addition to thermodynamic equilibrium concentrations, the microbalances can be utilized to analyze the time-dependent behavior of gas dissolution in ILs. During a typical isothermal microbalance experiment, the ionic liquid is evacuated followed by the introduction of the gas to be absorbed. Eventually, after enough time, the amount of gas dissolved in the IL reaches a constant value, which indicates a thermodynamic equilibrium at a given T and P. During the gas dissolution process, the amount of gas dissolved in the IL is recorded as a function of time starting from gas admittance to the end of the experiment at equilibrium. This time-dependent behavior of gas dissolution can be analyzed with a simplified

Fickian diffusion model developed by Shiflett and Yokozeki.[136] In this simplified model, the following assumptions are made:[67,136]

(i) the gas dissolves through a one-dimensional (vertical) diffusion process, and there is no convective flow in the liquid as depicted in Figure 5.1.

(ii) the interaction between gas and IL is physical,

(iii) a thin boundary layer between the IL and gas-phase exist, and the layer reaches a saturation concentration (C_s) at any given temperature and pressure (Boundary Condition 1),

(iv) temperature and pressure are constant (experimental design),

(v) the gas-IL solution is dilute, and the thermophysical properties are constant at a given *T* and *P* condition,

(vi) gas does not penetrate through the Pyrex® cup (Boundary Condition 2).

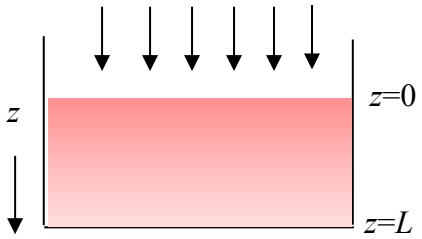

Figure 5.1. Schematic of a sample cup used in this study. Pink block represents an ionic liquid sample. The arrows demonstrate the direction of gas absorption.

Assumptions (*i*)-*(vi)* lead to the dissolution of gas in the IL for one dimensional (1D) mass diffusion due to the local concentration difference:

$$D\,\frac{\partial^2 C}{\partial z^2} = \frac{\partial C}{\partial t} \tag{5.1}$$

where *C* is the concentration of gas in IL, *t* is the time, *z* is the vertical location, and *L* is the depth of IL in the sample container. In this study, the depth (*L*) is estimated from the solution mass, the dimension of the sample cup, and the weight fraction averaged density of the solution at initial and final composition for a given *T* and *P*. Equation (5.1) can be analytically solved using a separation of variables technique and applying the proper initial and boundary conditions (Equation (5.2-5.4)), to obtain the concentration profile in the *z*-direction (Equation 5.5).[67,136]

Initial Condition:	t = 0	$0 < z < L$	$C = C_o$	(5.2)
Boundary Condition 1:	t > 0	$z = 0$	$C = C_s$	(5.3)
Boundary Condition 2:	t > 0	$z = L$	$\frac{\partial C}{\partial z} = 0$	(5.4)

$$C = C_s \left[1 - 2\left(1 - \frac{C_o}{C_s}\right)\sum_{n=0}^{\infty} \frac{\exp(-\lambda_n^2 Dt)\sin\lambda_n z}{L\,\lambda_n}\right] \tag{5.5}$$

Equation (5.5) shows the concentration profile in direction *z*. On the other hand, the concentration obtained in the microbalance is the average concentration at a given time, not the concentration profile in *z*; therefore, the concentration profile (Equation 5.5) is space averaged (Equation 5.6) to obtain the average concentration at a given time (Equation 5.7):

$$< C >= \int_0^L \frac{C}{L}\, dz \tag{5.6}$$

$$< C >= C_s \left[1 - 2\left(1 - \frac{C_o}{C_s}\right)\sum_{n=0}^{\infty} \frac{\exp(-\lambda_n^2 Dt)}{L^2\,\lambda_n^2}\right] \tag{5.7}$$

where $\lambda_n = [n+ (1/2)](\pi/L)$; $< C >$ is an average gas concentration in the liquid mixture at given temperature and pressure; C_0 and C_s are the initial and saturation concentrations of a liquid mixture, respectively; and L is the liquid depth of the solution in the sample container. Although Equation 5.7 has an infinite summation term, only the first few terms are required for most analysis, and the summation term was terminated when the numerical contribution is infinitely small. At any given T and P, the experimentally measured concentration as a function of time can be fit using Equation 5.7 to obtain D and C_s. The effective D value at each P for a given isotherm was obtained by averaging the calculated D obtained using a constant height of the solution at initial (C_0) and final (C_s, saturation) compositions. The analysis of Equation 5.7 requires nonlinear regression analysis. A MATLAB® code was developed (Appendix C) to solve Equation 5.7.

5.1.1. Diffusivity of Ammonia in Ionic Liquids

The time-dependent behavior of NH_3 diffusion into imidazolium-based ILs was measured using the XEMIS gravimetric microbalance. The results for C_s and D for NH_3 + $[C_4C_1im][PF_6]$, NH_3 + $[C_4C_1im][BF_4]$, NH_3 + $[C_2C_1im][NTf_2]$, and NH_3 + $[C_2C_1im][TFES]$ systems were summarized in Appendices A1, A2, A3, and A4, respectively. The effective D for each system as a function of temperature are summarized in Table 5.1. As expected, the diffusivity of NH_3 in $[C_4C_1im][PF_6]$, $[C_4C_1im][BF_4]$, and $[C_2C_1im][NTf_2]$ increases with an increase in temperature as the viscosity of the solution decreases. However, at constant T, the pressure dependence of D is rather weak compared to temperature.

Table 5.1. Average effective diffusion coefficients for NH_3 in $[C_4C_1im][PF_6]$, $[C_4C_1im][BF_4]$, and $[C_2C_1im][NTf_2]$ systems

	Diffusivity (x 10^{-10} $m^2 \cdot s^{-1}$)[a]			
Ionic Liquid	T = 283.15 K	T = 298.15 K	T = 323.15 K	T = 348.15 K
$[C_4C_1im][PF_6]$	1.9 ± 0.13	3.1 ± 0.07	4.0 ± 0.04	7.1 ± 0.22
$[C_4C_1im][BF_4]$	1.8 ± 0.09	3.3 ± 0.13	4.8 ± 0.05	6.0 ± 0.26
$[C_2C_1im][NTf_2]$	2.8 ± 0.25	5.2 ± 0.16	8.5 ± 0.65	18.3 ± 2.1
$[C_2C_1im][TFES]$	1.0 ± 0.20	0.5 ± 0.05	2.0 ± 0.14	2.1 ± 2.4

[a] The uncertainties are due to the random errors as a result of mass measurement in the balance and systematic error as a result of the change in L.

The diffusivity of NH_3 in $[C_2C_1im][TFES]$ is rather inconclusive. First, the D of NH_3 in $[C_2C_1im][TFES]$ is significantly lower than the D of NH_3 in $[C_4C_1im][PF_6]$, $[C_4C_1im][BF_4]$, and $[C_2C_1im][NTf_2]$. Since $[C_2C_1im][TFES]$ and $[C_2C_1im][NTf_2]$ are chemically similar in nature, one would expect similar D values. Furthermore, the change in D with a change in T is also unexpected and inconsistent. For example, the D of NH_3 in $[C_2C_1im][TFES]$ at 283.15 K is almost three times slower than the D of NH_3 in $[C_2C_1im][TFES]$ at 298.15 K. This is an unexpected observation because both an increase in T and NH_3 dissolution would cause a decrease in the viscosity of the mixture resulting in increased the average D of NH_3 in $[C_2C_1im][TFES]$ at 298.15 K while compensating for the slightly lower gas dissolution at higher temperature. In fact, the average D of NH_3 in $[C_2C_1im][TFES]$ at 323.15 and 348.15 K is higher compared to the average D of NH_3 in $[C_2C_1im][TFES]$ at 323.15 and 348.15 K. The question is why the D results are inaccurately predicted while the D of NH_3 in the other three imidazolium-based ILs have been predicted well.

One reason might be that the thermophysical properties of $[C_2C_1im][TFES]+NH_3$ may be insufficiently predicted (under- or over-) ,consequently, resulted in relatively inaccurate *D* values. One way to analyze the impact of the thermophysical properties might be to compare the momentum diffusivity and mass diffusivity. Assuming dilute concentration, the Schmidt number is calculated for the four ionic liquid systems using the pure viscosity and density of ionic liquids at 298.15 K. The Schmidt number is then plotted against the kinematic viscosity of the ILs at 298.15 K. As seen in Figure 5.2, the Schmidt number of $[C_4C_1im][PF_6]$, $[C_4C_1im][BF_4]$, and $[C_2C_1im][NTf_2]$ has shown linear relation with their corresponding kinematic viscosity at 298.15 K. However, the $[C_2C_1im][TFES]$ is an outlier due to extremely low *D* calculates. If the linear correlation between the Schmidt number and the kinematic viscosity holds true for $[C_2C_1im][TFES]$ system, then the *D* of NH_3 in $[C_2C_1im][TFES]$ can be predicted using the kinematic viscosity of $[C_2C_1im][TFES]$. Then, the *D* of NH_3 in $[C_2C_1im][TFES]$ should be estimated faster than the *D* of NH_3 in $[C_4C_1im][PF_6]$ and $[C_4C_1im][BF_4]$, and closer to the *D* of NH_3 in $[C_2C_1im][NTf_2]$. In fact, when the *D* of NH_3 in $[C_2C_1im][TFES]$ is calculated using the linear correlation at 298.15 K, the estimated *D* of NH_3 in $[C_2C_1im][TFES]$ (4.82×10^{-10} $m^2 \cdot s^{-1}$) is higher than the *D* of NH_3 in $[C_4C_1im][PF_6]$ and $[C_4C_1im][BF_4]$, and closer to the *D* of NH_3 in $[C_2C_1im][NTf_2]$. These results indicate that the diffusivity of NH_3 in $[C_2C_1im][TFES]$ might be properly modeled using the mass-based mass balance equation with direct inclusion of the density in the mass balance equations due to the impact of the density of the $[C_2C_1im][TFES]$ on the *D* results. In addition to the findings here, the NMR results in Chapter 6 clearly showed that the interaction of $[C_2C_1im][TFES]$ with NH_3 is different than the rest of the imidazolium-based ILs. Similarly, later discussed in this chapter, the interaction of $[C_2C_1im][TFES]$ with diols is also

unique such that it has shown complete miscibility, whereas the other ionic liquids have shown a miscibility gap. Surely, [C_2C_1im][TFES] also demonstrates quite a unique interaction with other substances.

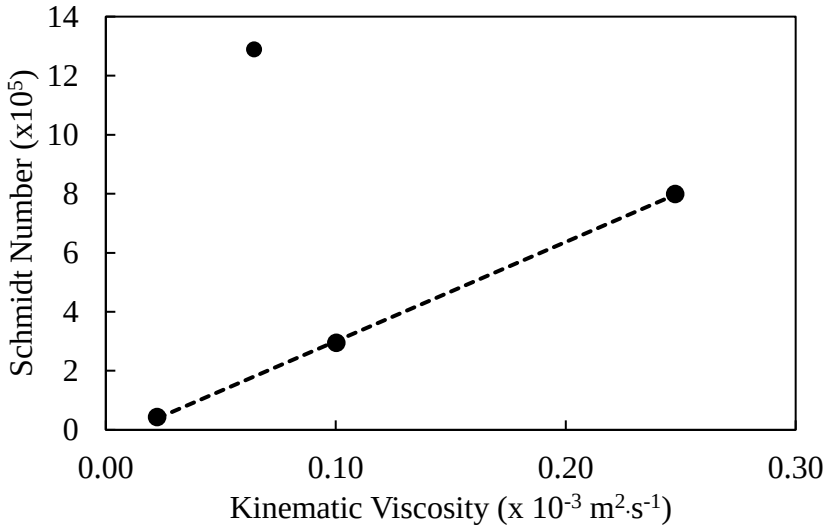

Figure 5.2. The Schmidt Number change with the kinematic viscosity of imidazolium-based ILs

Another parameter determined in the diffusion analysis is that the NH_3 solubility (C_s). The difference between the experimental solubility and model C_s values was less than ~1 mole % for all systems, which indicates the model reasonably predicts the C_s. A few comments also should be made regarding the D values. Contrary to the main assumptions of the model, the NH_3 + IL mixtures cannot be considered as a dilute solution, and consequently, the diffusion coefficients can depend on the concentration. In reality, the thermophysical properties of the mixture change upon gas dissolution, and L varies with the amount of gas dissolved in the IL. Even though the impact on the concentration is indirectly applied, the analyzed diffusion coefficients must be regarded as "effective" or "apparent" diffusion coefficients when we apply the present model.

A key finding in this part of the study is that the diffusivity of NH_3 in imidazolium-based ILs is lower than the diffusion of NH_3 in water. For example, the diffusivity of $[C_4C_1im][PF_6]$, $[C_4C_1im][BF_4]$, and $[C_2C_1im][NTf_2]$ is about 3 to 5 times lower than the diffusion of NH_3 in water such that the diffusivity of NH_3 in water at 298.15 K is 16 x 10^{-10} $m^2 \cdot s^{-1}$ [147] whereas the diffusivity of NH_3 in $[C_4C_1im][PF_6]$, $[C_4C_1im][BF_4]$, and $[C_2C_1im][NTf_2]$ at 298.15 K is 3.1 x 10^{-10}, 3.3 x 10^{-10}, and 5.2 x 10^{-10} $m^2 \cdot s^{-1}$, respectively.

Table 5.2. Diffusivity of CO_2 in 1-alkyl-1-methyl pyrrolidinium bis (trifluoromethyl-sulfonyl)imide ionic liquids ($[C_nC_1pyr][NTf_2]$ (n = 3,4,6))

		Diffusivity (D) (x10^{-10} m^2/s)					
T(K)[a]	P (MPa)[a]	$[C_3C_1pyr][NTf_2]$		$[C_4C_1pyr][NTf_2]$		$[C_6C_1pyr][NTf_2]$	
		D	$u_c(D)$[b]	D	$u_c(D)$[b]	D	$u_c(D)$[c]
298.15	0.1000	1.3	0.1	1.3	0.1	1.6	0.1
	1.0000	1.8	0.3	1.6	0.2	2.4	0.3
	2.0000	2.4	0.4	3.0	0.9	4.0	1.1
318.2	0.1000	2.7	0.1	2.2	0.1	2.3	0.1
	1.0000	3.0	0.3	2.9	0.3	3.8	0.4
	2.0000	3.7	0.8	3.3	0.7	3.8[b]	0.7

[a] The standard uncertainties of temperature u(T) = 0.01 K and pressure u(P) = 0.0008 MPa
[b] Combined standard uncertainty estimated on diffusivity analysis.
[c] This value is reported at 1.8 MPa as the D value could not be calculated due to scattered data.

5.1.2. Diffusivity of Carbon dioxide in Ionic Liquids

The time-dependent behavior of gas diffusion into ILs was also measured using the IGA gravimetric microbalance. In this study, the diffusivity of CO_2 in pyrrolidinium-based ILs was calculated from the analysis of time-dependent absorption data using Equation (5.7) as described in Section 5.1. The proper analysis of D requires buoyancy and volume expansion corrections on mass data obtained in the balance at each time point, and consequently, makes the analysis rigorous. Therefore, D values are only calculated herein at pressures of 0.1, 1, and 2 MPa and at 298.15 and 318.15 K for $[C_nC_1pyr][NTf_2]$ (n = 3,4,6), and reported in Table 5.2.

Table 5.3. Diffusivity Data Averaged over Pressures (0.1-2 MPa) for the CO_2 and 1-alkyl-1-methyl pyrrolidinium bis(trifluoromethylsulfonyl)imide ionic liquids ($[C_nC_1pyr][NTf_2]$ (n = 3,4,6))

Ionic Liquid	Diffusivity (D) ($x10^{-10}$ $m^2 \cdot s^{-1}$)			
	T = 298.15 K		T = 318.15 K	
	D	u_c(D)[a]	D	u_c(D)[a]
$[C_3C_1pyr][NTf_2]$	1.8	0.4	3.1	0.4
$[C_4C_1pyr][NTf_2]$	1.9	0.4	2.8	0.4
$[C_6C_1pyr][NTf_2]$	2.7	0.5	3.3	0.4

u_c(D) is the combined standard uncertainty.

The kinetic profile of the CO_2 absorption in $[C_3C_1pyr][NTf_2]$, $[C_4C_1pyr][NTf_2]$, and $[C_6C_1pyr][NTf_2]$ at 298.15 K are provided as examples in Figure 5.3. The *D* at 338.15 K were not calculated as the relatively fast CO_2 absorption during the pressure ramp made the analysis unreliable. The temperature dependence of effective *D* for CO_2 in $[C_nC_1pyr][NTf_2]$ (n = 3,4,6) are summarized in Table 5.3. As can be seen in Table 5.3, the increase in *T* increases diffusion of CO_2 in $[C_nC_1pyr][NTf_2]$ (n = 3,4,6) as expected. On the other hand, due to the overlapped error bars, reaching a conclusion about the impact of the cation alkyl chain length on *D* results is difficult; however, in general, the average effective diffusivity appears to be faster with an increase in the length of the alkyl chain at any given *T* and *P*. The diffusivity for CO_2 in pyrrolidinium ILs with $[NTf_2]$ anion is found to be within the same order of magnitude but slightly lower than the diffusivity of CO_2 in imidazolium-based ionic liquids with the $[NTf_2]$ anion. For example, Hou and Boltus reported the diffusivity of CO_2 in $[C_4C_1im][NTf_2]$[133] at 298.15 K was (7.8 ± 1.0) x 10^{10} $m^2 \cdot s^{-1}$ whereas the diffusivity of CO_2 in $[C_4C_1pyr][NTf_2]$ at 298.15 K was (1.9 ± 0.1) x 10^{-10} $m^2 \cdot s^{-1}$ in this study. This result is reasonable as pyrrolidinium- based ILs have higher viscosities compared to imidazolium-based ILs.

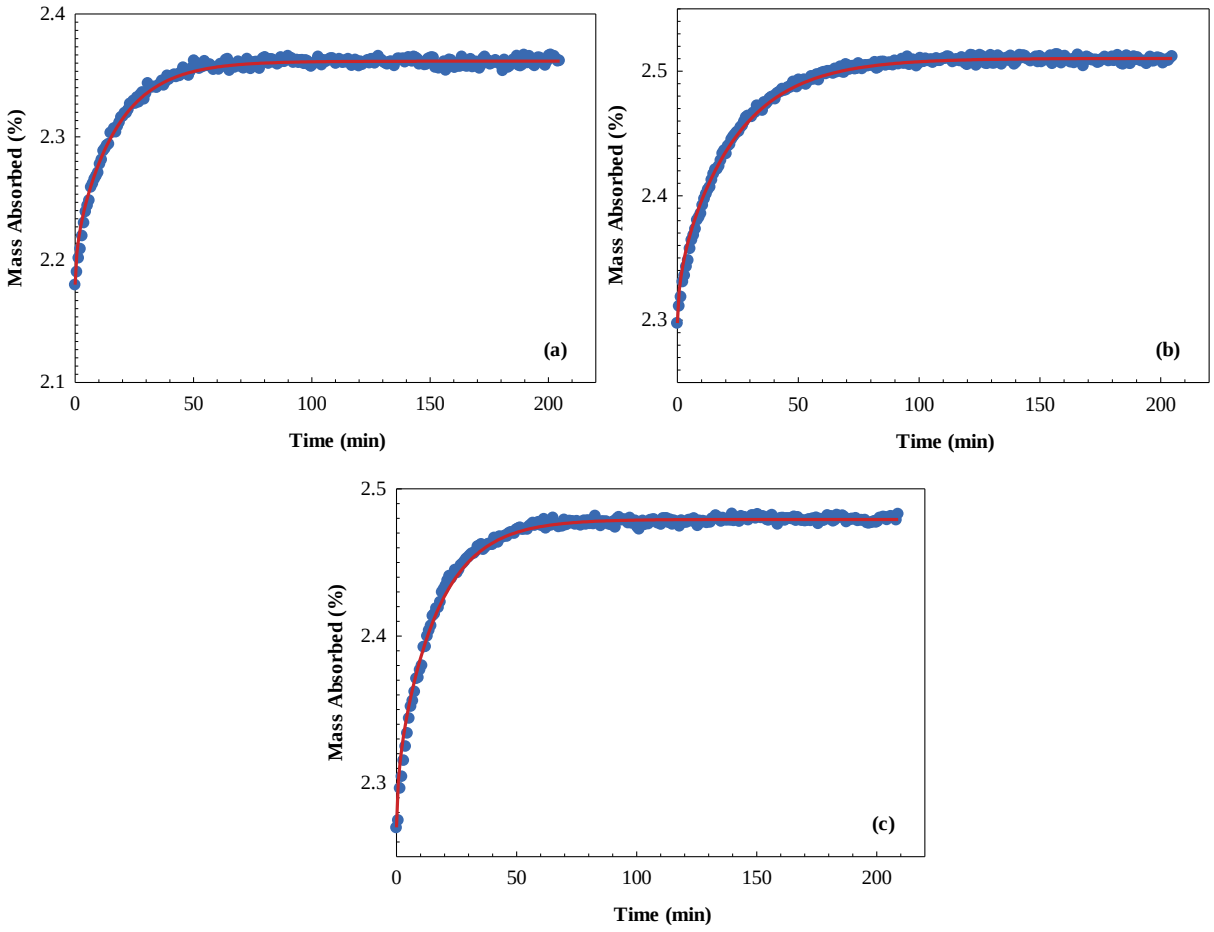

Figure 5.3. Kinetic CO_2 absorption in (a) [C_3C_1pyr][NTf_2], (b) [C_4C_1pyr][NTf_2], and (c) [C_6C_1pyr][NTf_2] with respect to time at 298.15 K. Symbol represent the experimental data and solid line represents the calculation with 1D kinetic model parameters reported in Table 5.2.

5.3. Stokes-Einstein Model

When a solute sphere (with radius r_A) moves through a continuum fluid, Stokes-Einstein equation correlates the diffusion coefficient (D_{AB}) and the viscosity of solvent (μ_B) assuming the diffusing particle is perfectly spherical where *k* is the Boltzmann constant and *T* is the temperature:

$$D_{AB} = \frac{kT}{6\,\pi\, r_A\, \mu_B} \tag{5.8}$$

An empirical correlation for diffusivity of gases was developed using a semi-theoretical Stokes-Einstein equation[67]:

$$D = \frac{kT}{6\pi r \mu_o (\mu/\mu_o)^b} \tag{5.9}$$

The linearized form of Equation (5.9) can be written as:

$$\ln(D/T) = a - b\ln(\mu/\mu_o) \tag{5.10}$$

where D is diffusivity ($m^2\ s^{-1}$), k is Boltzmann constant, T is temperature (K), μ_o is a unit viscosity (1 mPa·s) that is used as a normalization factor to have a proper dimension in the equation. $a = \ln(k/6\pi r\mu_o)$ and b are the adjustable parameters.

The mixture viscosity for an N-component solution can be estimated using the following model[67]:

$$\ln(\mu/\mu_o) = \sum_{i=1}^{N} \xi_i \ln(\mu_i/\mu_o) \tag{5.11}$$

where

$$\xi_i = M_i^c\ x_i / \sum_{i=1}^{N} M_i^c\ x_i \tag{5.12}$$

and M_i is the molecular weight of the ith species. The model has three empirical adjustable parameters (a, b, and c) to correlate the observed diffusivity data. The dynamic viscosity of a pure compound i is modeled as:

$$\ln(\mu_i) = A_i + \frac{B_i}{T} + C_i\,T + D_i T^2 \tag{5.13}$$

The coefficients for NH_3, $[C_4C_1im][PF_6]$, $[C_4C_1im][BF_4]$, $[C_2C_1im][NTf_2]$, and $[C_2C_1im][TFES]$ in Equation (5.13) are provided in Table 5.4.

Table 5.4. Coefficients for Equation (5.13)[a]

Compound i	A_i	B_i (K)	C_i (K^{-1})	D_i (K^{-2})
NH_3[b]	-5.130771	922.2	0	0
$[C_4C_1im][PF_6]$[c]	-182.774	24992.4	4.84019×10^{-1}	-4.44779×10^{-4}
$[C_4C_1im][BF_4]$[c]	-149.99	20757.8	3.91576×10^{-1}	-3.55363×10^{-4}
$[C_2C_1im][NTf_2]$[d]	-60.707	9364.9	1.49780×10^{-1}	-1.33200×10^{-4}
$[C_2C_1im][TFES]$[e]	41.72	0.000323	-2.03×10^{-1}	2.6078×10^{-4}

[a]Viscosity in mPa.s (or cP), and T in K. [b] Parameters obtained using linear fitting of viscosity data from Ref [73]. [c]Parameters are taken from Ref [148] [d] Parameters obtained using linear fitting of viscosity data from Ref [149]. [e] Parameters obtained using linear fitting of viscosity data from Ref[122].

The diffusivity of NH_3 in the ILs was correlated using this generalized form of the Stokes-Einstein equation. The adjustable parameters (*a*, *b*, and *c*) were obtained using non-linear regression, which is summarized in Table 5.4. The empirical parameter *a* consists of the physical parameter which is the radius of the diffusing solute. Therefore, the radius of NH_3 is calculated using the interaction parameter *a*. If the model is physically meaningful, the radius of NH_3 obtained using this model should be close to the molecular radius of NH_3 (or at least the same order of magnitude). Indeed, *r* in $[C_4C_1im][PF_6]$ = 0.127 nm, *r* in $[C_4C_1im][BF_4]$ = 0.165 and *r* in $[C_2C_1im][NTf_2]$ = 0.111 nm are remarkably close to the molecular radius of NH_3 (0.182 nm)[150]. The model calculations for NH_3 in $[C_4C_1im][PF_6]$, NH_3 in $[C_4C_1im][BF_4]$, and NH_3 in $[C_2C_1im][NTf_2]$ are compared with experimental diffusivity data in Figures 5.4, 5.5, and 5.6. The model calculations are in good agreement with a maximum error of less than 5 %. The model results for NH_3 in $[C_2C_1im][TFES]$ showed a very high deviation from experimental results, which

is also physically meaningless. The Stokes-Einstein results for the other three imidazolium-based ILs showed that the NH_3 molecules do not cluster while dissolving in the ILs. Therefore, assuming this observation would hold true for NH_3+ $[C_2C_1im][TFES]$ system, the Stokes-Einstein equation can be still used to approximate the *D* of NH_3 in $[C_2C_1im][TFES]$, excluding the experimental *D* values. The regression would be based on the viscosity of the solution, and the estimated experimental parameters (*a, b,* c), which would be estimated in a range that would give physically meaningful results (i.e., *r* of NH_3=0.182 nm). The approximated *D* of NH_3 in $[C_2C_1im][TFES]$ has been shown in Figure 5.7.

The results show that the modified form of the Stokes-Einstein equation[67]**,** along with the viscosity model, can be used to correlate the diffusion of NH_3 in imidazolium-based ILs. However, the Stokes-Einstein analysis is sensitive to the solution viscosity; therefore, experimental measurement of thermophysical properties (i.e., viscosity) of NH_3 + IL mixtures, which is not present in the literature, would more accurately validate the results.

Table 5.5. Determined Parameters for Equation (5.11) and (5.12)

System	*a* $(ln\ m^2 \cdot s^{-1} \cdot K^{-1})$	*b* $(ln\ m^2 \cdot s^{-1} \cdot K^{-1})$	*c*	*Radius* *(nm)*
NH_3 + $[C_4C_1im][PF_6]$	-25.880± 0.186	0.466 ± 0.046	0.502 ± 0.029	0.127 ± 0.024
NH_3 + $[C_4C_1im][BF_4]$	-26.142 ± 0.253	0.504 ± 0.095	0.438 ± 0.034	0.165 ± 0.042
NH_3 +$[C_2C_1im][NTf_2]$	-25.742 ± 0.240	0.458 ± 0.093	0.899 ± 0.021	0.111 ± 0.027

Errors are the standard uncertainty obtained in regression analysis.

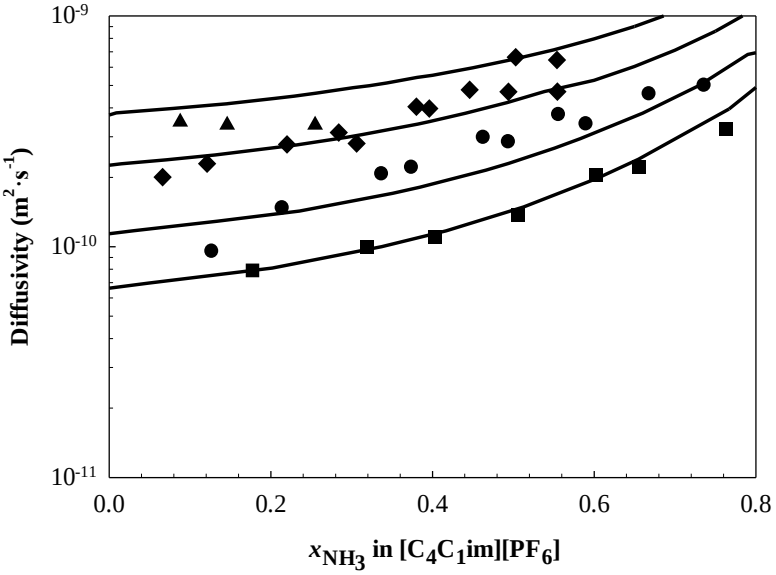

Figure 5.4. Diffusivity of NH_3 in $[C_4C_1im][PF_6]$. Lines represent the Stokes-Einstein model calculations, and symbols represent experimental data (■, 283.15 K; ●, 298.15 K; ♦, 323.15 K; ▲, 348.15 K).

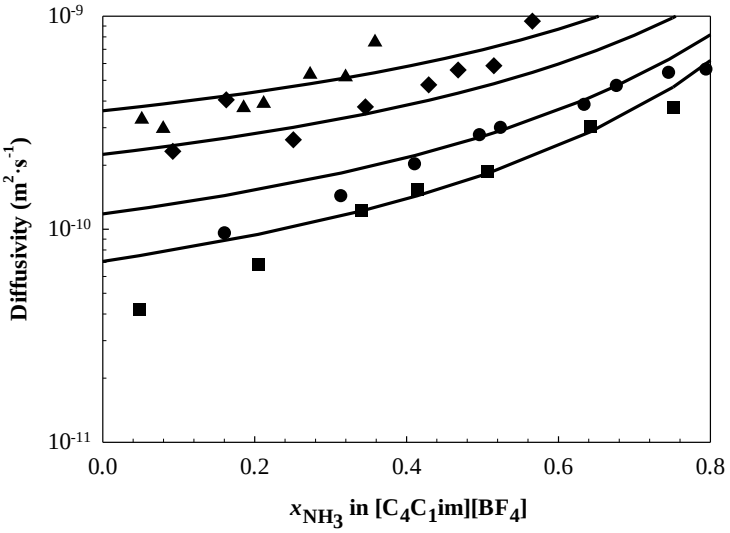

Figure 5.5. Diffusivity of NH_3 in $[C_4C_1im][BF_4]$. Lines represent the Stokes-Einstein model calculations, and symbols represent experimental data (■, 283.15 K; ●, 298.15 K; ♦, 323.15 K; ▲, 348.15 K).

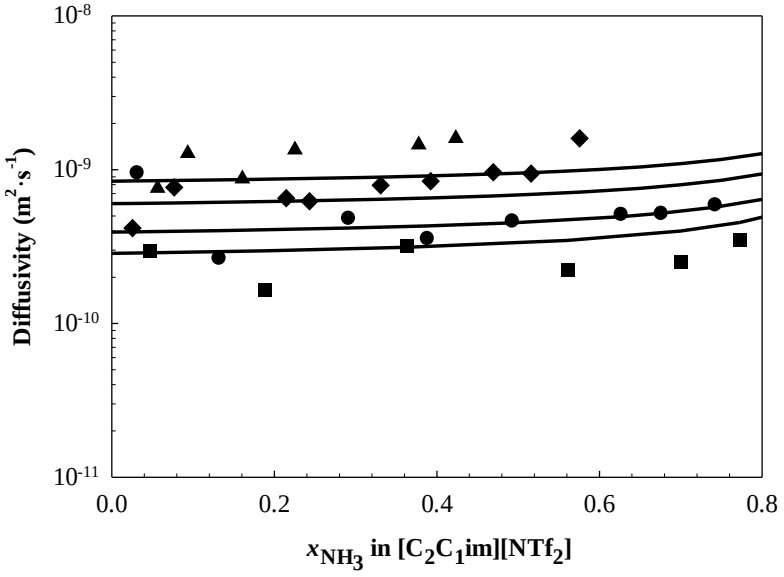

Figure 5.6. Diffusivity of NH_3 in $[C_2C_1im][NTf_2]$. Lines represent the Stokes-Einstein model calculations, and symbols represent experimental data (■, 283.15 K; ●, 298.15 K; ♦, 323.15 K; ▲, 348.15 K).

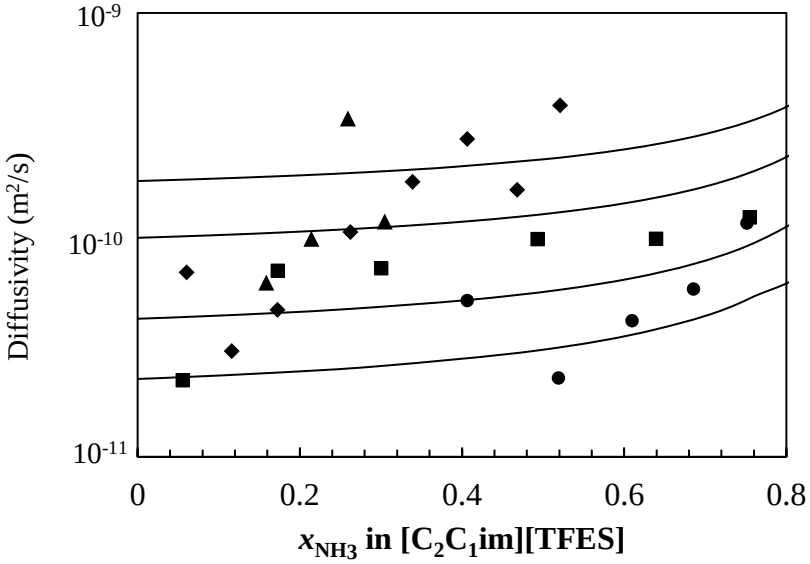

Figure 5.7. Diffusivity of NH_3 in $[C_2C_1im][TFES]$. Lines represent the Stokes-Einstein model calculations, and symbols represent experimental data (■, 283.15 K; ●, 298.15 K; ♦, 323.15 K; ▲, 348.15 K).

Chapter 6. Spectroscopic Analysis

"Basically, I have been compelled by curiosity."

Mary Leakey,

a British paleoanthropologist

Many chemicals are produced or used in both academia and industry every day, and spectroscopy is one of the characterization techniques to identify the structure of matter.[151] There are numerous spectroscopic techniques available for material characterization such as Ultraviolet (UV) Spectroscopy, X-Ray Photoelectron Spectroscopy (XPS), Auger Electron Spectroscopy, Nuclear Magnetic Resonance (NMR) Spectroscopy, or Vibrational Spectroscopy (Raman Spectroscopy, Infrared (IR) Spectroscopy) to name a few common ones.

Ionic liquids have distinctive properties such as low melting points and high viscosities such that "characteristic liquid structures cannot be associated with molecular liquids".[152] Herein, spectroscopic techniques play a vital role to elucidate the unique structure of ILs and their interaction with other substances. Among many spectroscopic techniques, Vibrational Spectroscopy (IR and Raman) and NMR are commonly used spectroscopic methods to characterize ILs. Vibrational spectroscopy at ultra-high vacuum is mostly utilized to elucidate the details of the surface features of ionic liquids, and can provide more comprehensive information about the molecular structure and properties of ILs as the chemical nature at the surface significantly differs from the bulk.[152] IR and Raman spectroscopies, which can be used at ambient or most realistic pressure conditions,[152] are mostly used to gain a more in-depth understanding of the nature of ionic interactions, anion−cation hydrogen bonds, and molecular conformations. [153]

Vibrational spectroscopy is an appropriate technique to study the intermolecular interactions in pure ionic liquids as well as in ionic liquids mixtures. However, NMR is the most frequently used technique in the field of ILs as it is a fast, simple, and inexpensive technique.

6.1. Nuclear Magnetic Resonance (NMR) Spectroscopy

Nuclear magnetic resonance (NMR) is one of the major tools to elucidate the ionic liquid structures in ionic liquids. The foundation of NMR spectroscopy lies in the magnetic properties of atomic nuclei.[154] Protons in a nucleus are charged particles in motion. In the absence of a magnetic field, the charged particles spin; and, consequently, generate a magnetic field with no net magnetization as the magnetic dipole moment of each proton orienting in all directions (Figure 5.1. (a)). When a strong external magnetic field is applied, nuclei orient in either parallel or antiparallel to the applied magnetic field (Figure 6.1. (b)). NMR is based on the response to the stimulation of this fully magnetized and oriented nuclei and is the measurement of the absorption of energy to the response to a radio frequency pulse under a strong and constant magnetic field. This absorption of energy is detected by a radio frequency receiver and recorded as a spectral line, the so-called *resonance* signal.[154] In this way, a *spectrum* can be generated for the molecules with non-zero magnetic moment nuclei such as ^{1}H, ^{13}C, ^{19}F, and ^{15}N.

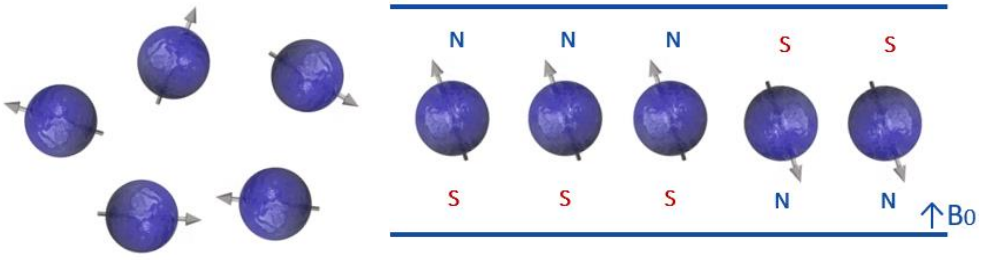

Figure 6.1. The nuclei orientation (a) with no magnetic field (b) under a strong magnetic field (Bo)[155]

The position (i.e., chemical shift or frequency) of each resonance is governed by the chemical environment of the nuclei.[156] The typical proton NMR spectrum shows the signal at the corresponding chemical shifts for the molecule (i.e., ^1H).[156] Proton chemical shifts cover a range of over 30 ppm, but the majority of the shifts of ^1H NMR appear in the region 0-10 ppm.[157] The chemical shifts are dimensionless units reported on the δ scale (in ppm).[151,156] The separation of a particular resonance from the standard signal depends on the total field strength (mostly 100, 400, and 600 MHz)[156], which is always much higher than the chemical shifts (typically less than 6000 Hz)[151]. To express the chemical shifts independent from the operating frequency of the spectrometer and to simplify the numerical values, the chemical shifts are given in parts per million (ppm) by introducing the factor 10^6. For reference, $\delta = ((\nu-\nu_o)/\nu_o) * 10^6$, where ν_o is the resonance frequency of the standard, ν is the frequency of the particular nucleus (^1H in this study), and the 10^6 is the scaling factor. The value of the δ can be used to make qualitative assessments about the presence of functional groups. The chemical shifts can be negative or positive based on the magnetic field experienced by the nuclei of a standard material. If the chemical shift is negative, the nucleus is considered shielded as the magnetic field of the proton is weaker than the magnetic field experienced by the nuclei of the standard materials. If the chemical shift is positive, the nucleus is considered deshielded as the magnetic field of the proton is stronger than the magnetic field experienced by the nuclei of the standard materials. In general, if the nucleus is closer to an electronegative element, the nucleus is more deshielded; consequently, δ is large.[156]

The purpose of Section 6.1 is to provide a basic NMR knowledge, which is used as a basis in the discussion in this chapter. However, NMR is a large field of study, and numerous books,

publications, and proceedings provide a more comprehensive background. These materials can be found in the references [151,154,156,157].

6.2. High-Pressure NMR Sample Preparation and Measurement

In this study, high-pressure ^{1}H NMR was used to understand the interaction of NH_3 with imidazolium-based ILs. The experimental system consists of a sample preparation system, which is an in-house designed sample preparation apparatus (Figure 6.2) and the NMR spectrometer (Figure 6.3). The high-pressure NMR sample preparation apparatus consists of high-pressure NMR tubes (Wilmad-Lab Glass, Product No. 522-PV-7), gas source (Anhydrous NH_3, Matheson, Lot No. 9108208561K5), pressure gauge (Omega Engineering, Model DPG5500B-3kg, 0-3000 psi), and thermometer (Ertco Eutechnics Digital Thermometer, Model 4400). High-pressure NMR tube operates at the pressures from 0.01 to 20 bar. The transparent part of the tube is made of Pyrex®, and the valve (or the plug) is made of Teflon™. The plug consists of Viton™ O-ring to ensure sealing. As Viton is not compatible with anhydrous ammonia, a custom-made o-ring was obtained from Micro Rubber & Plastics. The size of the O-ring is 1 mm cross-sectional diameter x 4.5 mm inner diameter and made of Markez® Z1026 (a batch number RDA411P0). In the NMR tube, a small hole on the side of the Teflon™ plug allows gas flow. When the plug is turned clockwise, the hole is sealed through the Pyrex® wall. When the plug is turned counterclockwise, the gas flows through the small hole. However, it is observed that the gas leaks from some of the tubes after the valve was opened despite the O-ring, which indicates that the sealing was not adequate. To promptly address this issue, two additional Markez® O-rings are placed in the Teflon™ part, as shown in Figure 6.2.

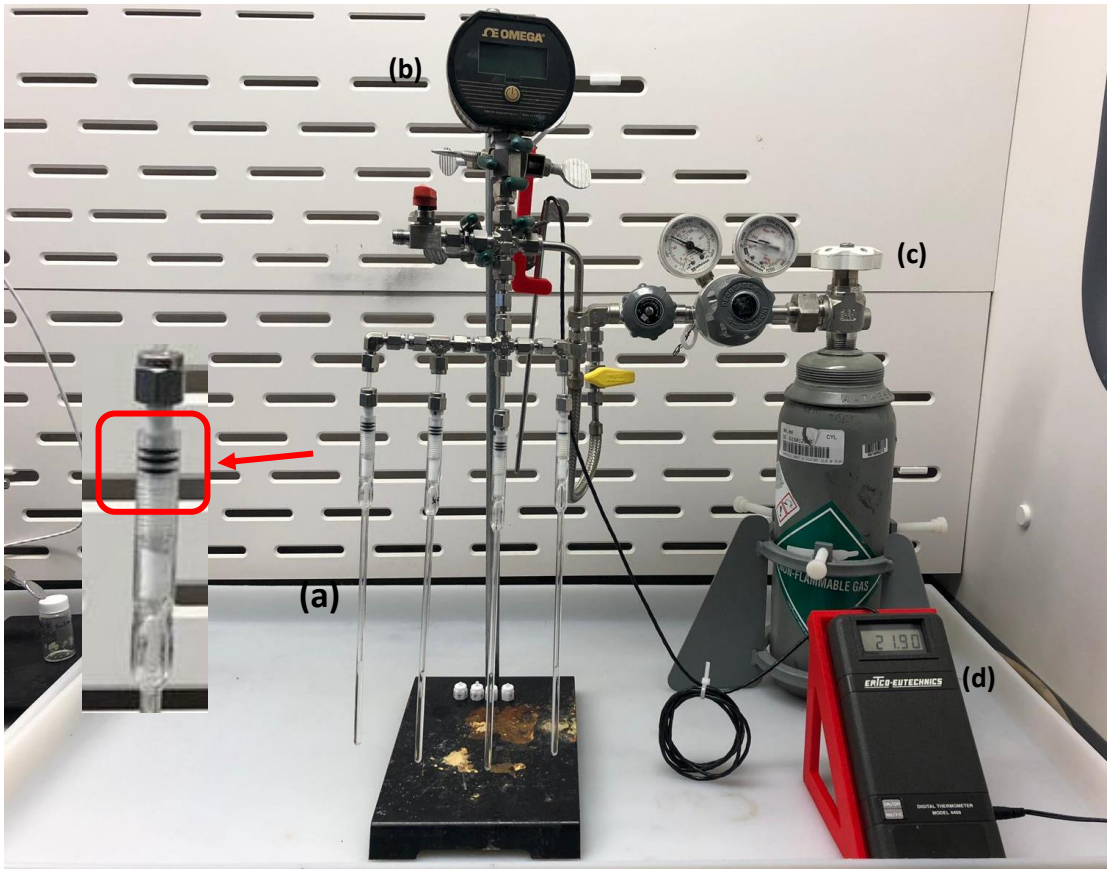

Figure 6.2. Sample preparation apparatus for High-Pressure NMR (a) High-Pressure NMR tubes (b) Pressure gauge (c) Anhydrous Ammonia (d) Ertco Thermometer

In a regular NMR experiment, the process beings with an NMR sample preparation. The first step is to prepare the solvent standard. In this study, instead of an internal standard, an external standard is used to eliminate the interaction between the standard solvent and the IL. Therefore, a minute amount of dimethyl sulfoxide (DMSO) is filled into a capillary tube and sealed in both ends by slowly melting the glass. The DMSO-filled capillary tube is then inserted in the high-pressure NMR tube. Then, the ILs are added into their corresponding NMR tubes. The tubes were attached to the system with Swagelok fittings and small fluoropolymer tubing (Chemfluor® 367, Saint-Gobain). The gas is evacuated using the backing pump before NH_3 admittance. NH_3 is

admitted to the NMR tubes at room temperature (295.15 K). The samples were kept at a given pressure for gas dissolution for one week, except the $[C_2C_1im][NTf_2]$ sample, which is kept at the given pressure for gas dissolution ~3 weeks. A Bruker DRX 500 MHz spectrometer (named "Paris" in the KU NMR Lab) was used to process the samples (Figure 6.3). The samples were run in a temperature-controlled environment in the NMR at 297.15 K. No weight change was observed before and after the ^1H NMR was taken.

Figure 6.3. Bruker DRX 500 MHz spectrometer in the University of Kansas ("Paris")[158]

6.3. High-Pressure NMR of Imidazolium-based ILs and NH_3

The hydrogen protons in the ILs, essentially protons in [C_2C_1im] and [C_4C_1im] cations, give resonance as a result of their response to the magnetic field in the ^{1}H NMR. In order to distinguish each resonance in the NMR spectra, elements from the molecule in each cation are numbered, as shown in Figure 6.4.

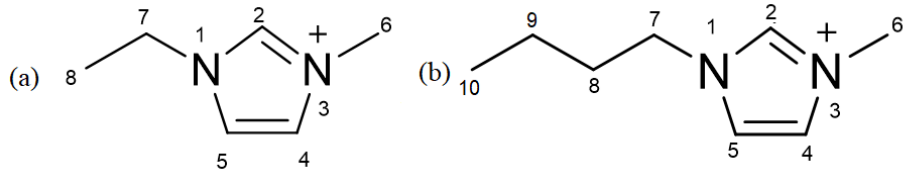

Figure 6.4. The numbering of the (a) [C_2C_1im] cation and (b) [C_4C_1im] cation

According to Figure 6.4, 6 proton resonances for [C_2C_1im][NTf_2] and [C_2C_1im][TFES], and 8 proton resonances for [C_4C_1im][PF_6] and [C_4C_1im][BF_4] should be observed on the ^{1}H NMR spectra. The ^{1}H NMR spectra of pure ILs ([C_4C_1im][PF_6], [C_4C_1im][BF_4], [C_2C_1im][NTf_2], and [C_2C_1im][TFES]) as well as their mixtures with NH_3 at various pressures were shown in the Figures 6.5 - 6.8. The numbers above the peaks in Figures 6.5 – 6.8 shows the position of the proton in the given cation, as depicted in Figure 6.4. The ^{1}H NMR of each pure IL is compared with the IL+NH_3 mixtures, where the degree of the shift depends on the concentration of NH_3 in the IL samples. Therefore, the chemical shifts observed in each spectrum, and the chemical shift change ($\Delta\delta$) upon gas dissolution are summarized in Table 6.1 - 6.4.

Figure 6.5 - 6.8 showed all proton peaks in the cations shifted compared their pristine form due to NH_3 dissolution even though the degree of chemical shift varies in each IL. This finding suggests NH_3 is interacting with all protons in the cation of the imidazolium-based ILs rather than interacting only with a specific proton. It is well-known that the formation of hydrogen bonds

causes the peaks to shift to a higher frequency (or higher ppm) due to deshielding.[154] Figures 6.5 - 6.7 showed all proton peaks are downshielded, which is due to deshielding. This result might suggest that the interaction between protons in the cation and NH_3 is dominated by hydrogen bonding. As mentioned earlier, the peaks in the ILs were shifted with different degrees. As can be seen in Figures 6.5, 6.6, and 6.8 as well as Tables 6.1, 6.2, and 6.4, the acidic proton peak in the $[C_4C_1im][PF_6]$, $[C_4C_1im][BF_4]$, and $[C_2C_1im][NTf_2]$ systems shifts more significantly compared to the rest of the proton peaks. For instance, as shown in Table 6.2, the acidic proton in the $[C_4C_1im][BF_4]$ downshielded 0.014 ppm, whereas the other protons downshielded less than or equal to 0.007 ppm when the pressure is increased from 1 bar to 5 bar. Similarly, as shown in Table 6.1, the acidic proton in the $[C_4C_1im][PF_6]$ downshielded 0.022 ppm, whereas the other protons downshielded less than or equal to 0.007 ppm. Again, as depicted in Table 6.4, the acidic proton in the $[C_2C_1im][NTf_2]$ downshielded ~ 0.2 ppm with an increased NH_3 concentration, whereas the rest of the protons downshielded less than or equal to 0.15 ppm. This observation is consistent with Shi and Maginn's finding using Monte Carlo simulations that the basic nitrogen of NH_3 more strongly associates with the acidic hydrogen that is attached to the C(2) carbon of the imidazolium ring.[18] Contrary to $[C_4C_1im][PF_6]$, $[C_4C_1im][BF_4]$, and $[C_2C_1im][NTf_2]$, the chemical shifts in the ^1H NMR spectra of $[C_2C_1im][TFES]$ system are rather different. As shown in Table 6.3, in the NH_3 + $[C_2C_1im][TFES]$ system, all proton peaks, including the acidic hydrogen, shifted with the same degree. For example, the peaks are shifted 0.10 ppm and 0.15 when the pressure was raised to 1 bar and 5 bar, respectively. This might be due to the interaction of NH_3 with an anion in IL. Shi and Maginn showed that using Monte Carlo simulations that the anion also has an effect on the solubility of NH_3 for $[C_2C_1im][NTf_2]$ even though it is less compared to the cation.

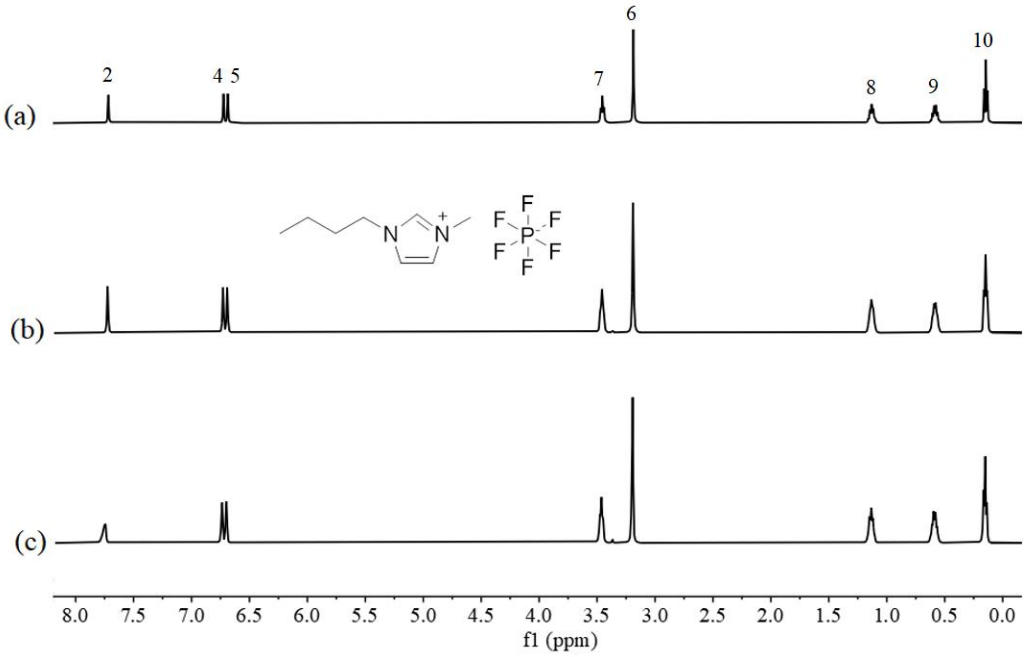

Figure 6.5.[1]H NMR spectra of (a) pure [C_4C_1im][PF_6] at atmospheric pressure, (b) the mixture of [C_4C_1im][PF_6] and NH_3 at 1 bar, (c) the mixture of [C_4C_1im][PF_6] and NH_3 at 5 bar. The numbers on the spectrum 1-8 show the resonance of the [1]H protons in [C_4C_1im][PF_6].

Table 6.1. The chemical shifts (*δ, ppm)* obtained for pure [C_4C_1im][PF_6], and NH_3 + [C_4C_1im][PF_6] system at 1 bar, and 5 bar.

Proton No.[a]	*δ, ppm pure IL*	*Δδ, ppm*[b]	*δ, ppm at 1 bar*	*Δδ, ppm*	*δ, ppm at 5 bar*
2	7.718	*+0.007*	7.725	*+0.022*	7.747
4	6.724	*+0.004*	6.728	*+0.008*	6.736
5	6.687	*+0.005*	6.692	*+0.007*	6.699
7	3.456	*+0.002*	3.458	*+0.004*	3.462
6	3.187	*+0.003*	3.190	*+0.003*	3.193
8	1.130	+0.002	1.132	*+0.003*	1.135
9	0.583	+0.003	0.585	*+0.004*	0.589
10	0.145	*+0.003*	0.148	*+0.003*	0.151

[a] Proton numbers are shown in Figure 6.9.
[b] *Δδ* shows the change in chemical shit upon gas dissolution.

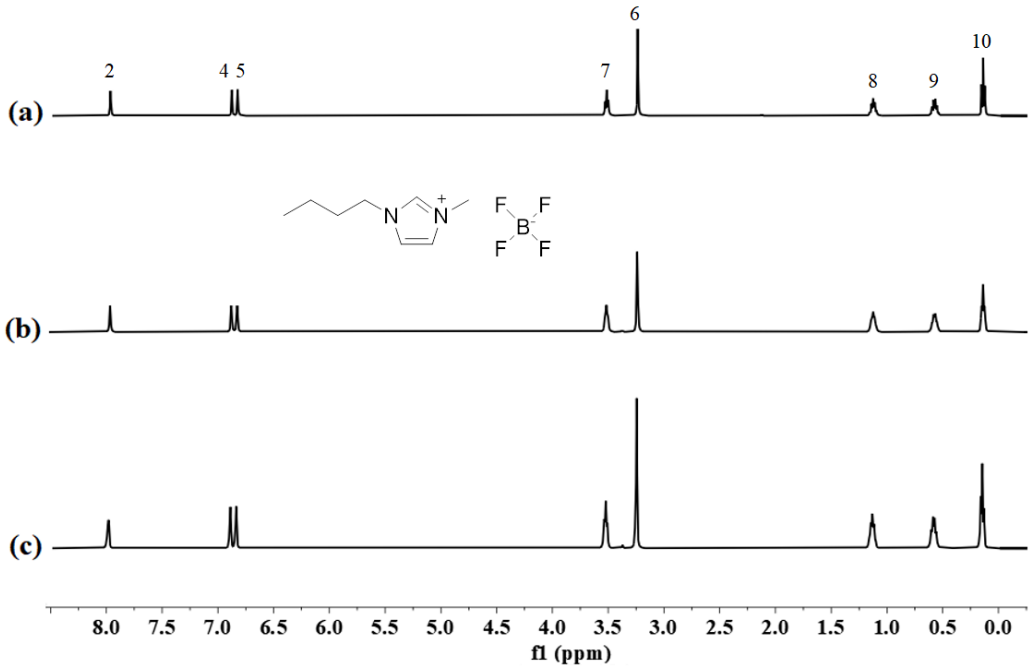

Figure 6.6. ^{1}H NMR spectra of (a) pure $[C_4C_1im][BF_4]$ at atmospheric pressure, (b) the mixture of $[C_4C_1im][BF_4]$ and NH_3 at 1 bar, (c) the mixture of $[C_4C_1im][BF_4]$ and NH_3 at 5 bar. The numbers on the spectrum 1-8 show the resonance of the ^{1}H protons in $[C_4C_1im][BF_4]$.

Table 6.2. The chemical shifts (*δ, ppm)* obtained for pure $[C_4C_1im][BF_4]$, and NH_3 + $[C_4C_1im][BF_4]$ system at 1 bar, and 5 bar.

Proton No.[a]	*δ, ppm pure IL*	*Δδ, ppm*[b]	*δ, ppm at 1 bar*	*Δδ, ppm*	*δ, ppm at 5 bar*
2	7.962	*+0.005*	7.967	*+0.014*	7.981
4	6.875	*+0.004*	6.879	*+0.008*	6.887
5	6.824	*+0.004*	6.828	*+0.007*	6.835
7	3.513	*+0.003*	3.516	*+0.005*	3.522
6	3.237	*+0.003*	3.240	*+0.004*	3.244
8	1.125	+0.002	1.127	*+0.006*	1.133
9	0.572	+0.002	0.574	*+0.006*	0.580
10	0.138	*+0.002*	0.140	*+0.005*	0.145

[a] Proton numbers are shown in Figure 6.8.
[b] *Δδ* shows the change in chemical shit upon gas dissolution.

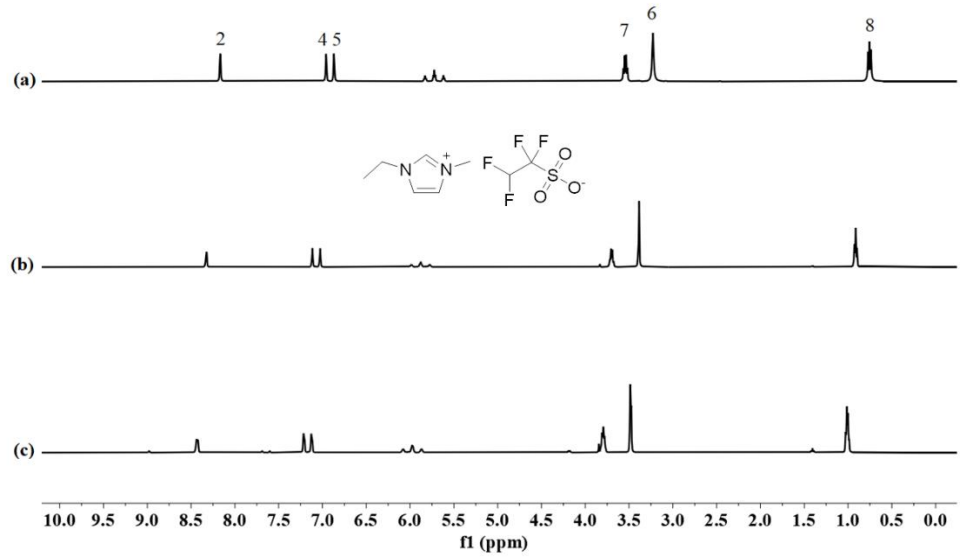

Figure 6.7. ^{1}H NMR spectra of (a) pure [C_2C_1im][TFES] at atmospheric pressure; (b-d) the mixture of [C_2C_1im][TFES] and NH_3 at 1 bar (b), 2 bar (c), and 5 bar (d). The numbers on the spectrum 1-8 show the resonance of the ^{1}H protons in [C_2C_1im][TFES].

Table 6.3. The chemical shifts (*δ, ppm)* obtained for pure [C_2C_1im][TFES], and NH_3 + [C_2C_1im][TFES] system at 1 bar, 2 bar and 5 bar.

Proton No.[a]	*δ, ppm pure IL*	*Δδ, ppm*[b]	*δ, ppm at 1 bar*	*Δδ, ppm*	*δ, ppm at 5 bar*
2	8.168	*+0.156* →	8.324	*+0.105* →	8.429
4	6.959	*+0.155* →	7.114	*+0.098* →	7.212
5	6.870	*+0.156* →	7.026	*+0.095* →	7.121
7	3.543	*+0.158* →	3.696	*+0.097* →	3.793
6	3.228	*+0.158* →	3.386	*+0.100* →	3.486
8	0.756	*+0.155* →	0.911	*+0.097* →	1.008

[a] Proton numbers are shown in Figure 6.7.
[b] *Δδ* shows the change in chemical shit upon gas dissolution.

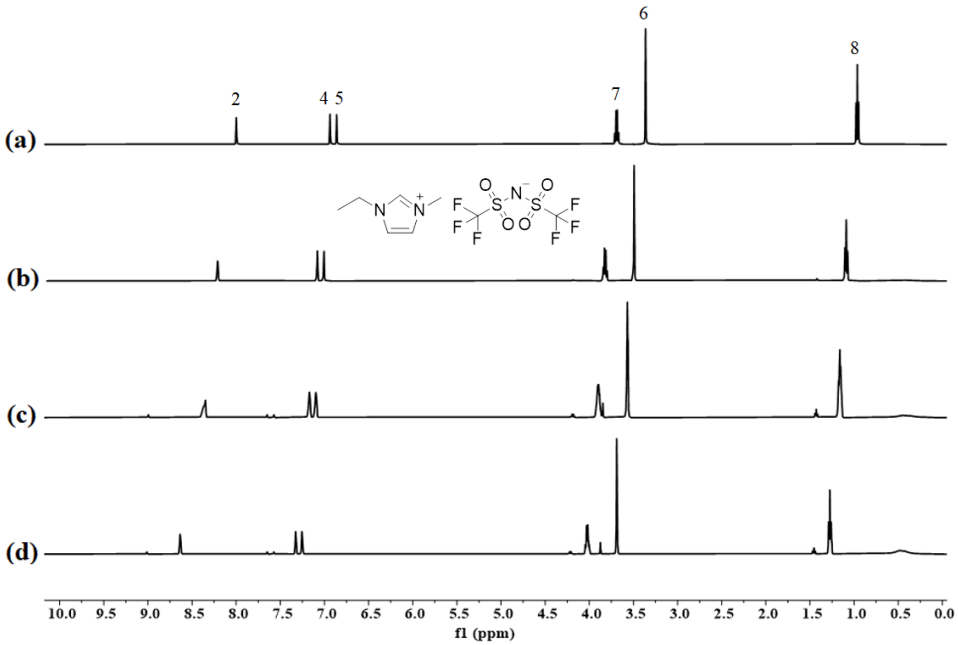

Figure 6.8. ^{1}H NMR spectra of (a) pure $[C_2C_1im][NTf_2]$ at atmospheric pressure; (b-d) the mixture of $[C_2C_1im][NTf_2]$ and NH_3 at 1 bar (b), 2 bar (c), and 5 bar (d). The numbers on the spectrum 1-8 show the resonance of the ^{1}H protons in $[C_2C_1im][NTf_2]$.

Table 6.4. The chemical shifts (*δ, ppm)* obtained for pure $[C_2C_1im][NTf_2]$, and NH_3 + $[C_2C_1im][NTf_2]$ system at 1 bar, 2 bar and 5 bar.

Proton No.[a]	*δ, ppm pure IL*	*Δδ, ppm*[b]	*δ, ppm at 1 bar*	*Δδ, ppm*	*δ, ppm at 2 bar*	*Δδ, ppm*	*δ, ppm at 5 bar*
2	8.022	*+0.211*	8.213	*+0.138*	8.351	*+0.287*	8.638
4	6.938	*+0.143*	7.081	*+0.091*	7.172	*+0.156*	7.328
5	6.862	*+0.144*	7.006	*+0.092*	7.098	*+0.157*	7.255
7	3.691	*+0.125*	3.820	*+0.075*	3.895	*+0.126*	4.021
6	3.363	*+0.130*	3.493	*+0.076*	3.569	*+0.121*	3.690
8	0.963	*+0.126*	1.089	*+0.073*	1.162	*+0.113*	1.275

[a] Proton numbers are shown in Figure 6.8.
[b] *Δδ* shows the change in chemical shit upon gas dissolution.

Furthermore, it is shown that the impact of the anion on the solubility increased with an increase in NH_3 composition.[18] Therefore, the equal shift in all protons in $[C_2C_1im][TFES]$ might be due to the intermolecular interaction of NH_3 with the anion. In fact, one evidence is that the impact of the anion can be seen in ^1H NMR of $[C_2C_1im][TFES]$. As can be seen in Figure 6.7, there is a triplet of triplets signal at 6 ppm, which is corresponding to the [TFES] anion.[159] It is striking that the [TFES] anion peak also shifts with the same degree as the protons in $[C_2C_1im]$ with NH_3 dissolution. These findings might indicate that the interaction of NH_3 and $[C_2C_1im][TFES]$ are dominated by both cation and anion. To make similar arguments for the other three imidazolium-based ionic liquids, ^{13}C, ^{19}F, and ^{15}N NMR should be used to complement ^1H NMR, which would provide a more comprehensive understanding of the interaction between cation and anion with NH_3 in a given IL.

As mentioned earlier, the time given for NH_3 saturation in $[C_2C_1im][NTf_2]$ is much longer than the time given for $[C_4C_1im][PF_6]$, $[C_4C_1im][BF_4]$, and $[C_2C_1im][TFES]$ systems. Therefore, the chemical shifts are more pronounced in the $[C_2C_1im][NTf_2]$ system, as shown in Figure 6.8. The minimal chemical shifts in ^1H NMR spectra clearly indicate that the time given for gas dissolution is not enough for in any case. In fact, the weight change in the ILs after gas dissolution showed that only less than 0.1 wt % NH_3 is dissolved in these ILs in any pressure. Therefore, the pressure statements above should be taken as only guidance to indicate increased NH_3 dissolution, not true equilibrium concentrations at a given pressure. The minimal dissolution is, in fact, quite expected because NH_3 is statically admitted to the NMR tubes with no mixing in the sample preparation. Assuming that the length of the IL sample in each tube is ~5 cm (excluding the volume added due to the external capillary tube), the dissolution in one direction, and the average *D* of

NH_3 in imidazolium-based ILs is 10^{-10} m^2/s (taken from the Chapter 5), the time required for dissolution can be approximated using Equation 5.5. The estimation shows that ~100 days would be required for complete gas dissolution if no mixing occurs. The ILs might be saturated in a shorter time upon gas dissolution due to the decrease in the viscosity of the solution. Regardless, the rate of dissolution should be still increased by means of agitation the solution. The design of agitation in NMR tubes requires more thorough investigation and thinking as ferromagnetic objects and materials must be avoided due to the strong magnetic field in the NMR. Regardless, the main purpose of the study is to investigate the interaction of ammonia and imidazolium-based ILs. To that end, the findings provided useful information about the interaction between NH_3 and IL such that even a minor amount of NH_3 makes a hydrogen bond with the ILs.

Chapter 7. Safety

"Life is not easy for any of us. But what of that?
We must have perseverance and above all confidence in ourselves.
We must believe that we are gifted for something and that this thing must be attained."
Marie Curie,
The first woman to win the Nobel Prize, and the first person to win the Nobel Prize twice

A risk management system is mostly well-implemented in industry, whereas the risk associated in the academic labs are usually either considered low or entirely neglected. A considerable amount of lab incidents, which ended with major injuries, fatalities, substantial financial and physical losses, clearly demonstrates the urgent need for the implication of risk management systems in academic labs. Even though safety in academia is receiving increased attention[160–166], there is still much room for improvement.[162]

One of the key components of safety management in academic institutions is a strong safety culture. It is clear that the strong safety culture cannot be accomplished without the presence of the leadership commitment to safety.[161] The leadership starts from the top management, such as university administrators and deans, and then comes to the department chairs, directors, faculty, and principal investigators, who are all responsible for the safety at the university laboratories. The leaders must commit to promoting the safety culture in their institutions by encouraging the implementation of safe practices and creating a strong safety culture through safety meetings, safety education, process safety management, and more. Even though the commitment to safety starts with the leadership, students, research assistants, and staff must also commit to safety.

7.1. Safety in the Department of Chemical and Petroleum Engineering

The importance of safety education is emphasized through the Process Safety and Sustainability class, which is one of the required classes in the curriculum of the Department of Chemical and Petroleum Engineering at the University of Kansas for chemical engineering undergraduate students. Even though the class focused on industrial-based processes, the concepts can also be adapted to academic laboratories.[160]

Part of the Chemical Engineering faculty is in collaboration with the Center for Environmental Beneficial Catalysis (CEBC). CEBC has a mandatory monthly safety meeting, where all CEBC researchers, students, faculty, and the director attend regularly. Although CEBC monthly safety meetings are not mandatory for all researchers in the Department of Chemical Engineering, faculty and graduate students who are directly or indirectly involved in the research activities at CEBC; are required to attend the CEBC mandatory safety meetings. These monthly meetings are an excellent way to remind researchers of the desired culture the organization wishes to achieve, to demonstrate facility-wide communication on safety topics, and to appreciate the involvement in the safety of everyone in the organization.

7.2. Safety in the Shiflett Foundation Research Laboratory

The Shiflett Foundation Research Laboratory is a research laboratory in the Department of Chemical and Petroleum Engineering Department. Safety is one of the most important parts of the graduate student education in the Shiflett laboratory. As part of the continuous safety education, and strong safety culture, the following activities are required:

1- Students complete an online EHS safety training program as part of their on-boarding process.

2- The senior personnel in the lab provide a detailed tour of the laboratory to show important safety features to new personnel such as the eyewash stations, safety showers, air monitoring systems, ventilation hoods and enclosures, personal protection equipment (PPE), etc.

3- The PI initiates one-on-one weekly research meetings asking about the potential hazards of the experiment that the researcher would like to discuss.

4- Researchers in the lab (graduate students and post-doctoral researchers) are conducting biweekly and monthly laboratory inspections, which are discussed at monthly group meetings.

5- Each graduate student and the post-doctoral researcher must prepare a process safety management documentation prior to the operation of any instrument, experimental system, or apparatus.

6- The gas sensors, water baths, or any other related instrumentation are quarterly inspected with their corresponding standards.

7- Biannual safety meetings are organized to review Process Safety Management documents, update the chemical inventory, inspect gas sensors, electrical components, etc.

In addition to having a strong safety culture, it is critically important to create a comfortable environment for researchers to voice their safety-related concerns or mistakes. Employees should always feel encouraged to report safety issues, which is also part of the Shiflett laboratory.

7.3. Process Safety Management Documentation

The Process Safety Management (PSM) documentation is to identify the hazards involved in instrumentation or experiments in a broad perspective prior to the operation. The PSM documentation used in the Shiflett laboratory was adopted from a similar process used by Dupont Central Research and Development and implemented into the laboratories with some

modifications due to the nature of the academic research environment. For example, the collaboration with the Department of Environmental Health and Safety at the University of Kansas be made mandatory in high-hazard category operations. The PSM does not only prevent risk but also significantly improves the startup procedure for new instruments or processes in the academic labs due to gained comprehension during the review process. Furthermore, the PSM is a written contract between the principal investigators and researchers to prove the proper safety precautions are taken, and the EHS safety training is completed. Even though some researchers may believe the implementation of the safety review documents might limit independently exploring new ideas for researchers in the lab, the potential unwanted outcome of unevaluated experiments is not worth compromising personal safety.

The main elements (or sections) of the PSM documentation in our laboratory consist of eleven major sections: electrical, emergency and operating procedures, environmental, equipment under pressure, facility process area, flammable materials, gases, high or low temperatures, mechanical motion, raw materials and products, and management of change. In addition to these main documents, authorized users are listed at the beginning of the documentation with their proper safety training certificates and written signatures.

7.3.1. Description of PSM Elements

7.3.1.1. Electrical

The "electrical" part of the PSM identifies the electrical requirements of the instrumentations and the compatibility.[160] The electrical investigation focuses on the power requirements, control panels, switches, the voltage and amperage of the equipment feed and source. For example, the information about the main disconnect switches and control panels should include the information

of location, panel number, voltage, amperage, equipment being fed, and the breaker or circuit number. In addition to the main power supplies, the instruments are checked for proper grounding and wiring. All cords in the equipment should be inspected to observe any physical damage to the cords or any half plugged/unplugged switches. In some operations, the power loss might be critical. Therefore, an uninterruptable power supply (UPS) might be in use. This section also questions the potential danger of the stored energy, the consequences of the main power supply, and restoring the electrical power.

7. 3.1.2. Emergency and Operating Procedures

Emergency procedures are vital for any experimental process. The operator needs to provide simple and explanatory guidelines in case of an emergency. The scope of the emergency procedures may vary from mild to high, depending on the potential hazards associated with the extent of the experimental procedure. Emergency procedures cover shutdowns, spills, gas leaks, and other related items.

Operating procedures describe the regular operation, including normal start-up, operation, and shut down, equipment clean up, and decontamination. Both operating and emergency procedures should be posted and readily available. In addition to emergency and operating procedures, the following procedures should also be readily available: lock, tag, clear, try, line break/first break, process modifications, and management of change.

7.3.1.3. Environmental

The environmental impact of the experiments in academic laboratories is mostly underestimated due to improper guidance. The poor implementation of the environmental impact of the experiments might be a result of poor knowledge or guidance of the principal investigators

of the laboratories.[161] The environmental element of the PSM documentation is to establish a written waste disposal procedure in order to handle chemical waste that needs to be released to the environment after or during the experiment. The procedure should address any special waste concerns and provide a clear and concise written disposal method. The amount of waste expected to be generated per day and in a week may be specified. If the process creates emissions, the amount of emission and the rate can be included. All waste is disposed of according to the EHS Department of the University of Kansas, and any questions or concerns about waste container use, disposal, or even labeling should be directed to the EHS Department.

7.3.1.4. Equipment Under Pressure

Most of the chemical engineering processes in academic laboratories involved extreme pressures (i.e., high pressure(explosion) or ultra-low vacuum(implosion)). This section of the PSM documentation is to provide a comprehensive inspection of the pressure in the system. The section identifies the source of the pressure and/or vacuum, maximum source pressure, maximum operating pressure, maximum allowable working pressure, pressure relief devices, pressure ratings. This section also identifies the chemical compatibility of the construction materials of the equipment parts such as valves, relief devices, seals, gauges, hoses/tubings, fittings, gaskets, and vessels with all process materials. In addition, the section questions a researcher to ensure enough headspace for expansion and/or decomposition during high-pressure operations, to analyze the event of pressure system failure, and to assess the required barrier/shield to protect personnel from a catastrophic release.

7.3.1.5. Facilities, Laboratory, Process Area

The review of the facility, laboratory, or process area recognizes any special requirements affecting laboratory personnel and visitors when entering the area. In some cases, special warning tools might be required, such as respirators, barricades or shields, alarms. The laboratory area element also identifies the route to the emergency exits, the location of the nearest fire/evacuation alarms, fire extinguishers, and up-to-date emergency contacts. Additionally, the element identifies the operators who work lone, after hours and weekend operations, and unattended experiments. The element questions a researcher whether the PSM documentation, the proper experiment in progress sign, the required procedures (emergency, shutdown, operating, etc.) are legible and readily available.

7.3.1.6. Gases

The "gases" element in the PSM identifies the gas source (house supply, cylinder, or generator), the pressure limits such as maximum supply pressure, allowable working pressure, the pressure relief devices, the compatibility of gas with the instrumentation, the safety interlocks, check valves, pressure ratings of the fittings, and gas sensors. The section also details the relief device setpoint, potential failures such as excess flow, the secure cylinder practice.

7.3.1.7. Flammable Gases, Liquids, Solids

The "flammable" element in the PSM documents is to question the reactivity, explosion, or decomposition hazards associated with the experiment or process, and to identify the presence of any ignition and fuel sources, and the flashpoints. If the automatic detection devices for gases, mixtures, or fire present, it is described in detail herein. Any specific operating hazards due to flammability issues are also detailed in this section.

7.3.1.8. High or Low temperature

The “high or low temperature” element in the PSM documents is to identify the temperatures in the system. The section is to detail the operating temperature range, the method of heating and cooling, the surface temperatures in the instrumentation, and the outcomes of rapid temperature changes. The element questions the researcher if any warning signs or barricades, any special personal protective equipment or safety interlocks are needed. In this section, it is important to report temperature units in both the metric and British unit system.

7.3.1.9. Raw Materials and Products

The “Raw Materials and Products” section identifies the detailed process description, process flow diagrams, mass and heat balances, safety data sheets of the reactants, products, and intermediates[160]. This element of the PSM also is to determine the transport, safe handling, and emissions of the materials, such as the compatibility of ductwork materials with the materials, the transportation of the materials through building and lab, etc.

7.3.1.10. Mechanical Motion

The “mechanical motion” of the PSM is to determine and report the parts in motion in the given instrument. This includes but not limited to identify rotation, sliding, reciprocating, cutting/sharp edges, and oscillating.

7.3.1.11. Management of Change

Management of Change (MOC) is one of the most important documents in the PSM documentation as the number of accidents due to the lack of MOC is significant.[167] Each of these accidents emphasizes the importance of having a systematic method and record for the MOC.

Therefore, MOC is to ensure safe operation after careful reviewing of the changes done in the system. The MOC identifies the type of change, type of hazard review, and the issues due to MOC.

7.4. Research Hazard Review for Ammonia Studies

Ammonia is both a combustible and highly toxic gas; therefore, it must be handled with extreme caution. Due to the hazardous nature of ammonia, the ammonia experiment using XEMIS gravimetric microbalance is selected as an example herein, among other many PSM documents are prepared.

Figure 7.1. Photohelic Unit with Emergency Crush Button

In the Shiflett laboratory, numerous safety features have been implemented to handle NH_3 safely.[160] The microbalance and temperature/pressure/vacuum control system are located in a specially designed ventilated enclosure that offers protection in the event of an NH_3 leak, as shown in Figure 2.1. The details of the custom design of the enclosure can be found elsewhere.[160] The ventilated enclosure is equipped with a fire sprinkler and a safety interlock system. The interlock system is connected to an emergency crash button outside the enclosure, a photohelic for

measuring the ventilation flowrate and two NH_3 gas monitors (3M Scott Safety, Freedom 5000, Serial 3568 with NH_3 sensor, 096-1965-0100 and 3M Scott Safety, Meridian Universal Gas Detector, Model 096-3480-01 with NH_3 sensor 096-3473-03). The photohelic unit is shown in Figure 7.1.

Figure 7.2. Pressure Gas Panel that houses the pressure gauges, Air-to-Open Valve, and vent lines

Figure 7.3. Ammonia Gas monitors (a) Scott Meridian Detector with Ammonia Sensor located in the ventilated enclosure (b) Freedom 5000 Detector with Ammonia Sensor located in the laboratory

Figure 7.4. Yokogawa Data Acquisition Unit to monitor the NH_3 concentration in the ventilated enclosure and the laboratory

In the event that the crash button is depressed, a loss of ventilation occurs, or either gas monitor detects an NH_3 leak, an air-to-open (ATO) valve on the NH_3 feed line located in the pressure gas panel will automatically close and shut off the NH_3 source (Figure 7.2). One NH_3 monitor is located inside the enclosure (Figure 7.3(a)), and the other NH_3 monitor is located outside the enclosure (Figure 7.3 (b). Both NH_3 monitors are calibrated and tested quarterly to ensure proper operation. Two alarms were set for an alert at 25 ppm (50% of NH_3 allowable exposure limit (AEL)) and warning at 15 ppm (30% NH_3 AEL). In addition, to the ATO valve closing, yellow and red warning lights flash, and a siren sounds in the lab for alert and warning alarms, respectively. A data acquisition system (Yokogawa, Model GM10 with Power Supply, Model GM90PS, and Module Base, Model GM90MB) (Figure 7.4) provides text and email messages to inform researchers when the NH_3 detector activates, or loss of ventilation occurs. Nitrogen gas is setup to purge NH_3 lines and the microbalance (three times) before opening the system. The ammonia cylinder is maintained in the flammable cabinet, which is also directly vented to ductwork, as shown in Figure 2.1. A process management documents were carefully prepared to evaluate and document all hazards including unattended operation, and only authorized operators

are allowed to use the equipment. The PSM analysis, procedures, and equipment have demonstrated that the XEMIS microbalance can be safely operated using flammable and toxic gases such as NH_3. The PSM documentation of ammonia in XEMIS microbalance is shown as an example in Appendix D.

Chapter 8. Conclusions and Recommendations

"Truth is powerful, and it prevails."

Sojourner Truth,

an African-American abolitionist and women's rights activist

This chapter summarizes the work discussed in the previous sections and provides recommendations for future studies.

8.1. The Phase Behavior, Kinetics, and Spectroscopic Analysis of Mixtures of Ammonia and Imidazolium-based Ionic Liquids

The vapor-liquid equilibrium measurements for the binary systems of NH_3 and four imidazolium-based ILs have been successfully measured the first time using a gravimetric microbalance technique. The solubility of NH_3 in $[C_4C_1im][PF_6]$, $[C_4C_1im][BF_4]$, $[C_2C_1im][NTf_2]$, and $[C_2C_1im][TFES]$ were measured at temperatures of 283.15, 298.15, 323.15 and 348.15 K and at pressures up to 0.7 MPa using the new Hiden XEMIS gravimetric microbalance. The VLE data were correlated using the Peng-Robinson EoS, and the NRTL and Flory-Huggins models. All models are in excellent agreement with the experimental data. Flory-Huggins model provided a better understanding of the factors affecting the gas solubility. In the extended Flory-Huggins model, the χ parameter is obtained, assuming it is only dependent on temperature. In future work, the composition dependence in the χ parameter might be included to improve the model fit. Furthermore, a few additional isotherms might be useful to ensure the T dependence of the χ parameter. In addition, the factors affecting the gas solubility in ILs is rather complicated than the estimation of the extended Flory-Huggins model due to complex the intramolecular and intermolecular interactions in the ionic liquid mixtures. In the future, molecular simulations can

be performed to provide insight into these interactions. In this study, the use of gravimetric microbalance has been proven as one of the most accurate techniques to measure the solubility gases in ionic liquids. In future studies, the global phase behavior of ammonia in ionic liquids might be measured using high-pressure view cell or using XEMIS microbalance with some modifications. The high-pressure view cell is an excellent technique at high-pressure measurements, although the accuracy at low pressures in ionic liquid studies is rather skeptical due to very low volume expansion. However, one of the main advantages of the technique is to provide the most accurate volume expansion data and the capability of visual inspection, which allows monitoring phase transitions. As discussed in detail in the previous chapter, XEMIS microbalance provides extremely accurate data even at low pressures. However, the balance needs some adjustments to operate NH_3 at higher pressure. One idea to overcome the design limitation might be including the means of heating in the tubing and attached a heated gas reservoir between the gas cylinder and the admit valve. Regardless of the improvements, the microbalance is always limited to the maximum operating temperature of electronic components of the balance (maximum ~333.15 K) unless the design is entirely renovated. Therefore, both gravimetric and volumetric techniques should be used to complement each other for future studies.

As discussed in Chapter 4, the ionic liquids used in the ammonia studies are commonly used, readily available, relatively cheap, and thermally stable ionic liquids. These ILs can be used in the applications where no water present, such as absorption-refrigeration cycles, excluding the possibility of hydrolysis. However, designing and synthesizing a new ionic liquid or ionic liquid mixtures as absorbents might be done in the future. Ionic liquid double salts, which have never been tested with ammonia, can also be investigated.

In addition to the phase equilibria, the Fickian diffusivities of NH_3 in imidazolium-based ILs were obtained fitting experimental concentration to the one-dimensional (1D) mass diffusion equation and found to be lower than the diffusion of NH_3 in water. There are several opportunities for future work regarding diffusion analysis. The diffusion analysis is an extremely rigorous and time-consuming procedure. The analysis requires a significant amount of data to be corrected for the buoyancy and volume expansion in an Excel spreadsheet prior to the analysis in MATLAB. In the future analysis, REFPROP can be incorporated into a new MATLAB code, which simultaneously calculates the solubility and the diffusivity in the MATLAB environment. Moreover, the diffusion analysis might be depending on the instrument and data acquisition interval. In the future, a standard system such as CO_2 + $[C_2C_1im][NTf_2]$ might be used to obtain the diffusivity of CO_2 in the ionic liquids to compare the diffusion results obtained in both IGA and XEMIS balances. Furthermore, the impact of the data acquisition interval on diffusivity might be investigated by varying the value from 1 s to 60 s. The diffusion model used in this study does not capture the impact of the gas sorption occurs during ramp time. In future modeling studies, the impact can be included in the model.

A semi-theoretical Stokes-Einstein equation was used to model diffusivities and to obtain the diffusing radius of NH_3 in imidazolium-based ILs. The Stokes-Einstein equation is found useful for correlating the diffusivity of NH_3 in imidazolium-based ILs when the thermophysical properties of the solution are known or properly estimated. It would be of interest to measure the viscosity of ammonia + ionic liquid mixtures at various temperatures and pressures and compare the model results with experimental measurements.

NMR results in this study provided a better understanding of the ammonia and IL interactions.

^{13}C, ^{19}F, and ^{15}N NMR are recommended to complement ^{1}H NMR, which would provide a more comprehensive understanding of the interaction between cation and anion with NH_3 in a given IL. Furthermore, molecular simulation dynamic studies would also highly recommended to support experimental and spectroscopic observations.

One of the missing experimental measurements in the literature is the heat of NH_3 absorption in ILs. A significant amount of time has been spent to set up Seteram BT 2.15 Calvet calorimeter and to develop an experimental procedure for this measurement. The procedures and equipment are under further development.

8.2. Phase Behavior and Kinetic analysis of mixtures of Pyrrolidinium-based Ionic Liquids and Carbon dioxide

The high-pressure vapor-liquid equilibrium for the binary systems of CO_2 and a series of 1-alkyl-1-methyl pyrrolidinium bis(trifluoromethylsulfonyl)imide ionic liquids ($[C_nC_1pyr][NTf_2]$ (n = 3,4,6)) are reported at 298.15, 318.15 and 338.15 K and at pressures up to 20 MPa. Experiments were conducted using gravimetric (IGA and XEMIS microbalances) and volumetric (high-pressure view cell) methods. The solubility of CO_2 in pyrrolidinium-based ionic liquids increases with decreasing temperature and increasing pressure. The CO_2 solubility also slightly increases with an increase in alkyl chain length on the pyrrolidinium cation. It is shown that at 298.15 K and at low CO_2 concentrations, the deviation from Raoult's law becomes larger with an increase in cation alkyl chain length. If the non-idealities at low concentrations (or low pressures) are truly a result of entropy effects, then all three ionic liquids should have the same solubilities when the impact of molecular weight is eliminated. In fact, when the CO_2 absorption is reported in molality (moles of CO_2 per kg of ionic liquid) at selected pressures of 2, 6 and 14 MPa and temperatures of

298.15, 318.15 and 338.15 K, the three pyrrolidinium-based ionic liquids have essentially the same solubilities up to 2 MPa which indicates the non-idealities at low pressures are a result of entropic effects. The scope of this part of the study was to investigate the phase behavior of CO_2 with pyrrolidinium-based IL in a wide pressure range at various temperatures. However, in the future, it might be of interest to test this hypothesis and experimental observation by applying the Flory-Huggins model, as done in the ammonia studies.

In addition to the solubility information, molar volume, and volume expansion of CO_2 + IL mixtures are also reported. The Fickian diffusion of CO_2 in pyrrolidinium-based ionic liquids (~10^{-10} $m^2 \cdot s$) was calculated at pressures up to 2 MPa and found to be slightly lower than the diffusivity of CO_2 in an imidazolium-based ionic liquid with the [NTf_2] anion. The recommendations given for diffusion analysis in Section 8.1 can be applied herein as well.

8.3. Phase Behavior of imidazolium-based ionic liquids and Dihydroxy alcohols

Binary liquid-liquid equilibria for the mixtures of dihydroxy alcohols and three imidazolium-based ionic liquids were measured. The dihydroxy alcohols were 1,3-propanediol, 1,4-butanediol, and 1,5-pentanediol and the ionic liquids were [C_2C_1im][BF_4], [C_2C_1im][NTf_2], and [C_2C_1im][TFES]. The experimental LLE data was well-correlated using the NRTL activity coefficient model. All binary diol systems with [C_2C_1im][BF_4] or [C_2C_1im][NTf_2] have an upper critical solution temperature between 310 to 360 K. An equimolar mixture of diols and [C_2C_1im][TFES] showed complete miscibility between 293.15 to 373.15 K. An increase in alkyl chain length of the dihydroxy alcohols and/or changing the anion from [BF_4] to [NTf_2] for a given [C_2C_1im] cation results in an increase in the UCST. The excess molar volume of diols with ILs was, in most cases, larger than those of ordinary solutions.

It would also be of interest to expand the phase equilibria studies on mixtures of other ILs containing non-fluorinated anions. One interesting work that can be done in the future is to investigate the liquid phases using NMR spectroscopy. The experimental method used in this study has been brought from DuPont Experimental Station and set up in the lab in a short period of time. Even though the experimental system is very accurate, there are several opportunities to optimize the experimental system for future work. The water tank might be covered to minimize the water evaporation rate. The cover might be designed with a few holes to allow airflow into the system to prevent mold growth. Alternatively, a few drops of chemicals can be added into the water. Furthermore, the accuracy of the cathetometer has an impact on the reading, which is also considered in the error analysis. However, using a more sensitive cathetometer can reduce the error associated with the measurements.

8.4. Future Directions in the field of Ionic Liquids

I first became familiar with the term “ionic liquids” approximately ten years ago in my senior year in college while working on my undergraduate thesis - supercritical fluids with Dr. Ayla Calimli. Twelve years later, I had an opportunity to explore the field and physically work with ionic liquids in the laboratory. Ionic liquids are a remarkable class of materials with one-of-a-kind characteristics. Surely, they offer opportunities to optimize current technologies in a variety of industries.

The current and well-known challenge in the field of ILs is to tune the characteristics of the ILs based on the desired application. As stated earlier, millions of possible ionic liquids can be synthesized. It is impossible to synthesize all possible ILs and to predict their properties. On the other hand, the number of ILs synthesized even with the relatively limited knowledge in the field

today, offer extraordinary capabilities in fields ranging from separations to reaction engineering. Furthermore, new possible ILs and mixtures of ILs spark the scientific curiosity about their undiscovered and unknown properties. I believe the future of the ionic liquids, like many other scientific fields, lies in the machine learning field. By allowing the machines to learn the substantial data that a person cannot scrutinize, and to predict the undiscovered compounds in a virtual laboratory environment will open a new era in the field of ILs.

While the machine learning field is beginning to develop rapidly, the lab-based discoveries of the ILs, the characterizations of ILs via spectroscopy, the accurate thermodynamic and kinetic measurements and models, and molecular simulation dynamic studies will guide the ILs studies in the near future.

References

(1) Turnaoglu, T.; Shiflett, M. B. 110th Anniversary: The First Thermodynamic and Kinetic Analysis of Ammonia in Imidazolium Based Ionic Liquids Using a Gravimetric Microbalance. *Ind. Eng. Chem. Res.* **2019**, *58* (11), 4644–4655.

(2) Turnaoglu, T.; Minnick, D. L.; Morais, A. R. C.; Baek, D. L.; Fox, R. V.; Scurto, A. M.; Shiflett, M. B. High-Pressure Vapor−Liquid Equilibria of 1-Alkyl-1-Methylpyrrolidinium Bis(Trifluoromethylsulfonyl)Imide Ionic Liquids and CO 2 . *J. Chem. Eng. Data* **2019**. https://doi.org/10.1021/acs.jced.8b01236.

(3) Turnaoglu, T.; Ritchie, S. G.; Shiflett, M. B. Liquid–Liquid Equilibria in Binary Mixtures of Dihydroxy Alcohols and Imidazolium-Based Ionic Liquids. *J. Chem. Eng. Data* **2019**, *64* (7), 3179–3186. https://doi.org/10.1021/acs.jced.9b00283.

(4) Minnick, D. L.; Turnaoglu, T.; Rocha, M. A.; Shiflett, M. B. Review Article: Gas and Vapor Sorption Measurements Using Electronic Beam Balances. *J. Vac. Sci. Technol. A* **2018**, *36* (5), 050801.

(5) MacFarlane, D. R.; Kar, M.; Pringle, J. M. *Fundamentals of Ionic Liquids from Chemistry to Applications*, 1st ed.; Wiley-VCH Verlag GmbH & Co. KGaA: Weinheim, Germany, 2017.

(6) *Kirk-Othmer Concise Encyclopedia of Chemical Technology*, 5th ed.; Kirk-Othmer, Ed.; Wiley.

(7) Earle, M. J.; Esperança, J. M. S. S.; Gilea, M. A.; Lopes, J. N. C.; Rebelo, L. P. N.; Magee, J. W.; Seddon, K. R.; Widegren, J. A. The Distillation and Volatility of Ionic Liquids. *Nature* **2006**, *439* (7078), 831–834. https://doi.org/10.1038/nature04451.

(8) *Ionic Liquids in Synthesis*; Wasserscheid, P., Welton, T., Eds.; Wiley-VCH Verlag GmbH & Co. KGaA: Weinheim, Germany, 2007. https://doi.org/10.1002/9783527621194.

(9) Welton, T. Ionic Liquids : Solvents for Sustainable Chemistry. *Green Chem.* **2011**, No. 13, 225.

(10) The Facts about Ammonia https://www.health.ny.gov/environmental/emergency/chemical_terrorism/ammonia_tech.htm (accessed Oct 23, 2019).

(11) Dincer, I. *Refrigeration Systems Ad Applications*, 3rd ed.; John Wiley & Sons, Incorporated, 2017.

(12) Kunioka, M.; Masuda, T.; Tachibana, Y.; Funabashi, M.; Oishi, A. Highly Selective Synthesis of Biomass-Based 1,4-Butanediol Monomer by Alcoholysis of 1,4-Diacetoxybutane Derived from Furan. *Polym. Degrad. Stab.* **2014**, *109*, 393–397. https://doi.org/10.1016/j.polymdegradstab.2014.05.011.

(13) Huang, K.; Brentzel, Z. J.; Barnett, K. J.; Dumesic, J. A.; Huber, G. W.; Maravelias, C. T. Conversion of Furfural to 1,5-Pentanediol: Process Synthesis and Analysis. *ACS Sustain. Chem. Eng.* **2017**, *5* (6), 4699–4706. https://doi.org/10.1021/acssuschemeng.7b00059.

(14) Burgard, A.; Burk, M. J.; Osterhout, R.; Van Dien, S.; Yim, H. Development of a Commercial Scale Process for Production of 1,4-Butanediol from Sugar. *Curr. Opin. Biotechnol.* **2016**, *42*, 118–125. https://doi.org/10.1016/j.copbio.2016.04.016.

(15) Yokozeki, A.; Shiflett, M. B. Ammonia Solubilities in Room-Temperature Ionic Liquids. *Ind. Eng. Chem. Res.* **2007**, *46* (5), 1605–1610. https://doi.org/10.1021/ie061260d.

(16) Yokozeki, A.; Shiflett, M. B. Vapor-Liquid Equilibria of Ammonia + Ionic Liquid

Mixtures. *Appl. Energy* **2007**, *84* (12), 1258–1273. https://doi.org/10.1016/j.apenergy.2007.02.005.

(17) Huang, J.; Riisager, A.; Berg, R. W.; Fehrmann, R. Tuning Ionic Liquids for High Gas Solubility and Reversible Gas Sorption. *J. Mol. Catal. A Chem.* **2008**, *279* (2), 170–176. https://doi.org/10.1016/j.molcata.2007.07.036.

(18) Shi, W.; Maginn, E. J. Molecular Simulation of Ammonia Absorption in the Ionic Liquid 1-Ethyl-3-Methylimidazolium Bis(Trifluoromethylsulfonyl)Imide ([Emim][Tf $_2$ N]). *AIChE J.* **2009**, *55* (9), 2414–2421. https://doi.org/10.1002/aic.11910.

(19) Li, G.; Zhou, Q.; Zhang, X.; LeiWang; Zhang, S.; Li, J. Solubilities of Ammonia in Basic Imidazolium Ionic Liquids. *Fluid Phase Equilib.* **2010**, *297* (1), 34–39. https://doi.org/10.1016/j.fluid.2010.06.005.

(20) Tomida, D.; Tani, Y.; Qiao, K.; Yokoyama, C. Vapor Pressure and Liquid Density of 1-Butyl-3-Methylimidazolium Hexafluorophosphate and Ammonia Mixtures. *High Temp. - High Press.* **2018**, *47* (2), 101–116.

(21) Palomar, J.; Gonzalez-Miquel, M.; Bedia, J.; Rodriguez, F.; Rodriguez, J. J. Task-Specific Ionic Liquids for Efficient Ammonia Absorption. *Sep. Purif. Technol.* **2011**, *82* (1), 43–52. https://doi.org/10.1016/j.seppur.2011.08.014.

(22) Bedia, J.; Palomar, J.; Gonzalez-Miquel, M.; Rodriguez, F.; Rodriguez, J. J. Screening Ionic Liquids as Suitable Ammonia Absorbents on the Basis of Thermodynamic and Kinetic Analysis. *Sep. Purif. Technol.* **2012**, *95*, 188–195. https://doi.org/10.1016/j.seppur.2012.05.006.

(23) Cera-Manjarres, A.; Salavera, D.; Coronas, A. Vapour Pressure Measurements of

Ammonia/Ionic Liquids Mixtures as Suitable Alternative Working Fluids for Absorption Refrigeration Technology. *Fluid Phase Equilib.* **2018**, *476*, 48–60. https://doi.org/10.1016/j.fluid.2018.01.006.

(24) Li, Z.; Zhang, X.; Dong, H.; Zhang, X.; Gao, H.; Zhang, S.; Li, J.; Wang, C. Efficient Absorption of Ammonia with Hydroxyl-Functionalized Ionic Liquids. *RSC Adv.* **2015**, *5* (99), 81362–81370. https://doi.org/10.1039/c5ra13730f.

(25) Chen, W.; Liang, S.; Guo, Y.; Gui, X.; Tang, D. Investigation on Vapor-Liquid Equilibria for Binary Systems of Metal Ion-Containing Ionic Liquid [Bmim]Zn2Cl5/NH3by Experiment and Modified UNIFAC Model. *Fluid Phase Equilib.* **2013**, *360*, 1–6. https://doi.org/10.1016/j.fluid.2013.09.011.

(26) Chen, W.; Bai, Y. Thermal Performance of an Absorption-Refrigeration System with [Emim]Cu2Cl5/NH3as Working Fluid. *Energy* **2016**, *112*, 332–341. https://doi.org/10.1016/j.energy.2016.06.093.

(27) Shang, D.; Zhang, X.; Zeng, S.; Jiang, K.; Gao, H.; Dong, H.; Yang, Q.; Zhang, S. Protic Ionic Liquid [Bim][NTf2] with Strong Hydrogen Bond Donating Ability for Highly Efficient Ammonia Absorption. *Green Chem.* **2017**, *19* (4), 937–945. https://doi.org/10.1039/c6gc03026b.

(28) Shang, D.; Bai, L.; Zeng, S.; Dong, H.; Gao, H.; Zhang, S. Enhanced NH3 Capture by Imidazolium-Based Protic Ionic Liquids with Different Anions and Cation Substituents. *J. Chem. Technol. Biotehcnology* **2018**, *93* (5), 1228–1236. https://doi.org/10.1002/jctb.5467.

(29) Carvalho, P. J.; Coutinho, J. A. P. Non-Ideality of Solutions of NH3, SO2, and H 2S in

Ionic Liquids and the Prediction of Their Solubilities Using the Flory-Huggins Model. *Energy and Fuels* **2010**, *24* (12), 6662–6666. https://doi.org/10.1021/ef100988z.

(30) Yokozeki, A.; Shiflett, M. B. Gas Solubilities in Ionic Liquids Using a Generic van Der Waals Equation of State. *J. Supercrit. Fluids* **2010**, *55* (2), 846–851. https://doi.org/10.1016/j.supflu.2010.09.015.

(31) Faúndez, C. A.; Díaz-Valdés, J. F.; Valderrama, J. O. Consistency Test of Solubility Data of Ammonia in Ionic Liquids Using the Modified Peng–Robinson Equation of Kwak and Mansoori. *Fluid Phase Equilib.* **2013**, *348* (348), 33–38. https://doi.org/10.1016/j.fluid.2013.03.012.

(32) Faúndez, C. A.; Quiero, F. A.; Valderrama, J. O. Correlation of Solubility Data of Ammonia in Ionic Liquids for Gas Separation Processes Using Artificial Neural Networks. *Comptes Rendus Chim.* **2014**, *17* (11), 1094–1101. https://doi.org/10.1016/j.crci.2014.01.025.

(33) Sun, G.; Huang, W.; Zheng, D.; Dong, L.; Wu, X. Vapor-Liquid Equilibrium Prediction of Ammonia-Ionic Liquid Working Pairs of Absorption Cycle Using UNIFAC Model. *Chinese J. Chem. Eng.* **2014**, *22* (1), 72–78. https://doi.org/10.1016/S1004-9541(14)60008-2.

(34) Ruiz, E.; Ferro, V. R.; De Riva, J.; Moreno, D.; Palomar, J. Evaluation of Ionic Liquids as Absorbents for Ammonia Absorption Refrigeration Cycles Using COSMO-Based Process Simulations. *Appl. Energy* **2014**, *123*, 281–291. https://doi.org/10.1016/j.apenergy.2014.02.061.

(35) Lei, Z. G.; Dai, C. N.; Chen, B. H. Gas Solubility in Ionic Liquids. *Chem. Rev.* **2014**, *114*

(2), 1289–1326. https://doi.org/10.1021/cr300497a.

(36) Chernikova, E. A.; Glukhov, L. M.; Krasovskiy, V. G.; Kustov, L. M.; Vorobyeva, M. G.; Koroteev, A. A. Ionic Liquids as Heat Transfer Fluids: Comparison with Known Systems, Possible Applications, Advantages and Disadvantages. *Russ. Chem. Rev.* **2015**, *84* (8), 875–890. https://doi.org/10.1070/RCR4510.

(37) Musiał, M.; Malarz, K.; Mrozek-Wilczkiewicz, A.; Musiol, R.; Zorębski, E.; Dzida, M. Pyrrolidinium-Based Ionic Liquids as Sustainable Media in Heat-Transfer Processes. *ACS Sustain. Chem. Eng.* **2017**, *5* (11), 11024–11033. https://doi.org/10.1021/acssuschemeng.7b02918.

(38) Watanabe, M.; Thomas, M. L.; Zhang, S.; Ueno, K.; Yasuda, T.; Dokko, K. Application of Ionic Liquids to Energy Storage and Conversion Materials and Devices. *Chem. Rev.* **2017**, *117* (10), 7190–7239. https://doi.org/10.1021/acs.chemrev.6b00504.

(39) He, T.; Wang, Y. F.; Zeng, J. H. Stable, High-Efficiency Pyrrolidinium-Based Electrolyte for Solid-State Dye-Sensitized Solar Cells. **2015**, 21381–21390. https://doi.org/10.1021/acsami.5b06035.

(40) Taher, M.; Shah, F. U.; Filippov, A.; de Baets, P.; Glavatskih, S.; Antzutkin, O. N. Halogen-Free Pyrrolidinium Bis(Mandelato)Borate Ionic Liquids: Some Physicochemical Properties and Lubrication Performance as Additives to Polyethylene Glycol. *RSC Adv.* **2014**, *4* (58), 30617–30623. https://doi.org/10.1039/C4RA02551B.

(41) Anthony, J. L.; Anderson, J. L.; Maginn, E. J.; Brennecke, J. F. Anion Effects on Gas Solubility in Ionic Liquids. *J. Phys. Chem. B* **2005**, *109* (13), 6366–6374. https://doi.org/10.1021/jp046404l.

(42) Hong, G.; Jacquemin, J.; Deetlefs, M.; Hardacre, C.; Husson, P.; Costa Gomes, M. F. Solubility of Carbon Dioxide and Ethane in Three Ionic Liquids Based on the Bis{(Trifluoromethyl)Sulfonyl}imide Anion. *Fluid Phase Equilib.* **2007**, *257* (1), 27–34. https://doi.org/10.1016/j.fluid.2007.05.002.

(43) Yim, J. H.; Song, H. N.; Yoo, K. P.; Lim, J. S. Measurement of CO2 Solubility in Ionic Liquids: [BMP][Tf2N] and [BMP][MeSO4] by Measuring Bubble-Point Pressure. *J. Chem. Eng. Data* **2011**, *56* (4), 1197–1203. https://doi.org/10.1021/je101100d.

(44) Yim, J. H.; Song, H. N.; Lee, B. C.; Lim, J. S. Corrigendum to "High-Pressure Phase Behavior of Binary Mixtures Containing Ionic Liquid [HMP][Tf2N], [OMP][Tf2N] and Carbon Dioxide" [Fluid Phase Equilib. 308 (2011) 147-152]. *Fluid Phase Equilib.* **2014**, *368*, 142. https://doi.org/10.1016/j.fluid.2014.02.017.

(45) Kim, S. A.; Yim, J. H.; Lim, J. S. High-Pressure Phase Behavior of Binary Mixtures Containing Methylpyrrolidinium Derivative Ionic Liquids and Carbon Dioxide. *Fluid Phase Equilib.* **2012**, *332* (1–2), 28–34. https://doi.org/10.1016/j.fluid.2012.07.006.

(46) Lourenço, T. C.; Aparicio, S.; Costa, G. C.; Costa, L. T. Local Environment Structure and Dynamics of CO2in the 1-Ethyl-3-Methylimidazolium Bis(Trifluoromethanesulfonyl)Imide and Related Ionic Liquids. *J. Chem. Phys.* **2017**, *146* (10), 104502/1-104502/12. https://doi.org/10.1063/1.4977786.

(47) Crosthwaite, J. M.; Aki, S. N. V. K.; Maginn, E. J.; Brennecke, J. F. Liquid Phase Behavior of Imidazolium-Based Ionic Liquids with Alcohols. *J. Phys. Chem. B* **2004**, *108* (16), 5113–5119. https://doi.org/10.1021/jp037774x.

(48) Heintz, A.; Klasen, D.; Lehmann, J. K.; Wertz, C. Excess Molar Volumes and Liquid-

Liquid Equilibria of the Ionic Liquid 1-Methyl-3-Octyl-Imidazolium Tetrafluoroborate Mixed with Butan-1-Ol and Pentan-1-Ol. *J. Solution Chem.* **2005**, *34* (10), 1135–1144. https://doi.org/10.1007/s10953-005-7692-y.

(49) Domańska, U.; Bogel-Łukasik, E.; Bogel-Łukasik, R. Solubility of 1-Dodecyl-3-Methylimidazolium Chloride in Alcohols (C2-C12). *J. Phys. Chem. B* **2003**, *107* (8), 1858–1863. https://doi.org/10.1021/jp021332o.

(50) Crosthwaite, J. M.; Aki, S. N. V. K.; Maginn, E. J.; Brennecke, J. F. Liquid Phase Behavior of Imidazolium-Based Ionic Liquids with Alcohols: Effect of Hydrogen Bonding and Non-Polar Interactions. *Fluid Phase Equilib.* **2005**, *228–229*, 303–309. https://doi.org/10.1016/j.fluid.2004.07.014.

(51) Qiao, Y.; Ma, W.; Theyssen, N.; Chen, C.; Hou, Z. Temperature-Responsive Ionic Liquids: Fundamental Behaviors and Catalytic Applications. *Chem. Rev.* **2017**, *117* (10), 6881–6928. https://doi.org/10.1021/acs.chemrev.6b00652.

(52) Makowska, A.; Papis, P.; Szydłowski, J. Miscibility of Tetrafluoroborate Ionic Liquids with Dihydroxy Alcohols. *J. Mol. Liq.* **2012**, *176*, 86–92. https://doi.org/10.1016/j.molliq.2012.06.013.

(53) Makowska, A.; Dyoniziak, E.; Siporska, A.; Szydłowski, J. Miscibility of Ionic Liquids with Polyhydric Alcohols. *J. Phys. Chem. B* **2010**, *114* (7), 2504–2508. https://doi.org/10.1021/jp911660a.

(54) Makowska, A.; Sztank, E.; Szydłowski, J. Liquid Phase Behavior of Hexafluorophosphate Ionic Liquids with Polyhydric Alcohols. *Fluid Phase Equilib.* **2012**, *314*, 140–145. https://doi.org/10.1016/j.fluid.2011.11.004.

(55) Forte, A.; Bogel-Łukasik, E.; Bogel-Łukasik, R. Miscibility Phenomena in Systems Containing Polyhydroxy Alcohols and Ionic Liquids. *J. Chem. Eng. Data* **2011**, *56* (5), 2273–2279. https://doi.org/10.1021/je101269p.

(56) Shiflett, M. B.; Yokozeki, A. Liquid - Liquid Equilibria in Binary Mixtures of 1,3-Propanediol + Ionic Liquids [Bmim][PF_6], [Bmim][BF_4], and [Emim][BF_4]. *J Chem Eng Data* **2007**, *52* (500), 1302–1306. https://doi.org/10.1021/je700037z.

(57) Trindade, C. A. S.; Visak, Z. P.; Bogel-łukasik, R.; Bogel-łukasik, E.; Nunes da Ponte, M. Liquid−Liquid Equilibrium of Mixtures of Imidazolium-Based Ionic Liquids with Propanediols or Glycerol. *Ind. Eng. Chem. Res.* **2010**, *49* (10), 4850–4857.

(58) Zhang, X.; Liu, Z.; Wang, W. Screening of Ionic Liquids to Capture CO2 by COSMO-RS and Experiments. *AIChE J.* **2008**, *54* (10), 2717–2728. https://doi.org/10.1002/aic.11573.

(59) Kumełan, J.; Tuma, D.; Kamps, Á. L. P. S.; Maurer, G. Solubility of the Single Gases Carbon Dioxide and Hydrogen in the Ionic Liquid [Bmpy][Tf2N]. *J. Chem. Eng. Data* **2010**, *55* (1), 165–172. https://doi.org/10.1021/je900298e.

(60) Song, H. N.; Lee, B.-C.; Lim, J. S. Measurement of CO2 Solubility in Ionic Liquids: [BMP][TfO] and [P14,6,6,6][Tf2N] by Measuring Bubble-Point Pressure. *J. Chem. Eng. Data* **2010**, *55* (2), 891–896. https://doi.org/10.1021/je9005085.

(61) Yim, J.-H.; Song, H. N.; Lee, B.-C.; Lim, J. S. High-Pressure Phase Behavior of Binary Mixtures Containing Ionic Liquid [HMP][Tf2N], [OMP][Tf2N] and Carbon Dioxide. *Fluid Phase Equilib.* **2011**, *308* (1–2), 147–152. https://doi.org/10.1016/J.FLUID.2011.06.023.

(62) Manic, M. S.; Queimada, A. J.; Macedo, E. A.; Najdanovic-Visak, V. High-Pressure

Solubilities of Carbon Dioxide in Ionic Liquids Based on Bis(Trifluoromethylsulfonyl)Imide and Chloride. *J. Supercrit. Fluids* **2012**, *65*, 1–10. https://doi.org/10.1016/J.SUPFLU.2012.02.016.

(63) Makino, T.; Kanakubo, M.; Umecky, T.; Suzuki, A.; Nishida, T.; Takano, J. Pressure-Volume-Temperature-Composition Relations for Carbon Dioxide+pyrrolidinium-Based Ionic Liquid Binary Systems. *Fluid Phase Equilib.* **2013**, *360*, 253–259. https://doi.org/10.1016/j.fluid.2013.09.036.

(64) Stevanovic, S.; Podgorsek, A.; Moura, L.; Santini, C. C.; Padua, A. A. H.; Costa Gomes, M. F. Absorption of Carbon Dioxide by Ionic Liquids with Carboxylate Anions. *Int. J. Greenh. Gas Control* **2013**, *17*, 78–88. https://doi.org/10.1016/j.ijggc.2013.04.017.

(65) Lee, B. C.; Nam, S. G. High-Pressure Solubility of Carbon Dioxide in Pyrrolidinium-Based Ionic Liquids: [Bmpyr][Dca] and [Bmpyr][Tf2N]. *Korean J. Chem. Eng.* **2015**, *32* (3), 521–533. https://doi.org/10.1007/s11814-014-0364-0.

(66) Altamash, T.; Haimour, T. S.; Tarsad, M. A.; Anaya, B.; Ali, M. H.; Aparicio, S.; Atilhan, M. Carbon Dioxide Solubility in Phosphonium-, Ammonium-, Sulfonyl-, and Pyrrolidinium-Based Ionic Liquids and Their Mixtures at Moderate Pressures up to 10 Bar. *J. Chem. Eng. Data* **2017**, *62* (4), 1310–1317. https://doi.org/10.1021/acs.jced.6b00833.

(67) Shiflett, M. B.; Yokozeki, A. Solubility and Diffusivity of Hydrofluorocarbons in Room-Temperature Ionic Liquids. *Aiche J.* **2006**, *52* (3), 1205–1219.

(68) Brennecke, J. F.; Lopez-Castillo, Z. K.; Mellein, B. R. Gas Solubilities in Ionic Liquids and Related Measurement Techniques. In *Ionic Liquids in Chemical Analysis*; Florida,

USA, 2009; pp 229–241.

(69) Shiflett, M. B.; Yokozeki, A. Phase Behavior of Gases Ionic Liquids. In *Ionic Liquids Uncoiled: Critical Expert Overviews*; Plechkova, N. V., Seddon, K. R., Eds.; John Wiley & Sons, 2012.

(70) Anthony, J. L.; Maginn, E. J.; Brennecke, J. F. Solution Thermodynamics of Imidazolium-Based Ionic Liquids and Water. *J. Phys. Chem. B* **2001**, *105* (44), 10942–10949.

(71) Shiflett, M. B.; Maginn, E. J. The Solubility of Gases in Ionic Liquids. *Am. Inst. Chem. Eng. J.* **2017**, *63* (11), 4722–4737. https://doi.org/10.1002/aic.15957.

(72) Hiden Isochema. XEMIS Brochure https://hidenisochema.com/content/uploads/2017/01/Hiden-Isochema-XEMIS-Brochure.pdf (accessed Oct 3, 2019).

(73) Lemmon, E. W.; Huber, M. L.; Mclinden, M. O. REFPROP 9.1. *NIST Stand. Ref. database* **2013**.

(74) Hiden. IGA-001 https://hidenisochema.com/hiden-products/iga-001/ (accessed Oct 8, 2019).

(75) Kohn, J. The Heterogeneous Phase and Volumetric Behavior of the Methane-Hydrogen-Sulfide System. **1957**, University of Kansas, PhD Dissertation.

(76) Scurto, A. M. High-Pressure Phase and Chemical Equilibria of <font Face="symbol">b</Font>-Diketone Ligands and Chelates with Carbon Dioxide. **2002**, University of Notre Dame, PhD Dissertation.

(77) Huie, N. C. The Heterogenous Phase Equilibria of Carbon Dioixide- Normal Paraffin Systems. **1972**, University of Notre Dame, PhD Dissertation.

(78) Ren, W.; Scurto, A. M. High-Pressure Phase Equilibria with Compressed Gases. *Rev. Sci. Instrum.* **2007**, *78* (12), 125104. https://doi.org/10.1063/1.2814025.

(79) Ren, W. High-Pressure Phase Equilibria of Ionic Liquids and Compressed Gases for Applications in Reactions and Absorption Refrigeration. **2009**, University of Kansas, PhD Dissertation.

(80) Shiflett, M. B.; Yokozeki, A. Vapor - Liquid - Liquid Equilibria of Hydrofluorocarbons + 1-Butyl-3-Methylimidazolium Hexafluorophosphate. *J. Chem. Eng. Data* **2006**, *51* (5), 1931–1939. https://doi.org/10.1021/je060275f.

(81) Shiflett, M. B.; Yokozeki, A. Vapor-Liquid-Liquid Equilibria of Pentafluoroethane and Ionic Liquid [Bmim][PF_6] Mixtures Studied with the Volumetric Method. *J. Phys. Chem. B* **2006**, *110* (29), 14436–14443. https://doi.org/10.1021/jp062437k.

(82) Gupta, S. V. Capillary Action in Narrow and Wide Tubes - A Unified Approach. *Metrologia* **2004**, *41* (6), 361–364. https://doi.org/10.1088/0026-1394/41/6/001.

(83) Wernecke, R.; Wernecke, J. *Industrial Moisture and Humidity Measurement : A Practical Guide*; John Wiley & Sons, Incorporated, 2014.

(84) Scholz, E. *Karl Fischer Titration: Determination of Water*; 1984.

(85) EMD. Karl Fischer Titration Basics https://www.emdmillipore.com/Web-US-Site/en_CA/-/USD/ShowDocument-Pronet?id=200907.358. (accessed Oct 9, 2019).

(86) Mettler Toledo DL36 Karl Fischer Coulometric Titration Manual. **1996**.

(87) Brignole, E.; Pereda, S. Phase Equilibrium Engineering; Elsevier, 2013.

(88) Prausnitz, J. M.; Lichtenthaler, R. N.; Gomes de Azevedo, E. *Molecular Thermodynamics of Fluid-Phase Equilibria*, Third.; Prentince Hall PTR, 1999.

(89) Smith, J. M.; Van Ness, H. C.; Abbott, M. M. *Introduction to Chemical Engineering Thermodynamics*, seventh.; McGraw Hill, 2005.

(90) Shiflett, M. B.; Yokozeki, A. Gaseous Absorption of Fluoromethane, Fluoroethane, and 1,1,2,2-Tetrafluoroethane in 1-Butyl-3-Methylimidazolium Hexafluorophosphate. *Ind. Eng. Chem. Res.* **2006**, *45* (18), 6375–6382.

(91) Van der Waals, J. H. Over de Continuited van Den Gas-En Vloeistoftoestand (On the Continuation of Gaseous and Liquid State). *1873* University of Lieden. PhD Dissertation.

(92) Redlich, O.; Kwong, J. N. S. On the Thermodynamics of Solutions. V. An Equation of State. Fugacities of Gaseous Solutions. *Chem. Rev.* **1949**, *44* (1), 233–244. https://doi.org/10.1021/cr60137a013.

(93) Soave, G. Equilibrium Constants from a Modified Redlich-Kwong Equation of State. *Chem. Eng. Sci.* **1972**, *27* (6), 1197–1203. https://doi.org/10.1016/0009-2509(72)80096-4.

(94) Goodwin, A. R. . .; Sengers, J. V.; Peters, C. J. *Applied Thermodynamics of Fluids*; The Royal Society of Chemistry, 2010.

(95) Lopez-Echeverry, J. S.; Reif-Acherman, S.; Araujo-Lopez, E. Peng-Robinson Equation of State: 40 Years through Cubics. *Fluid Phase Equilib.* **2017**, *447*, 39–71. https://doi.org/10.1016/j.fluid.2017.05.007.

(96) Peng, D. Y.; Robinson, D. B. A New Two-Constant Equation of State. *Ind. Eng. Chem. Fundam.* **1976**, *15* (1), 59–64. https://doi.org/10.1021/i160057a011.

(97) Weinhold, F. *Classical and Geometrical Theory of Chemical and Phase Thermodynamics*; John Wiley & Sons, Incorporated, 2009.

(98) Danesh, A. PVT and Phase Behaviour of Petroleum Reservoir Fluids; Elsevier, 1998; pp

129–149.

(99) Sandler, S. I. *Chemical, Biochemical and Engineering Thermodynamics*, 4th ed.; John Wiley & Sons, Inc., 2006.

(100) H., R.; J.M., P. Local Compositions in Thermodynamic Excess Functions for Liquid Mixtures. *AICHE J.* **1968**, *14* (1), 135–144.

(101) Wilson, G. M. Vapor-Liquid Equilibrium. XI. A New Expression for the Excess Free Energy of Mixing. *J. Am. Chem. Soc.* **1963**, *86* (2), 127–130. https://doi.org/10.1021/ja01056a002.

(102) Scott, R. L. Corresponding States Treatment of Nonelectrolyte Solutions. *J. Chem. Physcis* **1956**, *25* (2), 193–205.

(103) Gebreyohannes, S.; Neely, B. J.; Gasem, K. A. M. Generalized Nonrandom Two-Liquid (NRTL) Interaction Model Parameters for Predicting Liquid-Liquid Equilibrium Behavior. *Ind. Eng. Chem. Res.* **2014**, *53* (31), 12445–12454. https://doi.org/10.1021/ie501699a.

(104) Flory, P. J. *Principles of Polymer Chemistry*; Cornell University Presss, 1953.

(105) Flory, P. J. Thermodynamics of High Polymer Solutions. *J. Chem. Phys.* **1941**, *10* (9), 8–10. https://doi.org/10.1063/1.1750971.

(106) Flory, P. J. Themodynamics of High Polymer Solutions. *J. Chem. Phys.* **1942**, *10* (1), 51–61. https://doi.org/10.1063/1.1723621.

(107) Huggins, M. L. Solutions of Long Chain Compounds. *J. Chem. Phys.* **1941**, *9* (5), 440. https://doi.org/10.1063/1.1750930.

(108) Nagy, E. Chapter 18: Membrane Gas Separation. In *Basic Equations of Mass Transport*

Through a Membrane Layer; Elsevier, 2019; pp 457–481.

(109) Carvalho, P. J.; Coutinho, J. A. P. On the Nonideality of CO2 Solutions in Ionic Liquids and Other Low Volatile Solvents. *J. Phys. Chem. Lett.* **2010**, *1* (4), 774–780. https://doi.org/10.1021/jz100009c.

(110) Coutinho, J. A. P.; Andersen, S. I.; Stenby, E. H. Evaluation of Activity Coefficient Models in Prediction of Alkane Solid-Liquid Equilibria. *Fluid Phase Equilib.* **1995**, *103* (1), 23–39. https://doi.org/10.1016/0378-3812(94)02600-6.

(111) Sandler, S. I. *Chemical, Biochemical and Engineering Thermodynamics*, Fourth.; John Wiley & Sons, Inc., 2006.

(112) Domańska, U.; Głoskowska, M. Experimental Solid + Liquid Equilibria and Excess Molar Volumes of Alkanol + Hexylamine Mixtures. *Fluid Phase Equilib.* **2003**, *216* (1), 135–145. https://doi.org/10.1016/j.fluid.2003.10.007.

(113) Senichev, V. .; Tereshatov, V. V. Chapter 4: General Principles Governing Dissolution of Materials in Solvents. In *Handbook of Solvents Volume 1*; Wypych, G., Ed.; Elsevier, 2019; pp 133–275.

(114) Kroon, M. C.; Peters, C. J. Chapter 4:Phase Behavior of Ionic Liquid Systems. In *Applied Thermodynamics of Fluids*; Goodwin, A. R. . ., Sengers, J. V., Peters, C. J., Eds.; Royal Society of Chemistry, 2010.

(115) Chirico, R. D.; Diky, V.; Magee, J. W.; Frenkel, M.; Marsh, K. N. Thermodynamic and Thermophysical Properties of the Reference Ionic Liquid: 1-Hexyl-3-Methylimidazolium Bis[(Trifluoromethyl)Sulfonyl]Amide (Including Mixtures). Part 2. Critical Evaluation and Recommended Property Values (IUPAC Technical Report). *Pure Appl. Chem.* **2009**,

81 (5), 791–828. https://doi.org/10.1351/PAC-REP-08-09-22.

(116) Shiflett, M. B.; Yokozeki, A. Solubility of CO2 in Room Temperature Ionic Liquid [Hmim][Tf2N]. *J. Phys. Chem. B* **2007**, *111* (8), 2070–2074. https://doi.org/0.1021/jp067627+.

(117) Kumełan, J.; Pérez-Salado Kamps, Á.; Tuma, D.; Maurer, G. Solubility of CO2 in the Ionic Liquid [Hmim][Tf2N]. *J. Chem. Thermodyn.* **2006**, *38* (11), 1396–1401. https://doi.org/10.1016/J.JCT.2006.01.013.

(118) Raeissi, S.; Florusse, L.; Peters, C. J. Scott-van Konynenburg Phase Diagram of Carbon Dioxide + Alkylimidazolium-Based Ionic Liquids. *J. Supercrit. Fluids* **2010**, *55* (2), 825–832. https://doi.org/10.1016/j.supflu.2010.09.042.

(119) Fan, W.; Zhou, Q.; Sun, J.; Zhang, S. Density, Excess Molar Volume, and Viscosity for the Methyl Methacrylate + 1-Butyl-3-Methylimidazolium Hexafluorophosphate Ionic Liquid Binary System at Atmospheric Pressure. *J. Chem. Eng. Data* **2009**, *54* (8), 2307–2311. https://doi.org/10.1021/je900091b.

(120) Matkowska, D.; Hofman, T. High-Pressure Volumetric Properties of Ionic Liquids: 1-Butyl-3- Methylimidazolium Tetrafluoroborate, [C4mim][BF4], 1-Butyl-3-Methylimidazolium Methylsulfate [C4mim][MeSO4] and 1-Ethyl-3-Methylimidazolium Ethylsulfate, [C2mim][EtSO4]. *J. Mol. Liq.* **2012**, *165*, 161–167. https://doi.org/10.1016/j.molliq.2011.11.004.

(121) Fillion, J. J.; Brennecke, J. F. Viscosity of Ionic Liquid-Ionic Liquid Mixtures. *J. Chem. Eng. Data* **2017**, *62* (6), 1884–1901. https://doi.org/10.1021/acs.jced.7b00221.

(122) Larriba, M.; García, S.; García, J.; Torrecilla, J. S.; Rodríguez, F. Thermophysical

Properties of 1-Ethyl-3-Methylimidazolium 1,1,2,2-Tetrafluoroethanesulfonate and 1-Ethyl-3-Methylimidazolium Ethylsulfate Ionic Liquids as a Function of Temperature. *J. Chem. Eng. Data* **2011**, *56* (9), 3589–3597. https://doi.org/10.1021/je2004462.

(123) ASPEN Plus (R). Aspen Technology, Inc.

(124) Valderrama, J. O.; Robles, P. A. Critical Properties, Normal Boiling Temperatures, and Acentric Factors of Fifty Ionic Liquids. *Ind. Eng. Chem. Res.* **2007**, *46* (4), 1338–1344. https://doi.org/10.1021/ie0603058.

(125) Temperature and Concentration Dependence of Interaction Parameter http://polymerdatabase.com/polymer physics/Chi Temp dependence.html (accessed Nov 22, 2019).

(126) Greaves, T. L.; Drummond, C. J. Protic Ionic Liquids: Properties and Applications. *Chem. Rev.* **2008**, *108* (1), 206–237. https://doi.org/10.1021/cr068040u.

(127) Seki, S.; Tsuzuki, S.; Hayamizu, K.; Umebayashi, Y.; Serizawa, N.; Takei, K.; Miyashiro, H. Comprehensive Refractive Index Property for Room-Temperature Ionic Liquids. *J. Chem. Eng. Data* **2012**, *57* (8), 2211–2216. https://doi.org/10.1021/je201289w.

(128) Gardas, R. L.; Costa, H. F.; Freire, M. G.; Carvalho, P. J.; Marrucho, I. M.; Fonseca, I. M. A.; Ferreira, A. G. M.; Coutinho, J. A. P. Densities and Derived Thermodynamic Properties of Imidazolium- , Pyridinium- , Pyrrolidinium- , and Piperidinium-Based Ionic Liquids. **2008**, 805–811.

(129) Vranes, M.; Dozic, S.; Djeric, V.; Gadzuric, S. Physicochemical Characterization of 1-Butyl-3-Methylimidazolium and 1-Butyl-1-Methylpyrrolidinium Bis(Trifluoromethylsulfonyl)Imide. *J. Chem. Eng. Data* **2012**, *57* (4), 1072–1077.

https://doi.org/10.1021/je2010837.

(130) Nebig, S.; Liebert, V.; Gmehling, J. Measurement and Prediction of Activity Coefficients at Infinite Dilution (Γ∞), Vapor-Liquid Equilibria (VLE) and Excess Enthalpies (HE) of Binary Systems with 1,1-Dialkyl-Pyrrolidinium Bis(Trifluoromethylsulfonyl)Imide Using Mod. UNIFAC (Dortmund). *Fluid Phase Equilib.* **2009**, *277* (1), 61–67. https://doi.org/10.1016/j.fluid.2008.11.013.

(131) Yokozeki, A.; Shiflett, M. B.; Junk, C. P.; Grieco, L. M.; Foo, T. Physical and Chemical Absorptions of Carbon Dioxide in Room-Temperature Ionic Liquids. *J. Phys. Chem. B* **2008**, *112* (51), 16654–16663. https://doi.org/10.1021/jp805784u.

(132) Kumelan, J.; Kamps, I. P. S.; Tuma, D.; Maurer, G. Solubility of CO2 in the Ionic Liquid [Hmim][Tf2N]. *J. Chem. Thermodyn.* **2006**, *38* (11), 1396–1401. https://doi.org/10.1016/j.jct.2006.01.013.

(133) Hou, Y.; Baltus, R. E. Experimental Measurement of the Solubility and Diffusivity of CO2 in Room-Temperature Ionic Liquids Using a Transient Thin-Liquid-Film Method. *Ind. Eng. Chem. Res.* **2007**, *46* (24), 8166–8175. https://doi.org/10.1021/ie070501u.

(134) Aki, S. N. V. K.; Mellein, B. R.; Saurer, E. M.; Brennecke, J. F. High-Pressure Phase Behavior of Carbon Dioxide with Imidazolium-Based Ionic Liquids. **2004**. https://doi.org/10.1021/jp046895.

(135) Scurto, A. M.; Hutcheson, K.; Subranamiam, B. Gas-Expanded Liquids: Fundamentals and Applications; 2009; pp 3–37.

(136) Shiflett, M. B.; Yokozeki, A. Solubilities and Diffusivities of Carbon Dioxide in Ionic Liquids: [Bmim][PF6] and [Bmim][BF4]. *Ind. Eng. Chem. Res.* **2005**, *44* (12), 4453–

4464. https://doi.org/10.1021/ie058003d.

(137) Hefter, G. T.; Barton, A. F. M.; Chand, A. Semi-Automated Apparatus for the Determination of Liquid Solubilities: Mutual Solubilities of Water and Butan-2-Ol. *J. Chem. Soc. Faraday Trans.* **1991**, *87* (4), 591–596. https://doi.org/10.1039/FT9918700591.

(138) Ochi, K.; Saito, T.; Kojima, K. Measurement and Correlation of Mutual Solubilities in 2-Butanol + Water. *J. Chem. Eng. Data* **1996**, *41* (2), 361–364. https://doi.org/10.1021/je9502399.

(139) Mahajan, A. R.; Mirgane, S. R. Excess Molar Volumes and Viscosities for the Binary Mixtures of N-Octane, n-Decane, n-Dodecane, and n-Tetradecane with Octan-2-Ol at 298.15 K. *J. Thermodyn.* **2013**, 1–11. https://doi.org/10.1155/2013/571918.

(140) Rafiee, H. R.; Frouzesh, F. The Study of Partial and Excess Molar Volumes for Binary Mixtures of Nitrobenzene and Benzaldehyde with Xylene Isomers from T = (298.15 to 318.15) K and P = 0.087 MPa. *J. Adv. Res.* **2016**, *7* (5), 769–780. https://doi.org/10.1016/j.jare.2015.11.003.

(141) Grenner, A.; Klauck, M.; Kramer, M.; Schmelzer, J. Activity Coefficients at Infinite Dilution of Cylcohexylamine + Octane, Toluene, Ethylbenzene, or Aniline and Excess Molar Volumes in Binary Mixtures of Cyclohexylamine + Heptane, Octane, Nonane, Decane, Undecane, Aniline, or Water. *J. Chem. Eng. Data* **2006**, *51* (1), 176–180. https://doi.org/10.1021/je050316s.

(142) Chen, J. T.; Shiah, I. M.; Chu, H. P. Excess Molar Volumes and Viscosities for Binary Mixtures of Propylene Glycol Monomethyl Ether with Methacrylic Acid, Benzyl

Methacrylate, and 2-Hydroxyethyl Methacrylate at (298.15, 308.15, and 318.15) K. *J. Chem. Eng. Data* **2006**, *51* (6), 2156–2160. https://doi.org/10.1021/je060288t.

(143) Domańska, U.; Marciniak, M. Experimental (Solid + Liquid) and (Liquid + Liquid) Equilibria and Excess Molar Volume of Alkanol + Acetonitrile, Propanenitrile, and Butanenitrile Mixtures. *J. Chem. Eng. Data* **2005**, *50* (6), 2035–2044. https://doi.org/10.1021/je050262m.

(144) Freire, M. G.; Neves, C.; Marrucho, I. M.; Coutinho, J. A. P.; Fernandes, A. M. Hydrolysis of Tetrafluoroborate and Hexafluorophosphate Counter Ions in Imidazolium-Based Ionic Liquids. *J. Phys. Chem. A* **2010**, *114* (11), 3744–3749. https://doi.org/10.1021/jp903292n.

(145) Pirrung, M. *Handbook of Synthetic Organic Chemistry*, 2nd ed.; Elsevier: San Diego, California, 2017.

(146) Seddon, K. R.; Rogers, R. D. *Ionic Liquids Further UnCOILed : Critical Expert Overviews*; John Wiley & Sons, Inc., 2011.

(147) Terasaka, K.; Oka, J.; Tsuge, H. Ammonia Absorption from a Bubble Expanding at a Submerged Oriÿce into Water. **2002**, *57*, 3757–3765.

(148) Mark B. Shiflett, *,†; Mark A. Harmer, †; Christopher P. Junk, † and; Yokozeki‡, A. Solubility and Diffusivity of Difluoromethane in Room-Temperature Ionic Liquids. **2006**. https://doi.org/10.1021/JE050386Z.

(149) Jacquemin, J.; Husson, P.; Padua, A. A. H.; Majer, V. Density and Viscosity of Several Pure and Water-Saturated Ionic Liquids. **2006**, 172–180. https://doi.org/10.1039/b513231b.

(150) Kammeyer, C. W.; Whitman, D. R. Quantum Mechanical Calculation of Molecular Radii. I. Hydrides of Elements of Periodic Groups IV through VII. **1972**, *56* (9), 4419–4421.

(151) Balci, M. *Basic ^{1}H- and ^{13}C-NMR Spectroscopy*; Elsevier Science & Technology, 2005.

(152) Plechkova, N. V.; Seddon, K. R. *Ionic Liquids Completely UnCOILed: Critical Expert Overviews*; Wiley, 2015.

(153) Paschoal, V. H.; Faria, L. F. O.; Ribeiro, M. C. C. Vibrational Spectroscopy of Ionic Liquids. *ACS Chem. Rev.* **2017**, *117*, 7053−7112. https://doi.org/10.1021/acs.chemrev.6b00461.

(154) Gunther, H. *NMR Spectroscopy : Basic Principles, Concepts and Applications in Chemistry*; John Wiley & Sons, Incorporated, 2013.

(155) Nuclei Oreintation in Proton NMR https://gfycat.com/gifs/search/proton+spin.

(156) Carbajo, R. J.; Neira, J. L. *NMR for Chemists and Biologists*; Springer, 2013.

(157) Reich, H. J. 5-HMR-2 Chemical Shift https://www.chem.wisc.edu/areas/reich/nmr/05-hmr-02-delta.htm (accessed Nov 18, 2019).

(158) NMR in Malott https://nmrlab.ku.edu/instrumentation (accessed Nov 19, 2019).

(159) Vataščin, E.; Dohnal, V. Aqueous Solutions of [EMIM] 1,1,2,2-Tetrafluoroethanesulfonate and [EMIM] Trifluoromethanesulfonate: A Thermodynamic Study. *J. Chem. Thermodyn.* **2018**, *119*, 114–126. https://doi.org/10.1016/j.jct.2017.12.019.

(160) Gilbert, W. J.; Shiflett, M. Design and Safety in a New Chemical Engineering Research Laboratory at The University of Kansas. *J. Ind. Eng. Saf.* **2018**, *1* (1), 1–13.

(161) Olewski, T.; Snakard, M. Challenges in Applying Process Safety Management at

University Laboratories. *J. Loss Prev. Process Ind.* **2017**, *49*, 209–214. https://doi.org/10.1016/j.jlp.2017.06.013.

(162) Yang, Y.; Reniers, G.; Chen, G.; Goerlandt, F. A Bibliometric Review of Laboratory Safety in Universities. *Saf. Sci.* **2019**, *120* (March), 14–24. https://doi.org/10.1016/j.ssci.2019.06.022.

(163) Álvarez-Chávez, C. R.; Marín, L. S.; Perez-Gamez, K.; Portell, M.; Velazquez, L.; Munoz-Osuna, F. Assessing College Students' Risk Perceptions of Hazards in Chemistry Laboratories. *J. Chem. Educ.* **2019**, *96* (10), 2120–2131. https://doi.org/10.1021/acs.jchemed.8b00891.

(164) Nitsche, C. I. Promoting Safety Culture: An Overview of Collaborative Chemical Safety Information Initiatives. *J. Chem. Heal. Saf.* **2019**, *26* (3), 27–30. https://doi.org/10.1016/j.jchas.2018.12.004.

(165) Cadwallader, L. C.; Pawelko, R. J. Elements of Experiment Safety in the Laboratory. *J. Chem. Heal. Saf.* **2019**, *26* (4–5), 20–25. https://doi.org/10.1016/j.jchas.2019.01.002.

(166) Fivizzani, K. P. Where Are We with Lab Safety Education: Who, What, When, Where, and How? *J. Chem. Heal. Saf.* **2016**, *23* (5), 18–20. https://doi.org/10.1016/j.jchas.2015.11.001.

(167) Piong, H. S.; Chin, K. Y.; Bakar, H. T. A.; Ling, C. H.; Kidam, K.; Ali, M. W.; Hassim, M. H.; Kamarden, H. The Contribution of Management of Change to Process Safety Accident in the Chemical Process Industry. *Chem. Eng. Trans.* **2017**, *56*, 1363–1368. https://doi.org/10.3303/CET1756228.

Appendix A1. Experimental Vapor-Liquid Equilibrium and Modeled Diffusivity Data for NH_3(1) and $[C_4C_1im][PF_6]$ (2) System

T (K)	P (MPa)	C_o (mass %)	C_s[a] (mass %)	w_1 (mass %)	D[a] (* 10^{-10} $m^2 \cdot s^{-1}$)	$x_{1,\ calculated}$ (mol %)	$x_{1,\ measured}$[b] (mol %)	S (mass %)
283.15	0.0100	-	-	0.33	-	-	-	
283.15	0.0500	0.67	1.27	1.27	0.8 ± 0.01	17.9	17.7	0.18
283.15	0.1000	1.78	2.73	2.73	1.0 ± 0.03	31.3	31.9	0.39
283.15	0.1380	3.25	3.89	3.89	1.1 ± 0.03	40.3	40.3	0.23
283.15	0.1940	4.68	5.78	5.78	1.4 ± 0.04	50.5	50.6	0.19
283.15	0.2590	7.10	8.34	8.34	2.0 ± 0.07	60.1	60.3	0.12
283.15	0.3000	9.35	10.23	10.23	2.2 ± 0.07	65.4	65.5	0.09
283.15	0.4000	13.41	16.20	16.20	3.2 ± 0.21	76.2	76.3	0.12
283.15	0.5170	21.37	30.02	30.02	3.4 ± 0.66	87.7	87.7	0.11
298.15	0.0100	-	-	0.21	-	-	3.4	-
298.15	0.0500	0.34	0.86	0.86	1.0 ± 0.01	11.6	12.7	0.08
298.15	0.1000	1.14	1.60	1.60	1.5 ± 0.02	21.6	21.4	-
298.15	0.1740	2.27	2.96	2.96	2.1 ± 0.03	33.6	33.7	0.06
298.15	0.2000	3.19	3.46	3.46	2.2 ± 0.02	37.4	37.4	0.03
298.15	0.2720	4.19	4.92	4.92	3.0 ± 0.05	46.3	46.3	0.06
298.15	0.3000	5.23	5.54	5.54	2.8 ± 0.02	49.4	49.4	0.03
298.15	0.3620	6.21	6.97	6.97	3.7 ± 0.06	55.5	55.6	0.06
298.15	0.4000	7.48	7.94	7.94	3.4 ± 0.04	58.9	59.0	0.04
298.15	0.5000	9.45	10.78	10.78	4.6 ± 0.14	66.8	66.8	0.08
298.15	0.6000	12.70	14.32	14.32	5.0 ± 0.18	73.5	73.6	0.06
298.15	0.7000	16.69	19.08	19.08	4.8 ± 0.26	79.7	79.7	0.06
323.15	0.0100	-	-	0.11	-	-	1.8	-
323.15	0.0500	0.24	0.42	0.42	2.0 ± 0.01	6.5	6.6	0.04
323.15	0.1000	0.61	0.82	0.82	2.3 ± 0.01	12.1	12.1	0.02
323.15	0.2000	1.27	1.66	1.66	2.8 ± 0.01	21.9	22.0	0.04
323.15	0.2740	2.05	2.32	2.32	3.1 ± 0.02	28.4	28.4	0.03
323.15	0.3000	2.46	2.57	2.57	2.8 ± 0.01	30.6	30.6	0.02
323.15	0.4000	3.14	3.55	3.55	4.0 ± 0.04	38.0	38.0	0.05
323.15	0.4230	3.69	3.78	3.78	4.0 ± 0.03	39.6	39.6	0.03
323.15	0.5000	4.25	4.60	4.60	4.8 ± 0.04	44.6	44.6	0.04
323.15	0.5830	5.18	5.52	5.52	4.7 ± 0.04	49.4	49.4	0.04
323.15	0.6000	5.66	5.72	5.72	6.6 ± 0.11	50.3	50.3	0.04
323.15	0.7000	6.44	6.94	6.94	6.5 ± 0.08	55.4	55.4	0.03

(continued in the next page)

Appendix A1 (cont'd). Experimental Vapor-Liquid Equilibrium and Modeled Diffusivity Data for NH_3(1) and $[C_4C_1im][PF_6]$ (2) System

T (K)	P (MPa)	C_o (mass %)	C_s[a] (mass %)	w_1 (mass %)	D[a] (* 10^{-10} $m^2 \cdot s^{-1}$)	$x_{1,\ calculated}$ (mol %)	$x_{1,\ measured}$[b] (mol %)	S (mass %)
348.15	0.0100	-	-	0.18	-	-	2.9	-
348.15	0.1000	0.31	0.57	0.57	3.7 ± 0.02	7.4	8.8	0.03
348.15	0.1738	-	-	0.89	-	-	13.1	-
348.15	0.1983	-	-	1.00	-	-	14.4	-
348.15	0.2000	0.99	1.01	1.01	4.3 ± 0.09	14.6	14.6	0.05
348.15	0.3000	-	-	1.51	-	-	20.3	-
348.15	0.3450	-	-	1.71	-	-	22.5	-
348.15	0.4000	1.97	2.01	2.01	13.3 ± 0.54	25.5	25.5	0.08
348.15	0.5000	-	-	2.55	-	-	30.4	-
348.15	0.5459	-	-	2.74	-	-	32.0	-
348.15	0.6000	-	-	3.04	-	-	34.3	-
348.15	0.7000	-	-	3.61	-	-	38.5	-

T: Temperature; P: Pressure; C_o: Initial Concentration at T,P; C_s: Final concentration at T,P calculated with 1D Mass Model; w_1: NH_3 concentration in mass % obtained with XEMIS Microbalance; D: Diffusion Coefficient; $x_{1,\ calculated}$: NH_3 concentration in mole % obtained with 1D Mass Model, $x_{1,measured}$: NH_3 concentration obtained with XEMIS Microbalance; S is the standard error of the regression to show goodness of nonlinear fit.

[a] The average uncertainty in Cs = ± 0.01 mass %.

[b] The instrumental uncertainties are: T = 0.1 K; P = 0.0001 MPa; x_1 = 0.5 mole %.

Appendix A2. Experimental Vapor-Liquid Equilibrium and Modeled Diffusivity Data for NH_3 and $[C_4C_1im][BF_4]$ System

T (K)	P (MPa)	C_o (mass %)	C_s[a] (mass %)	w_1 (mass %)	D[a] (* 10^{-10} $m^2 \cdot s^{-1}$)	$x_{1,\ calculated}$ (mol %)	$x_{1,\ measured}$ (mol %)[b]	S (mass %)
283.15	0.0100	0.12	0.38	0.38	0.4 ± 0.00	4.8	4.8	0.01
283.15	0.0500	0.81	1.90	1.90	0.7 ± 0.01	20.4	20.4	0.01
283.15	0.1000	2.46	3.75	3.75	1.2 ± 0.03	34.1	34.1	0.02
283.15	0.1340	4.18	5.06	5.06	1.5 ± 0.03	41.4	41.4	0.02
283.15	0.1870	6.05	7.20	7.20	1.9 ± 0.05	50.6	50.7	0.02
283.15	0.2900	9.15	11.93	11.93	3.0 ± 0.17	64.2	64.3	0.03
283.15	0.3960	14.58	18.51	18.51	3.7 ± 0.30	75.0	75.1	0.04
283.15	0.4970	-	-	29.35	-	-	84.6	-
283.15	0.5100	-	-	31.67	-	-	86.0	-
298.15	0.0100	-	-	0.49	-	-	6.1	-
298.15	0.0500	0.74	1.42	1.42	1.0 ± 0.04	16.4	16.1	0.02
298.15	0.1280	2.07	3.34	3.34	1.4 ± 0.04	31.3	31.4	0.04
298.15	0.1960	4.01	5.00	5.00	2.0 ± 0.04	41.1	41.1	0.02
298.15	0.2720	5.74	6.92	6.92	2.8 ± 0.07	49.6	49.7	0.01
298.15	0.3000	7.20	7.67	7.67	3.0 ± 0.04	52.4	52.4	0.01
298.15	0.4370	9.84	11.57	11.57	3.8 ± 0.13	63.4	63.4	0.02
298.15	0.5000	12.55	13.64	13.64	4.7 ± 0.22	67.7	67.7	0.01
298.15	0.6130	15.87	18.10	18.10	5.4 ± 0.25	74.5	74.6	0.02
298.15	0.7000	19.87	22.61	22.61	5.6 ± 0.32	79.5	79.5	0.05
323.15	0.0100	-	-	0.31	-	-	4.0	-
323.15	0.0500	0.48	0.76	0.76	2.3 ± 0.02	9.2	9.2	0.06
323.15	0.1000	1.03	1.44	1.44	4.1 ± 0.04	15.2	16.2	0.06
323.15	0.1960	1.89	2.46	2.46	2.6 ± 0.03	25.2	25.1	0.03
323.15	0.3080	3.28	3.83	3.83	3.8 ± 0.04	34.6	34.6	0.01
323.15	0.4320	4.89	5.36	5.36	4.8 ± 0.05	42.9	42.9	0.01
323.15	0.5000	5.85	6.21	6.21	5.6 ± 0.04	46.9	46.8	0.01
323.15	0.6000	7.13	7.41	7.41	5.9 ± 0.03	52.0	51.5	0.01
323.15	0.7130	8.36	8.94	8.94	9.5 ± 0.12	56.6	56.6	0.02

(continued in the next page)

Appendix A2 (cont'd). Experimental Vapor-Liquid Equilibrium and Modeled Diffusivity Data for NH_3 and $[C_4C_1im][BF_4]$ System

T (K)	P (MPa)	C_o (mass %)	C_s[a] (mass %)	w_1 (mass %)	D[a] (* 10^{-10} $m^2 \cdot s^{-1}$)	$x_{1,\ calculated}$ (mol %)	$x_{1,\ measured}$ (mol %)[b]	S (mass %)
348.15	0.0100	-	-	0.15	-	-	1.9	-
348.15	0.0500	0.28	0.41	0.41	3.3 ± 0.16	5.1	5.1	0.02
348.15	0.1000	0.62	0.65	0.65	3.0 ± 0.19	9.0	7.9	0.02
348.15	0.2570	1.29	1.69	1.69	3.7 ± 0.04	18.5	18.5	0.01
348.15	0.3000	1.89	1.98	1.98	3.9 ± 0.14	21.3	21.2	0.01
348.15	0.4090	2.45	2.75	2.75	5.3 ± 0.08	27.2	27.3	0.01
348.15	0.5000	3.13	3.42	3.42	5.2 ± 0.07	31.9	32.0	0.01
348.15	0.5820	3.82	4.04	4.04	7.5 ± 0.19	35.9	35.8	0.01
348.15	0.7000	4.67	4.89	4.89	15.7 ± 1.22	40.6	40.6	0.02

T: Temperature; P: Pressure; C_o: Initial Concentration at T,P; C_s: Final concentration at T,P calculated with 1D Mass Model; w_1: NH_3 concentration in mass % obtained with XEMIS Microbalance; D: Diffusion Coefficient; $x_{1,\ calculated}$: NH_3 concentration obtained with 1D Mass Model, $x_{1,measured}$: NH_3 concentration obtained with XEMIS Microbalance; S is the standard error of the regression to show goodness of nonlinear fit.

[a] The average uncertainty in Cs = ± 0.01 mass %.

[b] The instrumental uncertainties are: T = 0.1 K; P = 0.0001 MPa; x_1 = 0.5 mole %.

Appendix A3. Experimental Vapor-Liquid Equilibrium and Modeled Diffusivity Data for NH_3 and $[C_2C_1im][NTf_2]$ System

T (K)	P (MPa)	C_o (mass %)	C_s[a] (mass %)	w_1 (mass %)	D[a] (* 10^{-10} $m^2 \cdot s^{-1}$)	$x_{1,\ calculated}$ (mol %)	$x_{1,\ measured}$ (mol %)[b]	S (mass %)
283.15	0.0100	0.07	0.21	0.21	2.9 ± 0.13	4.7	4.7	0.01
283.15	0.0500	0.6	1.00	1.00	1.7 ± 0.06	18.7	18.8	0.01
283.15	0.1139	1.8	2.42	2.42	3.2 ± 0.15	36.0	36.3	0.03
283.15	0.2220	4.4	5.27	5.27	2.2 ± 0.08	55.9	56.1	0.04
283.15	0.3300	7.8	9.21	9.21	2.5 ± 0.11	69.8	70.0	0.06
283.15	0.4000	11.2	12.88	12.88	3.5 ± 0.16	77.2	77.3	0.05
283.15	0.4790	15.8	19.37	19.37	3.7 ± 0.31	84.6	84.7	0.07
283.15	0.5700	-	-	38.50	-	-	93.5	-
283.15	0.5900	-	-	53.19	-	-	96.3	-
298.15	0.0100	-	-	0.14	-	-	3.1	-
298.15	0.0500	0.49	0.66	0.66	2.7 ± 042	12.9	13.2	0.03
298.15	0.1360	1.44	1.76	1.76	4.8 ± 0.18	29.1	29.1	0.01
298.15	0.2000	2.47	2.69	2.69	3.6 ± 0.07	38.8	38.8	0.00
298.15	0.2870	3.68	4.06	4.06	4.6 ± 0.08	49.3	49.3	0.01
298.15	0.4340	6.19	6.81	6.81	5.1 ± 0.11	62.7	62.7	0.01
298.15	0.5000	7.90	8.33	8.33	5.2 ± 0.09	67.6	67.6	0.01
298.15	0.6000	10.30	11.15	11.15	5.9 ± 0.15	74.2	74.2	0.01
298.15	0.6980	13.59	14.90	14.90	5.8 ± 0.20	80.1	80.1	0.02
323.15	0.0100	0.09	0.11	0.11	4.2 ± 0.14	2.6	2.5	0.00
323.15	0.0500	0.31	0.36	0.36	7.7 ±0.44	7.8	7.7	0.00
323.15	0.1711	1.01	1.17	1.17	6.5 ±0.06	21.5	21.5	0.00
323.15	0.2001	1.34	1.38	1.38	6.2 ±0.17	24.3	24.3	0.00
323.15	0.3000	1.97	2.10	2.10	7.9 ±0.22	33.1	33.1	0.00
323.15	0.3789	2.63	2.73	2.73	8.4 ±1.95	39.1	39.2	0.02
323.15	0.4999	3.56	3.71	3.71	9.6 ±0.43	46.9	46.9	0.00
323.15	0.5820	4.30	4.43	4.43	9.4 ±0.56	51.6	51.6	0.01
323.15	0.7000	5.44	5.57	5.57	16.0 ±1.84	57.6	57.6	0.01

(continued in the next page)

Appendix A3 (cont'd). Experimental Vapor-Liquid Equilibrium and Modeled Diffusivity Data for NH_3 and $[C_2C_1im][NTf_2]$ System

T (K)	P (MPa)	C_o (mass %)	C_s[a] (mass %)	w_1 (mass %)	D[a] (* 10^{-10} $m^2 \cdot s^{-1}$)	$x_{1,\ calculated}$ (mol %)	$x_{1,\ measured}$ (mol %)[b]	S (mass %)
348.15	0.0100	-	-	0.11	-	-	2.5	-
348.15	0.0499	0.24	0.26	0.26	7.6 ± 0.59	5.6	5.6	0.00
348.15	0.0999	0.41	0.45	0.45	12.8 ± 1.1	9.4	9.3	0.00
348.15	0.1960	0.78	0.83	0.83	8.7 ± 0.69	16.0	16.1	0.00
348.15	0.3000	1.21	1.25	1.25	13.5 ± 3.5	22.5	22.5	0.01
348.15	0.4569	1.88	1.91	1.91	-	31.0	31.0	0.01
348.15	0.4999	2.09	2.10	2.10	-	33.1	33.1	0.01
348.15	0.6001	2.52	2.58	2.57	14.5 ± 4.4	37.8	37.8	0.01
348.15	0.7090	-	-	3.10	-	-	42.3	-

T: Temperature; P: Pressure; C_o: Initial Concentration at T,P; C_s: Final concentration at T,P calculated with 1D Mass Model; w_1: NH_3 concentration in mass % obtained with XEMIS Microbalance; D D: Diffusion Coefficient; $x_{1,\ calculated}$: NH_3 concentration obtained with 1D Mass Model, $x_{1,measured}$: NH_3 concentration obtained with XEMIS Microbalance; S is the standard error of the regression to show goodness of nonlinear fit.

[a] The average uncertainty in Cs = ± 0.01 mass %.

[b] The instrumental uncertainties are: T = 0.1 K; P = 0.0001 MPa; x_1 = 0.5 mole %.

Appendix A4. Experimental Vapor-Liquid Equilibrium and Modeled Diffusivity Data for NH_3 and $[C_2C_1im]TFES]$ System

T (K)	P (MPa)	C_o (mass %)	C_s[a] (mass %)	w_1 (mass %)	D[a] (* 10^{-10} $m^2 \cdot s^{-1}$)	$x_{1,\ calculated}$ (mol %)	$x_{1,\ measured}$ (mol %)[b]	S (mass %)
283.15	0.0100	0.1	0.33	0.34	0.2 ± 0.01	5.4	5.6	0.02
283.15	0.0500	0.7	1.20	1.20	0.7 ± 0.02	17.2	17.3	0.02
283.15	0.1000	1.8	2.43	2.44	0.7 ± 0.02	30.0	30.0	0.03
283.15	0.2000	4.0	5.16	5.17	1.0 ± 0.02	48.3	49.3	0.04
283.15	0.3000	7.9	9.27	9.36	1.0 ± 0.03	63.7	63.9	0.07
283.15	0.4000	13.0	15.10	15.22	1.2 ± 0.03	75.3	75.5	0.11
283.15	0.5000	19.9	25.67	25.87	1.9 ± 0.03	85.6	85.7	0.16
283.15	0.6000	32.3	67.73	69.04	1.5± 0.01	97.2	97.5	1.2
298.15	0.0100	0.3	-	0.45	-	-	7.2	0.01
298.15	0.0500	0.5	1.15	1.19	0.2± 0.01	16.6	17.1	0.03
298.15	0.1000	1.2	2.01	2.03	0.5±0.24	26.1	26.3	0.03
298.15	0.2000	2.4	3.39	3.84	0.5±0.02	37.6	40.7	0.05
298.15	0.3000	5.1	5.86	5.92	0.2±0.01	51.6	51.9	0.05
298.15	0.4000	7.3	8.27	8.35	0.4±0.02	60.7	61.0	0.06
298.15	0.4998	10.1	11.18	11.27	0.6±0.02	68.3	68.5	0.07
298.15	0.6006	13.3	14.84	14.97	1.1±0.06	75.0	75.1	0.10
298.15	0.6999	17.8	19.95	20.21	0.5±0.03	81.0	81.3	0.18
323.15	0.0100	0.3	0.39	0.37	0.7±0.12	6.3	6.1	0.03
323.15	0.0500	0.6	0.76	0.76	0.3±0.02	11.6	11.6	0.02
323.15	0.1000	1.0	1.19	1.20	0.5±0.02	17.2	17.2	0.02
323.15	0.2000	1.9	2.04	2.03	1.0±0.09	26.3	26.3	0.02
323.15	0.3000	2.7	2.90	2.90	1.7±0.15	33.9	33.9	0.02
323.15	0.4000	3.5	3.84	3.84	2.7±0.15	40.7	40.6	0.02
323.15	0.5000	4.6	4.87	4.88	1.6±0.07	46.8	46.8	0.02
323.15	0.6000	5.7	5.95	5.96	3.8±0.24	52.1	52.1	0.01
323.15	0.6999	6.8	7.10	7.10	6.4±0.43	56.8	56.7	0.01

(continued in the next page)

Appendix A4 (cont'd). Experimental Vapor-Liquid Equilibrium and Modeled Diffusivity Data for NH_3 and [C_2C_1im]TFES] System

T (K)	P (MPa)	C_o (mass %)	C_s[a] (mass %)	w_1 (mass %)	D[a] (* 10^{-10} $m^2 \cdot s^{-1}$)	$x_{1,\ calculated}$ (mol %)	$x_{1,\ measured}$ (mol %)[b]	S (mass %)
348.15	0.0100	-	-	0.23	-	-	3.8	-
348.15	0.0500	0.3	0.42	0.42	0.1±0.16	6.8	6.8	0.01
348.15	0.1000	0.5	0.65	0.65	0.2±0.23	10.1	10.1	0.01
348.15	0.2000	1.0	1.10	1.09	0.6±0.92	16.1	15.9	0.02
348.15	0.3000	1.5	1.56	1.56	1.0±1.48	21.3	21.4	0.02
348.15	0.4000	1.9	2.00	2.00	3.35±5.27	25.9	26.0	0.02
348.15	0.5000	2.4	2.51	2.49	1.15±1.78	30.6	30.5	0.02
348.15	0.6002	-	-	3.03	-	-	34.9	-
348.15	0.7000	-	-	3.59	-	-	39.0	-

T: Temperature; P: Pressure; C_o: Initial Concentration at T,P; C_s: Final concentration at T,P calculated with 1D Mass Model; w_1: NH_3 concentration in mass % obtained with XEMIS Microbalance; D D: Diffusion Coefficient; $x_{1,\ calculated}$: NH_3 concentration obtained with 1D Mass Model, $x_{1,measured}$: NH_3 concentration obtained with XEMIS Microbalance; S is the standard error of the regression to show goodness of nonlinear fit.

[a] The average uncertainty in Cs = ± 0.01 mass %.

[b] The instrumental uncertainties are: T = 0.1 K; P = 0.0001 MPa; x_1 = 0.5 mole %.

Appendix A5. The comparison of the solubility of NH_3 in imidazolium-based ILs

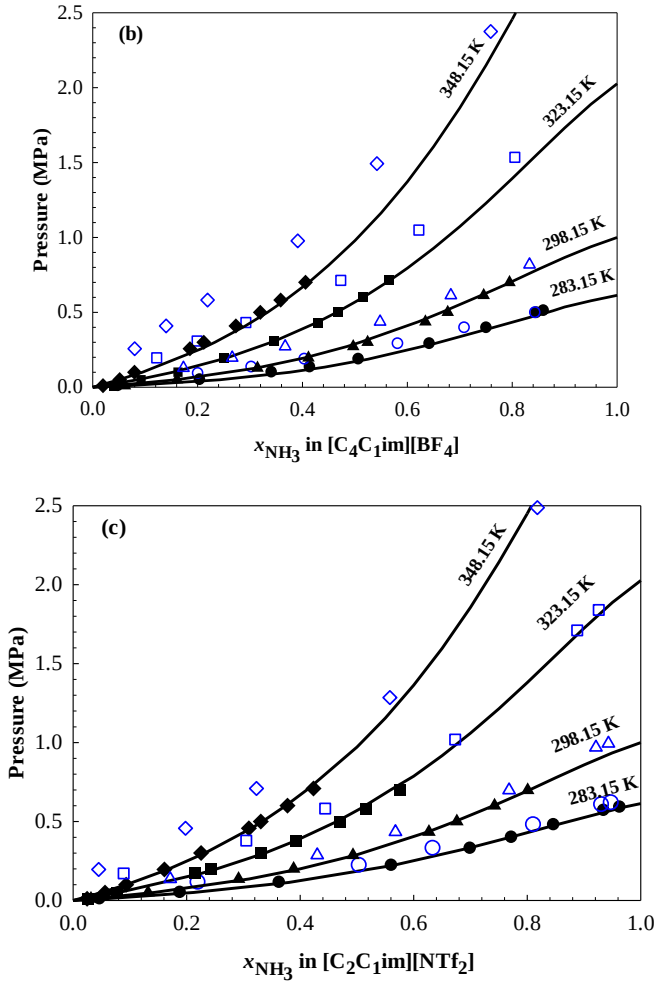

Figure A1. *PTx* phase diagram for NH_3 and (a) $[C_4C_1im][PF_6]$, (b) $[C_4C_1im][BF_4]$ and (c) $[C_2C_1im][NTf_2]$ at 283.15, 298.15, 318.15 and 338.15 K. Solid symbols represent experimental data in this study. Open symbols represent experimental data by Yokozeki and Shiflett[15]. Solid lines represent the NRTL model in this study

Appendix B1. Experimental Vapor-Liquid Equilibrium (VLE) Data for CO_2 (1) + $[C_3C_1pyr][NTf_2]$ (2)

T/K	P/MPa	x_1	$u_c(x_1)$	V_m (* 10^{-6})/ m^3/mol	$u_c(V_m)$	ρ/kg/m^3	$u_c(\rho)$	$(\Delta V/V_0)$/%	Method [a]
298.15	0.0250	0.0046	-	-	-	-	-	-	1
298.16	0.0500	0.0115	-	-	-	-	-	-	1
298.17	0.0750	0.0186	-	-	-	-	-	-	1
298.14	0.1000	0.0256	-	-	-	-	-	-	1
298.14	0.2000	0.0524	-	-	-	-	-	-	1
298.16	0.4000	0.1035	-	-	-	-	-	-	1
298.16	0.5998	0.1502	-	-	-	-	-	-	1
298.16	0.8000	0.1934	-	-	-	-	-	-	1
298.16	1.0001	0.2340	-	-	-	-	-	-	1
298.15	1.009	0.2360	0.0110	220.2	0.1	1464	3	0.8	2
298.14	1.2002	0.2717	-	-	-	-	-	-	1
298.19	1.4000	0.3054	-	-	-	-	-	-	1
298.14	1.5998	0.3384	-	-	-	-	-	-	1
298.15	1.8000	0.3675	-	-	-	-	-	-	1
298.17	2.0000	0.3955	-	-	-	-	-	-	1
298.15	2.028	0.389	0.008	187.9	0.1	1420	4	7.4	2
298.15	3.03	0.503	0.006	159.6	0.1	1411	4	12.2	2
298.15	3.507	0.553	0.004	146.9	0.1	1408	3	14.9	2
298.15	4.038	0.598	0.004	136.1	0.1	1401	3	18.2	2
298.15	4.517	0.632	0.003	128.2	0.1	1390	4	21.7	2
298.15	5.014	0.661	0.003	120.8	0.0	1386	4	24.7	2
298.15	5.505	0.688	0.003	113.9	0.0	1385	5	27.6	2
298.15	6.003	0.709	0.004	109.2	0.0	1373	6	31.3	2
298.15	6.397	0.725	0.007	105.9	0.0	1363	11	34.4	2
318.14	0.0250	0.0080	-	-	-	-	-	-	1
318.15	0.0500	0.0132	-	-	-	-	-	-	1
318.15	0.0750	0.0187	-	-	-	-	-	-	1
318.16	0.1000	0.0254	-	-	-	-	-	-	1
318.16	0.2000	0.0448	-	-	-	-	-	-	1
318.15	0.4000	0.0809	-	-	-	-	-	-	1
318.15	0.5031	0.1039	-	-	-	-	-	-	3
318.15	0.6000	0.1164	-	-	-	-	-	-	1
318.15	0.8000	0.1489	-	-	-	-	-	-	1
318.17	1.0000	0.1815	-	-	-	-	-	-	1
318.15	1.0065	0.1867	-	-	-	-	-	-	3
318.15	1.055	0.185	0.009	236.6	0.1	1441	3	0.2	2
318.16	1.2000	0.2100	-	-	-	-	-	-	1

(continued in the next page)

Appendix B1(cont'd). Experimental Vapor-Liquid Equilibrium (VLE) Data for CO_2 (1) + $[C_3C_1pyr][NTf_2]$ (2)

T/K	P/MPa	x_1	$u_c(x_1)$	V_m (* 10^{-6})/ m^3/mol	$u_c(V_m)$	ρ/kg/m^3	$u_c(\rho)$	$(\Delta V/V_0)$/%	Method [a]
318.15	1.4000	0.2378	-	-	-	-	-	-	1
318.15	1.5041	0.2490	-	-	-	-	-	-	3
318.14	1.6000	0.2636	-	-	-	-	-	-	1
318.14	1.8000	0.2904	-	-	-	-	-	-	1
318.15	2.0000	0.3116	-	-	-	-	-	-	1
318.15	2.0000	0.3077	-	-	-	-	-	-	3
318.15	2.223	0.323	0.007	200.6	0.1	1437	3	3.3	2
318.15	2.9979	0.4010	-	-	-	-	-	-	3
318.15	3.9989	0.4714	-	-	-	-	-	-	3
318.15	4.005	0.471	0.004	168.3	0.1	1407	3	9.8	2
318.15	5.0000	0.5267	-	-	-	-	-	-	3
318.15	5.004	0.528	0.004	155.1	0.1	1392	3	13.5	2
318.15	6.004	0.575	0.004	144.7	0.1	1374	3	17.5	2
318.15	7.01	0.621	0.004	134.4	0.1	1356	4	22.2	2
318.15	8.01	0.664	0.005	121.8	0.0	1366	5	25.1	2
318.15	9.999	0.701	0.008	-	-	-	-	-	2
318.15	11.991	0.713	0.005	-	-	-	-	-	2
318.15	16.527	0.731	0.002	102.6	0.0	1385	4	31.5	2
318.15	19.966	0.751	0.002	96.0	0.0	1406	3	32.8	2
338.15	0.0250	0.0044	-	-	-	-	-	-	1
338.15	0.0500	0.0078	-	-	-	-	-	-	1
338.15	0.0750	0.0134	-	-	-	-	-	-	1
338.13	0.1000	0.0202	-	-	-	-	-	-	1
338.16	0.2000	0.0306	-	-	-	-	-	-	1
338.13	0.4000	0.0587	-	-	-	-	-	-	1
338.14	0.6000	0.0858	-	-	-	-	-	-	1
338.15	0.8000	0.1113	-	-	-	-	-	-	1
338.16	1.0000	0.1356	-	-	-	-	-	-	1
338.15	1.009	0.065	0.012	274.8	0.1	1400	3	0.5	2
338.17	1.2000	0.1582	-	-	-	-	-	-	1
338.17	1.4000	0.1812	-	-	-	-	-	-	1
338.15	1.6000	0.2023	-	-	-	-	-	-	1
338.16	1.7996	0.2241	-	-	-	-	-	-	1
338.14	2.0000	0.2418	-	-	-	-	-	-	1
338.15	2.002	0.198	0.010	239.3	0.1	1405	3	2	2
338.15	2.508	0.249	0.007	228.0	0.1	1393	2	3.8	2

(continued in the next page)

Appendix B1(cont'd). Experimental Vapor-Liquid Equilibrium (VLE) Data for CO_2 (1) + $[C_3C_1pyr][NTf_2]$ (2)

T/K	P/MPa	x_1	$u_c(x_1)$	V_m (* 10^{-6})/ m^3/mol	$u_c(V_m)$	ρ/kg/m^3	$u_c(\rho)$	$(\Delta V/V_0)$/%	Method [a]
338.15	3.007	0.328	0.006	205.1	0.1	1408	3	4.4	2
338.15	4.008	0.413	0.006	183.7	0.1	1404	3	7.0	2
338.15	4.999	0.474	0.005	165.0	0.1	1427	3	7.3	2
338.15	6.006	0.536	0.005	149.0	0.1	1430	3	9.8	2
338.15	7.503	0.612	0.005	129.3	0.0	1435	5	13.8	2

T: Temperature; P: Pressure; x_1: Mole fraction of CO_2 in Ionic Liquids; ρ: Density of mixture; $\Delta V/V_0$:Volume Expansion of the Liquid (*See equation 4 in main text*).

[a] Experimental Method: 1) IGA-II Microbalance Standard Uncertainties u(T) = 0.01 K and u(P) = 0.0008 MPa, and Combined Standard Uncertainty $u_c(x_1)$ = 0.005; 2) High-pressure Viewcell Standard Uncertainties u(T) = 0.1 K and u(P) = 0.01 MPa, and Combined Standard Uncertainty $u_c(x_1)$ = reported at each point; 3) XEMIS Microbalance Standard Uncertainties u(T) = 0.1K and u(P) = 0.001 MPa, Combined Standard Uncertainty $u_c(x_1)$ = 0.005.

Appendix B2. Experimental Vapor-Liquid Equilibrium (VLE) Data for CO_2 (1) + $[C_4C_1pyr][NTf_2]$ (2)

T/K	P/MPa	x_1	$u_c(x_1)$	V_m (* 10^{-6})/ m^3/mol	$u_c(V_m)$	ρ/kg/m^3	$u_c(\rho)$	$(\Delta V/V_0)$/%	Method [a]
298.15	0.0250	0.0080	-	-	-	-	-	-	4
298.15	0.0500	0.0155	-	-	-	-	-	-	4
298.15	0.0750	0.0226	-	-	-	-	-	-	4
298.15	0.1000	0.0295	-	-	-	-	-	-	4
298.14	0.2000	0.0563	-	-	-	-	-	-	4
298.15	0.4001	0.1073	-	-	-	-	-	-	4
298.16	0.6000	0.1548	-	-	-	-	-	-	4
298.15	0.7999	0.1982	-	-	-	-	-	-	4
298.16	0.9998	0.2384	-	-	-	-	-	-	4
298.15	0.9960	0.199	0.011	250.6	0.1	1385	3	3.3	2
298.15	1.2001	0.2755	-	-	-	-	-	-	4
298.16	1.4002	0.3104	-	-	-	-	-	-	4
298.15	1.6000	0.3448	-	-	-	-	-	-	4
298.15	1.8001	0.3736	-	-	-	-	-	-	4
298.15	2.0000	0.4020	-	-	-	-	-	-	4
298.15	1.9970	0.379	0.008	202.6	0.1	1377	3	7.7	2
298.15	2.5020	0.449	0.005	184.2	0.1	1371	3	10.4	2
298.15	3.0310	0.510	0.004	168.7	0.1	1361	3	13.6	2
298.15	3.5110	0.559	0.004	156.0	0.1	1351	3	16.9	2
298.15	4.0130	0.602	0.003	144.3	0.1	1348	3	19.8	2
298.15	4.5040	0.638	0.003	134.5	0.0	1345	3	22.8	2
298.15	5.0020	0.674	0.003	125.1	0.0	1339	3	26.6	2
298.15	5.5120	0.702	0.003	117.4	0.0	1336	4	30.0	2
298.15	6.0400	0.728	0.004	110.9	0.0	1326	5	34.4	2
298.15	6.3780	0.745	0.005	105.7	0.0	1330	9	36.8	2
318.15	0.0250	0.0076	-	-	-	-	-	-	4
318.15	0.0500	0.0116	-	-	-	-	-	-	4
318.15	0.0750	0.0156	-	-	-	-	-	-	4
318.16	0.1000	0.0198	-	-	-	-	-	-	4
318.15	0.2001	0.0389	-	-	-	-	-	-	4
318.15	0.3999	0.0757	-	-	-	-	-	-	4
318.16	0.6001	0.1118	-	-	-	-	-	-	4
318.15	0.8000	0.1455	-	-	-	-	-	-	4
318.15	1.0000	0.1772	-	-	-	-	-	-	4
318.15	1.0050	0.156	0.012	261.8	0.1	1387	3	1.1	2
318.15	1.2000	0.2074	-	-	-	-	-	-	4
318.15	1.3999	0.2353	-	-	-	-	-	-	4

(continued in the next page)

Appendix B2 (cont'd). Experimental Vapor-Liquid Equilibrium (VLE) Data for CO_2 (1) + $[C_4C_1pyr][NTf_2]$ (2)

T/K	P/MPa	x_1	$u_c(x_1)$	V_m (* 10^{-6})/ m^3/mol	$u_c(V_m)$	ρ/kg/m^3	$u_c(\rho)$	$(\Delta V/V_0)$/%	Method [a]
318.15	1.6001	0.2624	-	-	-	-	-	-	4
318.15	1.8000	0.2880	-	-	-	-	-	-	4
318.16	2.0000	0.3122	-	-	-	-	-	-	4
318.15	2.0460	0.311	0.010	219.2	0.1	1391	3	3.6	2
318.15	3.0190	0.436	0.007	185.3	0.1	1389	3	7.1	2
318.15	4.0000	0.528	0.005	159.4	0.1	1397	4	10.0	2
318.15	6.0330	0.638	0.006	131.2	0.1	1380	6	18.0	2
318.15	8.0020	0.714	0.006	110.4	0.0	1378	9	25.8	2
318.15	10.0040	0.776	0.005	90.4	0.0	-	-	31.4	2
318.15	11.9890	0.804	0.003	79.2	0.0	-	-	31.4	2
318.15	13.9910	0.817	0.002	74.2	0.0	-	-	32.3	2
318.15	15.9990	0.828	0.001	70.4	0.0	-	-	33.5	2
318.15	19.8940	0.843	0.001	65.2	0.0	-	-	35.6	2
338.16	0.0250	0.0060	-	-	-	-	-	-	4
338.15	0.0500	0.0077	-	-	-	-	-	-	4
338.15	0.0750	0.0101	-	-	-	-	-	-	4
338.15	0.1000	0.0149	-	-	-	-	-	-	4
338.14	0.1999	0.0284	-	-	-	-	-	-	4
338.15	0.4001	0.0555	-	-	-	-	-	-	4
338.15	0.6000	0.0820	-	-	-	-	-	-	4
338.15	0.7999	0.1077	-	-	-	-	-	-	4
338.13	0.9993	0.1339	-	-	-	-	-	-	4
338.15	1.0190	0.123	0.012	274.7	0.1	1368	3	0.7	2
338.16	1.1999	0.1572	-	-	-	-	-	-	4
338.17	1.4001	0.1812	-	-	-	-	-	-	4
338.16	1.6000	0.2022	-	-	-	-	-	-	4
338.16	1.7999	0.2242	-	-	-	-	-	-	4
338.17	2.0000	0.2436	-	-	-	-	-	-	4
338.15	2.0110	0.230	0.102	246.9	0.1	1358	3	3.1	2
338.15	2.5200	0.301	0.007	225.3	0.1	1369	3	3.6	2
338.15	3.0040	0.345	0.007	213.4	0.1	1369	3	4.6	2
338.15	4.0000	0.435	0.006	188.1	0.1	1371	3	7.0	2

(continued in the next page)

Appendix B2 (cont'd). Experimental Vapor-Liquid Equilibrium (VLE) Data for CO_2 (1) + $[C_4C_1pyr][NTf_2]$ (2)

T/K	P/MPa	x_1	$u_c(x_1)$	V_m (* 10^{-6})/ m^3/mol	$u_c(V_m)$	ρ/kg/m^3	$u_c(\rho)$	$(\Delta V/V_0)$/%	Method [a]
338.15	4.0000	0.435	0.006	188.1	0.1	1371	3	7.0	2
338.15	5.0070	0.495	0.006	170.3	0.1	1380	4	8.4	2
338.15	6.0200	0.537	0.005	161.5	0.1	1357	4	12.1	2
338.15	7.5040	0.606	0.004	143.2	0.1	1348	4	16.8	2
338.15	10.0120	0.682	0.006	121.9	0.0	1349	8	23.0	2
338.15	12.4860	0.712	0.006	110.4	0.0	1384	9	23.4	2
338.15	14.8950	0.728	0.004	105.9	0.0	1387	6	25.2	2

T: Temperature; P: Pressure; x_1: Mole fraction of CO_2 in Ionic Liquids; ρ: Density of mixture; $\Delta V/V_0$: Volume Expansion of the Liquid (*See equation 4 in main text*).

[a] Experimental Method: 4) IGA-I Microbalance Standard Uncertainties u(T) = 0.01 K, u(P) = 0.0008 MPa, and Combined Standard Uncertainty $u_c(x_1)$ = 0.005; 2) High-pressure Viewcell Standard Uncertainties u(T) = 0.1 K, u(P) = 0.01 MPa, and Combined Standard Uncertainty $u_c(x_1)$ = reported at each point.

Appendix B3. Experimental Vapor-Liquid Equilibrium (VLE) Data for CO_2 (1) + $[C_6C_1pyr][NTf_2]$ (2)

T/K	P/MPa	x_1	$u_c(x_1)$	V_m (* 10^{-6})/ m^3/mol	$u_c(V_m)$	ρ/kg/m^3	$u_c(\rho)$	$(\Delta V/V_0)$/%	Method [a]
298.16	0.0250	0.0063	-	-	-	-	-	-	1
298.16	0.0500	0.0140	-	-	-	-	-	-	1
298.16	0.0750	0.0217	-	-	-	-	-	-	1
298.14	0.1000	0.0293	-	-	-	-	-	-	1
298.15	0.2000	0.0584	-	-	-	-	-	-	1
298.15	0.4000	0.1129	-	-	-	-	-	-	1
298.15	0.6000	0.1630	-	-	-	-	-	-	1
298.15	0.8000	0.2087	-	-	-	-	-	-	1
298.14	1.0000	0.2507	-	-	-	-	-	-	1
298.15	1.004	0.236	0.013	260.6	0.1	1360	4	1.1	2
298.15	1.2000	0.2896	-	-	-	-	-	-	1
298.15	1.4000	0.3255	-	-	-	-	-	-	1
298.16	1.6000	0.3589	-	-	-	-	-	-	1
298.15	1.8000	0.3899	-	-	-	-	-	-	1
298.14	2.0000	0.4189	-	-	-	-	-	-	1
298.15	2.03	0.403	0.009	211.6	0.1	1354	4	5.1	2
298.15	2.493	0.484	0.006	188.9	0.1	1343	3	8.5	2
298.15	3.003	0.531	0.005	174.5	0.1	1345	3	10.2	2
298.15	3.496	0.577	0.005	161.8	0.1	1336	4	13.3	2
298.15	3.999	0.614	0.004	151.6	0.1	1324	4	16.5	2
298.15	4.496	0.653	0.004	141.4	0.1	1308	4	20.8	2
298.15	4.998	0.683	0.004	132.9	0.1	1299	4	24.4	2
298.15	5.521	0.716	0.004	123.2	0.0	1294	5	28.7	2
298.15	5.995	0.738	0.004	117.4	0.0	1281	6	32.9	2
298.15	6.387	0.751	0.007	115.0	0.0	1263	11	36.8	2
318.15	0.0250	0.0082	-	-	-	-	-	-	1
318.14	0.0500	0.0136	-	-	-	-	-	-	1
318.15	0.0750	0.0200	-	-	-	-	-	-	1
318.15	0.1000	0.0267	-	-	-	-	-	-	1
318.14	0.2000	0.0478	-	-	-	-	-	-	1
318.16	0.4000	0.0879	-	-	-	-	-	-	1
318.14	0.6000	0.1249	-	-	-	-	-	-	1
318.16	0.8000	0.1612	-	-	-	-	-	-	1
318.15	0.9999	0.1951	-	-	-	-	-	-	1
318.15	1.005	0.179	0.014	280.8	0.1	1346	3	0	2
318.14	1.1999	0.2253	-	-	-	-	-	-	1
318.16	1.4001	0.2555	-	-	-	-	-	-	1

(continued in the next page)

Appendix B3 (cont'd). Experimental Vapor-Liquid Equilibrium (VLE) Data for CO_2 (1) + $[C_6C_1pyr][NTf_2]$ (2)

T/K	P/MPa	x_1	$u_c(x_1)$	V_m (* 10^{-6})/ m^3/mol	$u_c(V_m)$	ρ/kg/m^3	$u_c(\rho)$	$(\Delta V/V_0)$/%	Method [a]
318.14	1.6000	0.2838	-	-	-	-	-	-	1
318.17	1.8002	0.3085	-	-	-	-	-	-	1
318.14	2.0000	0.3330	-	-	-	-	-	-	1
318.15	2.021	0.315	0.011	242.1	0.1	1332	3	3.4	2
318.15	2.513	0.366	0.008	229.5	0.1	1315	3	5.9	2
318.15	2.996	0.416	0.007	212.9	0.1	1323	3	6.6	2
318.15	4.039	0.515	0.007	184.1	0.1	1311	4	11.0	2
318.15	6.032	0.632	0.007	148.8	0.1	1301	6	18.2	2
318.15	7.998	0.720	0.007	122.4	0.0	1291	10	27.7	2
318.15	9.884	0.783	0.010	98.3	0.0	1345	22	32.6	2
318.15	12.546	0.851	0.002	67.9	0.0	-	-	33.4	2
318.15	14.948	0.870	0.001	60.1	0.0	-	-	34.9	2
338.16	0.0250	0.0046	-	-	-	-	-	-	1
338.16	0.0500	0.0086	-	-	-	-	-	-	1
338.16	0.0750	0.0161	-	-	-	-	-	-	1
338.16	0.1000	0.0218	-	-	-	-	-	-	1
338.15	0.2000	0.0348	-	-	-	-	-	-	1
338.13	0.4000	0.0644	-	-	-	-	-	-	1
338.15	0.6000	0.0945	-	-	-	-	-	-	1
338.15	0.8000	0.1223	-	-	-	-	-	-	1
338.16	1.0000	0.1490	-	-	-	-	-	-	1
338.15	1.001	0.118	0.014	307.7	0.1	1307	3	0.8	2
338.15	1.2000	0.1739	-	-	-	-	-	-	1
338.17	1.4000	0.1978	-	-	-	-	-	-	1
338.18	1.6001	0.2201	-	-	-	-	-	-	1
338.12	1.8000	0.2424	-	-	-	-	-	-	1
338.15	2.0000	0.2637	-	-	-	-	-	-	1
338.15	2.028	0.264	0.012	267.1	0.1	1315	3	2.1	2
338.15	2.537	0.293	0.009	252.8	0.1	1311	3	3.2	2
338.15	3.03	0.346	0.008	236.3	0.1	1310	3	4.4	2

(continued in the next page)

Appendix B3 (cont'd). Experimental Vapor-Liquid Equilibrium (VLE) Data for CO_2 (1) + $[C_6C_1pyr][NTf_2]$ (2)

T/K	P/MPa	x_1	$u_c(x_1)$	V_m (* 10^{-6})/ m^3/mol	$u_c(V_m)$	ρ/kg/m^3	$u_c(\rho)$	$(\Delta V/V_0)$/%	Method [a]
338.15	3.03	0.346	0.008	236.3	0.1	1310	3	4.4	2
338.15	4.022	0.443	0.007	206.0	0.1	1313	3	6.8	2
338.15	5.027	0.508	0.006	186.1	0.1	1311	4	9.3	2
338.15	6.014	0.561	0.005	170.2	0.1	1307	4	11.9	2
338.15	7.501	0.637	0.004	146.2	0.1	1310	4	16.4	2
338.15	10.006	0.706	0.006	123.8	0.0	1319	8	21.8	2
338.15	12.478	0.752	0.005	109.3	0.0	1325	9	27.3	2
338.15	14.944	0.771	0.003	102.3	0.0	1341	6	28.9	2

T: Temperature; P: Pressure; x_1: Mole fraction of CO_2 in Ionic Liquids; ρ: Density of mixture; $\Delta V/V_0$:Volume Expansion of the Liquid (*See equation 4 in main text*).

[a] Experimental Method: 1) IGA-II Microbalance Standard Uncertainties u(T) = 0.01 K, u(P) = 0.0008 MPa, and Combined Standard Uncertainty $u_c(x_1) = 0.005$; 2) High Pressure Viewcell Standard Uncertainties u(T) = 0.1 K and u(P) = 0.1 bar, and Combined Standard Uncertainty $u_c(x_1)$ = reported at each point.

Appendix B4. Experimental Vapor-Liquid Equilibrium (VLE) Desorption Data for CO_2 (1) + $[C_nC_1pyr][NTf_2]$ obtained using Method 1[a] (2)

Ionic Liquid	T/K	P/MPa	x_1		T/K	P/MPa	x_1
$[C_3C_1pyr][NTf_2]$	318.2	2.00	0.3116	$[C_6C_1pyr][NTf_2]$	318.1	1.80	0.3085
	318.1	1.80	0.2891		318.2	1.60	0.2852
	318.2	1.60	0.2646		318.2	1.40	0.2573
	318.2	1.40	0.2398		318.1	1.20	0.2283
	318.2	1.20	0.2122		318.2	1.00	0.1981
	318.2	1.00	0.1838		318.1	0.80	0.1649
	318.2	0.80	0.1532		318.1	0.60	0.1295
	318.2	0.60	0.1210		318.1	0.40	0.0911
	318.2	0.40	0.0861		318.2	0.20	0.0514
	318.2	0.20	0.0491		318.1	0.10	0.0296
	318.2	0.10	0.0294		318.2	0.08	0.0196
	318.2	0.07	0.0204		318.2	0.05	0.0132
	318.2	0.05	0.0137		318.2	0.03	0.0072
	318.2	0.02	0.0083				
$[C_4C_1pyr][NTf_2]$	318.2	2.00	0.3122				
	318.2	1.80	0.2887				
	318.2	1.60	0.2640				
	318.2	1.40	0.2380				
	318.2	1.20	0.2102				
	318.2	1.00	0.1810				
	318.2	0.80	0.1516				
	318.2	0.60	0.1182				
	318.2	0.40	0.0831				
	318.2	0.20	0.0445				
	318.2	0.10	0.0241				
	318.2	0.07	0.0196				
	318.2	0.05	0.0147				
	318.2	0.03	0.0100				

T: Temperature; P: Pressure; x_1: Mole fraction of CO_2 in Ionic Liquids; [a] Experimental Method: 1) IGA-II Microbalance Standard Uncertainties u(T) = 0.01 K and u(P) = 0.0008 MPa, and Combined Standard Uncertainty $u_c(x_1)$ = 0.005.

Appendix C. Matlab Code Developed for Diffusion Analysis

```
% Copyright® 2017 Tugba Turnaoglu
% All rights reserved. No part of this code may be reproduced, used, or distributed in any form or by any means without permission in writing from Tugba Turnaoglu. When the code is used with permission, this thesis must be cited.

% 1D-Diffusion Coefficient Model.D and Cs Estimation.
% The code solves a spaced averaged concentration equation.
% Experimental Data nonlinear fit to spaced average concentration
% equation. The code will report model Cs and D values and plot both
% experimental and model data in the same plot.

function OneDimensionalDiffusionwithConfd
clear; clc;format compact; format short g
%  Concentration Data
   load BT.mat
   time= vertcat(BT{:,1});
   conc= vertcat(BT{:,2});

% Initial Guess for Cs and D. bo(1,1) is Cs guess, and b0(1,2) is D guess.
     b0=[23 0.00000000001];
% Best nonlinear fit values for coefficient
     [bsol,resid,J,CovB]=nlinfit(time,conc,@DiffusionModel,b0);
     display(bsol(1),'Cs,Saturation Concentration (mol% or mass%')
     display(bsol(2),'D,Diffusion Coefficient (m2/s)')

% Plot the Experimental and Model Data
     avgcon= DiffusionModel(bsol,time);
     plot(time,conc,'o',time,avgcon,'LineWidth',2,'MarkerSize',2);
     xlabel('Time (s)','Fontsize',12); ylabel('Mass CO2 Absorbed (%)', 'Fontsize',12);
     %title('[bmim][PF6] at 10C 0.05 MPa','Fontsize',12);
     legend('Location','southeast','Experimental','Model');

% Error Analysis
    % Confidence Interval
     confInt = nlparci(bsol, resid, 'covar', CovB);
     neg95CI = [confInt(1,1); confInt(2,1)];
     pos95CI = [confInt(1,2); confInt(2,2)];
     columnNames = {'Estimate', 'Std Error', '-95% CI', '+95% CI'};
     rowNames = {'Cs, wt%', 'n,D=10^-n', 'Co, wt%'};
     tableData = ...
     [transpose(bsol), sqrt(diag(CovB)), neg95CI, pos95CI];
```

```
    chart = uitable(...
    'Data', tableData,...
    'ColumnName', columnNames,...
    'RowName', rowNames,...
    'ColumnFormat', {'short g' ,'short g', 'short g', 'short g'},...
    'Units', 'normalized',...
    'Position', [0.05 0.01 0.68 0.24]);

% Coefficient of Determination (R-squared)
     r2=1-(sum((conc-avgcon).^2)/ sum((conc-mean(conc)).^2));
     display(r2,'Coefficient of Determination (R2)')

     % The Standard Error of Regression (S) (sometimes known as Fit
     % Standard Error. S has a unit depending on the parameters, but it is
     % strongly suggested statistical tool in non-linear regression.
     cost_func = 'MSE';
     fit=goodnessOfFit(conc,avgcon,cost_func)';
     RMSE=sqrt(fit);
     display(RMSE, 'The Standard Error of Regression (S)')

     % The mean Square Error or The Residual Mean Square (MSE).
     % MSE value closer to 0 indicated a fit that is more useful for
     % prediction.
     display(fit,'Mean Square Error (MSE)')

% Exporting Model Result to Excel File
     ResultSummary=table(time,conc,avgcon);
     filename = 'D_bmimBF4_75C_.xlsx';
     writetable(ResultSummary,filename,'Sheet',1);
     ResultSummary=table(bsol);
     filename = 'D_bmimBF4_75C_.xlsx';
     writetable(ResultSummary,filename,'Sheet',2);
     ResultSummary=table(r2,RMSE,fit);
     filename = 'D_bmimBF4_75C_.xlsx';
     writetable(ResultSummary,filename,'Sheet',3);
end

% Average Concentration Function
% numLam is the summation term.

 function avgcon=DiffusionModel(b,time)
   expterm=100;
   for i=1:expterm
     L=0.00073147;
```

```
   lamdas(i)=((i-1)+0.5)*pi/L;
  end

% Average Concentration Evaluation in Each Time
  co=19.87077; % Co is the initial concentration.
  L2=L^2; % Square of L in summation term.
  totaltimepoints=length(time);
  ExpTotalParts=zeros(totaltimepoints,1);
     for i=1:totaltimepoints
       for j=1:expterm
     part(j)=exp(-b(2)*time(i)*lamdas(j)^2)/(L2*lamdas(j)^2);
     ExpTotalParts(i)=ExpTotalParts(i)+part(j);
       end
   avgcon(i,1)=b(1)*(1- 2*(1-co/b(1))*ExpTotalParts(i));
     end
end
```

Appendix D. Process Safety Documentation Example for Ammonia Studies in the microbalance

Hazards Analysis and Method Selection Guidelines

Level or Review & Checklists Required[α]	Minimal	Low	Moderate	High
Materials and Products				
HMIS- Flammability (Volume <1L)	☒ 0-1	☐ 2-4		
HMIS- Flammability (Volume ≥1L)	☐ 0	☒ 1-2	☐ 3-4	
HMIS- Flammability (Volume ≥1L) under pressure or above flashpoint	☐ 0		☐ 1	☐ 2-4
HMIS- Reactivity	☐ 1	☐ 2	☒ 3-4	
HMIS- Health	☐ 0	☐ 1-2	☒ 3	☐ 4
Capable of Generating of Strong Odors	☐ No		☒ Yes	
Biological Materials		☐ Yes		
HIGH OR LOW TEMPERATURES – SURFACE	☐ > -30°C (-20°F) or <60°C (140°F)		☒ < -30°C (-20°F) or >60°C (140°F)	
HIGH OR LOW TEMPERATURES – INTERNAL TEMPERATURE OR EXOTHERMIC REACTION	☐ <60°C (140°F)		☒ >60°C (140°F) or reaction boiling	
EQUIPMENT UNDER PRESSURE/VACUUM	☐ Atmospheric Pressure	☐ Vacuum and 0-40 PSIG pressure for shielded glassware; rated vessels	☒ Unshielded glassware; non-rated vessels; >40 PSIG	
GASES- flammable, toxic, corrosive			☒ Yes	
GASES		☐ In Cylinder closet/hood	☒ Outside cylinder closet	
ELECTRICAL- Voltage	☐ < 110V	☐ 110-120V	☒ 208-220 V Protected	☐ >220V Protected
MECHANICAL MOTION			☒ Yes	
VENTILATION REQUIRED-fume hood		☐ Yes		
COMPUTER AND AUTOMATED CONTROL SYSTEMS			☒ Yes	
WORKING ALONE			☐ Yes	
UNATTENDED EXPERIMENTS- with proper interlock/safety system			☐ Yes, minimal hazard	☒ Yes > minimal hazard
LABORATORY ERGONOMICS		☐ Repetitive motion >4 hours/day or awkward height/posture		
NOISE LEVEL/NOISE CONTROL	☒ <85 dBA		☐ ≥85 dBA	
IONIZING RADIATION – SEALED RADIOACTIVE SOURCES			☐ Yes	
IONIZING RADIATION – UNSEALED RADIOACTIVE MATERIALS			☐ Yes	
IONIZING RADIATION – X-RAY		☐ <20 kv	☐ ≥20 kv	
NON-IONIZING RADIATION – INFRARED, MICROWAVE, RADIO, ULTRAVIOLET		☐ <TLV	☐ ≥TLV	
NON-IONIZING RADIATION – LASERS		☐ Class I - IIIA	☐ Class IIIB - IV	
NOVELTY- New Technology		☒ First time running experiment		☐ Unknown reactions
LEVEL OF REVIEW: Complete EHS Hazard Review Document if Moderate or High Risk	☐ Minimal	☐ Low	☐ Moderate	☒ High

[α] **Minimal:** Student with Student; **Low:** Student with Advisor; **Moderate:** Student with Advisor + Technical Expert(s)**; High:** Student with Advisor + Technical Expert(s) + Safety Resource with hazard experience. ***These are MINIMUM suggested methods; always consult with an advisor on the level of review required. By signing, you have acknowledged your understanding of the risk involved and the level of review required.***

Name: Tugba Turnaoglu Signature: _____ Date: 05/16/2017

Electrical

Equipment Name: Hiden XEMIS Gravimetric Microbalance

Experiment Description: 1- Ammonia absorption in various ionic liquids

2-Carbon dioxide (CO_2) absorption in 1-hexyl-3-methylimidazolium bis(trifluoromethylsulfonyl)imide ([hmim][Tf_2N])

Item Inspection List/Questionnaire	Yes	No	N/A
1. Does the equipment/experiment require power? If yes, fill out the information below:	☒	☐	☐
Is the equipment fed from multiple power sources?	☐	☒	☐

Equipment Feed			Source		
Type	**Voltage**	**Amperage**	**Type**	**Voltage**	**Amperage**
UPS	208 & 110	30	Generator Backup	208	30
Control Box	208	25	UPS	208	30
Pumps (x3)	110	15	UPS	110	15
Computers	110	15	UPS	110	15
Xemis	208	25	UPS	208	30
Safety Interlock Box	110	15	UPS	110	15
Yokogowa	110	15	UPS	110	15

2. Main disconnect switch(es)
   Provide information about all main disconnect switch(es) and control panel(s) in table below:

Equipment Type	20PL2 21,23				2NPL4 6
Location	Middle ventilated enclosure	Middle ventilated enclosure	Middle ventilated enclosure	Middle ventilated enclosure	Next to the Middle ventilated enclosure
Fed from Panel #	Electric Control Room	UPS	UPS	UPS	UPS
Voltage	208	110	208	208	110
Amperage	30	15	25	25	15
Equip Being Fed	UPS	Water Bath	Balance Cabinet	Control Box	Computer and Yokogowa
Breaker or Circuit #	21,23				

3. Is the equipment properly grounded?	☒	☐	☐
4. Is the equipment properly wired?	☒	☐	☐
5. Is there any temporary wiring? If yes, explain:	☐	☒	☐
6. Have equipment and electrical cords been inspected?	☒	☐	☐
7. Are there electrical safety interlocks? If yes, describe: Safety crash button. If yes, location of quarterly interlock tag: Left corner on the crush button panel.	☒	☐	☐
8. Is there potential for any stored energy? If yes, describe: All system is plugged into UPS.	☒	☐	☐
If yes, is it labeled?	☒	☐	☐
If yes, are warning signs required?	☒	☐	☐
9. Describe the consequences of a loss in electrical power: No electric loss will occur. The UPS continuously supply energy to the whole system.			

Emergency and Operating Procedures

Equipment Name: Hiden XEMIS Gravimetric Microbalance
Experiment Description:
1- Ammonia absorption in various ionic liquids
2-Carbon dioxide (CO_2) absorption in 1-hexyl-3-methylimidazolium bis(trifluoromethylsulfonyl)imide ([hmim][Tf_2N])

Item Inspection List/Questionnaire	**Yes**	**No**
1. Emergency Procedures: Have procedures been written for:		
• Emergency shutdown?	☒	☐
• Spills?	☒	☐
2. Is there an emergency crash button or system? If yes, location of quarterly interlock tag:	☒	☐
3. Operating Procedures: Have operating procedures been written for:		
• Normal start-up?	☒	☐
• Normal operation?	☒	☐
• Normal shutdown?	☒	☐
• Equipment clean-up and decontamination?	☒	☐
4. Are the operating procedures posted and readily available?	☒	☐
5. Have all authorized operators been properly trained and qualified with all related procedures and proper use of PPE?	☒	☐
6. Are the following written procedures readily available?		
• Lock, tag, clear, try?	☐	☐
• Line break/first break?	☒	☐
• Process modifications?	☐	☐
• Special operating hazards?	☒	☐
• Management of change?	☐	☐

By signing, you acknowledged that all items have been properly reviewed and deemed safe for your experimental operation.

Name: Tugba Turnaoglu Signature: _____ Date: 05/16/2017

Environmental

Equipment Name: Hiden XEMIS Gravimetric Microbalance
Experiment Description: 1- Ammonia absorption in various ionic liquids
2-Carbon dioxide (CO_2) absorption in 1-hexyl-3-methylimidazolium bis(trifluoromethylsulfonyl)imide ([hmim][Tf_2N])

Item Inspection List/Questionnaire	**Yes**	**No**	**N/A**
1. Waste Disposal (***attach copy of waste label***) • Has a written waste disposal method been established? If yes, describe: The sample cup should be cleaned with appropriate solvent such as acetone to remove ionic liquid. If the ionic liquid consists of halogens, the waste should be disposed to Halogenated Waste Container. If the ionic liquid does NOT consist of halogens, it should be disposed to Non-Halogenated Waste container. The amount of waste should be written down on the attached waste label. The gas in the system is vented to ductwork via exhaust lines. • Are there any special waste concerns? If yes, describe: • How much waste is expected to be generated? Number of days in a week experiment will run: 7 days Amount generated per day (g/day or L/day): 60-100 mg [hmim][Tf_2N] per experiment (~ 7 mg/day) 20 ml (max) solvent to clean the sample cup.	☒ ☐	☐ ☒	☐ ☐
2. Will the process create emissions? If yes, describe: The gas is vented to air duct. If yes, at what rate (g/day or L/day): Ammonia (NH_3) is vented to the ductwork. See attached emission calculations.	☒	☐	☐
3. Are there any planned discharge to drains or sewer systems? If yes, describe:	☐	☒	☐

Notes:
There is a set protocol for waste container labeling, use, and disposal. Any questions or concerns about waste disposal or labeling can be directed to an advisor or EHS.

Environmental Heath and Safety (EHS)
Phone: 785-864-4089
Web address: http://ehs.ku.edu
Waste container labels/forms: http://ehs.ku.edu/ehs-forms
Policies: http://ehs.ku.edu/ehs-policies

By signing, you acknowledged that all items have been properly reviewed and deemed safe for your experimental operation.
Name: Tugba Turnaoglu Signature: _____ Date: 05/16/2017

Equipment Under Pressure

Equipment Name: Hiden XEMIS Gravimetric Microbalance

Experiment Description: 1- Ammonia absorption in various ionic liquids

2-Carbon dioxide (CO_2) absorption in 1-hexyl-3-methylimidazolium bis(trifluoromethylsulfonyl)imide ([hmim][Tf_2N])

Item Inspection List/Questioner	**Yes**	**No**	**N/A**
1. Source of pressure/vacuum: CO_2 Gas Cylinder/ Ammonia Gas Cylinder / Vacuum Pump			
2. Maximum source pressure: Ammonia-8.87 bar (114 psig, 128.7psi, 0.786 MPa) Carbondioxide- 152 bar (15.2 MPa) Maximum operating pressure: 170 bar (17MPa). The pressure of gases MUST BE lower than the saturation points to keep the fluids in gas form in the system. See attached documents for saturation information obtained via REFPROP 9.1. Maximum allowable working pressure: 300 psig (314.7 psi= 21.7 bar= 2.17MPa) Pressure relief device set point: Relief Device on the panel: 350 psig (364.7psi=25.14bar=2.514MPa) Two pressure relief device set points: 67.5 barg (68.7 bar=996.4psi=6.87MPa) 225 barg (226.7 bar-=3288 psi=22.67 MPa)			
3. Is a pressure vessel involved?	☒	☐	☐
If yes, is the vessel approved by manufacturer, advisor, or safety resource?	☒	☐	☐
4. Are equipment Materials of Construction compatible with all process materials?			
• Valves/Reliefs	☒	☐	☐
• Seals	☒	☐	☐
• Gauges	☒	☐	☐
• Hoses/Tubing	☒	☐	☐
• Fittings	☒	☐	☐
• Gaskets	☒	☐	☐
• Vessel	☒	☐	☐
5. Have calculations been completed to ensure adequate headspace for expansion/decomposition during operation? If yes, *attach* calculations.	☐	☐	☒
6. Are all components (listed in #4) rated above pressure relief set point? If no, list components and pressure ratings:	☒	☐	☐
7. Are there pressure safety interlocks? If yes, describe: Magnetic safety interlock around the reactor which prevents damage to system due to any pressure difference. If yes, location of quarterly log:	☒	☐	☐
8. What precautions have been taken in the event of pressure system failure? - Pressure relief devices burst the gas to the ductwork. - Interlock system will stop the gas source.			
9. Are rotameters shielded? If yes, how?	☐	☐	☒
10. Is a barrier/shield required to protect personnel from a catastrophic release? If yes, describe: In case of catastrophic gas release: • If the gas released from ammonia tank, the gas will be vented to ductwork. • If the gas released from XEMIS, it will be vented through ductwork. • If the gas released from regular exhausts or pressure relief devices, it will be vented to ductwork. • If the gas released from any part of the system and the air ventilation stops working, the gas will be trapped in the ventilated enclosure: faceshield (8	☒	☐	☐

1. Is a barrier/shield required to protect personnel from a catastrophic release? If yes, describe: In case of catastrophic gas release: • If the gas released from ammonia tank, the gas will be vented to ductwork. • If the gas released from XEMIS, it will be vented through ductwork. • If the gas released from regular exhausts or pressure relief devices, it will be vented to ductwork. • If the gas released from any part of the system and the air ventilation stops working, the gas will be trapped in the ventilated enclosure: faceshield (8 inch minimum), tightly fitting safety googles, butyl robber gloves, complete suit protection.	☒	☐	☐
2. Are gauges located properly (i.e. facing operator, correct position)?	☒	☐	☐
3. Are gauges the proper range for the application?	☒	☐	☐
4. Are gauges compatible with material (e.g. corrosive)?	☒	☐	☐
5. Are high pressure hoses being used? If yes, describe: The hose connects the cylinder to the system. If yes, do the hoses have the proper pressure range? Do hoses require periodic inspection/replacement? Yes If yes, how often? Once every 3 months	☒ ☒	☐ ☐	☐ ☐
6. Are relief devices pointed in a safe direction and unrestricted for vent?	☒	☐	☐
7. Is the relief device rated for dual phase (gas and liquid) operation?	☐	☒	☐
8. At what temperature will the relief devices be operated? The pressure relief device between turbo and backing pump is at room temperature. The pressure relief device in the XEMIS is at 40.8 ± 0.1 °C. Are the relief devices rated for this temperature?	☒	☐	☐
9. Have the relief devices been tested?	☒	☐	☐
10. Have the consequences of potential leaks been considered? If yes, describe: - CO_2 is a minimally hazardous gas and its leak contained in the ventilated enclosure. Also, the potential CO_2 leak will be tested with soap solution. - Ammonia cylinder will be stored in the closed secondary containment. Any leak from ammonia cylinder is directly vented to the ductwork. - XEMIS is in the ventilated enclosure. Potential ammonia leak from the XEMIS will be vented to ductwork. - If the gas released from any part of the system and the air ventilation stops working, the gas will be trapped in the ventilated enclosure: faceshield (8 inch minimum), tightly fitting safety googles, butyl robber gloves, complete suit protection.	☒	☐	☐

By signing, you acknowledged that all items have been properly reviewed and deemed safe for your experimental operation.

Name: Tugba Turnaoglu **Signature: _____** **Date: 05/16/2017**

Facilities, Laboratory, Process Area

Equipment Name: Hiden XEMIS Gravimetric Microbalance

Experiment Description: 1- Ammonia absorption in various ionic liquids

2-Carbon dioxide (CO_2) absorption in 1-hexyl-3-methylimidazolium bis(trifluoromethylsulfonyl)imide ([hmim][Tf_2N])

Item Inspection List/Questionnaire	**Yes**	**No**	**N/A**
1. Is it necessary to limit the number of people that can be in the area while operating? If yes, explain:	☐	☒	☐
2. Is it necessary to restrict entry to laboratory or process area? If yes, explain: Process area (ventilated enclosure) due to equipment sensitivity and toxicity of ammonia.	☒	☐	☐
3. Are respirators required for any part of the process? If yes, attach exposure assessment.	☐	☒	☐
4. Describe special requirements affecting laboratory personnel/visitors when entering the area (high noise, specific PPE, biological safety level, high magnetic field, etc.)? Personal Protective Equipment is required. PPE: Safety googles, long pants and sleeves, lab coat, butyl rubber or nitrile or neoprene gloves.			
5. Are area alarms required? If yes, explain: Two gas detectors with ammonia sensor is available. **1- Meridian Universal Gas detector:** • Located inside of the enclosure. • Labeled as 2-1. • Can be monitored at Channel 1 in Quadscan. • <u>If the concentration of ammonia **INSIDE** of the enclosure reaches 25 ppm, the following happens simultaneously:</u> Meridian Ammonia Sensor gives **WARNING** so that **YELLOW** light flashes and stops Air to Open (ATO) Valve so that ammonia flow is stopped. • <u>If the concentration of ammonia **INSIDE** of the enclosure reaches 50 ppm, the following happens simultaneously:</u> gives **ALARM** so that **RED** light flashes and **HORN SOUNDS**. **2- Freedom Gas Detector**: • Located outside of the enclosure. • Labeled 2-2. Can be monitored at Channel 2 in Quadscan. • <u>If the concentration of ammonia OUTSIDE of the enclosure reaches 25 ppm, the following happens:</u> Freedom Ammonia Sensor gives **ALARM** so that **RED** light flashes and **HORN SOUNDS**.	☒	☐	☐
6. Is a barricade or shield required to protect personnel? If yes, explain: Contents under pressure and contained within ventilated enclosure. However, any personnel deals with ammonia should wear full protection as described in item 4.	☒	☐	☐
7. Describe the route to the two nearest emergency exits: 1- Leave the lab from the southeast side door, and the emergency exist is in the right. 2- Leave the lab from the northeast side door, proceed to stairs at the end of corridor and exit the building.			
8. Describe the location of the nearest: • Fire/Evacuation Alarm: Outside south lab door next to the emergency door. • Fire Extinguisher: Two, next to both lab doors; one,in the hallway. Enclosure has building water sprinkler. What type of extinguishers are available? ABC: Dry powder CO_2 Are the extinguishers compatible with the materials in use? If no, what type is needed prior to startup:	☒	☐	☐
9. Describe the location of the nearest: • Safety Shower: Outside south lab door in the hallway.			

• Eye Wash: Southeast side of the lab, next to the sink. • Telephone and Emergency Contacts: Is emergency contact information up-to-date? Are there at least two Emergency Contacts with home and office phone numbers posted on laboratory door? Are there at least two Emergency Contacts with home and office phone numbers posted on the experiment?	☒ ☒ ☒	☐ ☐ ☐	☐ ☐ ☐
1. Will a lone worker be used at any time? If yes, during what times: after 5pm, and possibly weekends	☒	☐	☐
2. Will there be after hours operation (5 pm – 7 am)? If yes, reference the specific operating procedure(s) for after-hours operation: I will inform the post-docs, and I will make the emergency contact information readily available in case of emergency.	☒	☐	☐
3. Will there be weekend hours of operation?	☒	☐	☐
4. Will the experiment be unattended at any time? If yes, describe: After working hours, weekends, lunch times. Experiment will be set to automatically operate once setup.	☒	☐	☐
5. Are the following items readily available in the area? • Standard Operating Procedure (SOP)? • Emergency Shutdown Procedure? • Emergency Spill Procedure? • Your EHS training documentation?	 ☒ ☒ ☒ ☒	 ☐ ☐ ☐ ☐	 ☐ ☐ ☐ ☐
6. Is there a potential for water leaks in the area? If yes, how are hazards mitigated: We have secondary containment under the water bath.	☒	☐	☐

By signing, you acknowledged that all items have been properly reviewed and deemed safe for your experimental operation.

Name: Tugba Turnaoglu Signature: _____ Date: 05/16/2017

Gases

Equipment Name: Hiden XEMIS Gravimetric Microbalance

Experiment Description: 1- Ammonia absorption in various ionic liquids

2-Carbon dioxide (CO_2) absorption in 1-hexyl-3-methylimidazolium bis(trifluoromethylsulfonyl)imide ([hmim][Tf_2N])

Item Inspection List/Questioner	**Yes**	**No**	**N/A**
1. Gas name (***one gas per sheet, no abbreviations***): Carbondioxide, Ammonia, Air			
2. List potential hazards: Gas cylinder is under pressure. Ammonia is toxic gas.			
3. Gas source:			
• House supply [AIR]	☒	☐	☐
• Gas cylinder [AMMONIA, CARBONDIOXIDE]	☒	☐	☐
• Gas generator	☐	☐	☒
4. Maximum supply pressure: Ammonia- 114 psig (128.7 psi or 8.87 bar) at 70°F (21.1°C)] Carbondioxide – 830 psig (844.7 psi or 58.2 bar) at 70°F (21.1°C)			
5. Normal operating pressure: XEMIS up to 170 bar			
6. Maximum allowable working pressure: 8 bar in ammonia system			
7. Pressure relief device setpoint: Relief Device on the panel: 350 psig (364.7psi=25.14bar=2.514MPa) Two pressure relief device set points: 67.5 barg (68.7 bar=996.4psi=6.87MPa) 225 barg (226.7 bar-=3288 psi=22.67 MPa)			
8. Are all components compatible with this gas?			
• Valves, Relief valves, Rupture Disks	☒	☐	☐
• Seals	☒	☐	☐
• Gauges	☒	☐	☐
• Hoses and Tubing	☒	☐	☐
• Fittings	☒	☐	☐
• Gaskets and O-rings	☒	☐	☐
• Reactor/Vessel	☒	☐	☐
9. Are all components (listed in #6) rated above pressure relief device set point? If no, list components and pressure ratings:	☒	☐	☐
10. Does the process require cleaning before use (i.e. oxygen)?	☐	☒	☐
11. Are there any gas safety interlocks? If yes, describe: If the ventilation stops working, the gas safety interlock will stop experiment. If yes, location of quarterly interlock tag: Left corner-on the interlock box	☒	☐	☐
12. Are there any gas sensors? If yes, describe type/location: Meridian gas detector with ammonia sensor inside the enclosure. Outside of the enclosure, oxygen, hydrogen and ammonia detectors are available. If yes, what is the calibration schedule: Once every 3 months	☒	☐	☐
13. What precautions have been taken in the event of a pressure system failure? High Pressure operation: If the pressure exceeds 350 psig, the the pressure relief valve on the panel will burst the pressure out of the system to the ductwork. If the pressure exceeds 225 barg, the pressure relief valve will burst the pressure out of the system to the ductwork.			

1. What precautions have been taken in the event of a pressure system failure? High Pressure operation: If the pressure exceeds 350 psig, the the pressure relief valve on the panel will burst the pressure out of the system to the ductwork. If the pressure exceeds 225 barg, the pressure relief valve will burst the pressure out of the system to the ductwork. Low Pressure: If the pressure exceeds 67.5 barg, the pressure relief valve will burst the pressure out of the system to ductwork. Also, the rupture disk prevents the pressure transducers to burn off.			
2. Are gauges located properly (i.e. facing operator, correct position)?	☒	☐	☐
3. Are gauges the proper range for the application?	☒	☐	☐
4. Are check valves needed? If yes, explain:	☐	☒	☐
5. Is there potential for cross contamination? If yes, explain:	☐	☒	☐
6. Are lines properly installed and labeled?	☒	☐	☐
7. Any mismatched fittings and/or tubing (i.e. plastic and metal together) If yes, describe:	☐	☒	☐
If yes, is the pressure approved for lowest material rating?	☒	☐	☐
8. Have regulator(s) been inspected for leaks, non-functioning/broken gauges, corrosion, etc.?	☒	☐	☐
9. Are relief devices pointed in a safe direction and unrestricted for vent?	☒	☐	☐
10. At what temperature will the relief devices be operated? Panel Relief Device at room temperature Xemis Relief Devices at cabinet temperature (40.8 °C= 105.44 °F) Are the relief devices rated for this temperature?	☒	☐	☐
11. Have the relief devices been tested and checked for leaks?	☒	☐	☐
12. Is gas flammable?	☐	☒	☐
If yes, ***complete the flammables checklist***			
If yes, has an excess flow valve been installed on the regulator?	☐	☐	☐
If yes, has a flame arrestor been installed on the regulator?	☐	☐	☐
13. Is the gas corrosive/toxic?	☒	☐	☐
If yes, list precautions that have been taken: 1- Small cylinder (limited quantity at risk) in use. 2- The ammonia cylinder is stored in the secondary containment. 3- All system is located in the ventilated enclosure. The ammonia is emitted to the ductwork in desorption rate by ensuring OSHA PEL.			
Is a scrubber or pollution device required?	☐	☒	☐
14. Is the cylinder protected from exposure to heat sources or flammable liquids?	☒	☐	☐
15. Where is the cylinder kept and secured when in use? The ammonia cylinder is secured by chain in flammable gas cabinet.			
16. Where is the cylinder kept and secured when not in use? Carbondioxide cylinder is inside ventilated enclosure. Ammonia is in flammable gas cabinet.			

By signing, you acknowledged that all items have been properly reviewed and deemed safe for your experimental operation.

Name: Tugba Turnaoglu Signature: _____ Date: 05/16/2017

Flammable Gases, Liquids, Solids

Equipment Name: Hiden XEMIS Gravimetric Microbalance
Experiment Description: 1- Ammonia absorption in various ionic liquids
2-Carbon dioxide (CO_2) absorption in 1-hexyl-3-methylimidazolium bis(trifluoromethylsulfonyl)imide ([hmim][Tf_2N])

Item Inspection List/Questionnaire	Yes	No	N/A
1. Are there any reactivity, explosion, or decomposition hazards associated with the experiment or process? If yes, describe: Ammonia is combustible gas (16-25% concentration in air)	☒	☐	☐
2. Are there any ignition sources such as sparking motors, switches, alarms, exposed heaters or static electricity? If yes, describe:	☐	☒	☐
3. Are there any fuel sources such as feedstocks, products, solvents, gaseous reaction products, insulation, etc. in the area that could be ignited? If yes, describe:	☐	☒	☐
4. Is the flammable material a gas? Ammonia is not flammable; however, it is combustible. If yes, name of gas and HMIS flammability rating: 1 • What precautions have been taken: Enclosure has sprinklers. • Are non-sparking tools required? If yes, also complete the gas checklist.	☐	☒	☐
5. Is the flammable material a liquid? If yes, name of liquid and HMIS flammability rating: If yes, what is the flashpoint? If yes, quantity of liquid: • Is liquid under pressure? If yes, also complete equipment under pressure checklist. • What precautions have been taken:	☐	☒	☐
6. Is the flammable material a solid? If yes, name of solid and HMIS flammability rating: If yes, quantity of solid: • What precautions have been taken:	☐	☒	☐
7. Are there automatic detection devices for flammable mixtures? If yes, describe: The flammable detector inside in the enclosure detects the ammonia. Also, ammonia detector outside of the cabinet detects the ammonia.	☒	☐	☐
8. Are there automatic detection devices for oxygen? If yes, describe: Yes. Oxygen detector.	☒	☐	☐
9. Are there automatic detection devices for fire? If yes, describe: Smoke detectors are located on the ceiling.	☒	☐	☐
10. Are flash arrestors needed?	☐	☒	☐
11. Are there any specific operating hazards due to flammability issues? If yes, explain:	☐	☒	☐
12. Is a barricade or shield required to protect personnel from a catastrophic release?	☒	☐	☐

By signing, you acknowledged that all items have been properly reviewed and deemed safe for your experimental operation.

Name: Tugba Turnaoglu **Signature: _____** **Date: 05/16 /2017**

High or Low Temperature

Equipment Name: Hiden XEMIS Gravimetric Microbalance

Experiment Description: 1- Ammonia absorption in various ionic liquids

2-Carbon dioxide (CO_2) absorption in 1-hexyl-3-methylimidazolium bis(trifluoromethylsulfonyl)imide ([hmim][Tf_2N])

Item Inspection List/Questioner	**Yes**	**No**	**N/A**
1. Describe operating temperature range below. • Celsius: 0°C to 80°C • Fahrenheit: 32 °F to 176 °F			
2. Describe method of heating: Standard Furnace heating, Water Bath 3. Describe related hazards: Standard furnace heating: The container might get hot. Water Bath: Potential water spill			
4. Method of cooling: Water Bath, Cryo • Recirculated cooling? • Once through cooling? (Example: using tap water through condenser to drain) If yes, describe:	☒ ☐	☐ ☒	☐ ☐
5. Describe the surface temperatures during normal operations. • Celsius: 0 °C to 80 °C • Fahrenheit: 32 °F to 176 °F			
6. Are warning signs or barricades needed? If yes, describe: Experiment in progress form will indicate the temperature and pressure.	☒	☐	☐
7. What is the minimum personal protective equipment required for working with high or low temperatures? Low Temperature- Safety glasses, lab coat, and insulated gloves High Temperature- Safety glasses, heat resistant gloves	☒	☐	☐
8. Can rapid temperature rise or fall create a hazard? If yes, describe what safeguards are in place: No part of an ammonia cylinder should be subjected to a temperature higher than 125°F (52°C). In case air conditioning is turned off, the temperature in the room is potentially not exceed 113°F (45 °C).	☒	☐	☐
9. Are there temperature safety interlocks? If yes, describe: Water bath. It is set to 90 °C. If yes, location of quarterly interlock tag: The interlock is attached behind of the water bath.	☒	☐	☐
10. Has a secondary over-temperature controller been installed as a backup to the primary control? Water bath has a secondary over temperature controller.	☒	☐	☐
11. Are independent temperature measuring devices (i.e. thermocouples) being used for the primary and over-temperature controls? The standard furnace has controller thermocouples both sample and tare side.	☒	☐	☐

By signing, you acknowledged that all items have been properly reviewed and deemed safe for your experimental operation.

Name: Tugba Turnaoglu **Signature: _____** **Date: 05/16/2017**

Mechanical Motion

Equipment Name: Hiden XEMIS Gravimetric Microbalance
Experiment Description:
1- Ammonia absorption in various ionic liquids
2-Carbon dioxide (CO_2) absorption in 1-hexyl-3-methylimidazolium bis(trifluoromethylsulfonyl)imide ([hmim][Tf_2N])

Item Inspection List/Questionnaire	Yes	No	N/A
1. Identify all of the following that apply to this equipment, and describe the safety guards and other safety precautions.			
• Rotating? If yes, describe:	☐	☒	☐
• Belts or Chains? If yes, describe:	☐	☒	☐
• Pinch Points? If yes, describe:	☐	☒	☐
• Sliding? If yes, describe:	☐	☒	☐
• Reciprocating? If yes, describe:	☐	☒	☐
• Cutting/Sharp Edges? If yes, describe:	☐	☒	☐
• Oscillating? If yes, describe:	☐	☒	☐
• Stored Potential Energy? If yes, describe: Pressure in the reactor, and UPS	☒	☐	☐
• Other? If yes, describe:	☐	☒	☐
2. Is a written "Lock-Out" procedure to prevent motion included in the standard operating procedure?	☐	☒	☐

By signing, you acknowledged that all items have been properly reviewed and deemed safe for your experimental operation.

Name: Tugba Turnaoglu Signature: _____ Date: 05/17 /2017

Raw Materials and Products

Equipment Name: Hiden XEMIS Gravimetric Microbalance

Experiment Description:

1- Ammonia absorption in various ionic liquids

2-Carbon dioxide (CO_2) absorption in 1-hexyl-3-methylimidazolium bis(trifluoromethylsulfonyl)imide ([hmim][Tf_2N])

Item Inspection List/Questionnaire	**Yes**	**No**	**N/A**
1. Complete the following items (where applicable) and attach to checklist:			
• Process description (include a list of reactants, products, and chemistry of reactions).	☒	☐	☐
• Process flow diagram/equipment drawing	☒	☐	☐
• MSDS (include reactants, products, and important intermediates)	☒	☐	☐
• Heat balance-	☐	☐	☒
• Material balance –	☒	☐	☐
2. Answer questions below describing the transport, safe handling, and emissions of the process materials.			
• Is the hood/ventilation working properly?	☒	☐	☐
• What is the ductwork material: Stainless steel			
• Is the ductwork compatible with experimental emissions?	☒	☐	☐
• Is there potential for condensate or dust collection in ventilation? If yes, explain:	☐	☒	☐
• How will experimental materials be stored: ionic liquids stored in glass containers within a nitrogen glove box. Is secondary containment required?	☐	☒	☐
• Is refrigeration required? If yes, what type:	☐	☒	☐
• How will materials be transported through building/lab: The chemicals will be transported in the containers. Gas cylinders will be removed using the cylinder cart and will be properly capped during the transportation.			
• Will any materials be shipped off site?	☐	☒	☐
• Is secondary containment (i.e. spill tray) available for the equipment? Water bath places within a spill tray. Ammonia cylinder is stored in secondary containment.	☒	☐	☐

1. Raw materials and Intermediates:

Identify the potential material hazards by *filling out and attaching the evaluation sheet* below (use as many as necessary). This form will include all raw materials and intermediates, in solid, liquid or gaseous form.

Fill out table. Attach additional tables if needed.

Material	**#1**	**#2**	**#3**
Material Name	Ammonia, Anhydrous	Carbon dioxide	[hmim][Tf2N]
Quantity	Cylinder Type UH, 2.26 kg	Cylinder Size 1A	~50 mg
CAS Number	7664-41-7	124-38-9	382150-50-7
MSDS - ***Attach***	☒	☒	☒
HMIS – Health (0-4)	3	1	NA
HMIS – Flammability (0-4)	1	0	NA
HMIS – Reactivity (0-4)	0	0	NA
Corrosive	☐	☐	☒
Carcinogen	☐	☐	☐
Developmental Toxin	☐	☐	☐
Reproductive Toxin	☐	☐	☐
Mutagen	☐	☐	☐
Pyrophoric	☐	☐	☐
Odor Generator (threshold)	☒(OSHO-5 ppm)	☐	☐
Shock Sensitive	☐	☐	☐
Light Sensitive	☐	☐	☐
Peroxidizable	☐	☐	☐
Radioisotope	☐	☐	☐
Temperature Sensitive	☐	☐	☒
Oxidizer	☐	☐	☐
TSCA Inventory List	☐	☐	☐
Other Hazards:	Toxic; irritant OSHA PEL:50 ppm NIOSH IDLH: 300 ppm AIHA ERPG-2: 200 ppm		Maybe unknown hazard

OSHA PEL: Occupational Safety and Health Administration Permissible Exposure Limit

NIOSH IDLH: the US National Institute for Occupational Safety and Health Immediately Dangerous to Life or Health

AIHA ERPG: American Industrial Hygiene Association Emergency Response Planning Guidelines. AIHA ERPG is the maximum airborne concentration below which it is believed that nearly all individuals could be exposed for up to 1 hour without experiencing or developing irreversible or other serious health effects of symptoms which could impair an individual's ability to take protective action.

By signing, you acknowledged that all items have been properly reviewed and deemed safe for your experimental operation.

Name: Tugba Turnaoglu Signature: _____ Date: 05/16/2017